ISBN 978-82-326-3178-0 (printed version)
ISBN 978-82-326-3179-7 (electronic version)
ISSN 1503-8181

Doctoral theses at NTNU, 2018:194

Chenyu Luan

Design and analysis for a steel braceless semi-submersible hull for supporting a 5-MW horizontal axis wind turbine

NTNU
Norwegian University of
Science and Technology
Faculty of Engineering
Department of MarineTechnology

NTNU
Norwegian University of
Science and Technology

Chenyu Luan

Doctoral Thesis

Doctoral theses at NTNU, 2018:194

NTNU

Chenyu Luan

Design and analysis for a steel braceless semi-submersible hull for supporting a 5-MW horizontal axis wind turbine

Thesis for the degree of Philosophiae Doctor

Trondheim, June 2018

Norwegian University of Science and Technology
Faculty of Engineering
Department of MarineTechnology

NTNU
Norwegian University of
Science and Technology

NTNU
Norwegian University of Science and Technology

Thesis for the degree of Philosophiae Doctor

Faculty of Engineering
Department of MarineTechnology

ISBN 978-82-326-3178-0 (printed version)
ISBN 978-82-326-3179-7 (electronic version)
ISSN 1503-8181

Doctoral theses at NTNU, 2018:194

Printed by Skipnes Kommunikasjon as

Abstract

This thesis deals with design and analysis of steel semi-submersible hulls for supporting MW-level horizontal axis wind turbines. The thesis address the following four topics: 1) conceptual design methods, 2) conceptual design of a steel braceless hull for supporting a reference wind turbine (denoted as 5-MW-CSC), 3) development, verification and validation of numerical approaches for analyzing global structural responses of structural components of semi-submersible hulls in wind and waves, and 4) case studies related to numerical simulations and experimental measurements for load and load effects on semi-submersible wind turbines.

Simplified design procedure, criteria and design check approaches for conceptual design with respect to safety have been systematically presented and discussed based on publicly accessible publications and the author's experience and practice in the past six years.

The 5-MW-CSC is developed based on the simplified design procedure, criteria and design check approaches. Numerical analysis shows that the 5-MW-CSC has very good intact stability, well designed natural periods and modes, moderate rigid-body motions in extreme environmental conditions and a reasonable structural design.

The structural design of the 5-MW-CSC is checked by using simplified ULS and FLS design checks. Two time-domain approaches, which can be easily implemented in various state-of-the-art computer codes to extend their capabilities to analyze sectional forces and moments in structural components of generic and specific floaters subject to environmental loads from wind and waves, were developed by the author. The developed approaches focus on modeling of inertia and external loads on the floaters and mapping of the loads in finite element model of the floaters. The floaters are considered as an assemblage of several structural components. The conventional hybrid frequency-time domain approach is extended to model the external loads on and inertia loads of each structural

component. Limitations of the developed time-domain approaches and future work for solving these limitations are discussed.

The developed approach for generic floaters were verified and validated by comparing with simulated responses given by other reference numerical models and measurements from a 1:30 scaled model test campaign using the ReaTHM® testing approach to overcome the limitations of conventional model test approaches. The verification and validation consist of five comparisons. Objectives and expected results of the five comparisons are illustrated. In general, the comparisons agree with the expectations while possible reasons for the deviations are thoroughly and quantitatively analyzed.

Effect of non-linear wave excitation loads, drag forces, each load component, and steady wind and wave loads induced by changes of the mean wetted body surface on rigid-body motions and sectional bending moments in five specified cross-sections on the hull of the 5-MW-CSC were analyzed by comparing the measurements of the model test campaign and carrying out numerical sensitivity study.

These analyses shed more light on features of the loads and load effect on and critical structural components of the hull of the 5-MW-CSC, and critical environmental conditions for the 5-MW-CSC with respect to fatigue damage and extreme load effects. The obtained understanding was used to simplify complexity of numerical models of the 5-MW-CSC to reduce computational cost of the design checks, and is helpful for reducing design conditions required by ULS and FLS design checks and structural optimization.

Experience acquired from design and analysis of the 5-MW-CSC and development of the time-domain approaches will promote development of novel and cost efficient designs of semi-submersible wind turbines; while the 5-MW-CSC and developed approaches can be used as reference to validate other computer codes for analyzing global responses of floating wind turbines.

Preface

This thesis is submitted to Norwegian University of Science and Technology (NTNU) in partial fulfilment of requirements for degree of Doctor of Philosophy.

The thesis is a result of my research work carried out at the Department of Marine Technology at NTNU, supervising by Prof. Torgeir Moan (my major supervisor) and Prof. Zhen Gao (my co-supervisor) from August 2011 to May 2018.

One objective of my Ph.D study is to develop a novel, cost effective and reliable design of semi-submersible hull for supporting wind turbines. This is a very challenge task which needs a huge effort since 1) design is an iterative process, 2) development of floating wind turbines is in its early stage, and 3) floating wind turbines are complex system with strongly coupled subsystems, i.e. the wind turbine, control system, hull and mooring system. Consequently, significant efforts were needed in addition to a normal 3-year Ph.D program.

To solve this challenge, in additional to the funding for my 3-year Ph.D study by the Norwegian Research Centre for Offshore Wind Technology (NOWITECH), additional funding was obtained from the Research Council of Norway through the Centre for Ships and Ocean Structures (CeSOS) and the Centre for Autonomous Marine Operations and Systems (AMOS), and the EU FP-7 project MARINA Platform project to contribute to these projects.

In the framework of CeSOS and NOWITECH, I cooperated with other researchers. By now, as first author or co-author, I have published five journal papers and seven conference papers while there is a paper has been submitted to a journal for review.

This thesis is paper-based and composed of a summary of five attached papers and an attached report. The summary highlights my contribution with respect to 1) conceptual design methods, 2) conceptual design and analysis of semi-submersible wind turbine hulls and 3) development, verification and validation for numerical approaches for analyzing global structural responses. While detailed information is referred to the attached papers and report.

I intend to make the summary easy to read, and to be a helpful, informative and suitable reference for readers of this thesis, in particular for inexperienced researchers, students and engineers who are working on or would like to work on design and numerical and experimental analysis of global responses of floating wind turbine hulls in wind and waves. Consequently, relevant background information is highlighted in the summary, while some detailed information with respect to the differences between the developed numerical approaches and conventional approaches and the procedure for verifying and validating the developed approach are included in the summary as well.

Acknowledgements

The work of this thesis was conducted at the Center for Ships and Ocean Structures (CeSOS) at the Norwegian University of Science and Technology (NTNU) in Trondheim, Norway. While the work is funded by the Research Council of Norway (RNC) through the Norwegian Research Centre for Offshore Wind Technology (NOWITECH), NTNU (Grant number 193823); the Norwegian Centre of Excellence (CoE), which is a part of the RNC funding scheme, through CeSOS (Grant number 146025/410) and the Centre for Autonomous Marine Operations and Systems (AMOS), NTNU (Grant number 223254); and the European Commission the 7th Framework Programme (MARINA Platform project, Grant Agreement 241402).

I highly appreciate that I could be supported to have seven years to work on research of floating wind turbines under supervision of my major supervisor, Prof. Torgeir Moan, and co-supervisor, Prof. Zhen Gao. They helped me gradually to know what is and how to do research work and bring me to academic society. They provided many great opportunities and support for me to build strong confidence in thinking from the first principle with rational analysis, and be aware of the importance of being clear about basic concepts and fundamental theories and being precise and professional. Now, I am used to make in-depth and broad thinking, be sensitive to new information and novel ideas, be innovative and creative, carry out independent study and analysis to find answers to my concerns, be helpful and pleasure to share knowledge, and cooperate with other researchers for interesting in common. Their very positive attitudes with respect to work, students and social life also strongly influenced me. They are examples for me.

I would like to thank my colleagues, scientific staff, and technical and administrative staff from the Department of Marine Technology of NTNU, CeSOS, AMOS, and NOWITECH.

I would like to thank Prof. Odd M. Faltinsen for teaching me hydrodynamic aspects of marine structures; Prof. Jørgen Amdahl for teaching me design of offshore structures, and buckling and collapse

of marine structures; Prof. Bernt J. Leira, Prof. Dag Myrhaug, Prof. Zhen Gao, and Associate Prof. Sverre K. Haver for lecturing me stochastic theory of sea loads; Prof. Stig Berge for teaching me fatigue and fracture; Prof. Carl Martin Larsen and Prof. Svein Sævik for teaching me dynamic analysis of slender structures; Prof. Sverre Steen for teaching me experimental methods in marine hydrodynamics; Prof. Torgeir Moan for teaching me finite element method for structural modelling and analysis and structural reliability analysis; and Michael Muskulus for teaching me design of offshore wind turbines. The high quality courses I learned at NTNU serves as a solid foundation of my research work presented in this thesis.

DNVGL's software, e.g. Genie, PULS, Sestra, DeepC (Simo-Riflex), HydroD, WADAM, and DNVGL standards and engineering practices are intensively used in my research work. I appreciate the help I received from the DNVGL software support, and rules and standards teams. I enjoy the discussions with Mr. Jan Henrik Berg-Jensen, Dr. Xu Xiang, Dr. Zhiyuan Pan, and Dr. Zhenju Chuang.

I would like to thank Dr. Jason Jonkman and Dr. Amy Roberson for hosting my scientific visit at NREL at beginning of my Ph.D study and the help with respect to computer codes FAST and Aerodyn. While, I enjoy the cooerpations with Dr. Valentin B. Chabaud, Associate Prof. Erin E. Bachynski, Dr. Marit I. Kvittem, Associate Prof. Amir R. Nejad, Dr. Mahmoud Etemaddar, Dr. Kai Wang, Dr. Constantine Michailides and Mr. Thomas M. Sauder.

I would like to thank Mr. Qinyuan Li, Mrs. Chenxing Li, Mr. Joakim D. Andersen, Prof. Muk Chen Ong, Associate Prof. Yanlin Shao, Dr. Huirong Jia, Mr. Jian Guo, Dr. Junbo Jia, Dr. Haibo Chen, Dr. Naiquan Ye, Prof. Shixiao Fu, Dr. Yihan Xing, Dr. Zhiyu Jiang, Dr. Ling Wan, Dr. Lin Li, Dr. Xiaopeng Wu, Dr. Zhijun Wei, Dr. Hui Liang, Dr. Madjid Karimirad, Dr. Made J. Muliawan, Dr. Jacobus B. De Vaal, Dr. Martin Storheim, Dr. Mia Abrahamsen Prsic, and many friends for interesting discussions in research work, constructive suggestions and memories of social activities.

Finally, I want to give my special thanks to my parents (Mr. Xiangdong Luan and Mrs. Xueling Yu) and my grandma (Mrs. Wenshen Wang). Their understanding and support encourage me.

List of Appended Papers

This thesis consists of an introductory part, five papers (two published journal papers, two published conference papers and one journal paper submitted for review) and a report for simplified method for conceptual design which is related to the objective of this thesis.

The following five papers are reported in Appendix A:

Paper A1

Development and verification of a time-domain approach for determining forces and moments in structural components of floaters with an application to floating wind turbines

Chenyu Luan, Zhen Gao and Torgeir Moan

Published in Marine Structures, Volume 51, pages 87-109, https://doi.org/10.1016/j.marstruc.2016.10.002.

Paper A2

Experimental validation of a time-domain approach for determining sectional loads in a floating wind turbine hull subjected to moderate waves

Chenyu Luan, Valentin Chabaud, Erin E. Bachynski, Zhen Gao and Torgeir Moan

Published in Energy Procedia, Volume 137, Pages 366-381, https://doi.org/10.1016/j.egypro.2017.10.361

Paper A3

Comparisons and analysis of simulated and measured motions and sectional loads in a floating wind turbine hull subjected to combined wind and waves

Chenyu Luan, Zhen Gao and Torgeir Moan

Submitted for review at Engineering Structures

Paper A4

Modelling and analysis of a semi-submersible wind turbine with a central tower with emphasis on the brace system

Chenyu Luan, Zhen Gao and Torgeir Moan

Published in 32nd International Conference on Ocean, Offshore and Arctic Engineering, no, OMAE2013-10408, Nantes, France.

Paper A5

Design and analysis of a braceless steel 5-mw semi-submersible wind turbine

Chenyu Luan, Zhen Gao and Torgeir Moan

Published in 35th International Conference on Ocean, Offshore and Arctic Engineering, OMAE2016-54848, Busan, Korea, June 19–24.

The report for simplified method for conceptual design which is related to the objective of this thesis is presented in Appendix B:

Paper B1

Report: Simplified method for conceptual design of semi-submersible wind turbines

Chenyu Luan, Zhen Gao and Torgeir Moan

Declaration of authorship

All the five papers and the report that serve as the core content of this thesis are co-authored. In all of these papers and report, I was the first author and responsible for initiating ideas, establishing numerical models, performing the analysis, post-processing numerical simulations and experimental measurements, presenting the results and discussions, writing the papers, and responding to comments and questions from reviewers and other readers. Professor Torgeir Moan is my major supervisor while Professor Zhen Gao is my co-supervisor. They are co-authors of all of the five papers and the report. They have contributed to the support, discussions and constructive comments to increase the scientific quality of the publications. Dr. Valentin Chabaud and Associate Professor Erin E. Bachynski are the second and third authors of Paper A2, respectively. They have contributed to 1) providing original data of the model test mentioned in Paper A2; 2) discussions of the comparison between experimental and numerical results; and 3) comments on the writing of the paper.

Additional Papers

As mentioned in Preface, significant efforts were needed in addition to a normal 3-year Ph.D program. To solve this challenge, in additional to the funding for my 3-year Ph.D study by NOWITECH, additional funding was obtained from CeSOS and the EU FP7 MARINA Platform project to contribute to these projects. Some major projects, which were supported by the additional funding and carried out during my Ph.D study, are listed in the following.

Papers C1, C2, and C3 shed light on the dynamic behavior of semi-submersible wind turbines in various complicated environmental conditions when compared to a TLP type and a Spar type floating wind turbines, while the strong coupling between the subsystems is addressed.

Paper C4 shed light on comparisons of dynamic behavior of a MW-level horizontal axis semi-submersible wind turbine and a MW-level vertical axis semi-submersible wind turbine in operational and extreme conditions.

Papers C5 and C6 shed light on the reduction of levelized cost of energy by using hybrid wind and wave energy converters for which the semi-submersible hulls are designed to support both of a MW-level horizontal axis wind turbine and three special designed flap-type wave energy converters.

Paper C7 describes design of the OC4 semi-submersible wind turbine, for which braces are used to connect the columns and pontoons of the design as an integrated structure. The OC4 semi-submersible wind turbine has been well known as a reference semi-submersible wind turbine and widely used by researchers. I was involved in design and analysis of the mooring system of this design.

Paper C8 focuses on numerical computer code to code comparisons for which conventional time-domain computer codes for analyzing global responses of floating wind turbines used by worldwide participants are collected and compared.

Paper C9 shed light on short-term fatigue damage on the tower of a semi-submersible wind turbine while a simplified time-domain aerodynamic code is used in the short term simulations.

The work done and presented in the additional papers are important to me to finalize the core content of the work, which is related to design and analysis of a braceless steel semi-submersible hull for supporting a MW-level horizontal axis wind turbine, presented in my Ph.D thesis. However, the corresponding papers of these additional studies are not considered part of this thesis. Instead, they are listed in the following.

List of additional papers:

[C1] Bachynski, E.E., Etemaddar, M., Kvittem, M.I., Luan, C., Moan, T., (2013) "Dynamic analysis of floating wind turbines during pitch actuator fault, grid loss, and shutdown", Energy Procedia vol. 35, 210-222. doi:10.1016/j.egypro.2013.07.174

[C2] Bachynski, E.E., Kvittem, M., Luan, C., and Moan, T., (2014). "Wind-wave misalignment effects on floating wind turbines: motions and tower load effects", ASME J. Offshore Mech. Arct. Eng., 136 (4), pp. 0419021–04190212.

[C3] Nejad, A.R., Bachynski, E.E., Kvittem, M.I., Luan, C., Gao, Z. and Moan, T., (2015), "Stochastic Dynamic Load Effect and Fatigue Damage Analysis of Drivetrains in Land-based and TLP, Spar and Semi-Submersible Floating Wind Turbines", Marine Structures, Vol 42, pp 137–153.

[C4] Wang, K., Luan, C., Moan, T., Hansen, M., (2014), "Comparative study of a FVAWT and a FHAWT with a semi-submersible floater", Proceedings of the Twenty-fourth (2014) International Offshore and Polar Engineering Conference, Busan, Korea.

[C5] Luan, C., Michailides, C., Gao, Z. and Moan, T., (2014), "Modeling and analysis of a 5 MW semi-submersible wind turbine combined with three flap-type Wave Energy Converters", in 33rd International Conference on Ocean, Offshore and Arctic Engineering, no.OMAE2014-24215, San Francisco, USA.

[C6] Michailides, C., Luan, C., Gao, Z. and Moan, T., (2014), "Effect of flap type wave energy converters on the response of a semi-submersible wind turbine", In 33rd International Conference on Ocean, Offshore and Arctic Engineering, no.OMAE2014-24065, San Francisco, USA

[C7] Robertson, A., Jonkman, J., Masciola, M., Song, H., Goupee, A., Coulling, A., and Luan C., (2012), "Definition of the Semisubmersible Floating System for Phase II of OC4", Offshore Code Comparison Collaboration Continuation (OC4) for IEA Task 30.

[C8] Robertson, A., Jonkman, J. Qvist, J.,Chen, X., Armendariz,J.A., Soares, C.G., Luan, C., Huang, Y., Yde, A.,Larsen, T., Nichols, J., Lei, Liu, Maus, K.J., Godreau, C., Heege, A., Vatne, S.R., Manolas,D., Qin, H., Riber, H., Abele, R., Yamaguchi, A., Pham,A. Alves,M., Kofoed-Hansen,H., (2014), "Offshore code comparison collaboration, continued: phase II results of a floating semisubmersible wind system", In Proceedings of the 33rd International Conference on Ocean, Offshore and Arctic Engineering, no. OMAE2014-24040, San Francisco, USA, 2014.

[C9] Kvittem, M.I., Moan, T., Gao, Z. and Luan, C, (2011), "Short-Term Fatigue Analysis of Semi-Submersible Wind Turbine Tower", Proceedings of the 30th International Conference on Ocean, Offshore and Arctic Engineering. 19-24 June 2011 - Rotterdam, the Netherlands.

Abbreviations

d.o.f.	Degree of freedom
DNVGL	Det Norske Veritas and Germanischer Lloyd
DOM	Design Overturning Moment
FDM	Frequency-domain Model
FLS	Fatigue Limit State
IEC	International Electrotechnical Commission
MW	Megawatt
NREL	National Renewable Energy Laboratory
NOWITECH	Norwegian Research Centre of Offshore Wind Technology
RAO	Response Amplitude Operator
RMC	Righting Moment Curve
RNA	Rotor Nacelle Assembly
SWL	Still Water Line
TDM	Time-domain Model
TLP	Tension-Leg Platform
ULS	Ultimate Limit State

Contents

List of Tables

List of Figures

Chapter 1

Introduction

Development of wind energy is driven by the fact that wind energy is an attractive solution to feed the huge demand of energy consumption in future. By now, onshore wind energy has been well developed. Wind power industry is moving from on-shore to offshore, from on-land and shallow water to deeper water, from bottom fixed wind turbines to floating wind turbines. Background information of these issues is introduced in Section 1.1 in together with a brief introduction (more details are given in later chapters of this thesis) with respect to the state-of-the-art knowledge, limitations and challenges about design and analysis of semi-submersible wind turbines. The research work included in this thesis intends to give contributions to solve these limitations and challenges. Four specified objectives and interconnection between the objectives and the appended papers are presented in Section 1.2.

1.1 Background

1.1.1 Wind Energy: An attractive solution to feed the huge demand of energy consumption in future

The 2017 Revision of World Population Prospects published by United Nations (2017) shows that the world population of 7.6 billion in the year 2017 is expected to reach 8.6 billion in 2030, 9.8 billion in 2050 and 11.2 billion in 2100. While, the United States Energy

Information Administration (IEO, 2017) projects that world energy consumption will grow by 28% between 2015 and 2040, from 575 quadrillion British thermal units (Btu) to 736 quadrillion Btu. Wind energy, which is clean and renewable, is more and more attractive to human civilizations to feed the huge demand of energy consumption in future as concern with sustainable development, global warming and climate change, and environmental protection keep increasing. As released by the Global Wind Energy Council (GWEC 2016) "more than 54 GW of clean renewable wind power was installed across the global market in 2016, which now comprises more than 90 countries, including 9 with more than 10,000 MW installed, and 29 which have now passed the 1,000 MW mark. Cumulative capacity grew by 12.6% to reach a total of 486.8 GW". As shown in the WindEurope's Central Scenario (Wind Europe 2017) "323 GW of cumulative wind energy capacity would be installed in the EU by 2030, 253 GW onshore and 70 GW offshore.

By now, onshore wind energy has been well developed. Arup, a leading engineering consultant firm, discovered that cost of onshore wind energy development now competitive with gas in the UK (Energy Manager Today, 2017). While, the potential of offshore wind energy is substantial, particularly in relatively deep water (e.g. deeper than 50 m (EWEA 2013)).

1.1.2 On-shore MW-level wind turbines

A modern on-shore MW-level horizontal axis wind turbine is composed of a Rotor Nacelle Assembly (RNA) and a tower. As shown in Figures 1.1 and 1.2, the tower is mounted on a foundation on ground and is used to support the rotor and nacelle. The rotor is composed of a hub and several blades, e.g. three blades or two blades. The blades are attached on the hub. A drive train system and a generator are located in the nacelle. The drive train is used to connect the rotor and generator. For a conventional generator, a speed increasing gearbox is needed. This means the drive train includes a low speed shaft, a high speed shaft and a speed increasing gearbox. One end of the low speed shaft is connected to the hub while one end of the high speed shaft is connected to the generator. The rest ends of the low speed and high speed shafts are connected to the gear box

which is used to transfer kinetic energy of the shafts. In additional to the conventional generator, there has been considerable development of generators driven directly by the wind turbine rotor without a speed increasing gearbox. For these generators, the hub is directly connected to the generator by a shaft.

Aerodynamic loads on the blades result in a torque which rotates the hub with respect to the axis of the low speed shaft while the generator provides a resistant moment on the high speed shaft and convert kinetic energy to electrical power. The blades are rotatable. A control system is used to adjust the pitch angle of the blades, see Figures 1.2, and the resistant moment provided by the generator to start-up and shut down the wind turbine, and to optimize output electrical power. A yaw drive, which is located on tower top, is used to rotate the nacelle to insure that, for an upwind rotor, the rotor plane is facing to the direction of incident winds and on the upwind side of the tower. Similarly, for a downwind rotor, the rotor plane is on the downwind side of the tower. The blades are deformed by external and inertial loads on the blades. Upwind rotor should be designed to have sufficient clearance between the blades and the tower. For downwind rotor, deformation of the blades induced by mean component of the external loads will increase the clearance between the blades and tower. However, for downwind rotor, effect of aerodynamic loads on the blades, which are induced by wake of the tower, needs to be appropriately analyzed.

In addition to MW-level horizontal axis wind turbines, which have been well developed, some conceptual designs of MW-level vertical axis wind turbines, see Figure 1.3, have been developed and analyzed by some researchers. Detailed information of vertical axis wind turbines is referred to (Wang et al., 2014).

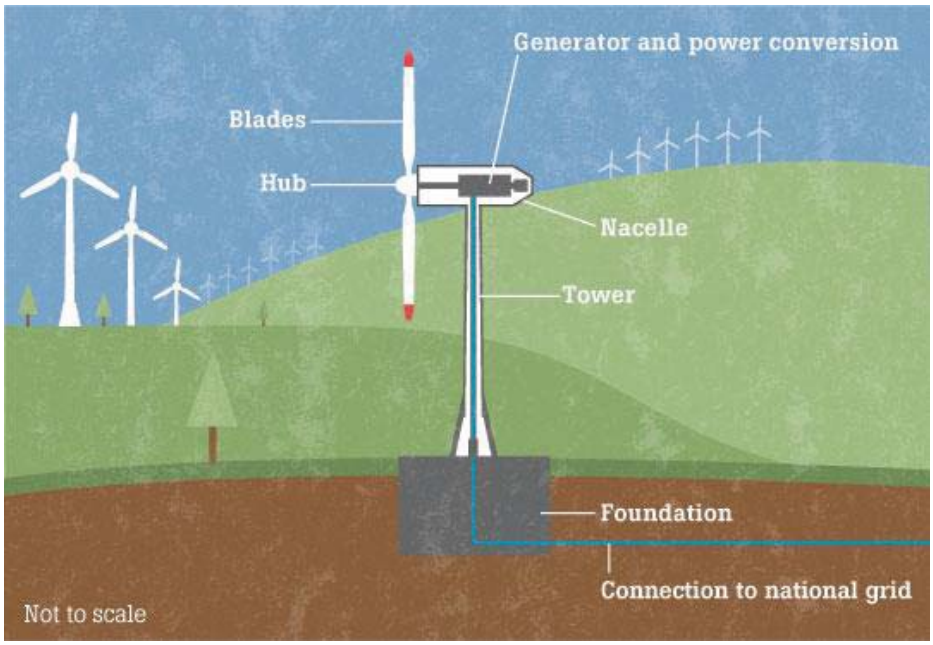

Figure 1.1 Configuration of on-land wind turbines (Renewable Energy Bangladesh, 2018)

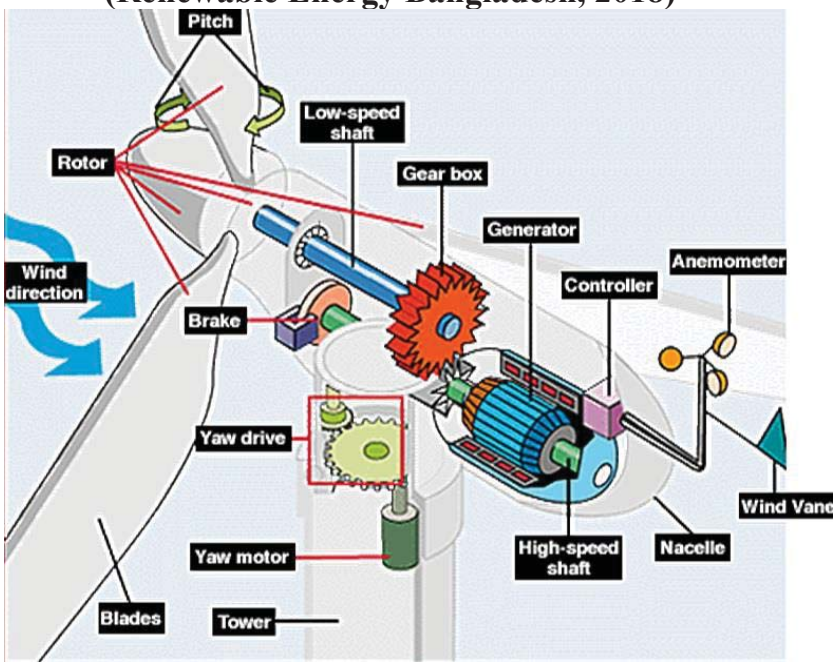

Figure 1.2 Rotor nacelle assembly (Wind Energy Programmatic EIS, 2018)

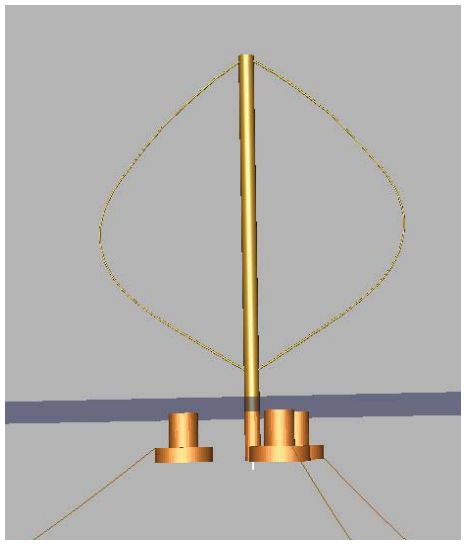

Figure 1.3 Configuration of a vertical-axis semi-submersible wind turbine (Wang et al., 2014)

1.1.3 Trend for developing offshore wind energy

Offshore wind power has several advantages over onshore wind power (Twidell and Gaudiosi, 2009). First, offshore wind sites generally produce stronger winds with less turbulence on average because sea surface is considerably smoother than land surface. Second, effects of noise and visual pollution from these sites on humans are negligible because of their distance from populated areas. Third, in most countries, sea is owned by government rather than private landlords, which allows for development of large offshore wind farms. Finally, good sea transport capabilities allow for construction of large wind turbines with high rated power (e.g., 5-10 MW).

1.1.4 Offshore fixed wind turbines

Offshore fixed wind turbines, which could be considered as a wind turbine mounted on a supporting structure fixed on sea bed, have been used by offshore wind industry to harvest wind energy in offshore sites. The supporting structure could be a monopile, a Tri-Pod structure, a jacket, a suction caisson or a gravity based structure,

see Figure 1.4. Compared to the on-shore wind turbines, hydrostatic and hydrodynamic load effects on the offshore fixed wind turbines must be appropriately accounted for.

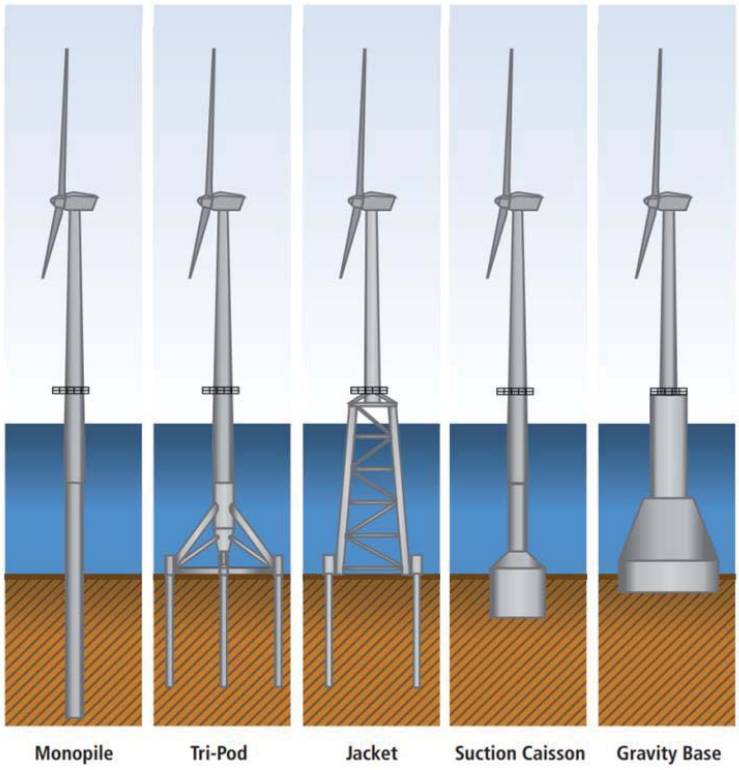

Figure 1.4 Configurations of five fixed offshore wind turbines (Edenhofer et al., 2011)

1.1.5 Motivations for developing floating wind turbines

With increase of water depth, cost of construction, installation and maintenance of the supporting structure will increase significantly since the supporting structure has to be designed to have sufficient global stiffness to avoid large amplitudes of global structural vibrations excited by first order wave loads. Large amplitudes of the global structural vibrations are not preferred to in view of design for safety and functionality as the structural vibrations could result in considerable fatigue damage on structural components of the offshore wind turbines. As the global stiffness of the supporting structure increases, the cost of installation and

maintenance may increase correspondingly. For example, for a monopile wind turbine, increasing the diameter of the monopile is an effective way to increase the global stiffness of the supporting structure. However, the difficulty for piling the monopile on the sea bed will increase with increase of the diameter of the monopile.

Floating wind turbine concepts are considered an attractive solution for harvesting offshore wind energy in relatively deep water, e.g. deeper than 80 m. By now, the offshore wind industry is moving from pilot prototype field tests to pilot commercial size floating wind farms while structural optimization for cost reduction is a focus of these pilot projects (Statoil As, 2017) (Principle Power Inc., 2017).

1.1.6 Floating wind turbines

Floating wind turbines could be considered as a wind turbine mounted on a hull (floater) that is moored by a mooring system, see Figure 1.5. According to different approaches for obtaining resistance with respect to overturning moments, floating wind turbines can be classified into spar-type, tension leg platform (TLP) and semi-submersible (which is also known as column stabilized)/barge wind turbines. More discussions with respect to classification of floating wind turbines are referred to (Butterfield et al., 2007).

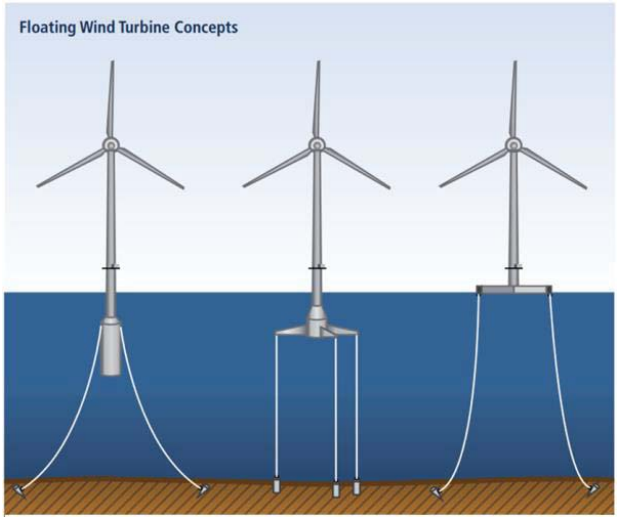

Figure 1.5 Configurations of three floating offshore wind turbines (Edenhofer et al., 2011)

1.1.7 Motivations for developing semi-submersible wind turbines

In general, semi-submersible wind turbines are expected to have better performance when compared to barge wind turbines which are considered as counterparts of the semi-submersible wind turbines. This is because the barge wind turbines may have relatively larger water plane area which means larger amplitudes of wave excitation loads and dynamic responses. Compared to spar-type or tension leg platform wind turbines, the advantages of semi-submersible wind turbines include, but are not limited to, 1) greater flexibility in terms of varying sea bed conditions and drafts and 2) significantly reduced installation costs due to their simpler installation, with full assembly at dock (Roddier et al., 2010). Some conceptual designs of semi-submersible wind turbines are shown in Figure 1.6.

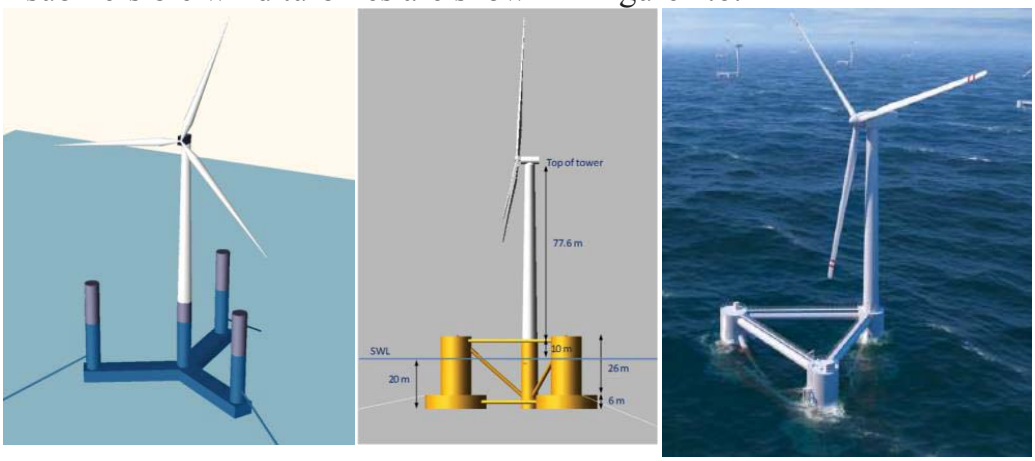

Figure 1.6 Configuration of 5-MW-CSC (left), OC4-Semi (middle) and WindFloat (right)

1.1.8 Design of semi-submersible wind turbine hulls

To enable semi-submersible wind turbines for harvesting wind energy in offshore wind farm, analyzes and tests must be appropriately carried out to demonstrate that 1) levelized cost of energy for development of semi-submersible wind farms can be reduced to a profitable level, and 2) developed semi-submersible wind farms achieve a desired level of reliability.

The IEC 61400-1 design standard (IEC 2005) specifies the design requirement for land-based wind turbines. The IEC 61400-3

design standard (IEC 2009) supplements the IEC 61400-1 design standard with design requirements for bottom-fixed offshore wind turbines. Current design standards for floating wind turbines, e.g. DNV-OS-J103 (DNV, 2013a), ABS #195 (ABS, 2013) and ClassNK guideline (ClassNK, 2012), are developed on base of combination of successful experience accumulated by the offshore oil and gas industry and wind power industry over the past decades.

In general, semi-submersible hulls for supporting offshore wind turbines are designed for serviceability and safety. The main serviceability criterion relates to stable power production, while the safety is specified as an agreed acceptable failure probability of failure events, such as capsizing/sinking and local and global structural failures, that may lead to catastrophic consequences, e.g. fatalities and environmental damage, and property damage of the floating wind turbines during their design lifetime. The design lifetime is composed of development of design, fabrication, operation and removal and reuse.

In general, cost of developments of floating wind turbines increases significantly when higher safety levels are incorporated. Reducing the costs of the produced power to a competitive level is an important challenge for the offshore wind energy development. Unlike offshore oil and gas platforms, floating wind turbines are unmanned during operation, limiting the consequences of failures to economic losses rather than loss of human life and/or environmental damage. In addition, these floaters are designed for different functionalities. For example, semi-submersible hulls used in the offshore oil and gas industry may need to be designed to have large space of upper deck to accommodate living and production facilities, equipment and buildings, and to have moderate motions in operating conditions as required by the compensator of risers. While the hulls of semi-submersible wind turbine should be designed to have a relatively large second moment of water plane area to ensure sufficient intact stability. Consequently, trade-off between the safety levels and the levelized cost of energy should be considered and addressed, while a significant reduction of the levelized cost of

energy is expected to be achieved by developing novel design of semi-submersible hulls (EWEA, 2013).

Note that hull design should not be performed in isolation; rather, the interactions of the subsystems, i.e., the wind turbine, control system, hull and mooring system, should be appropriately considered. This is because floating wind turbines have strongly coupled system behavious.

As pointed in (Wind Energy Programmatic EIS, 2018) (Moan, 2016), the accumulated experiences show that the requirements of serviceability and safety can be achieved by implementing risk control of accidental events and use limit states, i.e. ultimate equilibrium limit state (UELS), ultimate limit state (ULS), fatigue limit state (FLS), serviceability limit state (SLS) and accidental limit state (ALS)/ progressive failure limit state (PLS), as design criteria.

1.1.9 Conceptual designs of semi-submersible wind turbines

Most of the proposed MW level horizontal axis steel semi-submersible wind turbine concepts feature either three columns with a wind turbine on one side column or four columns with a wind turbine on the central column. The columns could be connected by braces (as in WindFloat (Roddier et al., 2010) (Roddier et al., 2011) and OC4-Semi (Robertson et al., 2012)) or pontoons (as in the 5-MW GustoMSC Tri-Floater (Huijs et al., 2013) and 5-MW-CSC concept (Paper A1)). Meanwhile, concrete semi-submersible wind turbines, e.g. VolturnUS (Viselli et al. 2014) and Dr.techn.Olav Olsen's concept (Dr. techn.Olav olsen As, 2018), multi-turbine concepts, e.g. Hexicon (Hexicon AB, 2018) and WindSea (WindSea AS, 2018), MW level vertical axis semi-submersible wind turbines, e.g. (Wang et al, 2014), and wind-wave hybrid concepts (for which semi-submersible wind turbines are combined with wave energy convertors), e.g. (Luan et al., 2014) (Michailides et al., 2014), are proposed and analyzed by designers and/or researchers from industry, research institutes and/or universities. Among existing concepts of semi-submersible wind turbines, by now, three full scaled prototype semi-submersible wind turbines (Roddier et al., 2017), i.e. the 2-MW WindFloat prototype semi-submersible wind turbine (Cermelli et al., 2010) (Cermelli et al., 2012), the Fukushima Mirai 4-column

prototype semi-submersible wind turbine (Saeki et al., 2014) (Ishihara, 2013), and the Fukushima Shinpuu V-shape prototype semi-submersible wind turbine (Komatsu et al., 2016), have been constructed and operated in real to prove technical and economic feasibility of development of semi-submersible wind turbines. The 2-MW WindFloat prototype semi-submersible wind turbine has been successfully operated for its design life (Roddier et al., 2017), from offshore commissioning (in December 2011) to decommissioning (July 2016 (4COffshore, 2018)), and demonstrates the technical and economic feasibility.

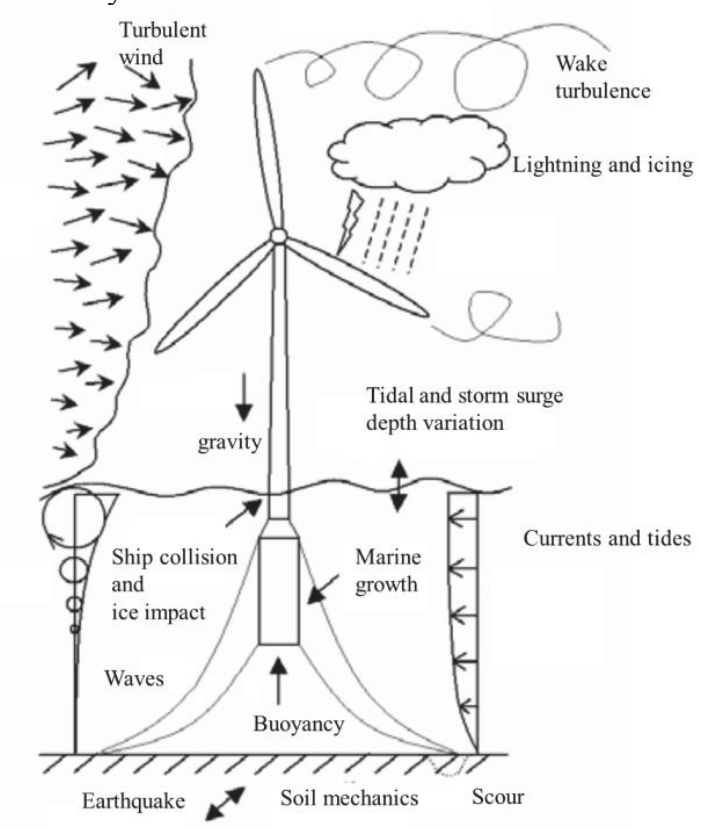

Figure 1.7 Environmental loads subjected on floating wind turbines (Butterfield et al., 2007)

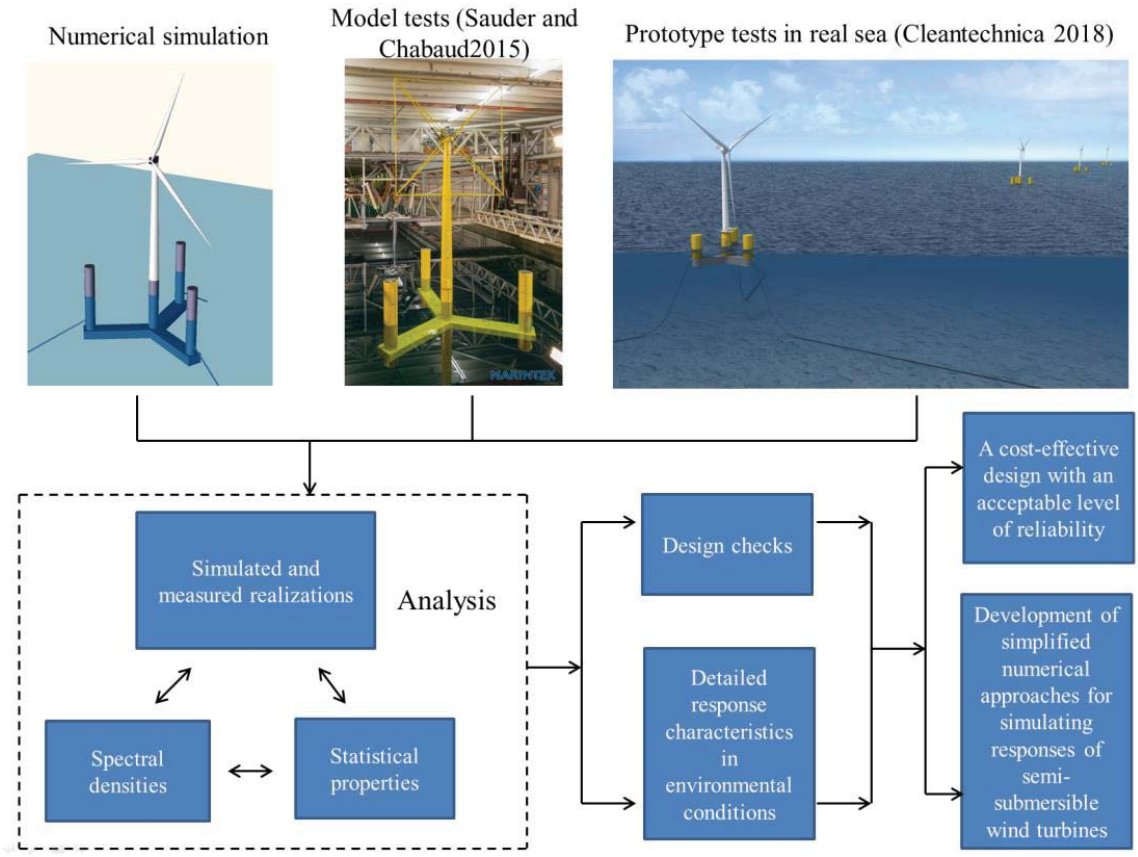

Figure 1.8 Description for the approaches for analyzing responses of semi-submersible wind turbines

1.1.10 Loads and load effects

Floating wind turbines operate in complex environmental conditions, see Figure 1.7. Design checks for serviceability and safety are carried out on base of analyses with respect to subjected loads and load effects. The load effects could be obtained by carrying out numerical simulations, experimental tests in laboratory and/or prototype tests in real, see Figure 1.8.

Meanwhile, the analyses with respect to subjected loads and load effects shed light on responses of semi-submersible wind turbines in environmental conditions. To develop a cost-effective design with an acceptable level of reliability and simplified numerical approaches for simulating responses of semi-submersible wind turbines, an in-

depth understanding with respect to responses of semi-submersible wind turbines is needed.

As mentioned in (EWEA, 2013), development of floating wind turbines is still in its young stage and facing considerable technical, economic and political challenges. Consequently, numerical simulations and model tests for analyzing global responses of floating wind turbines, which are in terms of motions and sectional forces and moments and required by relevant standards and guidelines for offshore wind turbines in wind and waves are hot research topics.

Due to limitations of conventional frequency-domain and time-domain numerical modelling approaches, which have been illustrated in detail in Chapter 4, numerical simulations with respect to responses, in terms of sectional forces and moments or stresses, of structural components of semi-submersible hulls in wind and waves are very limited. However appropriate design checks for structural design of semi-submersible hulls must be carried out while structural optimization for cost reduction is identified as a major focus of the existing pilot floating wind turbine projects for commercializing floating wind turbines (Statoil As, 2017) (Principle Power Inc., 2017).

1.2 Motivation and thesis objectives and organization

1.2.1 Motivation and thesis objectives

The author is motivated to give contributions for overcoming the challenges and existing limitations described in Section 1.1.8 and Section 1.1.10, and to promote large-scale development of semi-submersible wind turbines. Consequently four objectives are specified by the author and tabulated in Table 1.1.

Development of novel designs of floating wind turbines is encouraged and is expected to significantly reduce cost of development of floating wind turbines. Therefore, Objective 1 is to develop a novel conceptual design of semi-submersible hull for supporting a 5-MW horizontal axis reference wind turbine. Meanwhile, the developed design is planned to be published to public and be used as a reference semi-submersible wind turbine.

Table 1.1 List of thesis objectives

Objective 1	to develop a novel conceptual design of semi-submersible hull for supporting a 5-MW horizontal axis reference wind turbine (the developed design is considered as a reference model and used in numerical analysis and experimental model test)
Objective 2	to make contributions to the development of simplified design method and analysis approaches
Objective 3	to shed more light on the response characteristics of the reference semi-submersible wind turbine in wind and waves
Objective 4	to develop and validate a time-domain numerical approach for analyzing sectional forces and moments in hull of a generic floating wind turbine

The background information mentioned in Section 1.1 is used to guide the design work carried out by the author for developing the novel conceptual design. Design is an iterative process while simplified design approaches for developing conceptual designs are needed. Consequently, Objective 2 is to make contribution on development of simplified design method and analysis approaches.

The simplified design method and analysis approaches should be developed on base of an in-depth understanding with respect to features of responses of semi-submersible wind turbines in environmental conditions. However, floating wind turbines could be a complex system, operate in complex and harsh environmental conditions, and have the strongly coupled system behavious. While, development of floating wind turbines is still in its young stage. These facts mean that huge effects are still needed to shed more light on responses of floating wind turbines in wind and waves. Consequently, Objective 3 is to shed more light on responses of the reference semi-submersible wind turbine in wind and waves.

Objective 4 is to develop and validate a time-domain numerical approach for analyzing sectional forces and moments in generic floating wind turbine hulls to overcome the limitations of the conventional frequency-domain and time-domain numerical modelling approaches and to enable straightforward time-domain numerical simulation for the sectional forces and moments in

structural components of the floating wind turbines hulls with reasonable accuracy.

1.2.2 Thesis organization

The objectives of the thesis and interconnection between the appended papers are shown in Figure 1.9.

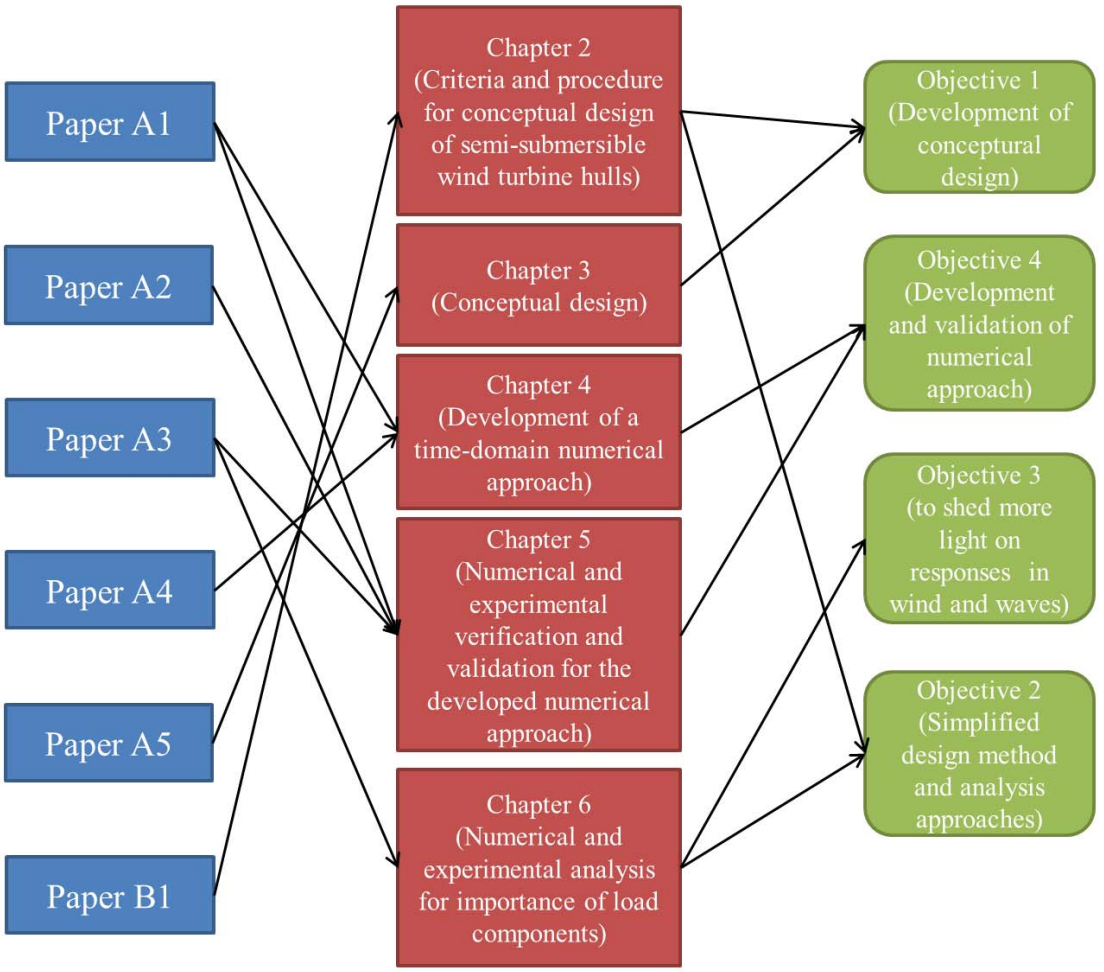

Figure 1.9 Objectives of the thesis and interconnection between the appended papers

Simplified design approaches implemented by the author for estimating mass and determining overall dimensions (e.g. the dimensions of the columns, pontoons and braces) of the hull of initial designs of semi-submersible hulls and discussions with respect to simplifications for design checks are illustrated in Paper B1 and summarized in Chapter 2.

The simplified design approaches presented in Chapter 2 serve as a base of development of the novel conceptual design which is a steel braceless semi-submersible hull for supporting a 5-MW horizontal axis reference wind turbine. The developed reference semi-submersible wind turbine is named 5-MW-CSC and corresponds to Objective 1. Design of the 5-MW-CSC, relevant design considerations, and methods and results of simplified design checks are published in Paper A5 and summarized in Chapter 3.

To achieve Objective 4, time-domain numerical approaches for generic and specific floating wind turbines were developed by the author to analyze sectional loads in floating wind turbine hulls in wind and waves, while conventional numerical approaches and their challenges and limitations are discussed, see Paper A1 and A4, and summarized in Chapter 4.

Comparisons of numerical simulations and experimental measurements were used to verify and validate the developed numerical approach for generic floating wind turbines step by step. Responses of a 1:30 scaled experimental model of the 5-MW-CSC in wind and waves were tested by SINTEF Ocean in its ocean basin via cooperation frame of (NOWITECH 2018) while the ReaTHM® testing approach (Chabaud, 2016) was used to overcome challenges in conventional experimental tests for floating wind turbines in ocean basin. The challenges result in uncertainties in measurements and should be considered in the validation for the developed numerical approach. Differences in spectral densities of the measurements and simulations were quantified while the reasons for the differences were thoroughly analyzed and discussed. Details of the issues mentioned in this paragraph are available in Papers A1, A2 and A3, and summarized in Chapter 5.

The developed numerical approach for generic floating wind turbines was used to simulate rigid-body motions and sectional loads in five specified cross-sections in the hull of the 5-MW-CSC. Numerical parametrical study and measurements of the experimental model in difference design conditions were compared and analyzed to shed more light on rigid-body motions and structural responses of the reference model in wind and waves. Simplification for numerical modelling for short-term analysis was proposed based on results of the analysis. Details of the issues mentioned in this paragraph are available in Paper A3 and summarized in Chapter 6.

Chapter 2

Conceptual design procedure and methods for semi-submersible wind turbine hulls

The current design standards, principles, methods and limitations for design of semi-submersible wind turbine hulls are introduced in Section 1.1.8. Design is an iterative process. Design procedure for developing a conceptual semi-submersible hull design, with respect to the safety, is shown in Figure 2.1. To control cost of conceptual design, simplified design methods need to be developed based on experience and understanding in design.

In this chapter, the author intends to systematically present and discuss conceptual design procedure and simplified design methods for semi-submersible wind turbine hulls in view of design for safety based on a review of publicly accessible publications and the author's experience and practice with respect to design and analysis of semi-submersible wind turbines in the past six years.

The conceptual design procedure can be summarized as follows:

As shown by the black lines in the Figure 2.1, Initial designs are selected from design base which is established on base of requirements stipulated by customer and authorities, and simplified design criterial and approaches. The requirements by the customer

(Party A) should be stipulated in contract between Party A and Party B (contractor). The requirements could be, but not limited to, 1) requirements with respect to certification, standards and regulations, 2) requirements with respect to functionality and safety, 3) operational location of the design, 4) approaches for fabrication and installation, 5) accessibility for inspection and maintenance, and so on. Meanwhile, the design shall comply with rules, requirements, principles, guidance, standards, regulations, and law specified by involved authorities.

The simplified design criteria and approaches are used in practice to improve work efficiency, and limit work effort and costs. Intact stability, natural periods and modes, and local and global structural strength of the selected initial design need to be appropriately analyzed to check whether or not the selected initial design satisfy the relevant stipulated requirements and criteria. If the selected initial design fails to satisfy the stipulated requirements and criteria, the design procedure will return back to make a new initial design as shown by the red dot-dash lines.

In additional to requirements for the safety, cost of the selected initial design should be estimated and controlled. To analyze responses of the selected initial design, numerical simulations and experimental tests need to be carried out by using appropriate approaches. Reasonable assumptions and simplifications are needed to reduce computational costs of the numerical simulations to an acceptable level, while cost-effective computer codes need to be developed and validated appropriately, see the black dot lines.

The state-of-the-art knowledge shows that the coupled system behaviours of semi-submersible wind turbines (see Paper B1) should be kept in mind in the design procedure in order to achieve a cost-effective design.

Accumulated design experience and understanding in responses of semi-submersible wind turbines in environmental conditions are continually used to support development of cost-effective designs and design methods, see the black dash lines.

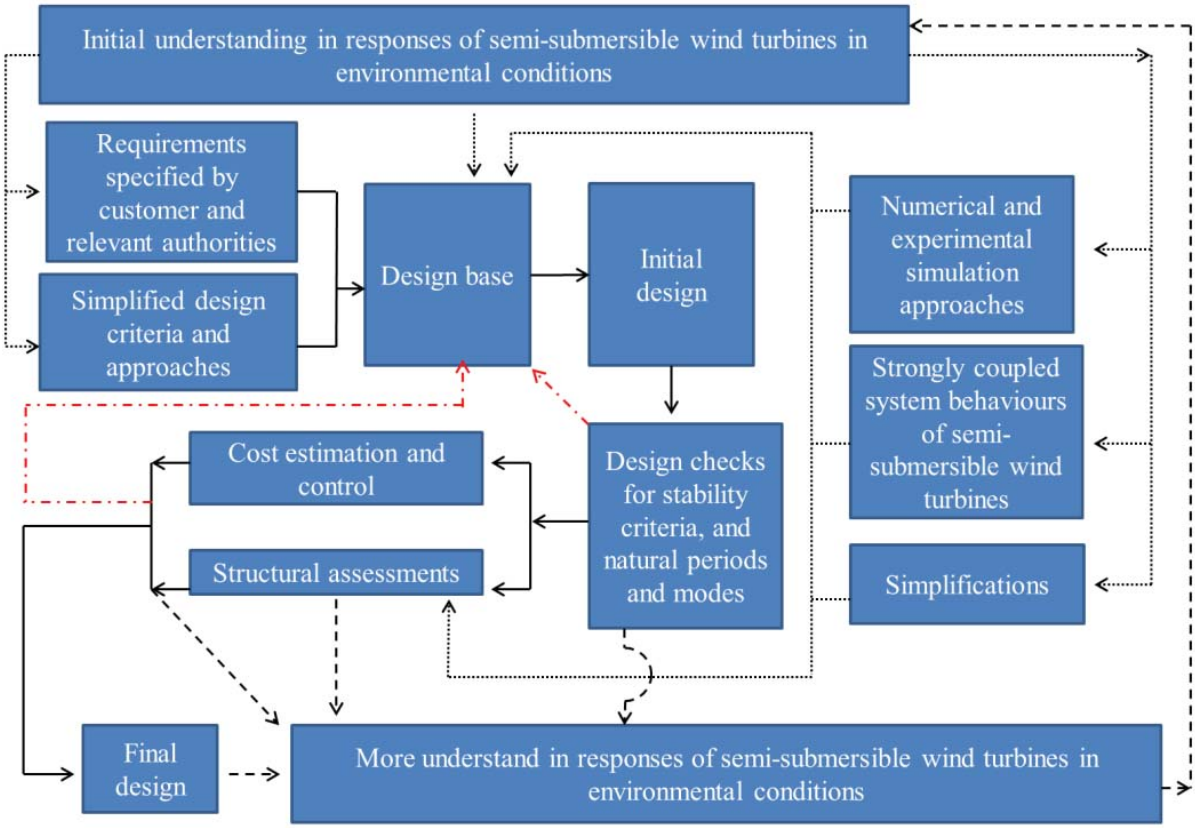

Figure 2.1 Design procedure for developing a novel conceptual semi-submersible hull design, with respect to safety

The simplified methods are composed of simplified criteria and analysis methods and as listed as follows:

- Simplified stability criterion, natural period requirements and simplified steel mass estimation methods that are used to develop design space for overall dimensions of initial designs of semi-submersible hulls.
- Simplifications for analyzing intact stability, and natural periods and modes.
- Simplifications for design conditions and numerical analysis approaches for analyzing structural responses that are required by design checks, such as ULS and FLS design checks.

More details about the simplified methods presented in this chapter is given in Paper B1 which served as a basis for the development of the 5-MW-CSC as required by Objective 1, see Section 1.2.

Chapter 3

Conceptual design of a steel braceless semi-submersible wind turbine

In this chapter, the author intends to present definition and design check results of the 5-MW-CSC, which is a conceptual design of a braceless steel 5-MW semi-submersible wind turbine developed by the author due to Objective 1. Detailed content of this chapter is referred to Paper A5 and Paper B1.

The hull of the 5-MW-CSC is designed to support a 5-MW NREL offshore base line wind turbine (Jonkman et al., 2009) at a site in the northern North Sea (Li, et al. 2015), see Figure 3.1.

The design work of the 5-MW-CSC started in April 2013 and initially inspired by the Dr.techn.Olav Olsen's concept (Dr.techn.Olav Olsen AS, 2018). In 2013, conventional semi-submersible hulls, such as the 5-MW WindFloat or the OC4-Semi, are consisted of pontoons and columns connected by braces. It can be very complex and expensive to weld the braces on the columns. Moreover, fatigue life of the brace-column joints can be a very critical issue due to stress concentration at the joints. In addition, to avoid heave resonant motions excited by first order wave loads, additional heave plates and/or pontoons may be needed. Construction of the additional heave plates can be complex and expensive as well.

In contrast to the conventional semi-submersible design with braces, a braceless concept may reduce design complexity and costs of the offshore wind turbine. By now, in addition to the 5-MW-CSC, other steel braceless semi-submersible wind turbine concepts, such as the 5-MW GustoMSC Tri-Floater (Huijs, et al., 2013), have been proposed.

Figure 3.1 Location of the design site (the selected site) (Li, et al. 2015)

3.1 Dimensions of the hull of the 5-MW-CSC

As shown in Figures 2.1 and 3.2, the hull of the 5-MW-CSC is composed of a central column, three side columns and three pontoons. The side columns are connected by the pontoons to the central column at the bottom to form an integrated structure. The added mass in the heave, roll and pitch is mainly provided by the pontoons. There are no heave plates or braces. The box-shaped cross-section of the pontoons could provide considerable viscous damping at the heave, roll and pitch resonant frequencies. Dimensions of the hull of the 5-MW-CSC are given in Table 3.1

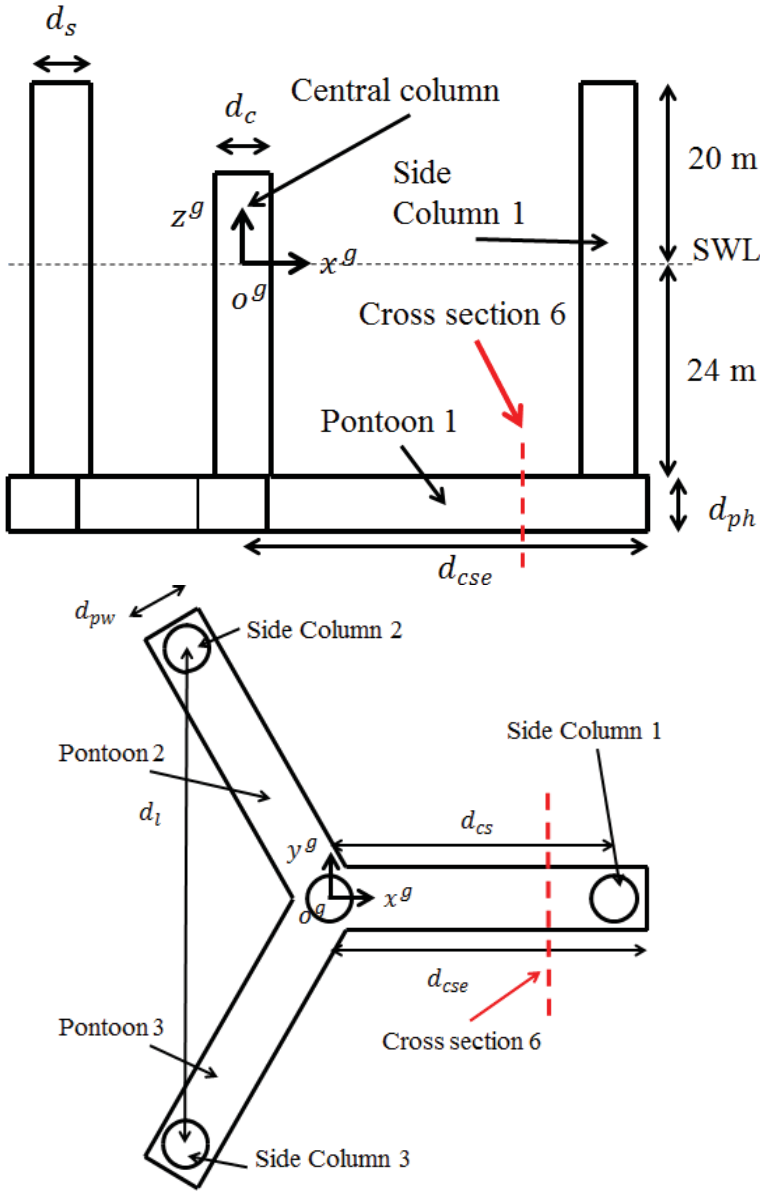

Figure 3.2 Side (left) and top (right) views of the hull of 5-MW-CSC

Table 3.1. Dimensions of the hull of the 5-MW-CSC

d_c [m]	6.5
d_s [m]	6.5
d_{ph} [m]	6
d_{pw} [m]	9
d_{cs} [m]	41
d_{cse} [m]	45.5
Operating draft [m]	30
Displacement [tonne]	10,555
Steel weight [tonne] (hull)	1,804
Equivalent thickness [m]	0.03

3.2 Design checks

Numerical analysis has been carried out to analyze the intact stability, natural periods and modes and structural strength of the design. Results of the numerical analysis show that the design has very good intact stability, well designed natural periods and modes, moderate rigid-body motions in extreme environmental conditions and a reasonable structural design.

Note that the design criteria, methods and simplifications discussed in Chapter 2 (Paper B1) are used to guide design checks for the 5-MW-CSC. The design checks are briefly introduced as follows.

3.2.1 Intact stability design check

The intact stability could be checked based on the curves of the righting and design overturning moments. Overturning moments come from aerodynamic loads on the RNA, tower and hull and make the semi-submersible wind turbine rotate with respect to a heeling axis in water plane area of the hull. Righting moment is generated by hydrostatic pressure forces on wetted body surface of the hull and gravity of the semi-submersible wind turbine. To find the most critical situation, overturning moments and righting moments corresponding to several different heeling axes need to be calculated and checked. The righting moment curves corresponding to different

rotational axes (represented by ϕ) and design overturning moment curve of the 5-MW-CSC are given in Figure 3.3. Standards, such as the DNV-OS-J103, require that the ratio of the area under the righting moment curve from 0 degrees heeling angle to the second intersection to the corresponding area under the design overturning moment curve should be more than a specified value, e.g. 1.3.

Detailed analysis with respect to determination of the design overturning moment is referred to Paper A5.

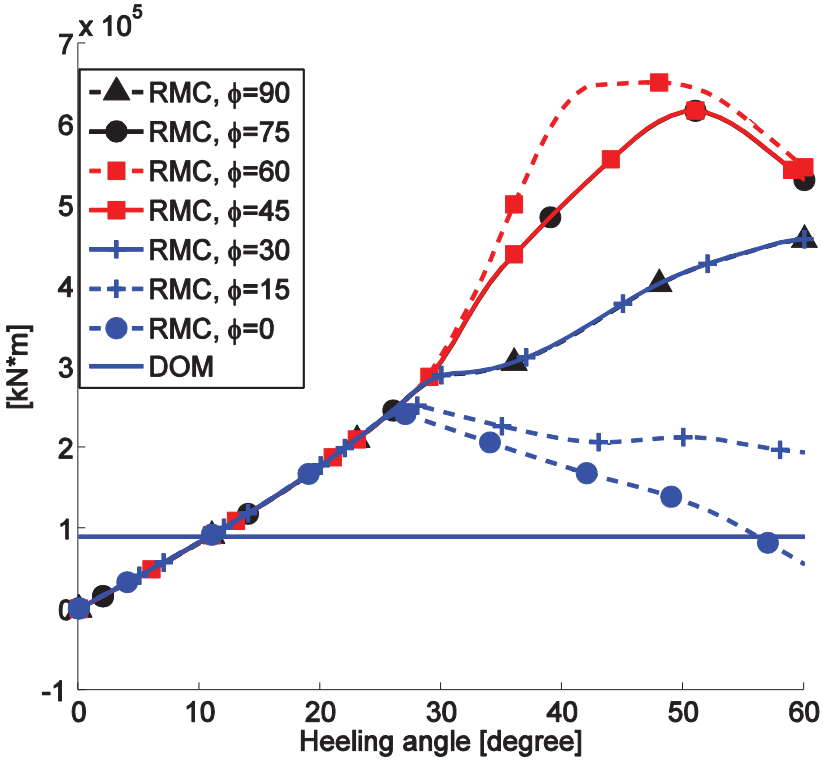

Figure 3.3 Righting moment curve (RMC) v.s. design overturning moment curve (DOM), intact stability analysis, ϕ represents different heeling axis.

3.2.2 Natural periods and modes

Resonant responses excited by dynamic excitation can result in large amplitudes of sectional forces and moments, and expensive structures (in order to have sufficient structural strength). Therefore, natural periods and modes, i.e. six rigid-body motion modes and structural vibrational modes of the structural components, should be well designed to, at least, avoid resonant responses induced by excitations with considerable energy, e.g., first-order wave load (3-25 seconds) and 1P (5-8.7seconds for the 5-MW-CSC) and 3P (1.7-2.9 seconds for the 5-MW-CSC) effects (Twidell and Gaudiosi, 2009). In general, a given 1-hour turbulent wind may include a wide range of frequency component. For semi-submersible wind turbines, resonant rigid-body motions excited by wind loads and low frequency wave loads cannot be avoid by tuning the natural periods, however, the resonance can be limited by aerodynamic and hydrodynamic damping which may be quite considerable (Papers A2 and A3). In addition, vibration modes and frequencies should also be considered. The vibration (flexible) modes may be excited due to: 1) the motivation of cost reduction may result in a flexible hull; 2) high-frequency rotor loads, e.g., the 3P effect; and 3) the modes and frequencies are affected by strong coupling effect between the hull and other components of floating wind turbines. If structural vibrations are excited by first-order wave loads, the effect of hydroelasticity on the hull must be considered.

Natural periods of the rigid-body motion modes can be obtained by carrying out decay test while the periods and structural vibrational modes of the structural components, in principle, should be calculated by solving the eigenvalue problem. Lanczos' method (Nour-Omid et al., 1983) is widely used in commercial codes to solve the eigenvalue problem, which is related to generalized mass and stiffness. Stiffness of the pontoons and columns are represented by beam elements with simplified cross-sections. For example, Figure 3.4 shows a realistic cross-section (Cross-section 6 shown in Figure 3.2) of a pontoon with structural details of the 5-MW-CSC. The realistic cross-section is represented by a simplified box-shape cross-section. The mass of the hull is represented by mass points

attached to the beam elements. Similarly, the mass and stiffness of the RNA and tower could be represented by mass points and beam elements. Note that the natural frequencies for the natural modes of the generator and drivetrain are expected to be very high. Therefore, the nacelle could be simply modeled by a mass point attached to a beam element, which represents global structural stiffness of the nacelle.

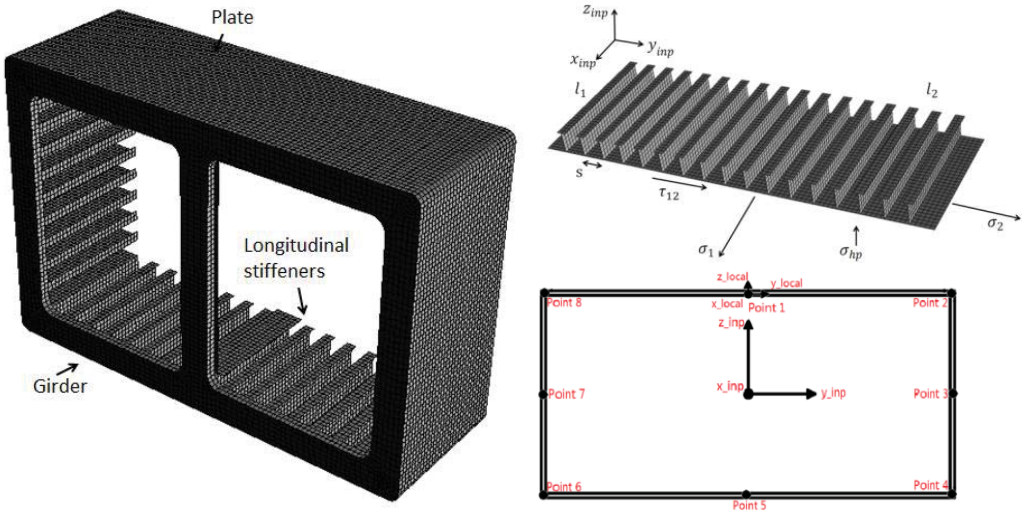

Figure 3.4 A realistic cross-section (left), stiffened plates (right top), and simplified box shape cross-section with equivalent thickness (right bottom)

In analysis for natural periods and modes, it is important to appropriately account for effect of flexibility of the hull, tower, RNA, mooring system, added mass and fluctuations of hydrostatic pressure and gravity on the natural modes and frequencies. For instance, as shown in Figure 3.5, numerical analysis shows that natural period of the side-to-side tower central column bending mode of the 5-MW-CSC is reduced from 3.08 seconds to 2.16 seconds if real flexibility of the hull is replaced by an assumption that the hull is considered as a rigid body. Rigid-body assumption for the hull is used in some conventional time-domain computer codes for analyzing global

responses, e.g. bending moment in tower base, rigid-body motions of the hull and mooring line tensions (Paper A1). The rigid-body assumption may result in artificial resonant structural vibrations exited by, for example, the 1P and 3P effects

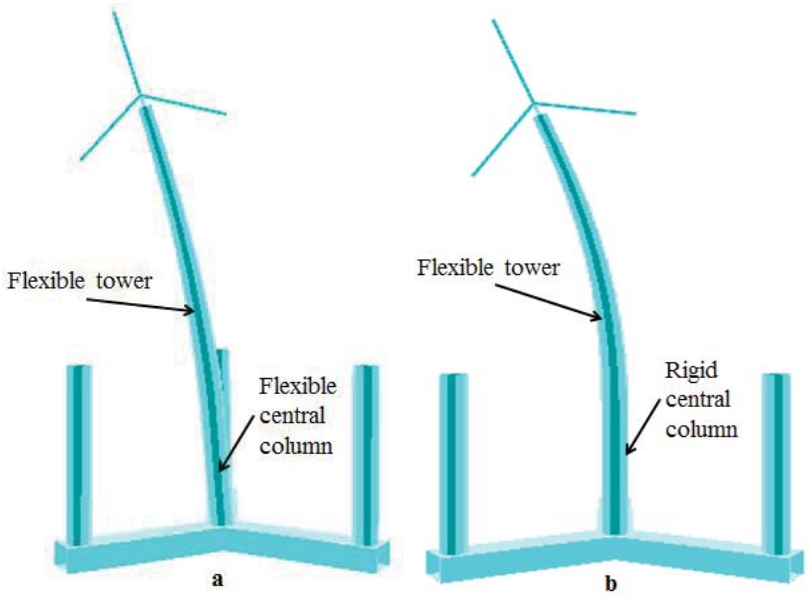

Figure 3.5 Side–to-side tower central column bending mode

3.2.3 Simplified ULS and FLS design check based on a limited number of design conditions

The pontoons of the 5-MW-CSC are composed of stiffened plates, girders and bulkheads. A stiffened plate is shown in Figure 3.4 and is assumed to be located in between of two transverse girders and the side surfaces of the pontoon. The stiffened plate is subjected to σ_{hp}, σ_1, σ_2 and τ_{12} which are explained in Table 3.2.

Buckling utilization factors for the stiffened plate in all the combinations of the design loads, i.e. σ_{hp}, σ_1, σ_2 and τ_{12}, are calculated by using the S3 element code of PULS (DNV 2009). PULS is a computerized buckling code for thin-walled plate construction and accepted by DNV-RP-C201 (DNV 2010a) for

checking buckling strength of plated structures. The code implements the Marguerre's non-linear plate theory in combination with stress control criteria.

As explained in Table 3.2, σ_1, σ_2 and τ_{12} are derived from sectional forces and moments in structural components of the hull. Numerical models and development of numerical approaches for simulating rigid-body motions and sectional forces and moments are addressed in Chapter 4 while discussions with respect to simplifications for design conditions used in ULS and FLS design checks are referred to Chapter 2 (Paper B1) and Paper A5.

Fatigue analysis for structural components of the hull is normally conducted by the S-N Palmgren-Miner rule approach. The stress ranges used in the S-N fatigue approach could be calculated by applying rainflow counting method to the time series of the hot-spot stress. Appropriate SN curves should be selected based on relevant standards, e.g., DNV-RP-C203 (DNV 2010b).

The hot-spot stresses are induced by stress concentration in particular at structural intersections or joints. Fatigue life is very sensitive to the hot-spot stresses (in the order of 3-5 due to the slope of the S-N curves), which may appear at the joints between the columns, pontoons or braces. Therefore, the structural details need to be well designed to reduce the hot-spot stresses.

For a complex joint or structural intersection, it is recommended that the hot-spot stress be calculated by finite element analysis (DNV 2010b). Sectional forces and moments in ends of the joint, which are given by carrying out global response analysis, are used as boundary conditions of the finite element model. Examples are referred to (Fredheim, 2012) (Marin, 2014).

For the compartments of the pontoons and columns that are in between of the joints, in general, the stress concentration effect is not critical. Therefore, the fatigue life for such compartments could be estimated by normal stresses of several representative points in the corresponding cross-section on the pontoons or columns multiplied by a specified stress concentration factor (SCF). A sensitivity study for the fatigue damage with respect to SCF is needed.

Table 3.2 Nominal and shear stresses used in ULS design check

σ_{hp}	Hydro-pressure on the plate (including hydrostatic pressure and hydrodynamic pressure on the outer surface of the plate and the ballast water induced pressure on the inner surface of the plate)
σ_1	Nominal uniform stress in stiffener direction
σ_2	Nominal uniform stress in perpendicular to stiffener direction
τ_{12}	Shear stress

Note

σ_1 and τ_{12} can be derived from Eq.(3.1) and Eq. (3.2) which are established on base of Euler–Bernoulli beam theory and the simplification for which, in finite element analysis, beam elements with simplified cross-sections are used to capture global load effects on the pontoons and columns of the hull. A simplified box shape cross-section is shown in Figure 3.4 as an example.

F_x, F_y, F_z, M_x, M_y, and M_z are obtained by solving the beam element finite element model and represent sectional forces and moments at the geometrical center of the cross-section (the origin of the x_inp-y_inp-z_inp coordinate system).

In Eq. (3.1) and Eq. (3.2), A is area of the cross-section. w_{y_inp} and w_{z_inp} are the corresponding section moduli. A_0 is the circumscribed area of the cross-section. t_c is the equivalent thickness of the cross-section. S_{y_inp} and S_{z_inp} are static moments corresponding to the y_inp and z_inp axes and the position of the point on the cross-section. I_{y_inp} and I_{z_inp} are the second moments of area of the cross-section. Compared with a realistic cross-section, which includes structural details, such as stiffeners, the thin wall box-shape approximation with t_c will underestimate the maximum shear stresses because the stiffeners carry the shear force inefficiently. Therefore, a reduction factor could be applied to t_c to compensate the underestimations for the shear stresses.

$$\sigma_1(y_{inp}, z_{inp}) = \frac{F_x}{A} + \frac{M_y}{w_{y_{inp}}} + \frac{M_z}{w_{z_{inp}}} \qquad (3.1)$$

$$\tau_{12}(y_{inp}, z_{inp}) = \frac{M_x}{2A_0 t_c} + \frac{F_y S_{z_{inp}}}{I_{z_{inp}} t_c} + \frac{F_z S_{y_{inp}}}{I_{y_{inp}} t_c} \qquad (3.2)$$

Chapter 4

Development of time-domain numerical approaches for determining sectional loads in floating wind turbine hulls

As introduced in Section 1.1.10, floating wind turbines operate in complex environmental conditions, see Figure 1.7, while design checks for serviceability and safety are carried out on the basis of analyses with respect to subjected loads and load effects. In addition, to develop a cost-effective design with an acceptable level of reliability and simplified numerical approaches for simulating load effects of floating wind turbines, an in-depth understanding with respect to loads and load effects of floating wind turbines is essential.

As shown in Figure 1.8, the load effects could be obtained by carrying out numerical simulations, experimental tests in the laboratory and/or prototype tests in the field.

Numerical approaches for modelling and simulating loads and global load effects on floating wind turbines are systematically presented in this chapter.

To simulate global load effects which are in terms of, for instance, motions and sectional forces and moments in structural components, of floating wind turbines, finite element models and/or rigid-body motion equations need to be generated and solved in appropriate coordinate systems, while external and inertial loads on the floating wind turbines need to be appropriately modelled by using frequency-domain or time-domain approaches in corresponding coordinate systems.

A general introduction with respect to numerical modelling approaches and their advantages and limitations is given in Section 4.1. As addressed in Section 4.1.3, the state-of-the-art knowledge suggests using time-domain computer codes to analyze the aero-hydro-servo-elastic responses of floating wind turbines and to account for nonlinear aerodynamic loads, automatic control and transient loading events. Consequently, the rest part of this chapter focuses on presenting two time-domain numerical approaches developed by the author.

The developed approaches focus on modelling of inertia and external loads on floating wind turbine hulls, and mapping of the loads in finite element model of the hulls. The developed approaches are extension of the conventional hybrid frequency-time domain approach. In the developed approaches, floating wind turbine hulls are modelled as multi-bodies instead of single body with 6 d.o.f.s. The developed approaches can be easily implemented in various state-of-the-art computer codes for wind turbine analysis, e.g. Simo/Riflex/Aerodyn (Moriarty and Hansen, 2005) (MARINTEK, 2011) (MARINTEK 2013) (Ormberg et al., 2011) (Luxcey et al., 2011) (Ormberg and Bachynski, 2012), OrcaFlex (Robertson et al., 2014) and FAST+CHARM3D (Robertson et al., 2014), to extend their capabilities to analyze sectional forces and moments in structural components of a generic floater and a specific floater, respectively.

Detailed content of the conventional and developed numerical approaches in together with analysis for their advantages and limitations is referred to Papers A1 and A4, and summarized and highlighted in Sections 4.2-4.5.

4.1 General information for numerical approaches

4.1.1 Coordinate systems

In general, four types of coordinate systems, as shown in Figure 4.1 and Table 4.1, could be used by time-domain and frequency-domain numerical approaches.

Table 4.1 Coordinate systems

O^g - x^g - y^g - z^g coordinate system	A global coordinate system for which the coordinate system is fixed. O^g could be fixed at an arbitrary position in space
O^f - x^f - y^f - z^f coordinate system	An earth fixed coordinate system located at mean position of geometrical center of water plane area of a floater, see Figure 4.1.
O^b - x^b - y^b - z^b coordinate system	A body-fixed coordinate system. Position of O^b and orientation of the body-fixed coordinate system rigidly follow rigid-body motions of the floater.
O^r - x^r - y^r - z^r coordinate system	A body-related coordinate system. O^r rigidly follows horizontal movements of O^b (the floater) but the orientation of the body-related coordinate system and vertical position of the O^r are fixed (as the same as the body-related coordinate system when the floater is located at its initial position).
Note	
When the floater is located at its mean position, the O^f-x^f-y^f-z^f, O^b-x^b-y^b-z^b and O^r-x^r-y^r-z^r coordinate systems are coincident.	

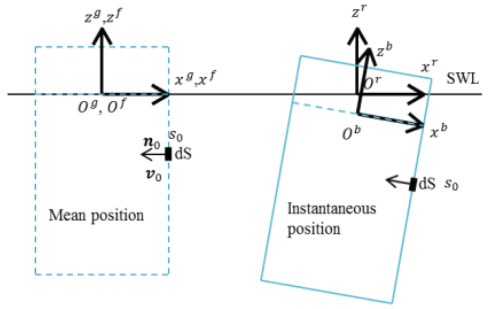

Figure 4.1 Definition of the coordinate systems for a floating body

4.1.2 Numerical approaches for analyzing load effects

Finite element analysis (based on shell and/or beam elements) is normally carried out to determine the load effects with appropriate methods for modelling the loads.

Shell elements might be employed to model structural details, e.g. bulkheads, girders and stiffeners in the hull, blades and tower; chains and wires of the mooring lines; and gear box, shaft and generator in nacelle.

Alternatively, we might consider that the structure is composed of several structural components (based on a multi-body formulation). For instance, the blades, rotational shaft, nacelle, tower, mooring lines and columns, pontoons and braces of the hull can be considered as structural components. Beam elements can be used to account for global structural behaviors of these structural components, e.g. sectional forces and moments in the structural components. The sectional forces and moments might be used as inputs of design formulas for structural strength design checks specified by relevant standards and guidelines from the International Electrotechnical Commission (IEC), International Organization for Standardization (ISO), American Petroleum Institute (API), the Norwegian petroleum industry, class societies such as Det Norske Veritas and Germanischer Lloyd (DNVGL) and the American Bureau of shipping (ABS) and so on. For example, buckling strength of plates, stiffeners and girders in global and local loads can be checked by the formulas specified in DNV-RP-C201 (DNV 2010a) and Section 3.2.3. The sectional forces and moments might be used in ULS design checks for tubular members and joints based on formulas specified in NORSOK-N004 (Standards Norway, 2004). An example is available in Paper A4. In addition, the sectional forces and moments might be used as boundary conditions in a sub-model finite element analysis to determine structural responses such as stresses, etc, see (Fredheim, 2012) (Marin, 2014).

Note that, in addition to finite element analysis, load induced motions could be obtained by generating and solving corresponding rigid-body motion equations. More detailed discussions are referred to Section 4.2. For a static determined structure, which means that a

cross-section on the structure can be divided into two parts, see the cross-Section 6 in Figure 3.2 as an example, sectional forces and moments in the cross-section are in equilibrium to inertial and external loads on each of the two parts. Consequently, the sectional forces and moments could be obtained.

4.1.3 Frequency-domain approaches versus time-domain approaches

The state-of-the-art knowledge suggests using time-domain computer codes to analyze the aero-hydro-servo-elastic responses of floating wind turbines and to account for nonlinear aerodynamic loads, automatic control and transient loading events. Reasons are explained in this section.

To explain the reasons, an introduction for a well-developed frequency-domain approach for modelling hydrodynamic loads is presented in this section. However, a focus of this thesis is on time-domain approaches. Consequently, introduction to conventional time-domain approaches for modelling aerodynamic and hydrodynamic loads are given in Section 4.1.4 and Section 4.1.5.

Frequency-domain approach for analyzing oscillating responses of a generic floater in waves with respect to its mean position has been well developed by the offshore oil and gas industry and implemented in computer codes, e.g. WADAM (DNV, 2013b). In these computer codes, perturbation analysis with the wave amplitude as a small parameter, Bernoulli's equation and velocity-potential, which is obtained by generating and solving corresponding boundary problem are used to efficiently analyze hydro-pressure forces on mean wetted body surface of the floater and the resulting wave-induced rigid-body motions. The hydro-pressure forces together with the inertial loads on the floater due to its motions can be used in a finite element analysis (DNV, 2013b) to efficiently determine structural responses such as stresses, etc. If the floater has a structural static determinate hull, sectional forces and moments in the hull can be obtained by integrating external and inertia loads which are acting on the corresponding structural components of the hull.

Finite element analysis in frequency-domain is very cost-effective. However, as addressed in Chapter 2 (Paper B1), subsystems, i.e., the RNA, control system, tower, hull and mooring system, of floating wind turbines need to be appropriately modelled as these subsystems could be strongly coupled. As indicated by Eq. (4.1), the resultant thrust force on the rotor is proportional to square of U_{rel} which is relative wind speed at the nacelle projected to the rotor plane. U_{rel} is related to speed of incident winds, rigid-body motions of the hull, which are excited by environmental loads, e.g. wind and wave loads, and deflection of the tower, as the tower is a flexible and slender structure. While, aerodynamic loads on the blades are also related to rotational speed of the rotor and pitch angles of the blades which are controlled by the controller of the turbine timely. These facts are known as aero-hydro-servo-elastic feature (Jonkman, 2007).

Consequently, it is a big challenge to develop a generic frequency-domain approach to model aerodynamic loads on the rotor. Instead, as shown in the work done by Kvittem and Moan (2015), relative wind speed to aerodynamic loads transfer functions could be derived from reference realizations of relative wind speed at the nacelle and aerodynamic loads on the rotor given by time-domain codes. However, validity of the derived transfer functions must be appropriately checked, in particular for novel designs of floating wind turbines, we still need to use time-domain simulations and model tests to shed more light on the aero-hydro-servo-elastic feature. Another limitation is that frequency-domain models cannot be used to account for transient loading events, e.g. wind turbine faults.

4.1.4 Conventional time-domain approaches for modelling aerodynamic loads

A general introduction with respect to conventional approaches for modelling aerodynamic loads on the RNA is available in De Vaal (2015). Environmental loads result in rigid-body motions in 6 d.o.f.s , i.e. surge, sway, heave, roll, pitch and yaw. The rigid-body motions could be described in a global coordinate system (denoted as O^g-x^g-y^g-z^g) as shown in Figure 4.2. Surge, sway and heave are oscillating

motions along the x^g, y^g, and z^g axes respectively while roll, pitch and yaw are oscillating rotational motions with respect to the x^g, y^g, and z^g axes respectively.

To analyze wind loads induced rigid-body motions, aerodynamic thrust force (denoted as T^{aero}), which is a resultant of aerodynamic loads on blades projected to the rotor, could in a simple and effective way be modelled by Eq. (4.1). ρ_{air} is air density. A_{rotor} is area of the rotor plane. $C_T^{aero,rotor}$ is a non-dimensional thrust coefficient which could be given as a function with respect to speed of the incident wind at the nacelle. U_{rel} is relative wind speed at the nacelle projected to the rotor plane. This practical approach is developed on base of the actuator disc concept, as shown in Burton et al. (2011), and used by time-domain computer codes, e.g. TDHMILL (Yttervik, 2009), to simulate the aerodynamic thrust force on the rotor. However, this approach cannot be used to simulate structural responses of the blades and variations in pitch angle of each blade due to pitch actual control (Jonkman et al., 2009) and rotational speed induced by difference between generator torque and aerodynamic torque on the rotor. Aerodynamic loads on the rotor are, in fact, resultants of aerodynamic pressure forces on the blades. Local peaks corresponding to NP frequency are observed in spectral densities of measured structural responses of prototype wind turbines, see Figure 4.3. P is equal to ω_{rotor} which is rotational speed of the rotor. N is an integer and is related to number of blades. N, could be, for example, 1, 2, 3, 4, or even a higher value. NP, for example, means that the frequency of the local peak is N times ω_{rotor}. The local peaks are excited by fluctuation of aerodynamic loads on the blades as incident wind speed at a given position on the rotor plane varies with respect to time and space while the blades rotate with rotational speed ω_{rotor}. Resonant structural vibrations could be excited by the fluctuation of the aerodynamic loads and result in large fatigue damage on the vibrated structure if NP is close to corresponding eigen frequencies of corresponding modes with respect to the structural vibrations. However, this important effect cannot be captured by the simplified approach shown in Eq. (4.1).

$$T_{rotor}^{aero} = \frac{1}{2}\rho_{air} A_{rotor} C_T^{aero,rotor} U_{rel}^2 \qquad (4.1)$$

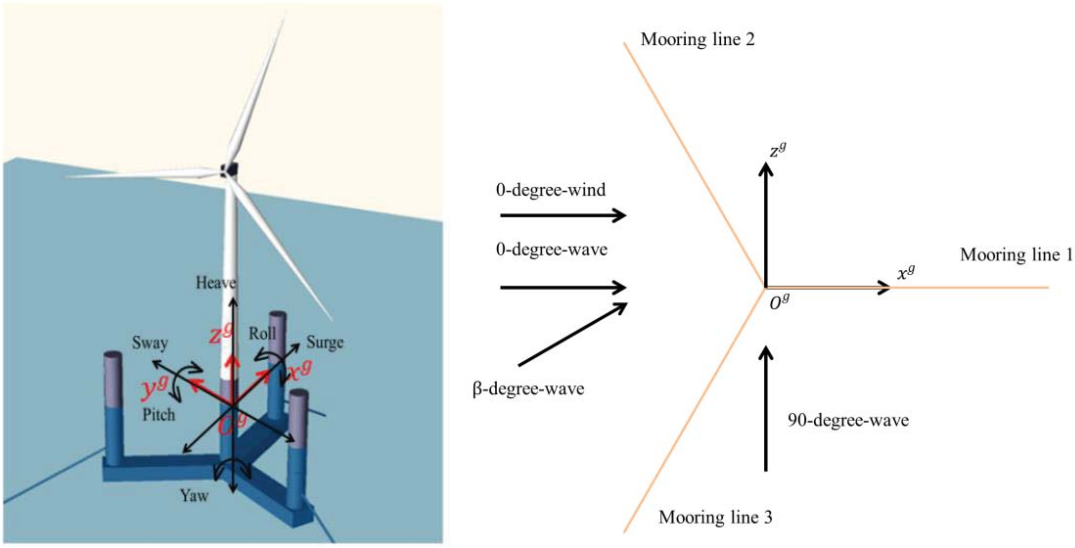

Figure 4.2 Layout of the 5-MW-CSC

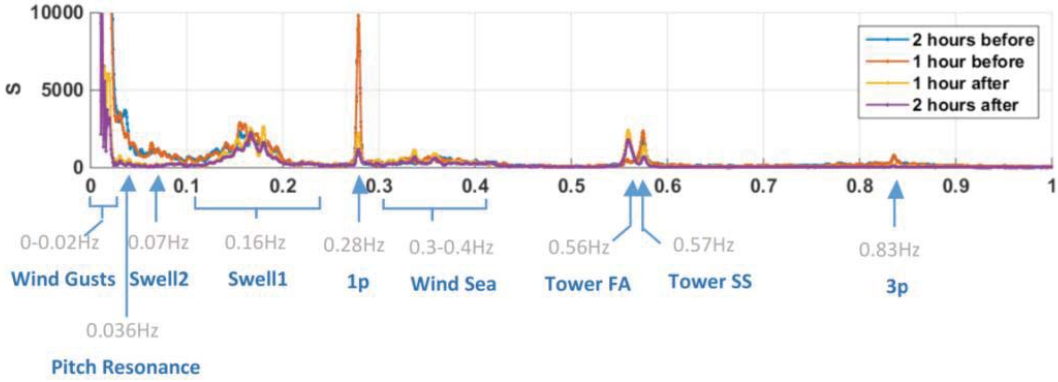

Figure 4.3 Spectral densities of measured structural responses of the WindFloat prototype (Roddier et al., 2017)

Time realizations of pressure and wind velocity vector of a given point in a wind field, for which floating wind turbine is operating in incident winds, could be obtained by using computational fluid dynamics method to numerically generate and solve corresponding Navier-Stokes equations (Matha et al., 2011). However, computational cost of this approach is extremely high and quality of

simulated result is very sensitive to quality of the generated numerical model.

The state-of-the-art time-domain aerodynamic computer codes, e.g. Aerodyn (Moriarty and Hansen, 2005), use the blade element momentum theory with necessary engineering corrections and/or generalized dynamic wave theory to simulate distributed aerodynamic loads on rotor blades in a given wind field while effect of configuration of the blades on the wind field is accounted for. Note that, in addition to the blade element momentum theory which is based on momentum analyses, vorticity-based methods can also be used for study of wind turbine aerodynamics. More detailed information for modelling of aerodynamic loads on the rotor blades are referred to (Hansen, 2008) (Branlard, 2017), as the focus of this chapter is on development of numerical time-domain approaches for analyzing sectional loads in floating wind turbine hulls by solving the challenges that are recognized as 1) how to accurately calculate hydro loads on the hull and 2) how to effectively map the loads in the finite element model.

4.1.5 Conventional time-domain approaches for modelling hydrodynamic loads

A review of conventional time-domain approaches for modelling hydrodynamic loads on floating wind turbine hulls and mooring lines is available in (Paper A1). Features of some conventional time-domain computer codes are tabulated in (Robertson et al., 2014). Morison formula and/or the conventional hybrid frequency-time domain approach (Paper A1) are used to model hydrodynamic loads on the floating wind turbine hulls. Note that computational fluid dynamic method is not considered to be practical due to its expensive computation cost and tens of thousands of time-domain simulation hours (IEC. 2005) (IEC. 2009) (Kvittem and Moan, 2015) as required by ULS and FLS design checks for floating wind turbines.

The Morison's formula is implemented in some cost effective computer codes (Robertson et al., 2014) to model the hydrodynamic loads. However, the Morison formula is an empirical formula. In general, it is applicable on a slender structure when wave length is

larger than five times diameter of the slender structure's cross-section (Faltinsen, 1990). Meanwhile, application of the Morison formula means memory effects of the hydrodynamic loads are neglected. In addition, additional pressure forces must be added to account for hydrodynamic loads in axial directions of the columns and pontoons (Robertson et al., 2014).

The computer codes which implement the conventional hybrid frequency-time domain approach in combination with drag term of Morison formula can accurately model the hydrodynamic loads on offshore structures and is frequently used in the offshore oil and gas industry but cannot capture sectional forces and moments in floating wind turbine hulls since the hull is modelled as a rigid-body with 6 d.o.f.s.

To solve this limitation, two time-domain approaches are developed by the author. The developed approaches are extensions of the conventional hybrid frequency-time domain approach. More detailed information with respect to the conventional hybrid frequency-time domain approach and developed approaches are referred to Sections 4.2-4.5.

4.2 Conventional hybrid frequency-time domain approach

4.2.1 Frequency-domain approaches for motion equations of a genetic floater in waves

As aforementioned, for a generic floater oscillating in waves with respect to its mean position, perturbation analysis with wave amplitude as a small parameter, Bernoulli's equation and velocity-potential can be used to effectively model potential hydrodynamic loads on hull of the floater. Consequently, if we assume that the floater is a rigid-body, linear motion equations in a sinusoidal wave in direction β, see Figure 4.2, could be generated as shown in Eq. (4.2). The terms in Eq. (4.2) are explained in Table 4.2. More details with respect to the terms are referred to (Faltinsen, 1990). $-\boldsymbol{M}^f\ddot{\boldsymbol{Y}}(\omega,t)$ and $-\boldsymbol{C}^f\boldsymbol{Y}(\omega,t)$ represent linearized inertial loads and restoring loads of the floater, respectively, in the O^f-x^f-y^f-z^f

coordinate system with respect to O^f. Second and higher order terms with respect to wave amplitude are not included in Eq. (4.2). While, $\boldsymbol{H}^f(\omega,\beta)$, $\boldsymbol{Y}(\omega,t)$, $\dot{\boldsymbol{Y}}(\omega,t)$ and $\ddot{\boldsymbol{Y}}(\omega,t)$ are complex values. $\mathcal{R}\{\}$ denotes the real part of the complex value inside the bracket.

$$\mathcal{R}\{\left(\boldsymbol{M}^f + \boldsymbol{A}^f(\omega)\right)\ddot{\boldsymbol{Y}}(\omega,t) + \boldsymbol{B}^f(\omega)\dot{\boldsymbol{Y}}(\omega,t) + \boldsymbol{C}^f\boldsymbol{Y}(\omega,t)\} = \mathcal{R}\{\boldsymbol{H}^f(\omega,\beta)X_\omega^{amp}e^{-i\omega t}\} \quad (4.2)$$

Table 4.2 Terms in linear motion equations of a generic floater in a sinusoidal wave in direction β

X_ω^{amp}	Oscillation amplitude of the sinusoidal wave
ω	Oscillation frequency of the sinusoidal wave
$\mathcal{R}\{\boldsymbol{H}^f(\omega,\beta)X_\omega^{amp}e^{-i\omega t}\}$	A 6×1 vector representing first order wave excitation loads on the floater
$\boldsymbol{Y}(\omega,t)$	A 6×1 vector representing the linear rigid-body motions of the floater in 6 d.o.f.s with respect to its mean position. $\boldsymbol{Y}(\omega,t)$ is described in the O^f-x^f-y^f-z^f coordinate system with respect to O^f.
$\dot{\boldsymbol{Y}}(\omega,t)$	First derivative of $\boldsymbol{Y}(\omega,t)$ with respect to time (t)
$\ddot{\boldsymbol{Y}}(\omega,t)$	Second derivative of $\boldsymbol{Y}(\omega,t)$ with respect to time (t)
$\boldsymbol{A}^f(\omega)$, $\boldsymbol{B}^f(\omega)$, and $\boldsymbol{H}^f(\omega,\beta)$	Hydrodynamic coefficients that are known as added mass coefficient matrix, potential damping coefficient matrix and first order wave excitation load transfer function, respectively
$\boldsymbol{M}^f$	Linearized mass matrix
$\boldsymbol{C}^f$	Restoring coefficient matrix
Note	
$\boldsymbol{A}^f(\omega)$, $\boldsymbol{B}^f(\omega)$, and $\boldsymbol{H}^f(\omega,\beta)$ can be calculated by 1) solving the potential-flow boundary value problem with assumption that the hull of the floater is a rigid-body in the O^f-x^f-y^f-z^f coordinate system, 2) calculating pressure forces on the mean wetted body surface of the hull based on the Bernoulli's equation and corresponding velocity potential, 3) integrating the pressure on the wetted body surface of the hull using the coordinate system O^f-x^f-y^f-z^f to obtain the integrated forces and moments acting on O^f, and 4) derive the hydrodynamic coefficients based on the corresponding resultant forces and moments on the O^f in the O^f-x^f-y^f-z^f coordinate system.	

4.2.2 Cummins's hybrid frequency-time domain approach for motion equations of a generic floater in waves

Cummins (Naess and Moan 2013) initially used a hybrid frequency-time domain approach to convert the motion equations from frequency-domain, as shown by Eq. (4.2), to time-domain, as shown by Eq. (4.3). Note that Eq. (4.3) does not include nonlinear wave loads, i.e. drag force and second and higher order wave loads.

$$(\boldsymbol{M}^f + \boldsymbol{A}^f(\omega = \infty))\ddot{\boldsymbol{y}}(t) + \int_{-\infty}^{+\infty} \boldsymbol{k}(t-\tau)\dot{\boldsymbol{y}}(\tau)d\tau + \boldsymbol{C}^f\boldsymbol{y}(t) = \boldsymbol{R}_{potential_{wave}}(t) \quad (4.3)$$

In Eq. (4.3), $\boldsymbol{y}(t)$, $\dot{\boldsymbol{y}}(t)$, and $\ddot{\boldsymbol{y}}(t)$ are time realizations of the position, velocity and acceleration of the floater in 6 d.o.f.s described in the O^f-x^f-y^f-z^f coordinate system. $\boldsymbol{A}^f(\omega = \infty)$ is the added mass matrix corresponding to infinite frequency. The radiation effect induced hydrodynamic loads, which are represented by $-\mathcal{R}\{\left(\boldsymbol{A}^f(\omega)\right)\ddot{\boldsymbol{Y}}(\omega,t) + \boldsymbol{B}^f(\omega)\dot{\boldsymbol{Y}}(\omega,t)\}$ in Eq. (4.2), are converted into $-\left(\boldsymbol{A}^f(\omega = \infty)\right)\ddot{\boldsymbol{y}}(t) - \int_{-\infty}^{+\infty}\boldsymbol{k}(t-\tau)\dot{\boldsymbol{y}}(\tau)d\tau$ in Eq. (4.3). $\int_{-\infty}^{+\infty}\boldsymbol{k}(t-\tau)\dot{\boldsymbol{y}}(\tau)d\tau$ is a convolution term. $\boldsymbol{k}$ is known as retardation or memory function and determined by $\boldsymbol{A}^f(\omega)$ or $\boldsymbol{B}^f(\omega)$ (Naess and Moan, 2013). $\boldsymbol{R}_{potential\_wave}(t)$ represents the resultants of first order wave excitation loads on the floater and is obtained by applying inverse Fourier transform on $\mathcal{R}\{\boldsymbol{H}^f(\omega,\beta)X_\omega^{amp}e^{-i\omega t}\}$. Note that the $\boldsymbol{R}_{potential\_wave}(t)$ can also be expressed by a convolution term as $\boldsymbol{R}_{potential\_wave}(t) = \int_{-\infty}^{+\infty}\boldsymbol{h}^f(t-\tau)x(\tau)d\tau$. $x(t)$ is realization of incident wave elevation. $\boldsymbol{h}^f$ is determined by $\boldsymbol{H}^f(\omega,\beta)$.

4.2.3 Conventional hybrid frequency-time domain approach for modelling floating wind turbines in wind and waves

The Cummins equations are implemented in some widely used time-domain computer codes to simulate global responses of a given floater in wind, wave and currents, e.g. Simo (MARINTEK, 2011) and Orcaflex (Robertson et al., 2014).

The motion equations could be approximately be expressed by Eq. (4.4) with the assumption that the floater is considered as a rigid-body with 6 d.o.f.s. $\boldsymbol{R}_{drag}(t)$ represents resultants of hydro drag forces on the floater induced by viscous effects of hydro fluid and could be modelled by the drag term of the Morison formula. Note that, for a floater, the hydro drag forces induce a quadratic damping effect which is shown mathematically in the Morison formula. $\boldsymbol{R}_{ext}(t)$ represents other resultant forces and moments on the floater, e.g. second and higher order wave excitation forces and moments, wind drag forces and moments, wave drift damping, forces and moments from the mooring lines and structures that are attached on the floater, and other specified forces and moments. $\boldsymbol{R}_{drag}(t)$ and $\boldsymbol{R}_{ext}(t)$ are dependent on states, e.g. motion, velocity and acceleration, of the floater. Note that, in principle, the motion equations could be generated and solved in an earth fixed coordinate system, while kinetics of the floater, and inertial and environmental loads on the floater could be appropriately modelled in appropriate coordinate systems, but be, eventually, transferred to the earth fixed coordinate system.

$$\left(\boldsymbol{M}^f + \boldsymbol{A}^f(\omega=\infty)\right)\ddot{\boldsymbol{y}}(t) + \int_{-\infty}^{+\infty} \boldsymbol{k}(t-\tau)\dot{\boldsymbol{y}}(\tau)d\tau + \boldsymbol{C}^f\boldsymbol{y}(t) = \boldsymbol{R}_{potential_{wave}}(t) + \boldsymbol{R}_{drag}(t) + \boldsymbol{R}_{ext}(t) \quad (4.4)$$

For modelling of a generic horizontal axis floating wind turbine, the flow chart of a time-domain numerical model, which implements the hybrid frequency-time domain approach and is developed in the computer code Simo/Riflex/Aerodyn, is given in Figure 4.4 as an example. The hull of the floating wind turbine is considered as a rigid-body with 6 d.o.f.s, while the tower base and fairleads of the mooring lines rigidly follow the motions of the hull. Six motion equations that are composed of the resultant external loads, e.g. viscous loads, gravity loads and hydro loads, on and inertial loads of the hull are generated in Simo with necessary input, e.g. mass properties of the hull, drag coefficients, hydrodynamic coefficients, i.e. the added-mass coefficient matrices ($\boldsymbol{A}^f(\omega)$), potential damping coefficient matrices ($\boldsymbol{B}^f(\omega)$) and first order wave excitation load transfer function ($\boldsymbol{H}^f(\omega,\beta)$), and specified forces, moments and

restoring stiffness matrix. A finite element model, for which the mooring lines, tower and RNA are modelled as bar and beam elements and coupled to the motion equations of the hull are generated and solved in Riflex (MARINTEK 2013) with necessary input, e.g. relevant mass and structural properties and drag and added mass coefficients. Aerodyn and a Java controller (Ormberg and Bachynski, 2012) are coupled to Riflex through a dll file (Ormberg and Bachynski, 2012) to account for the aerodynamic loads on the RNA and tower, effect of pitch control on aerodynamic loads on the three blades and effect of the generator inside the nacelle on the power production and generator torque. More details are available in the later part of this chapter and Bachynski (2014).

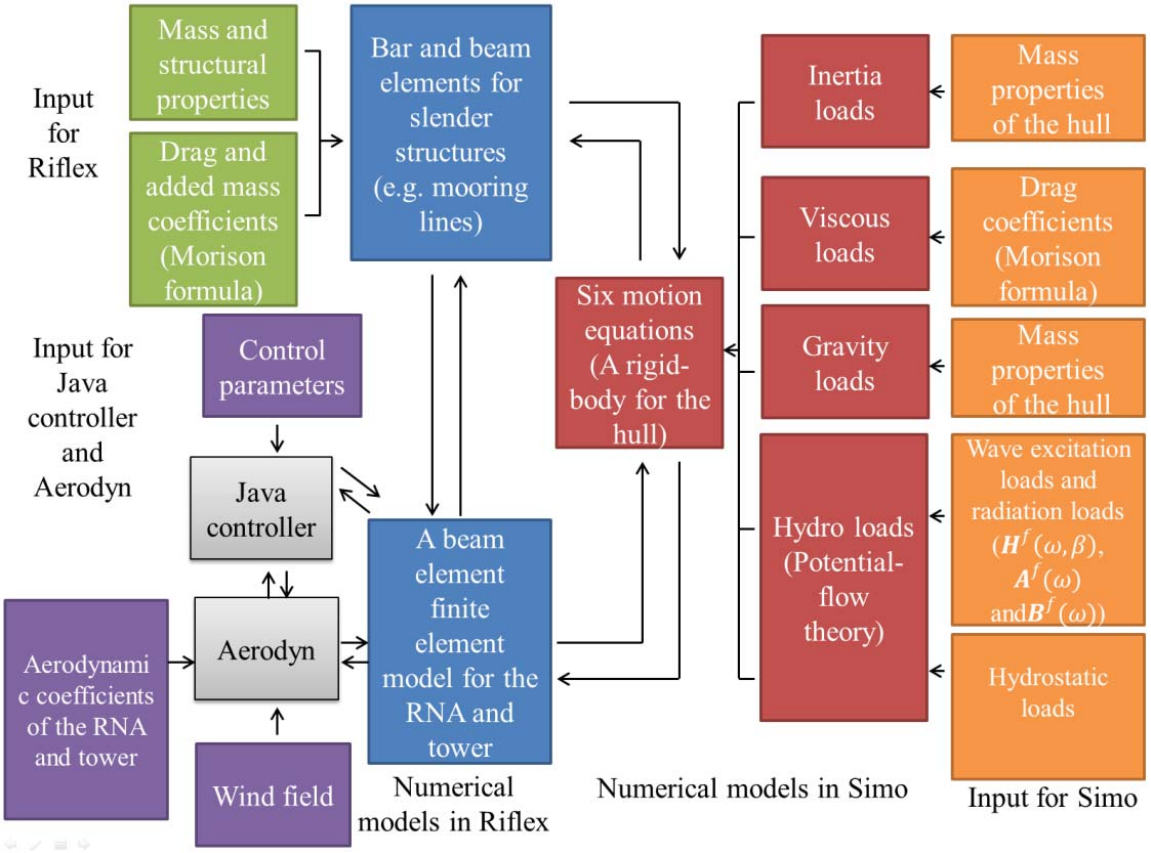

Figure 4.4 The flow chart of a time-domain numerical model of a generic horizontal axis floating wind turbine developed in Simo/Riflex/Aerodyn (the conventional approach)

The conventional hybrid frequency-time domain approach is considered as the state-of-the-art approach and has been used by researchers, e.g. Bachynski (2014), (Nejad et al., 2015), Moan (2015), (Bachynski et al., 2013), to analyze structural responses of the RNA, tower and mooring lines and rigid-body motions of the hull of floating wind turbines. However, to calculate structural responses of the hull, we must develop a finite element model of the hull rather than a rigid-body formulation; while, to map the loads in the finite element model, we must develop accurate and effective time-domain approach to model the loads on the hull as distributed loads rather than three integrated forces and moments.

To solve this challenge, time-domain approaches for modelling generic and specific floaters are developed by the author, see Sections 4.3 and 4.4.

4.3 Development of a time-domain approach for generic floaters

The developed approach for generic floaters is presented in this section and Paper A1.

In general, numerical models in finite element codes are developed in an earth fixed coordinate system, such as the global coordinate system (O^g-x^g-y^g-z^g) shown in Figure 4.5.

In the developed (proposed) time-domain approach for generic floaters, the hull of floating structures is considered as an assemble of d structural components. d is specified by designer. A beam element finite element model, which includes d nodes (red colored in Figure 4.5), can be developed in the global coordinate system to represent the global stiffness of the structural components. Each node has 6 d.o.f.s and corresponds to a structural component. The external loads on and inertia loads of each structural component are calculated, integrated and transferred to the node that corresponds to the structural component in the finite element model. In particular, hydrostatic and the hydrodynamic loads on each structural component are obtained by integrating hydrostatic and

hydrodynamic pressure loads on wetted body surface of the structural component. The pressure loads are normally calculated based on a frequency-domain hydrodynamic code using a panel method. Sectional forces and moments in structural components of the hull can be obtained by carrying out a finite element analysis using a time-domain code. Accurate sectional forces and moments are given at the cross-sections corresponding to the red dashed lines, see Figure 4.5. The number of the structural components and quality of the finite element model of the hull affect the accuracy of the sectional forces and moments. The beam element finite element model of the hull should accurately represent the global stiffness of the hull, in particular for static indeterminate structures.

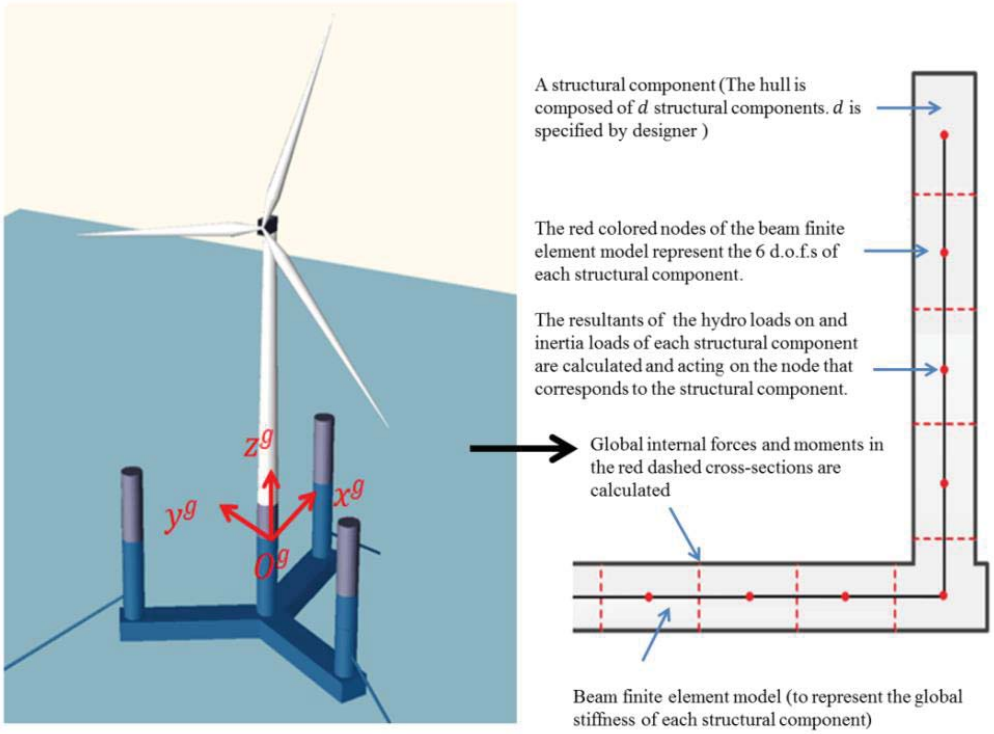

Figure 4.5 Definition of a finite element model of the hull

The flow chart of a time-domain numerical model of a generic horizontal axis floating wind turbine which implements the proposed approach and is developed in the computer code Simo/Riflex/Aerodyn is given in Figure 4.6. Comparing to Figure 4.4 (the conventional hybrid frequency-time domain approach), the

proposed approach models the hull as a beam element finite element model while detailed approaches for modeling the external on and inertia loads of each structural component are referred to Paper A1. The approaches are developed by extending the conventional approaches used in the state-of-the-art computer codes. Therefore, the proposed approach can be easily implemented in various state-of-the-art computer codes to extend their capabilities. Note that different coordinate systems, as shown in Section 4.1, are used to describe the kinetics of the system and model each component of the inertial and external loads on the hull.

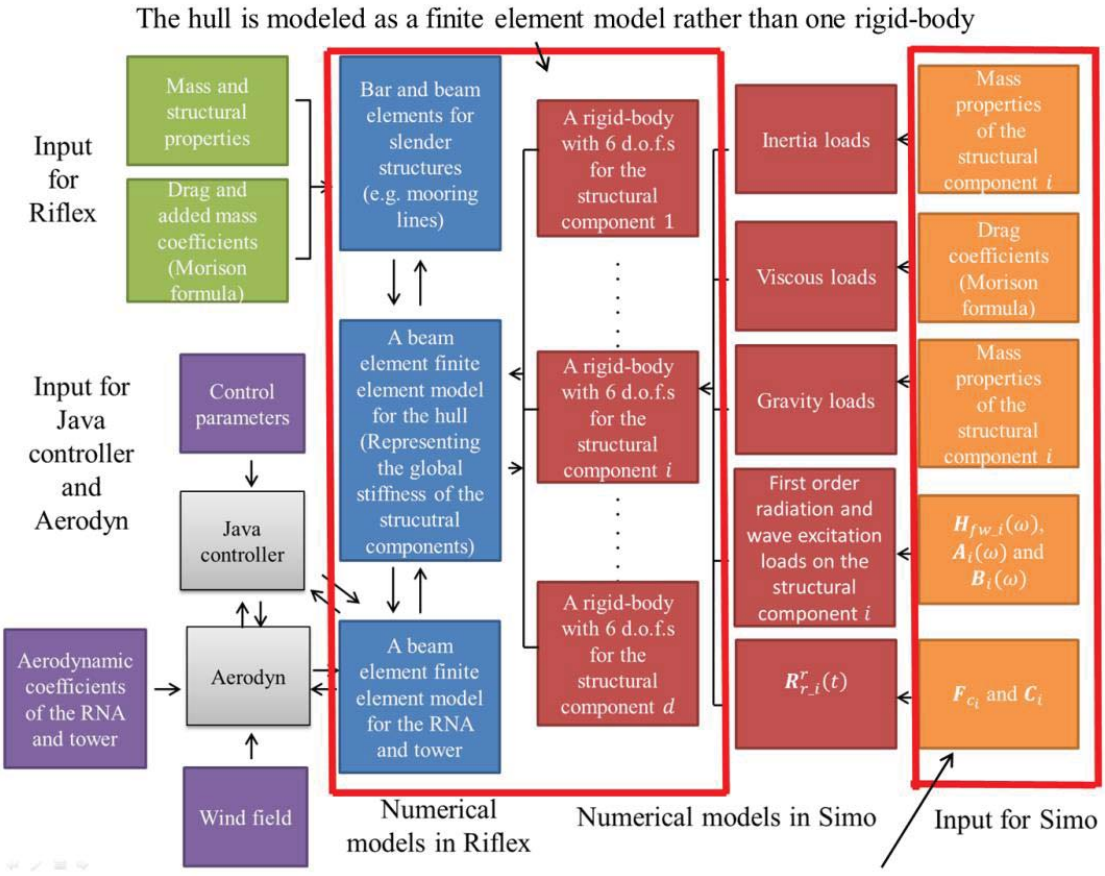

Relevant approaches are developed to modify the input for Simo, which is used to model the external and inertial loads on each structural component.

Figure 4.6 The flow chart of a time-domain numerical model of a generic horizontal axis floating wind turbine developed in Simo/Riflex/Aerodyn (the developed approach)

4.4 Development of a time-domain approach for specific floaters

The specific floaters mentioned in this thesis are floaters for which columns and pontoons of floater hulls are connected by braces, e.g. the OC4 semi-submersible wind turbine and WindFloat, see Figure 1.6. The braces of the specific floaters are considered as critical structural components while global and local load effects on the braces need to be analysed. Consequently, the author developed a time-domain approach for simulating sectional forces and moments in the braces. The developed approach is presented in this section and Paper A4. Note that the developed approach can be used to simulate responses of a generic floater as long as corresponding hydrodynamic coefficients could be appropriately obtained, see more discussions in Section 4.5, the future work mentioned in Chapter 7, later part of the present section and Paper A4.

For the specific floaters, Morison formula could be sufficient to model hydrodynamic loads on the braces since diameter of the braces could be very small when compared to wave length of the incident waves.

Each of the columns and pontoons, for which the braces are attached on, could be treated as a structural component. In contrast to the wetted body surfaces of structural components of the hull of a generic floater illustrated in Section 4.3, e.g. Figure 4.5, wetted body surface of each of the columns and pontoons, itself or with the still water plane area, can be approximately considered as a closed surface in boundary value problem for solving velocity potential and hydro pressure forces on the wetted body surface, e.g. the OC4-semi. This is because that area of interfaces between the columns and braces is small when compared to area of wetted body surface of the columns, and has negligible effects on value and distribution of the corresponding velocity potential and hydro pressure forces on the wetted body surface.

For such specific floaters, each of the columns and pontoons could be modelled as a rigid-boy with 6 d.o.f.s,, while the braces are modelled as beam elements attached on the columns. In another

word, the semi-submersible hull could be modelled as a multi-body system connected by beam elements. Motion equations for the multi-body system could be established as shown in Eq. (4.5) by extending the Eq. (4.4). Dimensions of matrices and vectors in Eq. (4.4) are 6×6 and 6×1, respectively. The dimensions of these matrices and vectors are extended to $6n \times 6n$ and $6n \times 1$. n is number of the rigid-bodies. For the OC4-semi submersible wind turbine, n is 4. Expression of the $\boldsymbol{k}_{6n\times6n}$ is given in Eq. (4.6). $\boldsymbol{k}_{6\times6}^{u,v}$ is a 6×6 matrix. $\boldsymbol{k}_{6\times6}^{u,v}$ is used to account for hydrodynamic loads on body u due to memory effect of hydrodynamic loads and rigid-body motions of body v. $\boldsymbol{k}_{6\times6}^{u,v}$ can be calculated by $\boldsymbol{A}(\omega)_{6\times6}^{u,v}$ or $\boldsymbol{B}(\omega)_{6\times6}^{u,v}$. $\boldsymbol{A}(\omega)_{6\times6}^{u,v}$ is added mass matrix of body u induced by motions of body v. $\boldsymbol{B}(\omega)_{6\times6}^{u,v}$ is potential damping matrix of body u induced by motions of body v. $\boldsymbol{R}_{potential_{wave\_}6n\times1}(t)$ represents the resultants of first order wave excitation loads on the structural components of the hull and is obtained by applying inverse Fourier transform on $\mathcal{R}\{\boldsymbol{H}_{6n\times1}(\omega,\beta)X_{\omega}^{amp}e^{-i\omega t}\}$.

$$\begin{aligned}\left(\boldsymbol{M}_{6n\times6n}+\boldsymbol{A}_{6n\times6n}(\omega=\infty)\right)\ddot{\boldsymbol{y}}_{6n\times1}(t)&\\ +\int_{-\infty}^{+\infty}\boldsymbol{k}_{6n\times6n}(t-\tau)\dot{y}_{6n\times1}(\tau)d\tau&\\ +\boldsymbol{C}_{6n\times6n}\boldsymbol{y}_{6n\times1}(t)&\\ =\boldsymbol{R}_{potential_{wave\_}6n\times1}(t)+\boldsymbol{R}_{drag\_6n\times1}(t)&\\ +\boldsymbol{R}_{ext\_6n\times1}(t)&\qquad(4.5)\end{aligned}$$

$$\boldsymbol{k}=\begin{bmatrix}\boldsymbol{k}_{6\times6}^{1,1} & \cdots & & \cdots & \boldsymbol{k}_{6\times6}^{1,n}\\ & \ddots & & & \\ \vdots & & \boldsymbol{k}_{6\times6}^{i,j} & & \vdots\\ & & & \ddots & \\ \boldsymbol{k}_{6\times6}^{n,1} & \cdots & & \cdots & \boldsymbol{k}_{6\times6}^{n,n}\end{bmatrix}_{6n\times6n}\qquad(4.6)$$

Hydrodynamic coefficients, e.g. $\boldsymbol{A}(\omega)_{6\times6}^{u,v}$, $\boldsymbol{B}(\omega)_{6\times6}^{u,v}$, and $\boldsymbol{H}_{6n\times1}(\omega,\beta)$, used in Eq. (4.5), can be easily calculated by commercial hydrodynamic codes, e.g. WAMIT, as long as the wetted body surface of each of the columns and pontoons can be

approximately considered as a closed surface or the wetted body surface with the water plane area can be approximately considered as a closed surface.

Sectional forces and moments in braces that are attached on the columns and pontoons can be obtained by solving the motion equations as shown in Eq. (4.5). More detailed description of the developed approach and a case study, for which forces and moments in braces of the OC4-semi in wind and waves are calculated and used in ULS design check for the braces, are referred to Paper A4.

4.5 Summary of assumptions and limitations of the conventional hybrid frequency-time domain approach and the developed approaches

The differences between the conventional hybrid frequency-time domain approach and developed approaches are related to 1) structural model of the hull and 2) numerical approaches for modelling hydro-pressure forces on wetted body surface of the hull. These differences are summarized and highlighted in Table 4.3 in together with corresponding implemented assumptions of the numerical approaches and their limitations.

The structural model of the hull in the conventional hybrid frequency-domain approach is a rigid-boy with 6 d.o.f.s while, in the proposed (developed) approaches for generic and specific floaters, the hull is modelled as a multi-body system connected by beam elements which are used to model flexibility of the hull.

The hydro-pressure forces on wetted body surface of the hull are composed of viscous drag forces, which are modelled by using the drag term of the Morison formula, and potential hydrodynamic loads and hydrostatic pressure forces. Summaries of approaches for modelling hydrostatic pressure forces and hydrodynamic loads are given in Section 4.5.1 and Section 4.5.2, respectively.

Additional terms could be added in the motion equations or expressions of the hydrodynamic loads on each structural components mentioned by the conventional and proposed approaches

to account for second and higher order hydro load effects. Method for deriving the additional terms for the conventional approach is referred to MARINTEK (2011), while method for modelling second and higher order hydro loads on the structural components of the proposed approaches needs to be developed in the future.

Accuracy of simulated motions given by the conventional approach for offshore platforms has been widely accepted by offshore oil and gas industry. Validations for the proposed approach for generic floaters are presented in Chapter 5. The proposed approach for specific floaters needs to be validated in the future.

4.5.1 Summary of approaches for modelling hydrostatic pressure forces

According to the Bernoulli's equation, hydrostatic pressure on a given point on wetted body surface of the hull could be expressed as $-\rho g z$. ρ is density of the hydro fluid. g is gravity acceleration. z is vertical position of the point in an earth fixed coordinate system. The hydrostatic pressure on the point fluctuates when the hull oscillating around its mean position.

The author derived a generic expression for the resultant forces and moments of the hydrostatic pressure forces on the outer surface and the atmospheric pressure forces on the inner surface of the structural component i when the structural component is located at its instantaneous position described by $\boldsymbol{\eta}^i(t) = [\eta_1^i, \eta_2^i, \eta_3^i, \eta_4^i, \eta_5^i, \eta_6^i]^T$ in an earth fixed coordinate system. The resultant forces and moments are denoted as $\boldsymbol{R}_{r\_i}^r(t)$. By neglecting the second order and higher order terms with respect to wave elevation, the expression of the $\boldsymbol{R}_{r\_i}^r(t)$ is given by Eq. (4.7).

$$\boldsymbol{R}_{r\_i}^r(t) = \boldsymbol{F}_{c_i} + (-1) * \boldsymbol{C}_i \boldsymbol{\eta}^i(t) \qquad (4.7)$$

$\boldsymbol{F}_{ci}$ is a 6×1 vector. $\boldsymbol{C}_i$ is a 6×6 matrix with real coefficients. The expressions of $\boldsymbol{F}_{ci}$ and $\boldsymbol{C}_i \boldsymbol{\eta}^i(t)$ are referred to Paper A1. Eq. (4.7) could be used by the conventional hybrid frequency-time domain approach except that the hydrostatic pressure forces on the wetted body surface of the hull, instead of the wetted body surface of the structural component i, are integrated.

We use the origin of a body-fixed coordinate system to represent rigid-body motions of a hull. As shown in Figure 4.1, when the hull is located at its mean position, the origin of the body-fixed coordinate system is located at center of water plane area, while the body-fixed coordinate system is coincident to the global coordinate system and the O^f-x^f-y^f-z^f coordinate system. The instantaneous position of the body-fixed coordinate system is described by $\boldsymbol{\eta}(t) = [\eta_1, \eta_2, \eta_3, \eta_4, \eta_5, \eta_6]^T$. The resultant of hydrostatic pressure forces on the hull is denoted as $\boldsymbol{R}_r^r(t)$. Note that $\boldsymbol{R}_r^r(t)$ is acting on origin of a body-related coordinate system, which corresponds to the body-fixed coordinate system as shown in Figure 4.1, and described in the body-related coordinate system. By using Eq. (4.7), an analytical expression of $\boldsymbol{R}_r^r(t)$ can be easily derived due to the fact that the wetted body surface of the hull and the water plane area form a closed surface, see Eq. (4.8).

$$\boldsymbol{R}_r^r(t) = \boldsymbol{F}_c + (-1) * \boldsymbol{C}\boldsymbol{\eta}(t) \qquad (4.8)$$

We assume that the buoyancy of the hull is $\rho g V_{dis}^{mean}$, pointing upward and acting on (x_B^b, y_B^b, z_B^b) in the body-fixed coordinate system, when the hull is at its mean position. V_{dis}^{mean} is volume of displaced water. Then, $\boldsymbol{F}_c = [0, 0, \rho g V_{dis}^{mean}, y_B^b \rho g V_{dis}^{mean}, -x_B^b \rho g V_{dis}^{mean}, 0]^T$ and $\boldsymbol{C}$ is expressed by Eq. (4.9). In Eq. (4.9), A_w^{mean} is mean water plane area. $I_{xb,xb}^{mean}$ and $I_{yb,yb}^{mean}$ are second moment of water plane area with respect to the axes of x_B^b and y_B^b, respectively.

$$\boldsymbol{C} = \begin{bmatrix} 0 & 0 & 0 & 0 & 0 & 0 \\ 0 & 0 & 0 & 0 & 0 & 0 \\ 0 & 0 & \rho g A_w^{mean} & 0 & 0 & 0 \\ 0 & 0 & 0 & \rho g I_{xb,xb}^{mean} + \rho g V_{dis}^{mean} z_B^b & 0 & -\rho g V_{dis}^{mean} x_B^b \\ 0 & 0 & 0 & 0 & \rho g I_{yb,yb}^{mean} + \rho g V_{dis}^{mean} z_B^b & -\rho g V_{dis}^{mean} y_B^b \\ 0 & 0 & 0 & 0 & 0 & 0 \end{bmatrix} \qquad (4.9)$$

Eq. (4.8) can be used by the proposed approach for specific floaters since, in this approach, wetted body surface of each structural component is approximately considered as a closed surface. However, Eq. (4.8) cannot be used in the proposed approach for generic floaters.

4.5.2 Summary of approaches for modelling hydrodynamic pressure forces

In the conventional approach, hydrodynamic pressure forces on wetted body surface of a hull are integrated and represented by three resultant forces and moments which are expressed in form of the convolution terms as shown in Eq. (4.4) and are determined by hydrodynamic coefficients $\boldsymbol{A}^f(\omega)$, $\boldsymbol{B}^f(\omega)$ and $\boldsymbol{H}^f(\omega,\beta)$. These coefficients are derived from resultant of corresponding hydrodynamic pressure forces on mean wetted body surface of the hull.

In the proposed approaches, hydrodynamic pressure forces on wetted body surface of each structural component of the hull are integrated and represented by three resultant forces and moments which are expressed in form of the convolution terms as shown in Eq. (4.10) and Eq. (4.5), respectively, and are determined by hydrodynamic coefficients $\boldsymbol{H}_{fw\_i}(\omega,\beta)$, $\boldsymbol{A}_i(\omega)$ and $\boldsymbol{B}_i(\omega)$, and $\boldsymbol{H}_{6n\times1}(\omega,\beta)$, $\boldsymbol{A}_{6n\times6n}$ and $\boldsymbol{B}_{6n\times6n}$, respectively.

$$\boldsymbol{L}^t_{external,i} = \boldsymbol{R}_{potential\_wave\_i}(t) - \int_{-\infty}^{+\infty} \boldsymbol{k}_i(t-\tau)\dot{\boldsymbol{\eta}}^i(\tau)d\tau - \boldsymbol{A}_i^{\infty}\ddot{\boldsymbol{\eta}}^i(t) \qquad (4.10)$$

Note that, in the proposed approach for generic floaters, the resultants of the first order radiation and wave excitation loads on the structural component i are represented by $\boldsymbol{L}^t_{external,i}$, see Eq. (4.10). $\boldsymbol{L}^t_{external,i}$ is described in a body-related coordinate system of the structural component i and acting on the origin of the coordinate system. $\boldsymbol{\eta}^i(t)$ and $\ddot{\boldsymbol{\eta}}^i(t)$ represent velocity and acceleration of the structural component i. $\boldsymbol{R}_{potential\_wave\_i}(t)$, $\boldsymbol{k}_i$, and $\boldsymbol{A}_i^{\infty}$ are determined by the hydrodynamic coefficients, i.e. $\boldsymbol{H}_{fw\_i}(\omega,\beta)$, $\boldsymbol{A}_i(\omega)$ and $\boldsymbol{B}_i(\omega)$.

$\boldsymbol{H}_{fw\_i}(\omega,\beta)$, $\boldsymbol{A}_i(\omega)$ and $\boldsymbol{B}_i(\omega)$, and $\boldsymbol{H}_{6n\times1}(\omega,\beta)$, $\boldsymbol{A}_{6n\times6n}$ and $\boldsymbol{B}_{6n\times6n}$ are derived from resultant of corresponding hydrodynamic pressure forces on mean wetted body surface of each structural component.

The hydrodynamic pressure forces are given by the Bernoulli's equation on base of corresponding velocity potential which is obtained by solving the corresponding boundary value problem. In the conventional approach and the proposed approach for generic floaters, the corresponding boundary value problems are generated and solved by considering the hull as a rigid-body. This means that, in the proposed approach for generic floaters, the kinematics of different structural components is constrained by the rigid-body assumption. Consequently, although the hydrodynamic interaction effects between the structural components are included in the hydrodynamic loads on each structural component, the proposed approach for generic floaters may not be able to well model the hydroelasticity effect. Therefore, it is not recommended to be applied on floating structures with relatively large flexibility, for which hydroelasticity effect can be important.

In contrast, in the proposed approach for specified floaters, the corresponding boundary value problem is generated and solved by considering the hull as a multi-body system for which each of the structural components of the hull is considered as an independent rigid-body with 6 d.o.f.s. This means the boundary value problems, for which one structural component is oscillating about its mean position while the rest structural components are fixed at their mean position, are generated and solved. Consequently, both of the hydrodynamic interaction effects between the structural components, and linear component of interaction effects between structural vibration of the hull and the structural vibration induced hydrodynamic loads are accounted for in the proposed approach for specific floaters. To solve the boundary value problems by using the state-of-the-art commercial hydrodynamic codes, e.g. WAMIT, the wetted body surface of each structural component must be a closed surface or the wetted body surface and the water plane must form a closed surface. However, this requirement cannot be satisfied by a generic floater. This limitation of the commercial hydrodynamic codes limits application of this approach.

Table 4.3 Summary of differences, assumptions and limitations of the conventional and proposed time-domain numerical modelling approaches

	The conventional hybrid frequency-time domain approach for generic floaters	The proposed approach for generic floaters	The proposed approach for specific floaters (Analysis for responses of braces)
Structural model of the hull	A rigid-body with 6 d.o.f.s	Multi-bodies attached on a beam element finite element model. Each body has 6 d.o.f.s	Each of the columns and pontoons is modelled as a rigid-body with 6 d.o.f.s while the attached braces are modelled by beam elements
Viscous drag forces	Drag term of the Morison formula		
Hydrostatic pressure forces	Eq. (4.7) or Eq. (4.8)	Eq. (4.7)	Eq. (4.7) or Eq. (4.8)
hydrodynamic loads (based on potential flow theory)	Three resultant forces and moments on the hull which are expressed by the convolution terms as shown in Eq. (4.4).. The convolution terms are related to hydrodynamic coefficients $\boldsymbol{A}^f(\omega)$, $\boldsymbol{B}^f(\omega)$ and $\boldsymbol{H}^f(\omega,\beta)$	Three resultant forces and moments on each structural component which are expressed by the convolution terms as shown in Eq. (4.10). The convolution terms are related to hydrodynamic coefficients $\boldsymbol{H}_{fw\_i}(\omega,\beta)$, $\boldsymbol{A}_i(\omega)$ and $\boldsymbol{B}_i(\omega)$	Three resultant forces and moments on each structural component which are expressed by the convolution terms as shown in Eq. (4.5). The convolution terms are related to hydrodynamic coefficients $\boldsymbol{H}_{6n\times 1}(\omega,\beta)$, $\boldsymbol{A}_{6n\times 6n}$ and $\boldsymbol{B}_{6n\times 6n}$

Table 4.3 continuing			
Boundary value problem	The boundary value problems are generated and solved by considering the hull as a rigid-body.		The boundary value problems are generated and solved by considering the hull as a multi-body system.
Limitations	Structural responses of the hull cannot be captured by the structural model of the hull except for the rigid-body motions in 6 d.o.f.s	Flexibility effects of the hull on the hydro loads are not accounted for. The approach may not be able to well model the hydroelasticity effect.	The wetted body surface of each structural component is required to be a closed surface or the wetted body surface and the water plane are required to form a closed surface by state-of-the-art commercial hydrodynamic codes for generating and solving the boundary value problem.
Notes	Additional terms could be added in the motion equations to account for second and higher order hydro load effect.	The hydrodynamic interaction effects between the structural components are included in the hydrodynamic loads on each structural component. Method for modelling second and higher order hydro loads on the structural components of the proposed approaches needs to be developed in future	
Validations	Accuracy of simulated motions of offshore platforms has been widely accepted by offshore oil and gas industry	The approach has been validated, see Chapter 5.	The approach need to be validated in future

Chapter 5

Numerical and experimental verification and validation for the developed numerical approach

Several numerical models which implements the proposed approach for generic floaters as presented in Chapter 4 have been generated to analyze global responses, e.g. rigid-body motions and sectional forces and moments, of the 5-MW-CSC, which has a braceless and static determinate hull and been presented in Chapter 3. To verify and validate the proposed approach, the simulated responses of the numerical models are compared to simulations of the other reference numerical models and measurements of experimental tests, in a systematical way and step by step. An introduction for the procedure, results, analysis and limitations with respect to the verification and validation is presented in this chapter. Detailed information is referred to Papers A1, A2 and A3. Note that validation for the proposed approach for specific floaters is not included in this thesis but is proposed as future work.

5.1 Summary of reasons for verifying and validating the developed approach for generic floaters

The proposed approach for generic floaters is an extension of the conventional hybrid frequency-time domain approach which has been widely used by offshore oil and gas industry to simulate rigid-body motions and mooring line tensions of offshore platforms in

waves, see Eq. (4.4). Although accuracy of simulated rigid-body motions by using the conventional hybrid frequency-time domain approach has been accepted by offshore oil and gas industry, still, there is a need to validate the proposed approach. The reasons are highlighted as follows:

- Accuracy of the rigid-body motions is an indicator of resultant hydro loads on the hull. However, situation of sectional forces and moments in the hull could be more complicated. For instance, the cross-section 6, as shown in Figure 3.2 divided the hull into two parts. We denote the part without the tower as Part A. The sectional forces and moments ($\boldsymbol{R}^s\ (t)$), and inertial and external loads of the Part A (denoted as $\boldsymbol{R}^i\ (t)$ and $\boldsymbol{R}^e\ (t)$ respectively) are in equilibrium as the hull is a static determinate structure. This means accuracy of the sectional forces and moments is actually affected by accuracy of local inertial and external loads. Consequently, accuracy of distributions of the simulated inertial and external loads on the hull is important to the accuracy of the simulated sectional forces and moments, and need to be appropriately validated.
- The resultant of hydro loads on the hull may be dominated by first order potential loads. However, second and higher order hydro load effect may be considerable for sectional forces and moments in some locations of the hull. To quantify this effect, comparisons between numerical simulations and experimental measurements are needed.
- The $\boldsymbol{R}^i\ (t)$ and $\boldsymbol{R}^e\ (t)$ could be out of phase and result in a cancellation effect on $\boldsymbol{R}^s\ (t)$ which means that, in some situations, $\boldsymbol{R}^s\ (t)$ could be a small part when compare to either $\boldsymbol{R}^i\ (t)$ or $\boldsymbol{R}^e\ (t)$. Consequently, $\boldsymbol{R}^s\ (t)$ may be more sensitive to relative differences between simulations and corresponding reference values of $\boldsymbol{R}^i\ (t)$ and $\boldsymbol{R}^e\ (t)$, respectively.
- Due to limited profit margin, an over conservative structural design of the hull is not preferred by offshore wind industry.

Therefore, the structural design of floating wind turbines may be more sensitive to accuracy of relevant numerical approaches. Consequently, uncertainties of the numerical approaches need to be appropriately quantified.

5.2 Verification procedure (comparisons in numerical simulations)

The procedure of the verification discussed in this chapter and relevant numerical models are shown in Figures 5.1 and 5.2. Detailed information is referred to Paper A1.

Three comparisons, i.e. Comparison A, Comparison B and Comparison C, have been carried out to verify the proposed approach step by step on base of numerical simulations given by five numerical models. These numerical models and the comparisons are briefly explained below and illustrated in Figure 5.1 and Figure 5.2, respectively.

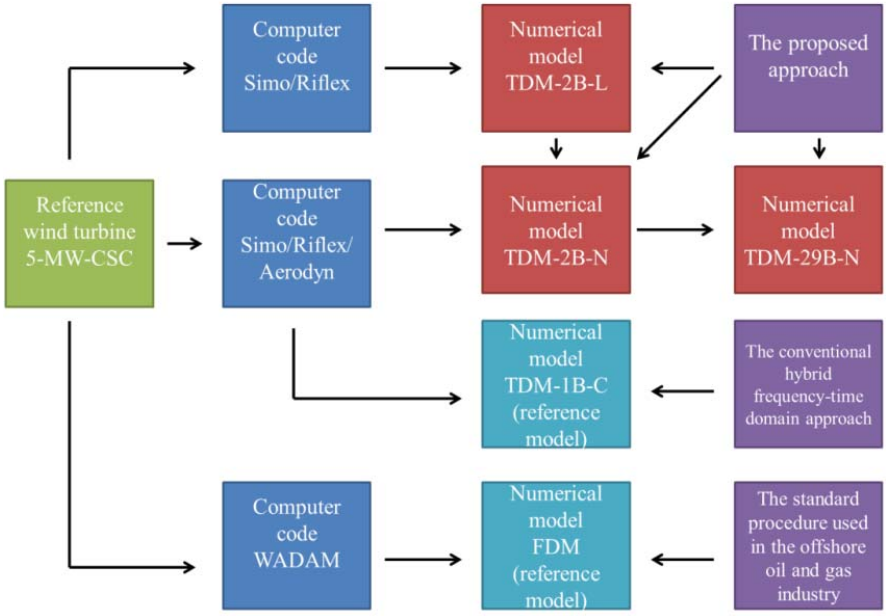

Figure 5.1 Numerical models developed in the verification procedure

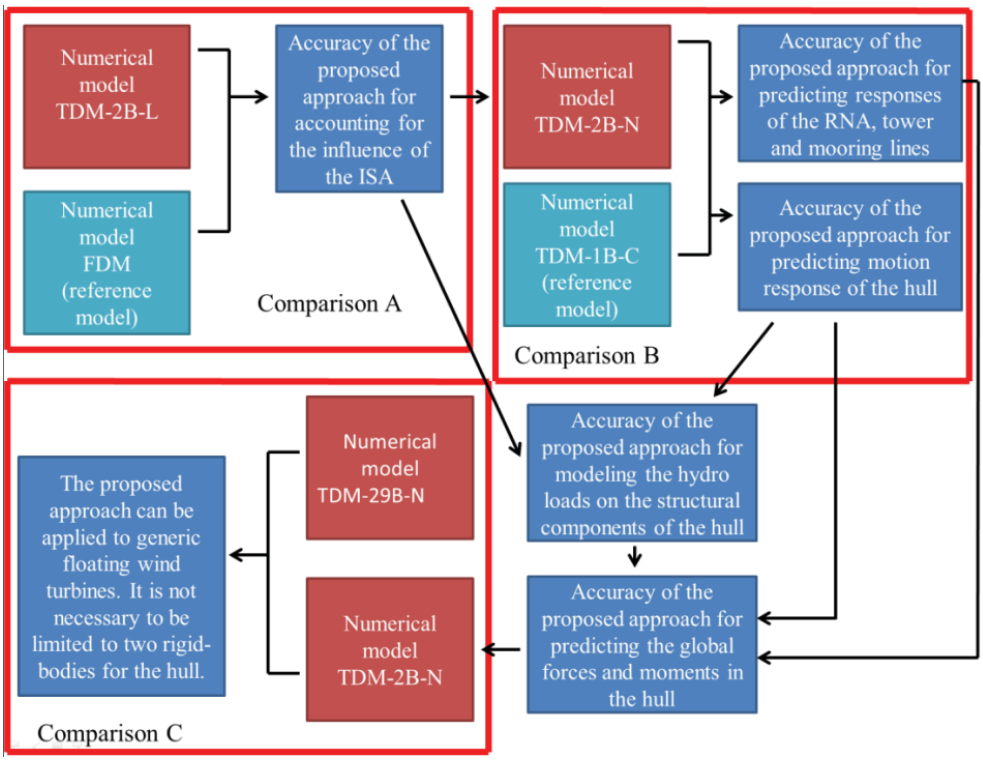

Figure 5.2 Verification procedure

5.2.1 Numerical models used in the verification

FDM is a frequency-domain model of the 5-MW-CSC developed in WADAM to calculate wave induced sectional forces and moments by implementing a standard procedure used in the offshore oil and gas industry (DNV, 2013b). A summary of the features of the time-domain models is available in Table 5.1. More details are referred to Paper A1.

Among the time-domain numerical models, see Table 5.1, it is expected that the TDM-2B-N can calculate sectional forces and moments in the cross-section as shown by the dashed line in Figure 3.2 while the time-domain model TDM-29B-N can calculate the sectional forces and moments in the same cross-section and the other twenty-seven cross-sections.

Table 5.1 Summary of the features of the time-domain models developed in the verification procedure

Mass and structural models	**TDM-2B-L (Time-domain model, two rigid bodies for the hull, linear model)**	**TDM-1B-C (Time-domain model, One rigid bodies for the hull, conventional approach)**	**TDM-2B-N/ TDM-29B-N (Time-domain model, two/twenty nine rigid bodies for the hull, developed approach)**
The hull	The floating wind turbine is divided into two parts: "Part A" and "Part B". The two parts are modeled as two rigid-bodies. Each rigid-body has 6 d.o.f.s. The two rigid-bodies are connected by three artificial beam elements. Integrated mass (corresponding to each rigid-body).	The hull is modeled as one rigid-body with 6 d.o.f.s. Integrated mass.	The hull is discretized as two rigid-bodies: "Body1" and "Body2" / twenty-nine rigid-bodies. Each rigid-body has 6 d.o.f.s. The two rigid-bodies are connected by three artificial beam elements / The twenty-nine rigid-bodies are connected by beam elements. Integrated mass (corresponding to each rigid-body)
Nacelle	Rigid-bodies with integrated mass (Included in the rigid-body for the "Part B").	Mass point attached to tower top	Identical to TDM-1B-C
hub		Mass point attached to shaft	
Tower		Flexible bodies Beam elements Distributed mass	
Blades			
Shaft			
Mooring lines	The finite element model of the mooring lines is not developed.		
External load model	**TDM-2B-L**	**TDM-1B-C**	**TDM-2B-N/ TDM-29B-N**
The hull	1) Gravity loads 2) Extended hybrid frequency-time domain approach 3)Hydrostatic pressure force 4) Rayleigh damping (the part that is proportional to the structural stiffness) 5) Linearized restoring forces and moments provided by the mooring lines.	1) Gravity loads 2) Conventional hybrid frequency-time domain approach 3) Viscous force (Drag term of the Morison formula) 4) Hydrostatic pressure force	1) Gravity loads 2) Extended hybrid frequency-time domain approach 3) Viscous force (Drag term of the Morison formula. The drag coefficients are identical to TDM-1B-C) 4) Hydrostatic pressure force 5) Rayleigh damping (the part that is proportional to the structural stiffness)
Nacelle	1) Gravity loads	1) Gravity loads 2) Rayleigh damping (the part that is proportional to the structural stiffness)	Identical to TDM-1B-C
hub			
Tower			
Blades		1) Gravity loads 2) Aerodynamic loads (Aerodyn) 3) Rayleigh damping (the part that is proportional to the structural stiffness)	
Shaft		1)Generator torque	
Mooring lines	None	1) Gravity and Buoyancy loads 2) Morison formula	

Table 5.1 continuing
Note
• TDM-2B-L is a time-domain model of the 5-MW-CSC developed in Simo/Riflex. The proposed approach is implemented to calculate wave induced sectional forces and moments in the cross-section as shown by the dashed line in Figure 3.2. Aerodynamic loads are not available in the TDM-2B-L. • TDM-1B-C is a time-domain model developed in Simo/Riflex/Aerodyn. Aerodynamic loads on the RNA and tower are appropriately accounted for in the TDM-1B-C, while the conventional hybrid frequency-time domain approach is implemented to model the hydro loads on the semi-submersible hull. The modeling approach implemented in the TDM-1B-C is considered as the state-of-the-art approach that has been used by researchers to analyze responses of floating wind turbines in wind and waves except for the sectional forces and moments in the hull since the approach models the hull as one rigid-body with 6 d.o.f.s. • TDM-2B-N is an extension of the TDM-1B-C. The proposed approach is implemented to calculate sectional forces and moments in the hull (in the cross-section as shown by the dashed line in Figure 3.2). The TDM-1B-C and TDM-2B-N are identical except for the finite element model of the hull and method for modeling the external and inertial loads on the hull. • TDM-29B-N is an extension of the TDM-2B-N. The TDM-2B-N includes two rigid-bodies for the hull, while, the TDM-29B-N includes twenty-nine rigid-bodies for the hull, see Figure 5.3. The TDM-29B-N model is developed and compared to the TDM-2B-N model in order to show that the proposed method can be generalized to a model consisting of any number of structural components. From the practical use point of review, it is convenient to use the TDM-29B-N model to obtain the dynamic responses at any critical position of the hull by just one time-domain model. While, using the TDM-2B-N approach, many different numerical models need to be built and analyzed.

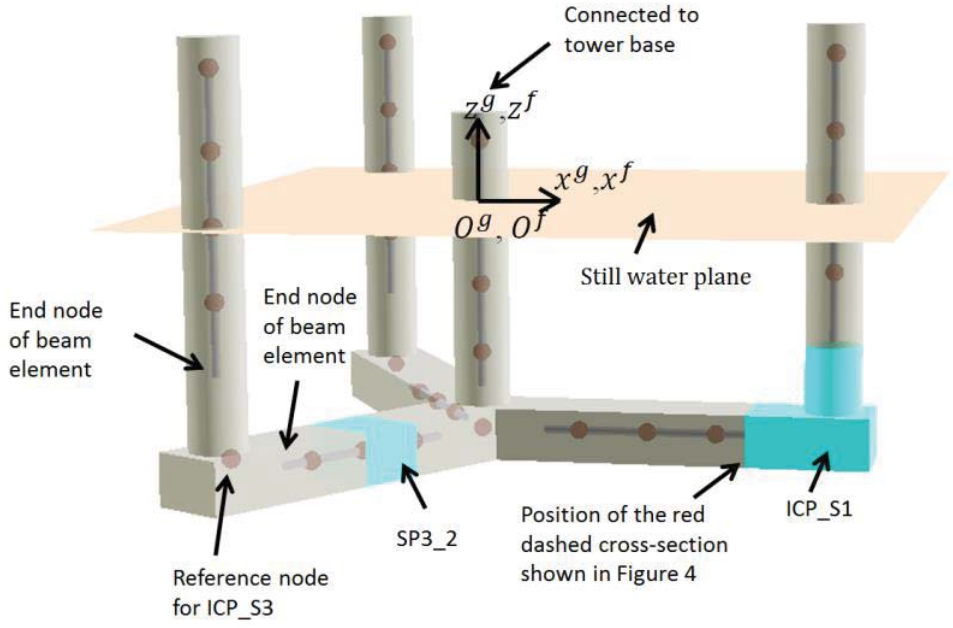

Figure 5.3 The finite element model of the hull with twenty-nine bodies

5.2.2 Objectives and expectations of Comparison A, Comparison B and Comparison C

Accuracy of the calculated responses is related to two modeling issues: 1) whether or not the computer codes can accurately calculate the wind and waves induced external and inertial loads on the floating wind turbines and map the loads to the generated finite element models of the floating wind turbines; and 2) whether or not the finite element models generated in the computer codes can accurately represent the global stiffness of the floating wind turbines and calculate the structural responses for given loads. These two features are coupled.

The hull of the 5-MW-CSC is a static determinate structure. For a static determinate structure, in general, the accuracy of the responses in the structure is purely determined by accuracy of external loads acting on the structural components. In linear theory, hydrodynamic and hydrostatic loads on structural components of the hull are determined by two issues. We denote these issues as ISA and ISB, respectively.

- ISA: Configuration and shape of mean wetted body surfaces of the structural components.
- ISB: Motion responses of the structural components.

The accuracy of the sectional forces and moments in the hull calculated by the TDM-2B-N is indicated by the results of Comparison A and Comparison B. Comparison A focuses on verifying that the influence of the ISA on the hydro loads on the structural components can be accurately modeled in finite element codes which implement the proposed approach. Comparison B focuses on verifying that finite element codes which implement the proposed approach can accurately predict motion responses of the structural components and responses of the RNA, tower and mooring lines of the reference semi-submersible wind turbine in wind and waves. Comparison C is carried out, to some extent, to address that the proposed approach can be applied to generic floating wind turbines, for which the hull may need to be modeled by any number of structural components. The proposed approach is not necessarily limited to two rigid-bodies for the hull. Due to the limitation of the

proposed approach, we do not account for the hydroelasticity effect in the comparisons discussed in the present paper.

More explanations with respect to the comparisons and numerical models used in the comparisons are given as follows:

In Comparison A, the FDM is used as a reference model for the transfer functions of wave to sectional forces and moments in the hull. While the transfer functions can also be derived from structural responses of the hull calculated by carrying out regular and/or irregular wave analysis in time-domain numerical models that implement the proposed approach, e.g. TDM-2B-L, TDM-2B-N and TDM-29B-N. The FDM is a linear system and does not account for non-linear effects on the sectional forces and moments, while TDM-2B-L is developed to be, as much as possible, a linear system and equivalent to the FDM. The agreement in the transfer functions calculated in the FDM and TDM-2B-L is expected to be good if the proposed approach accurately models the hydro pressure forces on the structural components of the hull and maps the forces on the finite element model of the hull.

TDM-2B-L models the 5-MW-CSC as two structural components connected by three artificial beam elements. Aerodynamic loads are not accounted for in the TDM-2B-L. In contrast, aerodynamic loads are accounted for in the TDM-2B-N while the TDM-2B-N models the hull of the 5-MW-CSC as two structural components connected by three artificial beam elements and the mooring lines, tower and blades as beam elements. The mean wetted body surfaces of the two structural components of the TDM-2B-L are identical to the mean wetted body surfaces of the two structural components of the TDM-2B-N correspondingly and respectively. Consequently, if the influence of the ISA on the hydro loads on the structural components can be accurately modeled in the TDM-2B-L, the influence can be accurately modeled in the TDM-2B-N as well.

The motions of the hull and responses of the RNA, tower and mooring lines predicted by the TDM-2B-N and TDM-1B-C are compared in Comparison B. TDM-1B-C is used as a reference model except for the sectional forces and moments in the hull. TDM-1B-C

and TDM-2B-N are identical except for the finite element model of the hull and method for modeling the external and inertial loads on the hull. Therefore, agreement in the compared responses is expected to be good.

Since the hull of the 5-MW-CSC is a static determinate structure, it is expected that the global structural stiffness of the hull does not affect the sectional forces and moments in the structural components of the hull except for the inertia loads and hydro loads induced by the flexible modes of the hull. The global structural stiffness of the hull is determined by properties of the equivalent cross-sections of the pontoons and columns and material properties, e.g. Young's modulus and modulus of rigidity. In Comparison C, artificial material properties are implemented to make the global structural stiffness of the hull of the TDM-29B-N to be of the same magnitude as the one of the TDM-2B-N. Consequently, the sectional forces and moments calculated by the TDM-2B-N and TDM-29B-N are expected to be identical.

5.3 Validation procedure (comparisons between numerical simulations and experimental measurements)

In the validation procedure, comparisons between numerical simulations and experimental measurements, i.e. Comparison D and Comparison E, see Figure 5.4. Detailed information is referred to Papers A2 and A3.

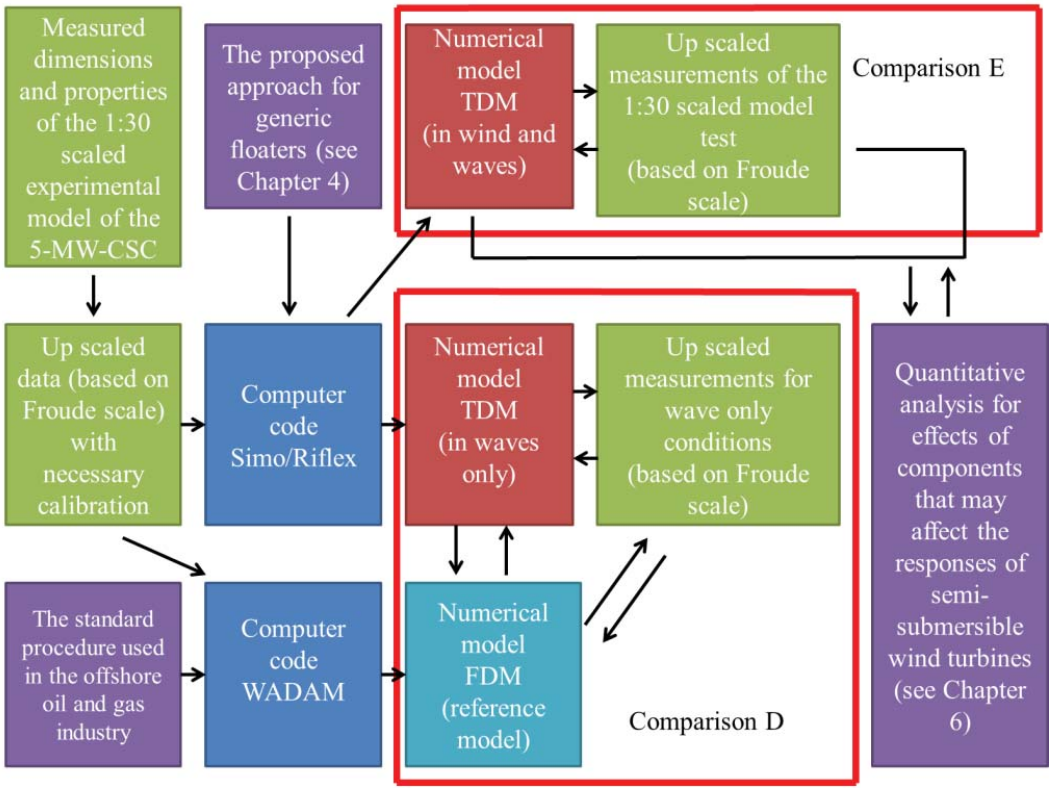

Figure 5.4 Validation procedure

5.3.1 Limitations of current model tests and uncertainties of measured data

Global responses of floating wind turbines in wind and waves can be measured (and analyzed) by carrying out model tests. Limitations of the model tests and uncertainties of the measured data must be aware when measured data is used to validate numerical codes.

Conventional model tests for measuring wave induced responses of a floating unit are designed to satisfy geometrical and kinematic similarities and equality according to Froude number ensure similarity between inertia and gravity forces of experimental and actual models. However, similarity between inertia and viscous forces of the models cannot be achieved since, in practice, equality in Reynolds number cannot be satisfied at the same time. Different Reynolds number may indicate different patterns of fluid flows

around the experimental and actual models. Necessary corrections are needed if the measurements are sensitive to the viscous forces. Due to the same reason, similarity between inertia and aerodynamic loads on the RNA, which are important to responses of floating wind turbines, cannot be achieved either, see (Goupee et al., 2012b) (Goupee et al., 2012a) (Koo et al., 2012). To solve this problem, various forms of "non-geometrical scaling" of the wind turbine rotor have been developed to improve the aerodynamic load modeling in wind-wave model tests. For example, one form of non-geometrical scaling is to replace the wind turbine rotor with a drag disk, e.g. (Roddier et al., 2010) (Wan et al., 2015). A more sophisticated method of non-geometrical scaling is to modify the wind turbine airfoil shape and chord length to obtain improved performance at low Reynolds numbers (Kimball et al., 2014) (Fowler et al., 2013) (Bottasso et al., 2014) (Fernandes et al., 2014). These non-geometrical scaled wind turbines can be designed to achieve the same non-dimensional thrust coefficient as the reference full scale wind turbine in a specified steady condition (calm water, constant wind speed, and fixed rotational speed and pitch angle of blades). Therefore, the "non-geometrical scaled" wind turbines can be used to physically analyze static response of the experimental model of floating wind turbines in steady conditions. However, it is still a challenge, which has not been solved yet, to make a performance-matched wind turbine model, which means to use the non-geometrical scaled wind turbines in model tests to accurately mimic Froude scaled actual aerodynamic loads on the rotor of the corresponding full scale reference wind turbine in dynamic conditions (turbulent winds, and/or regular or irregular waves, and/or with or without controller for blade pitch angle and rotational speed). This is because it is a challenge to design a non-geometrical scaled wind turbine for which the non-dimensional thrust coefficient is always identical to the corresponding coefficient of the reference full scale wind turbine in an arbitrary steady condition. As shown in (Kimball et al., 2014), the non-dimensional thrust coefficient versus tip speed ratio curves of the non-geometrical scaled wind turbines can be very sensitive to wind speed (the Reynolds number). It is also

a challenge to generate and/or measure constant and turbulent wind fields in a classical towing tank or ocean basin (Helder and Pietersma, 2013) as well. Implementation of real-time hybrid model testing approach, e.g. ReaTHM® (Sauder et al., 2016), and (Hall et al, 2017), is a recent development for accurate modelling the actual aerodynamic loads in ocean basin. ReaTHM® relies on assumption that actual aerodynamic loads on the full scaled reference wind turbine can be captured by state-of-the-art aerodynamic computer codes, e.g. Aerodyn. A numerical finite element model for the RNA and control system of the full scale reference wind turbine and numerical model of wind field are generated in a computer code which implements the state-of-the-art aerodynamic computer code to calculate aerodynamic loads on the RNA in the wind field. The resultants of the calculated aerodynamic loads are down scaled (based on Froude scale) and physically applied on a Froude scaled model of the floating wind turbine, while in the computer code the hub of the RNA rigidly follows measured rigid-body motions, which has been up scaled (based on Froude scale), of the experimental model.

5.3.2 Experimental approach and measured data used in the validation

Rigid-body motions and sectional forces and moments in tower base and base of a side column of a 1:30 scaled model of the 5-MW-CSC in several wave-only and wind-wave conditions were measured by SINTEF Ocean in its ocean basin (Bachynski et al., 2016) by using the ReaTHM® testing approach. The ReaTHM® can appropriately address effects of the control system on aerodynamic loads while actual loaded forces can be measured in a straight-forward manner. A detailed description of the approach and its feasibility is available in (Sauder et al., 2016) and Chabaud (2016). The measurements are used in Comparison D and Comparison E.

5.3.3 Comparisons of simulated and measured responses in moderate waves

Comparison D focuses on comparisons of the responses of the semi-submersible wind turbine in moderate waves with less non-linear effects for which frequency-domain commercial computer codes, e.g. WAMIT, WADAM, can be used as a reference model. A frequency-domain model is developed in WADAM. While a time-domain model is developed in Simo/Riflex by using the proposed approach. Wave-induced transfer functions for rigid-body motions and fore-aft and side-to-side bending moments in base of the side column derived from time-domain and frequency-domain simulations and measurements are compared. The developed time-domain model is expected to give the same results as the commercial computer codes, while the time-domain model can be further used to analyze the sectional forces and moments in the hull in combined wind and wave loads in a straightforward manner but the frequency-domain codes cannot.

5.3.4 Comparisons of simulated and measured responses in operational conditions (in wind and waves)

Comparison E focuses on comparisons of the responses of the semi-submersible wind turbine in operational conditions (in wind and waves).

In previous, comparisons of simulated and measured responses of floating wind turbines have been analyzed by some researchers, e.g. Wendt et al., (2017). Geometrical scaled or non-geometrical scaled wind turbine, which cannot correctly mimic the Froude scaled aerodynamic loads on the corresponding full scale reference wind turbine in dynamic condition, are used in the model tests mentioned by the researchers in their publications, while these model tests are not designed for capturing sectional forces and moments in hull of floating wind turbines. For each model test, the wind turbine of the experimental model is modelled in its corresponding numerical model to simulate aerodynamic loads on the wind turbine while numerical wind field is generated based on measured wind speed at

one specified fixed position in the model test. Consequently, the differences between the measurements and simulations are due to the differences between 1) the numerical wind field and actual wind field in the model test, 2) performance of the numerical and experimental models of the wind turbine and 3) mass properties of the numerical and experimental models and 4) hydro loads on the hull of the numerical and experimental models. These differences are mixed and make it be difficult to analyze the reasons for the differences between the measurements and simulations in quantity. To avoid this difficult situation, the aerodynamic loads which are actually loaded on the 1:30 scaled model analyzed in Comparison E are measured and loaded on its corresponding numerical model to ensure identical aerodynamic loads. Consequently, differences in simulated and measured responses only indicate differences in simulated and actual hydro loads on the hull, and differences in modeled and actual mass properties of the semi-submersible wind turbine.

The differences in the mass properties can be reduced to a negligible level by carrying out quality control and calibrations. Note that the "model-the-model" principle, which means to simulate the actual model tests as closely as possible (Ormberg et al., 2003), is used in development of the frequency-domain and time-domain numerical models used in Comparison D and Comparison E. Rational calibration procedures are referred to Paper A2 and Paper A3.

To analyze the differences between measurements and simulations, effects of components that may affect the rigid-body motions and sectional bending moments are analyzed in quantity. The results and conclusion of this analysis is summarized in Chapter 6. Detailed information is referred to Paper A3.

5.4 Summary of key results and conclusions with respect to the verification and validation

5.4.1 Comparison of TDM-2B-L and FDM (Comparison A)

As shown in Figure 5.2, objective of Comparison A is to validate the accuracy of the proposed approach for accounting for the

influence of the ISA issue by comparing transfer functions given by the FDM, which is a frequency-domain model and is considered as a reference model, and transfer functions that are derived from simulated realizations which are obtained by carrying out irregular wave analysis or regular wave analysis by using the TDM-2B-L.

Regular wave analysis can directly give the moduli and phase angles of the transfer functions; however, the phase angles are very sensitive to numerical issues. Alternatively, wave induced transfer function ($H_{xy}(\omega)$), which is composed of the response amplitude operator (RAO), which is also known as transfer function modulus, and phase angle (α), can be derived from realizations of the incident waves (input, denoted as x) and corresponding responses (output, denoted as y), as shown in Eq. (5.1) and Eq. (5.2). G_{xy} and G_{xx} are one-side spectra that are derived from the corresponding cross-correlation and autocorrelation with respect to the realizations of x and y, respectively (Bendat, 2010). $H_{xy}(\omega)$ is a complex number. Real and imaginary parts are denoted as Re and Im, respectively.

$$H_{xy}(\omega) = \frac{G_{xy}(\omega)}{G_{xx}(\omega)} = Re + iIm \tag{5.1}$$

$$\text{RAO} = \sqrt{Re^2 + Im^2} \tag{5.2}$$

Note that transfer functions of wave induced axial and shear stresses are determined by transfer functions of wave induced sectional forces and moments, as shown by Eq. (3.1) and Eq. (3.2).

Good agreement in transfer function moduli for wave induced axial and shear stresses given by two models indicates that agreement in transfer function moduli and phase angle of wave induced sectional forces and moments given by these models is good. Therefore, we focus on comparing the transfer function moduli for wave induced sectional forces and moments, and axial and shear stresses.

The relative difference (R_b) in the obtained transfer function is employed to show the difference in two groups of data, see Eq. (5.3). R_b is used to address the relative difference with respect to corresponding maximum value in entire wave frequency range (from

0.35 rad/s to 2 rad/s). For example, $e(\omega) = \{e(\omega_1), e(\omega_2), \dots e(\omega_i), \dots\}$ and $f(\omega) = \{f(\omega_1), f(\omega_2), \dots f(\omega_i), \dots\}$ represent transfer function moduli for wave induced axial force. $e(\omega)$ and $f(\omega)$ are calculated by carrying out irregular wave analysis and regular wave analysis, respectively. ω_i is a given frequency.

$$R_b(\omega_i) = \left| e(\omega_i) - f(\omega_i) \right| \Big/ \max\{e(\omega), f(\omega)\} \times 100\% \qquad (5.3)$$

We find that, as expected, agreement in transfer function moduli obtained by carrying out regular and irregular wave analysis in the TDM-2B-L is good. The largest R_b for the transfer function moduli for axial and shear stresses is less than 6%. For most of the transfer function moduli, R_b is less than 3%.

Wave induced axial and shear stress transfer function moduli given by the FDM and TDM-2B-L are compared, while the transfer function moduli given by the TDM-2B-L are obtained by carrying out irregular wave analysis. The agreement is very good. The relative differences (R_b) vary with respect to the wave frequency and wave direction. In general, peak values of R_b may appear at frequencies nearby troughs of the transfer function modulus curves. However, the effect of the peak values of R_b on the accuracy of the sectional forces and moments calculated by the TDM-2B-L is very limited. This is because, in the frequency range from 0.35 rad/s to 2 rad/s, for most of the transfer function moduli, R_b is less than 2.5%. The maximum value of R_b for the transfer function moduli for stresses and for sectional forces and moments is no more than 8% and 5.9% respectively. Two examples are available in Figures 5.5 and 5.6. Position of the points on the cross-section is shown in Figure 3.4. The difference is induced by: 1) inherent difference between frequency-domain and time-domain models; 2) accuracy limitation for the numerical solver and other numerical issues. Detailed discussions are referred to Paper A1.

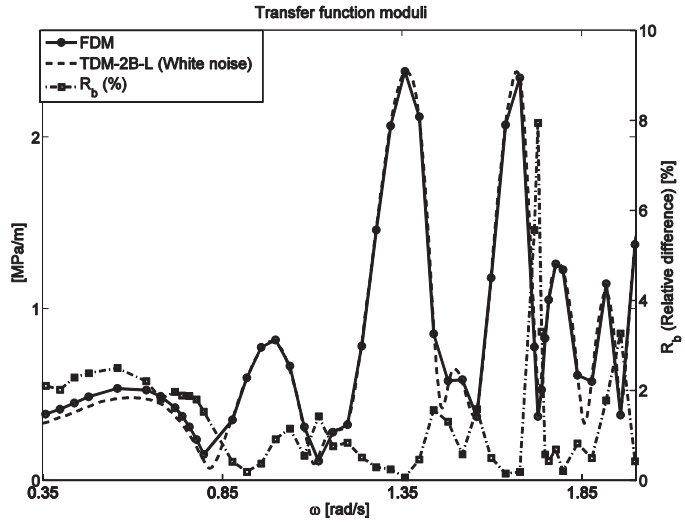

Figure 5.5 Comparison of transfer function modulus curves for the axial stress at the point 6 given by the FDM and TDM-2B-L subjected to 120-degree-wave

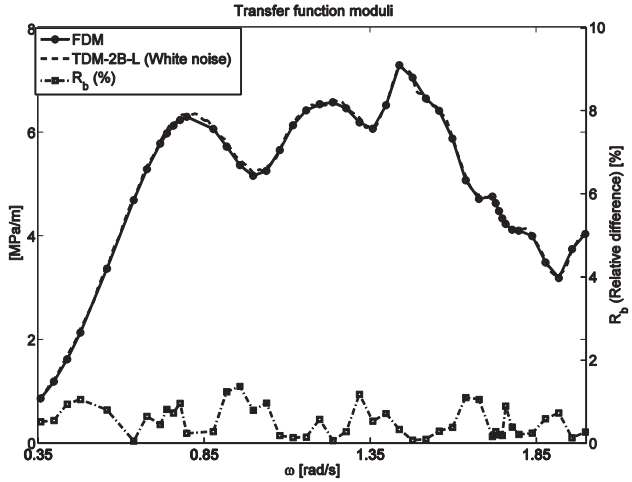

Figure 5.6 Comparison of transfer function modulus curves for the axial stress at the point 1 given by the FDM and TDM-2B-L subjected to 10-degree-wave

5.4.2 Comparisons of TDM-2B-N, TDM-1B-C and TDM-29B-N (Comparison B and Comparison C)

As shown in Figure 5.2, objective of Comparison B is to verify the accuracy of the proposed approach for predicting responses of the RNA, tower, mooring lines and motions of the hull by comparing simulated realizations given by the TDM-2B-N and TDM-1B-C. The TDM-1B-C is developed by using the conventional hybrid frequency-time domain approach and considered as a reference model.

Ten combined wind and wave conditions are selected from a site in northern North Sea (Li et al., 2015) and tabulated in Paper A1. The combined wind and wave conditions are composed of five different mean wind speeds covering below rated, at rated, above rated and parked wind speed and two wave directions. In addition, we also looked at wave only conditions by removing the winds from the combined conditions. For each condition, one 1-hour time-domain simulation is carried out in the TDM-1B-C, TDM-2B-N and TDM-29B-N respectively. Identical random seeds are used to eliminate stochastic uncertainties. Responses, i.e. the pitch angle of each blade, azimuth angle and rotational speed of the rotor, aerodynamic forces and moments on the rotor, torque on the rotational shaft of the drive train, generator torque, generated power, sectional forces and moments in a given cross section of the tower, global rigid-body motions of the hull and mooring line tension at the top end (fairlead) of each mooring line, are calculated and compared.

The responses of the TDM-1B-C and TDM-2B-N subjected to the wave only conditions are firstly compared. We find that the responses are identical to each other (the difference is negligible). Part of the realization of the fore-aft bending moment at the tower base, in EC02000 (wave only), is given as an example, see Figure 5.7.

Detailed comparisons of responses of the TDM-1B-C and TDM-2B-N in wind and waves are referred to Paper A1.

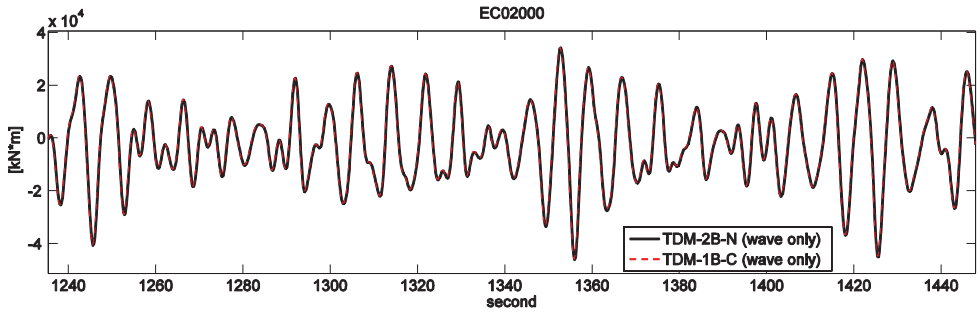

Figure 5.7 An example of the time series of the fore-aft bending moment at the tower base of the TDM-1B-C and TDM-2B-N, EC02000 (wave only)

Regarding Comparison C, we compare the responses of the TDM-2B-N and TDM-29B-N in wave only and in combined wind and wave conditions. Observations of the comparisons of the responses of the RNA, tower and mooring lines of the TDM-2B-N and TDM-29B-N are similar to the observations of the comparison of the TDM-1B-C and TDM-2B-N which have been illustrated in above. For each condition, time realizations of the sectional forces and moments of the TDM-2B-N and TDM-29B-N are in phase and almost identical. An example is given in Figure 5.8.

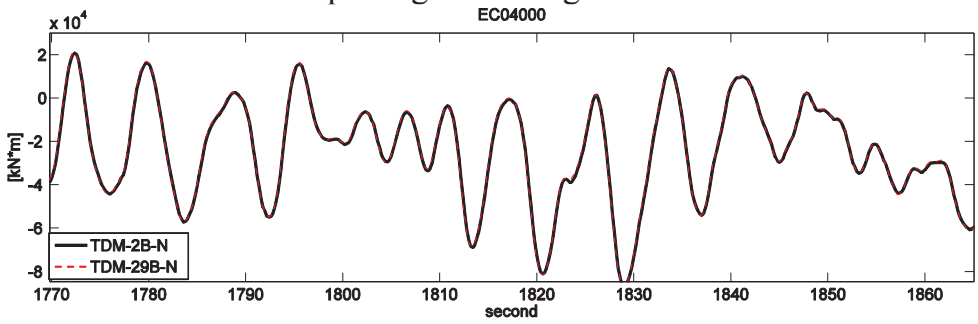

Figure 5.8 An Example of the time series of the M_y (bending moment) of the TDM-2B-N and TDM-29B-N, EC04000

5.4.3 Comparisons of simulations and measurements in moderate waves (Comparison D)

In Comparison D, measured and simulated responses, i.e. the fore-aft and side-to-side bending moments and rigid-body motions, of the 1:30 scaled model of the 5-MW-CSC in moderate wave-only conditions are compared. Note that necessary calibrations have been done as we follow the "model-the-model" principle (Ormberg et al., 2003). Descriptions of the model test, post-processing for the measured data and development of time-domain and frequency-domain numerical models are referred to Paper A2.

Skewness and kurtosis (Bendat, 2010) of the measured and simulated realizations and waves are around 0 and 3, respectively, and indicate that, in moderate waves, the experimental model and time-domain model are linear systems with respect to waves (input, denoted as x) and corresponding response (output, denoted as y). Therefore, wave induced transfer function ($H_{xy}(\omega)$), which is composed of the response amplitude operator (RAO) and phase angle (α), are derived by using Eq. (5.1) and Eq. (5.2). The phase angle (α) is derived based on the corresponding values of Re and $-Im$. A negative phase angle (α) means the y lags the x.

Note that computation of the phase angle of the $H_{xy}(\omega)$ derived from measurements of the incident waves and corresponding responses is very sensitive to the synchronization in particular for high-frequency components of the transfer functions. For example, a 0.4 seconds mismatch means a 9-degree-shift and a 32-degree-shift of the phase angle for the wave components for which the frequency is 0.4 rad/s and 1.4 rad/s, respectively.

The linear characteristic of the system can also be checked by calculating corresponding coherence function $\gamma_{xy}^2(\omega)$, see Eq. (5.4), (Bendat, 2010). The values of γ_{xy}^2 will always satisfy $0 \leq \gamma_{xy}^2 \leq 1$. The γ_{xy}^2 will equal to one for an ideal constant parameter linear system. G_{yy} is one-side spectrum that is derived from the corresponding autocorrelation with respect to the realizations of y.

$$\gamma_{xy}^2(\omega) = \frac{|G_{xy}(\omega)|^2}{G_{xx}(\omega)G_{yy}(\omega)} \tag{5.4}$$

Transfer functions are derived from 1-hour measurements of the pink noise and Jonswap spectrum model tests, i.e. model test 2310, 2321 and 2420, and the corresponding simulations. Reasonably good agreement between the RAOs of the experimental and numerical models is observed, see Figure 5.9 for example.

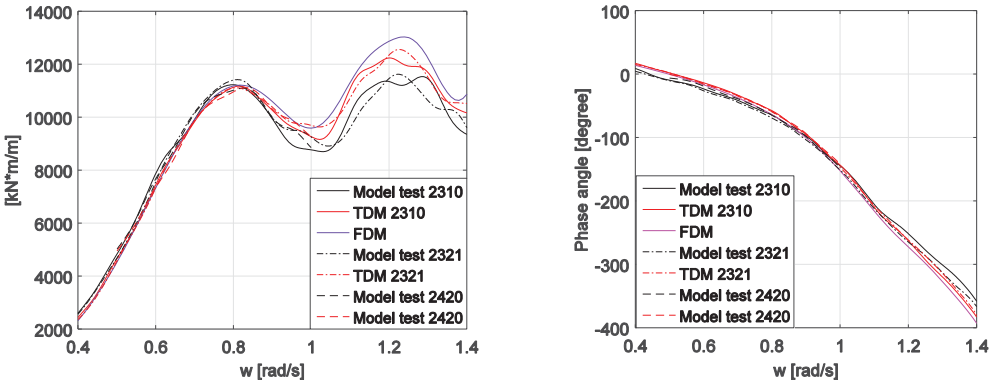

Figure 5.9 Transfer function for the fore-aft bending moment, derived from 1-hour realizations, pink noise, $H_s = 2$ m (2310) and $H_s = 4$ m (2321), and Jonswap spectrum, $H_s = 3.6$ m and $T_p = 10.2$ seconds (2420)

Some explanations for differences in the transfer functions between the time-domain model and experimental model are 1) some non-linear effects, e.g. second and higher order hydrodynamic loads and non-linear wave kinematics, which inherently exist in the model tests but are not modelled numerically, and 2) uncertainties, noise and unknown errors in the measurements. Some relevant observations are referred to Paper A2.

Coherence functions are expected to equal to one when the time-domain model and experimental model are subject to small incident waves, e.g. the pink noise model test 2310. However, as shown in Figure 5.10, significant deviations can be observed in the coherence function of the measurements in the frequency range from 1 rad/s to 1.4 rad/s. The deviations indicate that one or more of three possible physical situations exist. The three possible situations are 1)

extraneous noise is present in the measurements; 2) the system relating the incident wave (input) and the corresponding response (output) is not linear; and 3) the response is an output due to an input of the wave elevation as well as to other inputs.

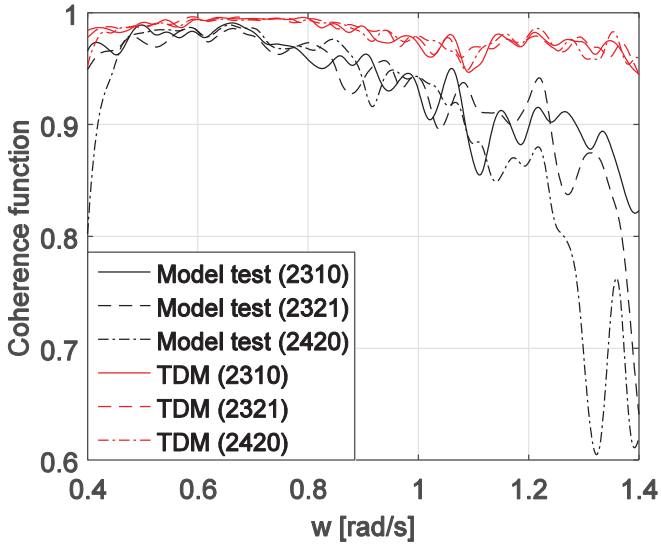

Figure 5.10 Coherence functions between incident waves (input) and the fore-aft bending moment (output), derived from 1-hour realizations, pink noise, $H_s = 2$ m (2310) and $H_s = 4$ m (2321), and model test 2420, $H_s = 3.6$ m and $T_p = 10.2$ s

Spectral densities and realizations of the simulated and measured responses, i.e. the fore-aft and side-to-side bending moments and rigid-body motions, of the model in a moderate wave-only condition (model test 2420) are compared. The difference in the standard deviation of the simulated and measured fore-aft bending moment is 1.4% and good agreement is seen in the spectrums and realizations, see Figure 5.11 and A30. In major wave frequency range of the simulated waves (from 0.4 rad/s to 1.4 rad/s), good agreement is seen in spectrums of measured and simulated rigid-body motions. Motions induced by the slow varying drift force on the experimental model can be observed in the low frequency range in the spectrums of the measurements, while second and higher order hydrodynamic loads,

expect for viscous drag forces, are not included in the time-domain model.

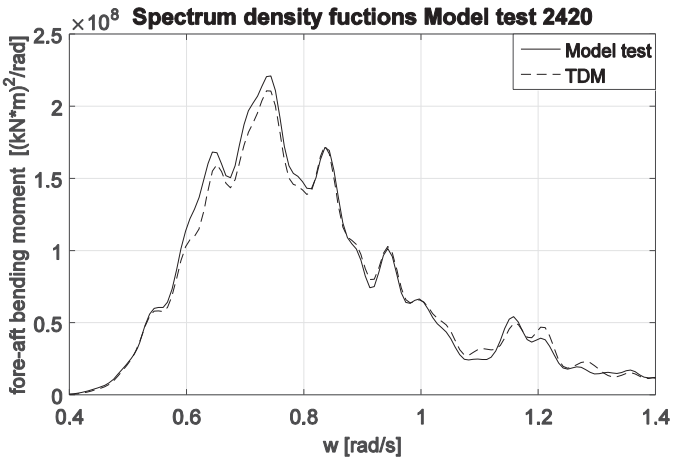

Figure 5.11 Spectral density functions of the fore-aft bending moment, derived from 1-hour realizations, moderate wave only, $H_s = 3.6$ m and $T_p = 10.2$ s

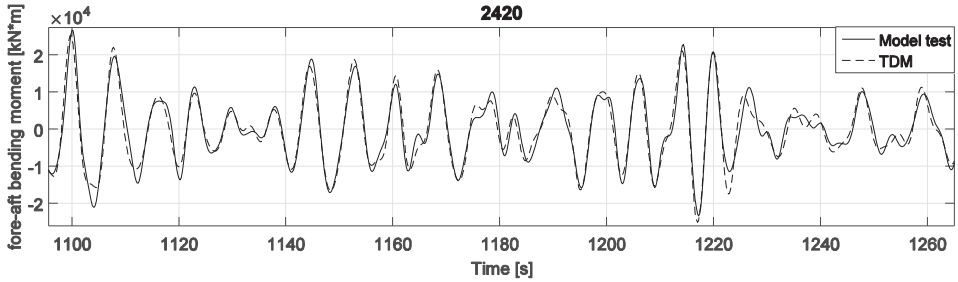

Figure 5.12 Part of measured and simulated fore-aft bending moment, moderate wave only, $H_s = 3.6$ m and $T_p = 10.2$ s

5.4.4 Comparisons of simulations and measurements in operational conditions (Comparison E)

In Comparison E, measured and simulated responses, i.e. the fore-aft and side-to-side bending moments and rigid-body motions, of the 1:30 scaled model of the 5-MW-CSC in several operational conditions (operating in wind and waves, including three different turbulent wind conditions, which includes turbulent winds with mean wind speed below (8 m/s), at (11 m/s) and above (25 m/s) the rated wind speed of the 5-MW wind turbine) are compared. Note that necessary calibrations have been done as we follow the "model-the-

model" principle (Ormberg et al., 2003). Descriptions of the model test, post-processing for the measured data and development of time-domain numerical models are referred to Paper A3.

The relative difference (n_r) of standard deviations of simulations and measurements are calculated based on the area under the corresponding spectral density curves in the corresponding specified frequency range, see Eq. (5.5) and Naess and Moan (2013),. In Eq. (5.5), $m_{0,s}$ represents the area of the part under the spectral density curve of a simulated response in a specified frequency range, i.e. full frequency-range, low frequency-range (defined as from 0 rad/s to 0.3 rad/s) and wave-frequency-range (defined as from 0.3 rad/s to 2 rad/s). Similarly, $m_{0,m}$ represents the area of the part under the spectral density curve of a measured response in a specified frequency range.

$$n_r = \frac{\sqrt{m_{0,s}} - \sqrt{m_{0,m}}}{\sqrt{m_{0,m}}} * 100\% \qquad (5.5)$$

In general, agreement between simulated and measured rigid-body motions, in terms of spectral densities and phase angle, is very good. The relative difference of standard deviations of simulated and measured pitch in full frequency-range is less than 4%, see Figure 5.13 for example. The differences in phase angle between simulated and measured motions are no more than 20 degrees, see Figure 5.14. For the phase angles, we focus on the differences in frequency range from 0 rad/s to 1 rad/s since the responses in the rest frequency range are very limited.

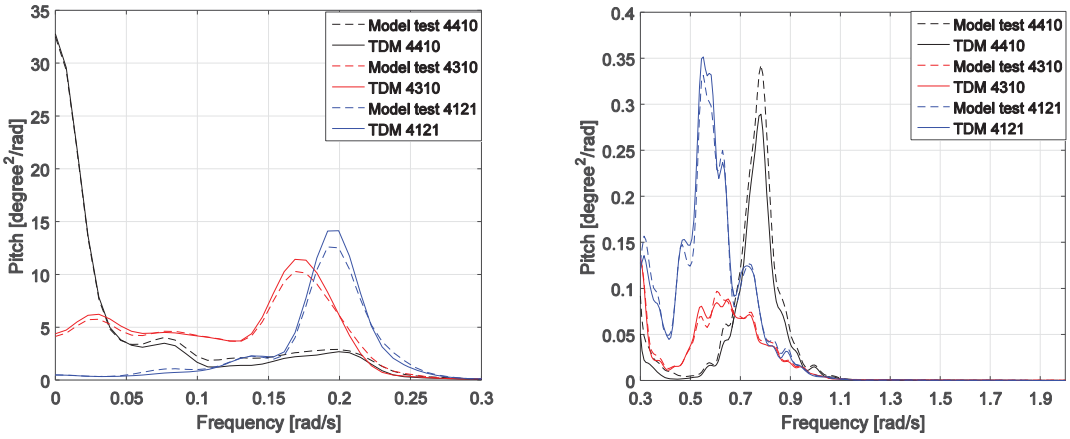

Figure 5.13 Comparisons of spectral densities of simulated and measured pitch motions in operational conditions

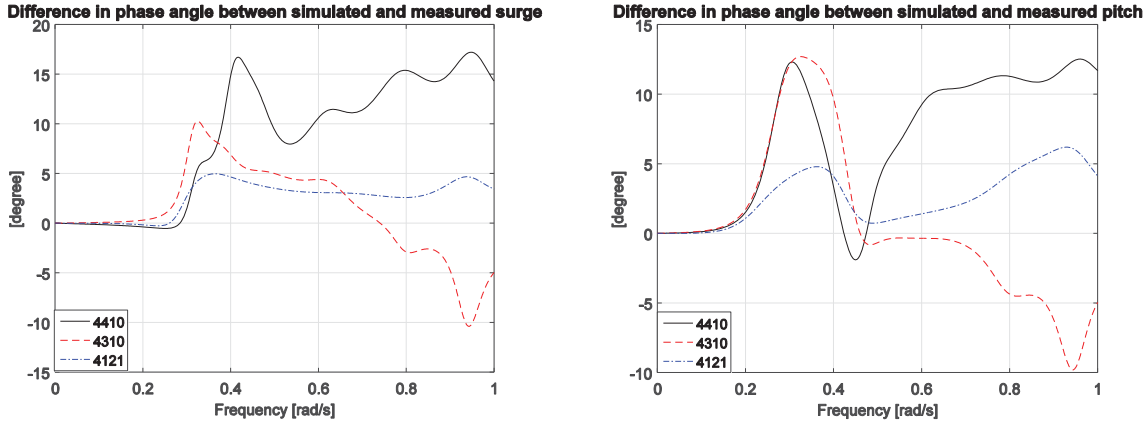

Figure 5.14 Difference in phase angle between simulated and measured surge (Left Figure) and pitch (Right Figure) motions in operational conditions

In general, agreement between simulated and measured fore-aft bending moments, in terms of spectral densities and phase angle, is very good. $|n_r|$ for standard deviations of simulated and measured fore-aft bending moment in full frequency-range in tower base and base of the side column 1 are less than 4% and 10%, respectively.

While the differences in phase angle between simulated and measured bending moments are no more than 25 degrees, see Figures 5.15 and 5.16 for example.

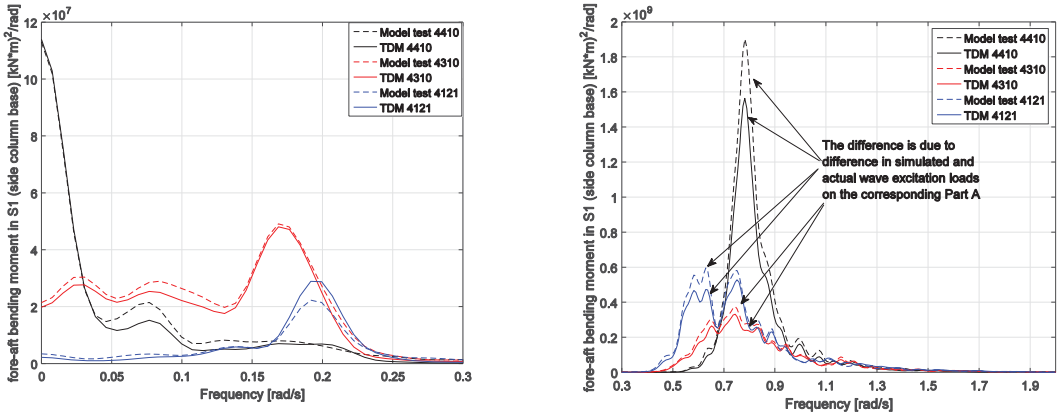

Figure 5.15 Comparisons of spectral densities of simulated and measured fore-aft bending moments in base of side column 1(S1)

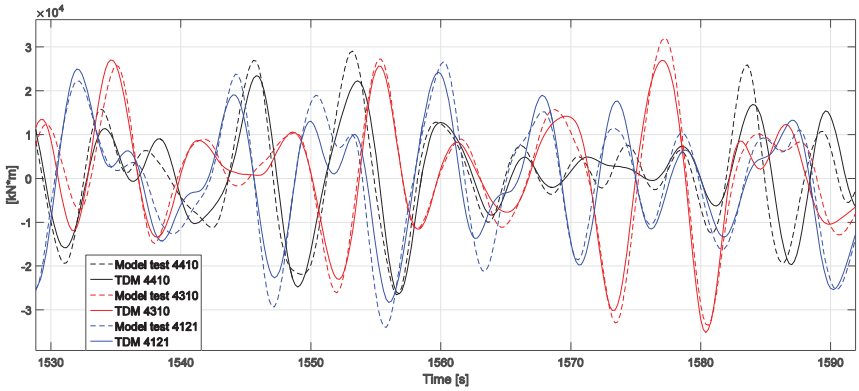

Figure 5.16 Comparisons of simulated and measured realizations of fore-aft bending moments in base of side column 1(S1) (mean values have been removed)

The external loads are composed of aerodynamic loads, hydro loads and gravity forces. The differences between simulated and actual inertial loads and gravity forces are related to uncertainties in the mass properties and differences in measured and simulated rigid-body motions. We can assume that the differences between the simulated and actual aerodynamic loads are negligible since the

measured aerodynamic loads are applied on the numerical model as prescriptive loads. The numerical model cannot completely account for all the components of second and higher order hydro loads however these loads inherently exist. In addition, the drag term of Morison formula (DNV 2010c) is used to model the viscous drag forces on the hull and mooring lines. This is an empirical formula. While, the coefficients for simulating the viscous drag forces are determined according to the Reynolds number, Keulegan-Carpenter numbers and surface roughness which correspond to the full size model rather than the Froude law scaled model. Consequently, the drag coefficients need to be appropriately calibrated. The hydro loads can be further classified as wave excitation loads, radiation loads, and hydrostatic pressure forces, see (Paper A1). Note that these loads are related to the configuration of the wetted body surface of the hull.

The sensitivity study and comparisons of measurements in different conditions are used to analyze effects of these components on rigid-body motions and sectional bending moments, see Chapter 6. The effect of these components is used to identify the reasons for the differences between the measurements and simulations presented in this section.

As analyzed in (Chabaud, 2016), we expected that the differences between the applied aerodynamic loads on the numerical and experimental model are negligible. The major reasons for the difference between wave-frequency components of the simulated and measured bending moments are identified as:

- Differences in the modelled and actual wave excitation loads and radiation loads.
- Differences in the rigid-body motions.

The major reasons for the difference between low frequency components of the simulated and measured bending moments are identified as:

- Differences in the modelled and actual fluctuations of hydrostatic pressure forces and viscous drag forces.
- Differences in the rigid-body motions.

Detailed discussions and analysis are referred to Paper A3. It should be highlighted that the numerical model based on the

proposed approach (linear potential-flow theory) underestimates the standard deviation of wave-frequency components of the fore-aft bending moments in base of the side-column 1 (see Figure 6.1) by 5% to 10%. Differences in simulated and actual excitation loads are considered as the major reason for the differences. More experimental tests designed for distinguishing linear and non-linear hydro loads are needed.

The aerodynamic loads applied on the numerical models are prescriptive loads measured from model tests. Analysis shows that the actual aerodynamic loads on the experimental model can be accurately measured. Consequently, the difference between the measurements and simulations only indicate differences in the hydro loads on the hull and the mass properties of the numerical and experimental models. If the deviation between simulated and measured rigid-body motions is large, the prescriptive loads will fail to represent the right dependency of the aerodynamic loads with respect to the rigid-body motions. Fortunately, the agreement between simulated and measured rigid-body motions is very good. This limitation can be avoided by developing a numerical model for the wind turbine of the experimental model to simulate aerodynamic loads in time-domain simulations based on numerical wind field and the simulated rigid-body motions. However, increase of uncertainties due to differences between the numerical and actual wind fields, and differences between performance of the numerical and experimental models of the wind turbine must be considered.

Analysis and discussions given in this paper are based on available measurements. More systematical and step by step model tests for quantifying and minimizing uncertainties in measurements and identifying first order and higher order wave excitation loads are welcome in future.

Chapter 6

Numerical and experimental analysis of important load components

To shed more light on sectional forces and moments in the hull of semi-submersible wind turbines submitted to combined wind and wave loads, the measurements of the 1:30 scaled model test in SINTEF Ocean and corresponding numerical simulations are analyzed thoroughly. Relevant work is highlighted in this chapter. Detailed information is given in Section 5 of Paper A3, for which effect of non-linear wave excitation loads, drag forces, each load component, and steady wind and wave loads induced changes with respect to mean wetted body surface on rigid-body motions and sectional bending moments in five specified cross-sections on the hull are analyzed by comparing measurements in different conditions and carrying out numerical sensitivity study. Positions of the five cross-sections, which are denoted as S1, S2, S3, S4 and S5, are shown in Figure 6.1.

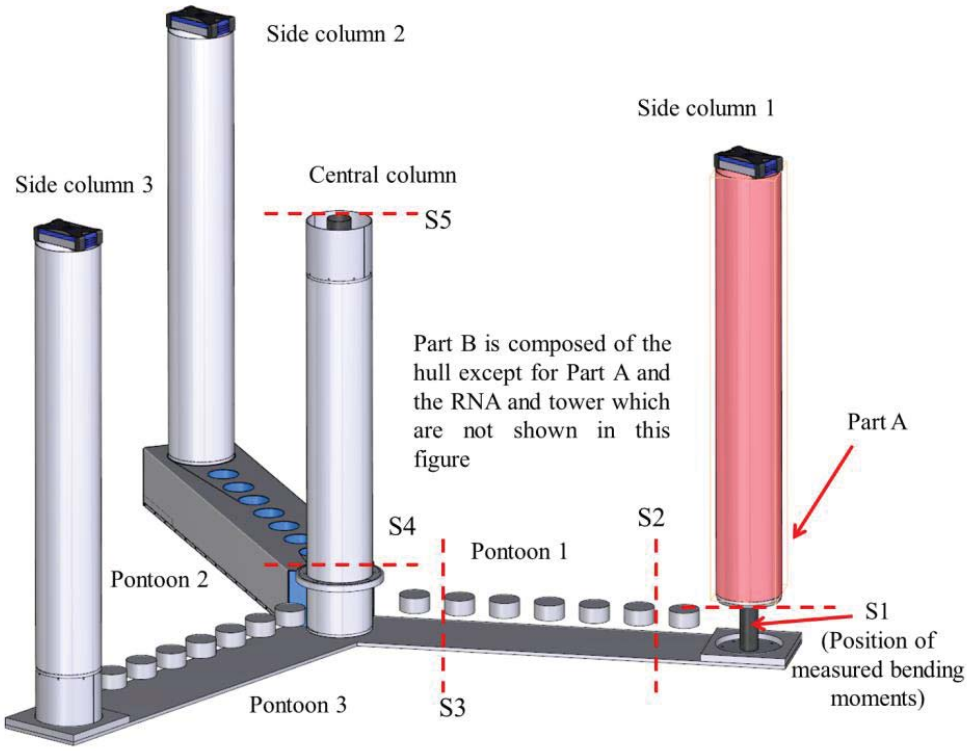

Figure 6.1 A layout of the hull of the experimental model, courtesy of Fredrik Brun (SINTEF Ocean). Note that the configurations of the three pontoons are identical. Some parts of the configurations of Pontoon 1 and 3 are not shown.

Note that external load on a semi-submersible hull could be composed of linear and high-order wave excitation loads, added mass forces, potential damping forces, gravity, hydrostatic forces, and drag forces. Relative importance of load components on the fore-aft bending moments depends on wind and wave conditions, location of the cross-section in the semi-submersible hull, amplitudes and phase angles of the rigid-body motions, and configuration of corresponding wetted body surface of the hull. Configurations of mean wetted body surface of the hull in wind and waves and in wave only are different due to differences in mean components of the wind loads on the rotor, tower and hull of the model. The difference means that hydrodynamic coefficients that are calculated for modeling

hydro loads on the hull are different since values and distributions of hydro pressure forces on the hull are changed. This may result in a considerable change in resultant sectional forces and moments of the hull even though change in resultant of the hydro pressure forces on the whole wetted body surface of the hull could be very limited.

For the 5-MW-CSC, in operational conditions with moderate waves, e.g. model test 4310, second and higher order wave excitation loads and drag excitation forces are negligible while increased second and higher order wave excitation loads are expected in model test 4121 and 4410 as significant wave height increases. In addition to low frequency excitation loads, resonant responses are sensitive to the damping level of the model. Drag force on a 2-D cross-section of a structural component, e.g. column, and pontoon, is expressed by Eq. (6.1), see DNV (2013a). v and $\dot{r}$ are corresponding velocities of fluid and the cross-section. $\dot{r}$ can be derived from the motions of the hull. We can see that $L_{drag}^{2D}(v,\dot{r})$ is composed of terms that are related to v^2, $\dot{r}^2$, and $v\dot{r}$. The terms related to v^2 behave as excitation forces while the terms related to $\dot{r}^2$ and $v\dot{r}$ behave as damping forces. ρ is density of fluid. C_D is non-dimensional drag coefficient. D is characteristic length corresponding to the cross-section of the structural component. Terms related to $\dot{r}^2$ and $v\dot{r}$ indicate that the damping level of the model is related to incident waves. Results of numerical simulations show that the analyzed incident waves result in increase of damping level of the numerical model, while, as a result, low frequency motions in frequency ranges around its natural frequency of surge, heave and pitch motions can be significantly reduced, see Figure 6.2 as an example. Further investigation based on experimental measurements is recommended.

$$L_{drag}^{2D}(v,\dot{r}) = \frac{1}{2}\rho C_D D(v-\dot{r})|v-\dot{r}| \qquad (6.1)$$

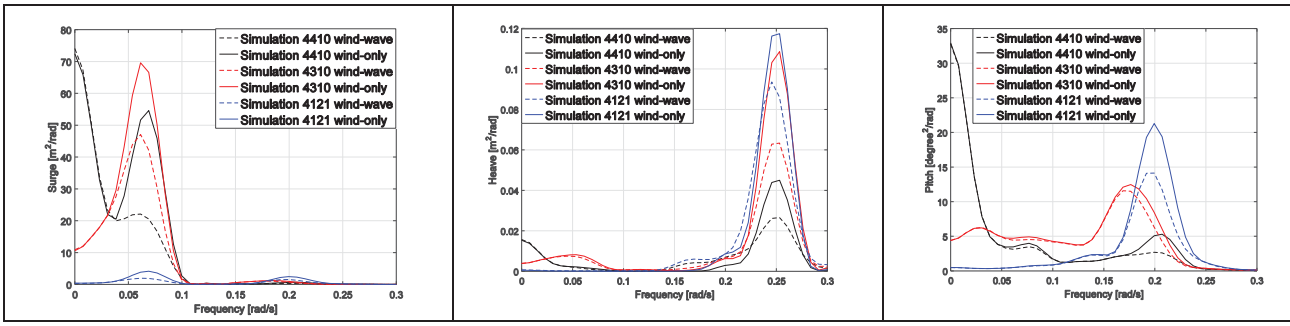

Figure 6.2 Comparisons of spectral densities of simulated surge, heave and pitch motions in wind-only and wind-wave conditions. Note that the only difference between numerical model for a wind-wave condition and its corresponding wind-only condition is that the model for the wind-only condition is in calm water. Note that second and higher order wave excitation loads are not included.

For the 5-MW-CSC, important load components on simulated fore-aft bending moments in the five cross-sections of the hull is summarized in Section 5 of Paper A3.

For the 5-MW-CSC within the analyzed operational conditions, the generated convolutional terms in the time-domain simulations have very limited effect on simulated responses and could be removed from the numerical models, while a sensitivity study shows that, for the analyzed model, simulated fore-aft bending moments of the model in wind and waves could be obtained by superimposing the corresponding simulations of the model subjected to its corresponding wind only condition, and wave only condition except that three constant forces and moments which are the corresponding averaged wind induced forces and moments are applied. Note that mean values of the simulations should be removed as the focus is on dynamic responses and spectral densities which are important to fatigue limit state design checks. This simplification can significantly reduce the number of cases of short-term analysis required in long-term analysis. However, note that the simplification is related to relative importance of each load component on the sectional forces and moments. Applicability of the simplification should be analyzed case by case.

Simulated sectional forces and moments in the five cross-sections are compared. The interface between the pontoons and central column is identified as the most critical part. Both low frequency and wave frequency components of load effects could be important. From cross-section S1 to cross-section S4, value of standard deviation of first order wave excitation load induced fore-aft bending moment increases. The effect of fluctuation of hydrostatic pressure on the wetted body surface of the hull and fluctuation of gravity forces are important to fore-aft bending moments in cross-sections in the tower and central column and in cross-sections that are on the pontoons and close to the central column. Phase difference between simulated surge and pitch motions can be close to 180 degree in the frequency range from 0.4 rad/s to 0.6 rad/s and means a cancellation effect for the bending moments induced by the inertial loads which are associated to acceleration in surge and pitch.

More detailed information is referred to Section 5 of Paper A3

Chapter 7

Conclusions and future work

7.1 Summary and conclusions

This thesis deals with the design and analysis of steel semi-submersible hulls for supporting MW-level horizontal axis wind turbines. The thesis consists of 1) conceptual design methods, 2) conceptual design of a steel braceless hull for supporting a reference wind turbine (denoted as 5-MW-CSC), 3) development, verification and validation of numerical approaches for analyzing global structural responses of structural components of semi-submersible hulls in wind and waves, and 4) case studies related to numerical simulations and experimental measurements for loads and load effects on semi-submersible wind turbines.

The experience acquired from design and analysis of the 5-MW-CSC and the development, verification and validation of the time-domain approaches can be used to 1) develop novel and cost efficient designs of semi-submersible wind turbines, 2) validate other developed computer codes for analyzing global responses of floating wind turbines, 3) shed more light on loads and their effects on floating wind turbines, 4) develop simplified design methods and reduce computational cost of design and 5) improve the design of experimental tests.

The conclusions of this thesis are as follows:

7.1.1 Conclusions with respect to simplified design method and the design of the 5-MW-CSC

Conceptual design procedure, criteria and design check approaches, with respect to safety, have been systematically presented and discussed based on publicly accessible publications and the author's experience and practice in the past six years.

The allowable heeling angle, which is the upper limit of the critical heeling angle induced by the design overturning moment about the critical axis, could be used as a simplified stability criterion, in together with a criterion with respect to natural periods of rigid-body motions of semi-submersible wind turbines and two practical approaches for estimating value and distribution of steel and ballast mass of the hull, for developing initial designs of semi-submersible hulls.

To satisfy the criterion with respect to natural periods of rigid-body motions, sufficient added mass and mass of displaced water are required. Heave plates could be used to efficiently increase added mass of the hull but will significantly increase the system complexity and construction and maintenance costs. For semi-submersible wind turbines without heave plates, a relatively high roll/pitch restoring stiffness and the restriction of the heave natural period to beyond the wave range result in a large displaced volume and steel mass of the semi-submersible hull.

The design of the 5-MW-CSC is developed based on the presented conceptual design procedure, criteria and design check approaches. In contrast to the conventional designs, the 5-MW-CSC is a braceless semi-submersible wind turbine, for which the columns are connected by pontoons rather than braces to reduce design complexity.

Numerical analysis shows that the 5-MW-CSC has very good intact stability, well designed natural periods and modes, moderate rigid-body motions in extreme environmental conditions and a reasonable structural design. Details of relevant analysis approaches and results are presented and discussed. The structural design of the 5-MW-CSC is checked by using simplified ULS and FLS design checks.

Simplification of the methods for estimating the load effect on the hull is discussed. To appropriately account for the aero-hydro-servo-elastic feature of semi-submersible wind turbines, time-domain finite element analysis should be used. However, for some design, structural responses of some structural components in wind and waves could be dominated by first order wave excitation loads, and inertial and radiation loads which are related to wave induced motions. Consequently, these structural components could be designed based on wave induced responses calculated by using the frequency-domain approach described in Paper B1.

7.1.2 Conclusions with respect to development, verification and validation of the time-domain approaches for determining sectional forces and moments in floating wind turbine hulls

Two time-domain approaches, which can be easily implemented in various state-of-the-art computer codes to extend their capabilities to analyze sectional forces and moments in structural components of generic and specific floaters subject to environmental loads from wind and waves are developed by the author. While the developed approaches for generic floaters has been appropriately verified and validated step by step.

The developed approaches focus on modeling the inertia and external loads on the hull and mapping the loads in the finite element model of the hull. In the developed approaches, floating wind turbines are considered as an assemblage of several structural components. The conventional hybrid frequency-time domain approach is extended to model the external loads on and inertia loads of each structural component. Summary of differences, assumptions and limitations of the conventional and developed time-domain numerical modelling approaches are tabulated in Table 4.1.

Several numerical models which implement the developed approach for generic floaters have been generated to analyze global responses, e.g. rigid-body motions and sectional forces and moments, of the 5-MW-CSC.

Procedure, development of numerical models, calibrations, results, analysis and limitations with respect to the verification and

validation are presented. To avoid uncertainties due to limitations of conventional experimental tests, the measurements come from a 1:30 scaled model test of the 5-MW-CSC which implements the ReaTHM® testing approach.

The verification and validation procedure of the developed approach for generic floaters are divided into five comparisons. Expected results and objectives of the comparisons are illustrated in Sections 5.2 and 5.3 while key results of the comparisons are summarized in Section 5.4.

In general reasonable good agreement is observed in these comparisons, e.g. the relative difference of standard deviations of simulated and measured fore-aft bending moment in full frequency-range in tower base and base of the side column 1 in the operational conditions are less than 4% and 10%, respectively.

Reasons for differences between each compared two realizations in these comparisons are thoroughly analyzed and are referred to Section 5.4.

7.1.3 Conclusions with respect to numerical and experimental analysis for importance of load components

Effect of non-linear wave excitation loads, drag forces, each load component, and steady wind and wave loads induced changes with respect to mean wetted body surface on rigid-body motions and sectional bending moments in five specified cross-sections on the hull are analyzed by comparing measurements in different conditions and carrying out numerical sensitivity study.

We find that:

- Low frequency rigid-body motions of the 5-MW-CSC are dominated by wind loads, second and higher order wave excitation loads, and restoring stiffness while resonant motions are sensitive to the damping forces and moments. The low frequency fore-aft bending moments in tower base and cross-sections in structural components of the hull of the 5-MW-CSC are dominated by wind loads, and pitch motion related fluctuations of gravity forces and hydrostatic pressure forces. Inertial load effects on the low frequency responses

are limited except for responses with frequency components around pitch natural frequency.

- Effect of second and higher order wave excitation loads on fore-aft bending moments is observed and discussed. In general the effect is relatively limited in the analyzed operational conditions but can be critical in extreme conditions.
- Mean forces and moments from wind and waves result in a change in configuration of mean wetted body surface of the hull when compared to the configuration in calm water. This may result in a considerable change in resultant sectional forces and moments, e.g. more than 20% difference in standard deviations, even though change in resultant of the hydro pressure forces on the whole wetted body surface could be very limited.
- A summary of important load components on simulated fore-aft bending moments in the five cross-sections is available in Table 11 of Paper A3. Relative importance of load components on the fore-aft bending moments depends on wind and wave conditions, location of the cross-section in the hull, amplitudes and phase angles of the rigid-body motions, and configuration of corresponding wetted body surface of the hull.
- The interface between the pontoons and central column of the 5-MW-CSC is identified as the most critical part. Both low frequency and wave frequency components of load effects could be important. The effect of fluctuation of hydrostatic pressure on the wetted body surface of the hull and fluctuation of gravity forces are important to fore-aft bending moments in cross-sections in the tower and central column and in cross-sections that are on the pontoons and close to the central column. Phase difference between simulated surge and pitch motions can be close to 180 degree in the frequency range from 0.4 rad/s to 0.6 rad/s and means a cancellation effect for the bending moments induced by the inertial loads which are associated to acceleration in surge

and pitch.

- The convolutional terms have very limited effect on simulations and could, for the 5-MW-CSC in the analyzed operational conditions, be removed from the numerical models to significantly reduce modelling complexity and computational cost for short-term analysis in this case. Applicability of the simplification should be analyzed case by case.
- For the analyzed model of the 5-MW-CSC in the operational conditions, simulated fore-aft bending moments of the model in wind and waves could be obtained by superimposing the corresponding simulations of the model subjected to its corresponding wind only condition, and wave only condition except that three constant forces and moments which are the corresponding averaged wind induced forces and moments are applied. This simplification can significantly reduce the number of cases of short-term analysis required in long-term analysis. However, the simplification is related to relative importance of each load component on the sectional forces and moments. Applicability of the simplification should be analyzed case by case.

7.2 Future work

- The developed two time-domain approaches can be further extended to use other finite element models (instead of beam elements) to represent global stiffness of structural components of hulls and to account for full expressions of second and/or higher order hydrodynamic loads and hydroelastisity. While, future work for improving numerical model of the drag forces, which able to model the drag forces with an acceptable accuracy in blind tests, is highly recommended.
- More systematical and step by step model tests and sensitivity studies for quantifying and minimizing uncertainties in measurements are recommended in future, in particular for the extreme condition. More experimental studies designed for distinguishing linear and non-linear hydro loads are needed, e.g.

numerical modelling approach for full second order wave excitation loads should be developed, while wave excitation loads on the hull, when the hull is fixed at its mean position in wind and waves, should be measured in future test programs.

- The configuration of mean wetted body surface of the hull of the 5-MW-CSC indicates that the effect of frequency dependent radiation and diffraction hydrodynamic loads on the hull could be more significant when the hull is subjected to irregular waves, for which major wave energy is in frequency range from 1 rad/s to 2 rad/s. Consequently, these model tests should be scheduled in future.
- Validation for the developed time-domain approach for specific floaters is not included in this thesis but is proposed as future work.
- Further developments of commercial and/or academic hydrodynamic computer codes are recommended to obtain corresponding hydrodynamic coefficients which enable the developed time-domain approach for specific floaters being used to simulate responses of generic floaters.
- Analysis with respect to design of the semi-submersible hull against accidental events, such as ship collision, loss of a mooring line and flooding in a column, needs to be done in future. While, numerical and experimental analysis for the reference floating wind turbines in extreme conditions and fault conditions are recommended as future work as well.

7.3 Original contributions

Original contributions made by the author in this thesis are briefly summarized as follows:

Establishing a simplified approach for the initial (preliminary) design of semi-submersible hulls

An efficient simplified design approach is developed and used by the author to determine initial designs of semi-submersible hulls (the dimension of the hull and estimation of the value and distribution of the mass of the hull) is illustrated in this thesis.

Development of design of a reference braceless steel semi-submersible hull for supporting a 5-MW horizontal axis reference wind turbine.

The 5-MW-CSC has been developed by the author by using the simplified design approach mentioned above. In contrast to the conventional designs, the 5-MW-CSC is a braceless steel semi-submersible wind turbine, for which the columns are connected by pontoons rather than braces to reduce design complexity and construction and maintenance cost.

Numerical analysis show that the 5-MW-CSC has very good intact stability, well designed natural periods and modes, moderate rigid-body motions in extreme environmental conditions and a reasonable structural design.

Details of relevant approaches and results are presented and discussed in this thesis and appended papers.

The 5-MW-CSC has been used as a reference model. The design of the 5MW-CSC has been published and is accessible to public. The design has already been used by several researchers, while a 1:30 scaled model of the design has been experimentally tested in ocean basin of SINTEF Ocean.

The experience acquired by the design and analysis of the 5-MW-CSC can be used to develop other novel and cost efficient designs of semi-submersible wind turbines.

Development of time-domain numerical approaches for analyzing sectional forces and moments in structural components of hulls in wind and waves

Two time-domain approaches are developed by the author and were implemented in Simo/Riflex to extend its capabilities to analyze sectional forces and moments in structural components of a generic floater and a specific floater, respectively. However, note that the approaches can be easily implemented in various state-of-the-art computer codes for wind turbine analysis to extend their capabilities as well.

Differences, assumptions and limitations of the conventional and developed time-domain numerical modelling approaches are addressed.

The developed approaches could be used to validate other developed computer codes for analyzing global responses of floating wind turbines and be used to shed more light on short-term and long-term loads and load effects on floating wind turbines.

Verification and validation for the developed approaches by using numerical simulations and experimental measurements in a systematical and sequential manner

To verify and validate the developed approach for generic floaters, the simulated responses of the numerical models are compared to simulations of the other reference numerical models and measurements of experimental tests, in a systematical way and step by step manner. The procedure, development of numerical models, calibrations, results, analysis and limitations with respect to the validation are presented.

The obtained results and experiences are helpful for improving design of model tests in the future.

Numerical and experimental analysis for quantifying loads and load effects on the 5-MW-CSC

Effect of non-linear wave excitation loads, drag forces, each load component, and steady wind and wave loads induced changes with respect to mean wetted body surface on rigid-body motions and sectional bending moments in five specified cross-sections on the hull are analyzed by comparing measurements in different conditions and carrying out numerical sensitivity study.

The acquired insight was used to simplify complexity of numerical models of the 5-MW-CSC to reduce computational cost of the design checks, and is helpful for reducing design conditions required by ULS and FLS design checks and structural optimization.

REFERENCES

4COffshore, (2018), http://www.4coffshore.com/windfarms/windfloat-fully-decommissioned-nid4600.html, accessed 5th Jan. 2018

ABS, (2013), "Guide for Building and Classing Floating Offshore Wind Turbine Installations", American Bureau of Shipping.

Bachynski, E.E., Etemaddar, M., Kvittem, M.I., Luan, C., Moan, T., (2013) "Dynamic analysis of floating wind turbines during pitch actuator fault, grid loss, and shutdown", Energy Procedia vol. 35, 210-222. doi:10.1016/j.egypro.2013.07.174

Bachynski, E.E., (2014). "Design and Dynamic Analysis of Tension Leg Platform Wind Turbines", Ph.D thesis, Norwegian University of Science and Technology, Trondheim, Norway

Bachynski, E. E., Thys, M., Chabaud, V., and Sauder, T., (2016). "Realtime Hybrid Model Testing of a Braceless Semi-submersible Wind turbine. Part II: Experimental Results". In 35th International Conference on Ocean, Offshore and Arctic Engineering, no OMAE2016-54437.

Bendat, J. S., and Piersol, A. G., (2010). "Random Data: Analysis and Measurement Procedures, 4th Edition". John Wiley & Sons, Inc. ISBN: 978-0-470-24877-5, page 180.

Bottasso, C. L., Campagnolo, F., and Pectrovic, V., (2014). "Wind tunnel testing of scaled wind turbine models: Beyond aerodynamics".

Journal of Wind Engineering and Industrial Aerodynamics, 127, pp. 11–28.

Branlard, E., (2017), "Wind Turbine Aerodynamics and Vorticity-Based Methods", Springer International Publishing AG.

Burton, T., Jenkins, N., Sharpe, D., and Bossanyi, E., (2011), "Wind Energy Handbook Second Edition", Wiley, New York, United States.

Butterfield, S., Musial, W., Jonkman, J. and Sclavounos, P., (2007), "Engineering challenges for floating offshore wind turbines", Technical report NREL/CP-500-38776, National Renewable Energy Laboratory

Chabaud, V., (2016), "*Real-Time Hybrid Model Testing of Floating Wind Turbines*". Ph.d thesis, ISBN 978-82-326-2083-8., NTNU, Norway.

Cermelli, C., Roddier, D., and Weinstein, A., (2012), "Implementation of a 2MW floating wind turbine prototype offshore Portugal", Offshore Technology Conference OTC 23492, Houston

Cermelli, C., Aubault, A., Roddier, D., and McCoy, T. , (2010), "Qualification of a Semi-Submersible Floating Foundation for Multi-Megawatt Wind Turbines", Offshore Tech. Conf., Houston, OTC-20674-PP.

ClassNK, (2012), "Guidelines for Offshore Floating Wind Turbine Structures", Nippon Kaiji Kyokai.

Cleantechnica, (2018), https://cleantechnica.com/2016/09/01/ge-labels-floating-offshore-wind-turbines-renewable-energy-future/, accessed 12.January.2018

DeepWind, (2018), http://www.deepwind.eu/The-DeepWind-Project, accessed 5th Jan. 2018.

De Vaal, J., (2015), "*Aerodynamic Modelling of Floating Wind Turbines*". Ph.d thesis, NTNU, Norway.

DNV, (2009), "Nauticus Hull User Manual PULS", Det Norske Veritas.

DNV, (2010a), "Recommended Practice – Buckling strength of plated structures", DNV-RP-C201, Det Norske Veritas

DNV, (2010b), "Recommended Practice – Fatigue Design of Offshore Steel Structures", DNV-RP-C203, Det Norske Veritas.

DNV, (2010c), "Recommended Practice - Environmental Conditions and Environmental Loads", DNV-RP-C205, Det Norske Veritas.

DNV, (2013a), "Offshore standard – Design of Floating Wind turbine Structures", DNV-OS-J103, Det Norske Veritas.

DNV, (2013b), SESAM User Manual HydroD, Det Norske Veritas.

Dr.techn.Olav Olsen AS, (2018), http://www.olavolsen.no/en/node/17, accessed 2nd.January.2018.

Edenhofer, O., Pichs-Madruga, R., Sokona, Y., et al, (2011), "Special Report on Renewable Energy Sources and Climate Change Mitigation", Cambridge University Press, USA, Cambridge, UK/New York

Energy Manager Today, (2017), https://www.energymanagertoday.com/cost-onshore-wind-energy-development-now-competitive-gas-uk-0171193/, accessed 5th Jan. 2018

EWEA, (2013), "Deep water The next step for offshore wind energy", European Wind Energy Association, ISBN: 978-2-930670-04-1.

Faltinsen, O.M., (1990), “Sea loads on ships and offshore structures”, Cambridge University Press, UK.

Fernandes, G., Make, M., Gueydon, S., and Vaz, G., (2014). “Sensitivity to aerodynamic forces for the accurate modelling of floating offshore wind turbines”. In RENEW2014, G. Soares, ed., no. ISBN: 978-1-138-02871-5.

Fowler, M. J., Kimball, R. W., Thomas, D. A., and Goupee, A. J., (2013). “Design and testing of scale model wind turbines for use in wind/wave basin model tests of floating offshore wind turbines”. In 32nd International Conference on Ocean, Offshore and Arctic Engineering, no. OMAE2013- 10122.

Fredheim, Ø., (2012), “Fatigue Analysis of Column-Brace Connection in a Semi-submersible Wind Turbine”, Master thesis, Norwegian University of Science and Technology, Trondheim, Norway.

Goupee, A. J., Koo, B. J., Lambrakos, K., and Kimball, R. W. , (2012a), “Model tests for three floating wind turbine concepts,” in Proceedings of the 2012 Offshore Technology Conference, Houston, Texas, USA, 30 April 2012–3 May 2012.

Goupee, A. J., Koo, B., Kimball, R. W., Lambrakos, K. F., and Dagher, H. J. (2012b), “Experimental comparison of three floating wind turbine concepts,” in Proceedings of the 31st ASME International Conference on Offshore Mechanics and Arctic Engineering, Rio de Janeiro, Brazil, 1–6 July 2012.

GWEC, (2016), “Global Wind Report 2016- Annual market update”, Global Wind Energy Council.

Hall, M., Goupee, A., and Jonkman, J., (2017), “Development of performance specifications for hybrid modeling of floating wind turbines in wave basin tests”, Journal of Ocean Engineering and Marine Energy.

Hansen, M., (2008), "Aerodynamics of wind turbines, second edition", Earthscan Publications Ltd.

Helder, J., and Pietersma, M., (2013), "UMAINE-DEEPCWIND/OC4 SEMIFLOATING WIND TURBINE", 27005-1-OB. Wageningen, NL:MARIN.

Hexicon AB, (2018), https://www.hexicon.eu/, accessed 5th Jan. 2018

Huijs, F., Mikx, J., Savenije, F., and Ridder, E., (2013), "Integrated design of floater, mooring and control system for a semisubmersible floating wind turbine", European Wind Energy Association (EWEA) Offshore, Frankfurt.

IEC, (2005), "Wind turbines – Part 1: Design requirements", IEC-61400-1, International Electrotechnical Commission.

IEC, (2009), "Wind turbines: Part 3: Design requirements for offshore wind turbines", IEC-61400-3, International Electrotechnical Commission.

IEO, (2017), "International Energy Outlook 2017", U.S. Energy Information Administration.

Ishihara, T., (2013), "Current Status and Future Prospects for Fukushima Floating Offshore Wind Farm Demonstration Project,", Journal of Japan Wind Energy Association, Vol.36, No.4, pp. 553–556 in Japanese.

Jonkman, J., (2007), "Dynamics Modeling and Loads Analysis of an Offshore Floating Wind Turbine", Ph.D. Thesis, Department of Aerospace Engineering Sciences, University of Colorado, Boulder, CO, 2007; NREL/TP-500-41958, Golden, CO: National Renewable Energy Laboratory.

Jonkman J., Butterfield, S., Musial, W. and Scott, G., (2009), "Definition of a 5-MW Reference Wind Turbine for Offshore System Development", NREL/TP-500-38060, National Renewable Energy Laboratory, Golden, CO, U.S.A.

Kimball, R., Goupee, A. J., Fowler, M. J., de Ridder, E.-J., and Helder, J., (2014). "Wind/wave basin verification of a performance-matched scale-model wind turbine on a floating offshore wind turbine platform". In Proceedings of the ASME 2014 33rd International Conference on Ocean, Offshore and Arctic Engineering, no. OMAE2014-24166.

Komatsu, M., Kumamoto, H., Ohta, M., Tanaka, H., Mori, H., and Miyazaki, H., (2016), "Development of Offshore Wind Turbine Floater that Blends into Japanese Waters - Evaluation of the Validity for Design and Applied Methods for V-shaped Semi-submersible Floating structure", Mitsubishi Heavy Industries Technical Review Vol. 53 No. 2.

Koo, B., Goupee, A. J., Lambrakos, K., and Kimball, R. W., (2012), "Model tests for a floating wind turbine on three different floaters," in Proceedings of the 31st ASME International Conference on Offshore Mechanics and Arctic Engineering, Rio de Janeiro, Brazil, 1–6 July 2012.

Kvittem, M. I., Moan, T., (2015), "Time domain analysis procedures for fatigue assessment of a semi-submersible wind turbine", Marine Structures. vol. 40.

Li, L., Gao, Z., Moan, T., (2015), "Joint Distribution of Environmental Condition at Five European Offshore Sites for Design of Combined Wind and Wave Energy Devices", Journal of Offshore Mechanics and Arctic Engineering. 137(3), 031901 (16 pages). doi: 10.1115/1.4029842.

Luan, C., Gao, Z., and Moan, T., (2013), "Modelling and analysis of a semi-submersible wind turbine with a central tower with emphasis

on the brace system", In 32nd International Conference on Ocean, Offshore and Arctic Engineering, no, OMAE2013-10408, Nantes, France.

Luan, C., Michailides, C., Gao, Z. and Moan, T., (2014), "Modeling and analysis of a 5 MW semi-submersible wind turbine combined with three flap-type Wave Energy Converters", In 33rd International Conference on Ocean, Offshore and Arctic Engineering, no.OMAE2014-24215, San Francisco, USA

Luan, C., Gao, Z., and Moan, T., (2016), "Design and analysis of a braceless steel 5-mw semi-submersible wind turbine", In 35th International Conference on Ocean, Offshore and Arctic Engineering, OMAE2016-54848, Busan, Korea, June 19–24.

Luan, C., Gao, Z., and Moan, T., (2017), "Development and verification of a time-domain approach for determining forces and moments in structural components of floaters with an application to floating wind turbines", Marine Structures, Volume 51, pages 87-109, https://doi.org/10.1016/j.marstruc.2016.10.002.

Luan, C., Chabaud, V., Bachynski, E., Gao, Z., and Moan, T., (2017), "Experimental validation of a time-domain approach for determining sectional loads in a floating wind turbine hull subjected to moderate waves", Energy Procedia, Volume 137, Pages 366-381, https://doi.org/10.1016/j.egypro.2017.10.361

Luan, C., Gao, Z., and Moan, T., (2018), "Comparisons and analysis of simulated and measured motions and sectional loads in a floating wind turbine hull subjected to combined wind and waves", Accepted for publication in Engineering Structures.

Luan, C., Gao, Z., and Moan, T., (2018), "Report: Simplified method for conceptual design of semi-submersible wind turbines", Report.

Luxcey, N., Ormberg, H., and Passano, E., (2011), "Global analysis of a floating wind turbine using an aero-hydro-elastic numerical

model. Part 2: Benchmark study". In 30th International Conference on Ocean, Offshore, and Arctic Engineering,no, OMAE2011-50088, Rotterdam, Netherlands.

Marin, T.I., (2014), "Fatigue Analysis of the Column-Pontoon Connection in a Semi-Submersible Floating Wind Turbine", Master thesis, Norwegian University of Science and Technology, Trondheim, Norway.

MARINTEK, (2011). SIMO User's Manual.

MARINTEK, (2013). RIFLEX User's Manual.

Matha, D., Schlipf, M., Cordle, A., Pereira, R., and Jonkman, J., (2011). "Challenges in Simulation of Aerodynamics, Hydrodynamics, and Mooring-Line Dynamics of Floating Offshore Wind Turbines", Proceedings of the 21st International Offshore and Polar Engineering Conference, Maui, Hawaii, USA, Vol. 1, pp. 421–428.

Michailides, C., Luan, C., Gao, Z. and Moan, T., (2014), "Effect of flap type wave energy converters on the response of a semi-submersible wind turbine", In 33rd International Conference on Ocean, Offshore and Arctic Engineering, no.OMAE2014-24065, San Francisco, USA

Moan, T., (2015), "Recent development of analysis and design of offshore wind turbines for deep water". Renewable Energies Offshore - 1st International Conference on Renewable Energies Offshore, RENEW 2014, Lisbon, Portugal

Moan, T., (2016), "Limit States and Systems Effects", The 3rd Offshore Structural Reliability Conference (OSRC2016), 14-16 September, Stavanger, Norway

Moriarty, P. J., and Hansen, A. C., (2005), AeroDyn theory manual, Tech. Rep, NREL/TP-500-36881.

Naess, A. and Moan, T., (2013), "Stochastic dynamics of marine structures", Cambridge University Press, UK.

Nejad, A.R., Bachynski, E.E., Kvittem, M.I., Luan, C., Gao, Z. and Moan, T., (2015), "Stochastic Dynamic Load Effect and Fatigue Damage Analysis of Drivetrains in Land-based and TLP, Spar and Semi-Submersible Floating Wind Turbines", Marine Structures, Vol 42, pp 137–153.

Nour-Omid, B., Parlett, B.N.,Taylor, R.L.,(1983), "Lanczos versus Subspace Iteration for Solution of Eigenvalue Problems", International Journal for Numerical Methods in Engineering, Vol. 19, pp. 859-871.

NOWITECH, (2018), https://www.sintef.no/en/projects/nowitech-norwegian-research-centre-for-offshore-wi/, accessed 5th Jan. 2018

Ormberg, H., Baarholm, R., and Stansberg, C.T., (2003). "Time-domain coupled analysis of deepwater TLP, and verification against model tests". Proc. 13th ISOPE Conf., Honolulu, Hawaii, USA.

Ormberg, H., Passano, E., and Luxcey, N., (2011), "Global analysis of a floating wind turbine using an aero-hydro-elastic model. Part 1: Code development and case study". In 30th International Conference on Ocean, Offshore, and Arctic Engineering,no, OMAE2011-50114, Rotterdam, Netherlands.

Ormberg, H., and Bachynski, E. E., (2012). "Global analysis of floating wind turbines: Code development, model sensitivity and benchmark study". In 22nd International Ocean and Polar Engineering Conference, Vol. 1, pp. 366–373.

Principle Power Inc., (2017), http://www.principlepowerinc.com/, accessed 12.January.2018

Renewable Energy Bangladesh, (2018), http://foundation.e-arttic.com/wiki/tiki-index.php?page=Wind+technologie+overview, accessed 5th Jan. 2018

Robertson, A., Jonkman, J., Masciola, M., Song, H., Goupee, A., Coulling, A., and Luan C., (2012), "Definition of the Semisubmersible Floating System for Phase II of OC4", Offshore Code Comparison Collaboration Continuation (OC4) for IEA Task 30.

Robertson, A., Jonkman, J. Qvist, J.,Chen, X., Armendariz,J.A., Soares, C.G., Luan, C., Huang, Y., Yde, A.,Larsen, T., Nichols, J., Lei, Liu, Maus, K.J., Godreau, C., Heege, A., Vatne, S.R., Manolas,D., Qin, H., Riber, H., Abele, R., Yamaguchi, A., Pham,A. Alves,M., Kofoed-Hansen,H., (2014), " Offshore code comparison collaboration, continued: phase II results of a floating semisubmersible wind system", In Proceedings of the 33rd International Conference on Ocean, Offshore and Arctic Engineering, no. OMAE2014-24040, San Francisco, USA, 2014.

Roddier, D., Cermelli, C., Aubault, A., and Weinstein, A., (2010), "WindFloat: A floating foundation for offshore wind turbines", Journal of Renewable and Sustainable Energy 2, 033104, doi:10.1063/1.3435339.

Roddier, D., Peiffer, A., Aubault, A., and Weinstein, J., (2011), "A generic 5 MW WindFloat for numerical tool validation & comparison against a generic spar", In 30th International Conference on Ocean, Offshore and Arctic Engineering, no, OMAE2011-50278, Rotterdam, the Netherlands

Roddier, D., Cermelli, C., Aubault, A, and Peiffer, A., (2017), "Summary and conclusions of the full life-cycle of the WindFloat FOWT prototype project", Proceedings of the 36th International Conference on Ocean, Offshore and Arctic Engineering, OMAE2017-62561, Trondheim, Norway, June 25-30.

Saeki, M., Tobinaga, I., Sugino, J., and Shiraishi, T., (2014) , "Development of 5-MW Offshore Wind Turbine and 2-MW Floating Offshore Wind Turbine Technology", Hitachi Review Vol. 63 (2014), No. 7 pp. 414-421

Sauder, T, and Chabaud, V., (2015), "MARINTEK technical memo: preliminary test campaign for the milestone tests", MARINTEK, Trondheim, Norway

Sauder, T., Chabaud, V., Thys, M., Bachynski, E. E., and Sæther, L. O., (2016). "Real-time hybrid model testing of a braceless semi-submersible wind turbine: Part I: The hybrid approach". In 35th International Conference on Ocean, Offshore and Arctic Engineering, no. OMAE2016-54435.

Standards Norway, (2004), "Design of steel structures", NORSOK STANDARD N-004, Standards Norway

Statoil AS, (2017), http://www.statoil.com/en/TechnologyInnovation/NewEnergy/RenewablePowerProduction/Offshore/HywindScotland/Pages/default.aspx?redirectShortUrl=http%3a%2f%2fwww.statoil.com%2fHywindScotland, accessed 12.January.2018

Twidell, J. and Gaudiosi, G., (2009), "*Offshore Wind Power*", Multi-Science Publishing Co.Ltd.

United Nations, (2017), "World Population Prospects The 2017 Revision Key Findings and Advance Tables", Department of Economic and Social Affairs Population Division, United Nations, New York, United States.

Viselli, A. M., Goupee, A. J., and Dagher, H., (2014), "Model Test of a 1:8 Scale Floating Wind Turbine Offshore in the Gulf of Maine", In 33th International Conference on Ocean, Offshore and Arctic Engineering, no, OMAE2014-23639, San Francisco, CA, USA.

Wan, L., Gao, Z., and Moan, T., (2015). “Experimental and numerical study of hydrodynamic responses of a combined wind and wave energy converter concept in survival modes”. Coastal Engineering, 104, pp. 151 – 169.

Wang, K., Luan, C., Moan, T., Hansen, M., (2014), “Comparative study of a FVAWT and a FHAWT with a semi-submersible floater”, Proceedings of the Twenty-fourth (2014) International Offshore and Polar Engineering Conference, Busan, Korea.

Wendt, F., Robertson, A., and Jonkman, J., (2017), “FAST model calibration and validation of the OC5-DeepCwind floating offshore wind system against wave tank test data”, the 27th International Ocean and Polar Engineering Conference, San Francisco, California, U.S.A..

Wind Energy Programmatic EIS, (2018), http://windeis.anl.gov/guide/basics/, accessed 5th Jan. 2018

Wind Europe, (2017), “Wind energy in Europe, Scenarios for 2030”.

WindSea AS, (2018), http://www.nordicgreen.net/startups/wind/windsea , accessed 5th Jan. 2018

Yttervik R., (2009), “TDHMILL3D-User documentation”, Statoil, Norway.

Appendix A

Appended papers

A.1 Paper A1

Paper A1:
Development and verification of a time-domain approach for determining forces and moments in structural components of floaters with an application to floating wind turbines
Chenyu Luan, Zhen Gao and Torgeir Moan
Published in Marine Structures, Volume 51, pages 87-109,
https://doi.org/10.1016/j.marstruc.2016.10.002.

Development and verification of a time-domain approach for determining forces and moments in structural components of floaters with an application to floating wind turbines

Chenyu Luan*

Email: chenyu.luan@ntnu.no
PhD Candidate
Norwegian Research Centre for Offshore Wind Technology (NOWITECH)
Centre for Ships and Ocean Structures (CeSOS), NTNU
Centre for Autonomous Marine Operations and Systems (AMOS), NTNU
NO-7491 Trondheim, Norway

Zhen Gao
Email: zhen.gao@ntnu.no
PhD, Professor
CeSOS and AMOS, NTNU
Department of Marine Technology, NTNU
NO-7491 Trondheim, Norway

Torgeir Moan
Email: torgeir.moan@ntnu.no
PhD, Professor
CeSOS and AMOS, NTNU
NOWITECH
Department of Marine Technology, NTNU
NO-7491 Trondheim, Norway

ABSTRACT

Structural design of the floater is an important aspect in developing cost efficient and reliable floating wind turbines. It is difficult to well account for the effect of strong non-linear dynamic characteristics and transient loading events, e.g. wind turbine faults, of floating wind turbines in a frequency-domain finite element analysis. The time-domain approach which implements the Morison's formula cannot accurately account for the hydrodynamic loads on the hull of floating wind turbines. While, the conventional hybrid frequency-time domain approach (based on the potential flow theory) fails to capture structural responses of the hulls since a rigid-body global model rather than a finite element model of the hull is employed. The present paper deals with the development and verification of a time-domain approach that can be easily implemented in various state-of-the-art computer codes for wind turbine analysis, e.g. Simo/Riflex/Aerodyn, OrcaFlex and FAST+CHARM3D, to extend their capabilities to analyze global forces and moments in structural components of a generic floater subject environmental loads from e.g. wind and waves. The global forces and moments in the structural components might be used as inputs of design formulas for structural strength design checks and/or used as boundary conditions in a sub-model finite element analysis to determine structural responses such as stresses. The proposed approach focuses on modeling of the inertia and external loads on the hull and mapping of the loads in the finite element model of the hull. In the proposed approach, floating wind turbines are considered as a system of several structural components, e.g. blades, rotational shaft, nacelle, tower, mooring lines, columns, pontoons and braces, rather than one rigid-body, while a finite element model for the hull is developed to represent the global stiffness of the structural components. The external and inertial loads on the hull are modeled as distributed loads rather than the integrated forces and moments. The conventional hybrid frequency-time domain approach, which is available in the state-of-the-art computer codes, is implemented to model the hydrodynamic loads on each structural component with essential modifications with respect to the corresponding hydrodynamic coefficients, e.g. added mass and potential damping coefficients and wave excitation forces. Approaches for modeling the hydrostatic pressure forces, gravity loads, drag forces and inertial loads on each structural component are also illustrated. Second order and higher order terms of the hydrostatic and hydrodynamic loads and the hydroelasticity effects are not accounted for in the present paper but can be further included. So far, the proposed approach has been implemented in the computer code Simo/Riflex/Aerodyn to analyze global forces and moments in the hull of a semi-submersible wind turbine. Good agreement between the reference values and the simulation results has been observed and indicates that the developed time-domain numerical models are reliable. The simulation results show that the low-frequency aerodynamic loads and fluctuations of hydrostatic pressure forces on and gravity of the floating wind turbine are important contributions to the structural responses, in particular, in the low-frequency range.

1 Introduction

By now, onshore wind energy has been well developed while the potential of offshore wind energy is substantial, particularly in relatively deep water (e.g. deeper than 80 m). Moving from onshore and shallow water to deep water, floating wind turbines might be more economically competitive than bottom fixed wind turbines in particular for large wind turbines with high rated power (e.g. 5-10 MW).

In general, a floating wind turbine is composed of a Rotor Nacelle Assembly (RNA), a tower, a hull and a mooring system. Current floating wind turbines can be classified as spar-type [1,2], TLP [3-9] and semi-submersible wind turbines [10-17].

In the structural design, ultimate limit state (ULS) and fatigue limit state (FLS) design checks must be carried out based on structural responses of the floating wind turbine in relevant design conditions. Finite element analysis is normally carried out to determine the load effects for the design checks with appropriate models of the loads.

Shell elements might be employed to model structural details, e.g. bulkheads, girders and stiffeners in the hull, blades and tower; chains and wires of the mooring lines; and gear box, shaft and generator in nacelle. Alternatively, we might consider that the structure is composed of several structural components (based on a multi-body formulation). For instance, the blades, rotational shaft, nacelle, tower, mooring lines and columns, pontoons and braces of the hull can be considered as structural components. Beam elements can be used to account for the global structural behaviors of these structural components, e.g. the global forces and moments in the structural components. The global forces and moments might be used as inputs of design formulas for structural strength design checks specified by relevant standards and guidelines from the International Electrotechnical Commission (IEC), International Organization for Standardization (ISO), American Petroleum Institute (API), the Norwegian petroleum industry, class societies such as Det Norske Veritas and Germanischer Lloyd (DNVGL) and the American Bureau of shipping (ABS) and so on. For example, buckling strength of plates, stiffeners and girders in global and local loads can be checked by the formulas specified in DNV-RP-C201 [19]. The global forces and moments might be used in ULS design checks for tubular members and joints based on formulas specified in NORSOK-N004 [20]. In addition, the global forces and moments might be used as boundary conditions in a sub-model finite element analysis to determine structural responses such as stresses, etc.

Finite element analysis in frequency domain is very cost-effective. However, the major limitations are that 1) it is a big challenge to appropriately account for the strong non-linear dynamic characteristics, which is known as the aero-hydro-servo-elastic feature [35], of floating wind turbines; and 2) transient loading events, such as wind turbine faults, cannot be modeled in frequency domain.

Regarding the finite element analysis in time domain, 19 computer codes used by participants from various organizations in several countries were compared through a code-to-code verification activity [22]. However, none of the developed numerical models can be used to predict the global forces and moments in the hull of the reference semi-submersible wind turbine. The challenges are 1) how to accurately calculate hydro loads on the hull and 2) how to effectively map the loads in the finite element model.

As pointed by Matha et al. [36], the Morison's formula, potential flow theory and computational fluid dynamics methods can be used to model hydrodynamic loads on the hull and mooring lines. ULS and FLS design checks require tens of thousands of time-domain simulation hours [37-39]. Therefore, the computational fluid dynamic method is not considered to be practical for ULS and FLS design checks due to the extremely expensive computational cost.

The Morison's formula is implemented in some cost effective computer codes [22] to model the hydrodynamic loads on the hull of floating wind turbines. However, the Morison formula is an empirical formula. In general, it is applicable when wave length is larger than five times the diameter of the slender structure's cross-section [23]. Meanwhile, the application of the Morison formula means the memory effects of the hydrodynamic loads are neglected. In addition, additional pressure forces must be added to account for hydrodynamic loads in axial directions of the columns and pontoons [22].

The potential flow theory combined with the drag term of the Morison formula can accurately model the hydrodynamic loads on offshore structures and is frequently used in the offshore oil and gas industry. A set of equations of motions can be established,

as initially proposed by Cummins [25], and solved to obtain the motion responses of the platforms in waves. In these equations, the platform is assumed as one rigid-body with 6 d.o.f.s, while a hybrid frequency-time domain approach is implemented to convert the frequency dependent hydrodynamic pressure loads due to wave diffraction and radiation to the integrated forces and moments corresponding to these 6 d.o.f.s. While, wind loads on blades and tower are typically considered as distributed loads. This approach has been implemented in some computer codes [22] to analyze structural responses of the RNA, tower and mooring lines and rigid-body motions of the hull of floating wind turbines [21,40-45].

The flow chart of a time-domain numerical model of a generic horizontal axis floating wind turbine which implements the hybrid frequency-time domain approach and is developed in the computer code Simo/Riflex/Aerodyn [29-32] is given in Figure 1 as an example. The hull of the floating wind turbine is considered as a rigid-body with 6 d.o.f.s, while the tower base and fairleads of the mooring lines rigidly follow the motions of the hull. Six motion equations that are composed of the resultant external loads, e.g. viscous loads, gravity loads and hydro loads, on and inertial loads of the hull are generated in Simo [27] with necessary input, e.g. mass properties of the hull, drag coefficients, hydrodynamic coefficients, i.e. the added-mass coefficient matrices ($\boldsymbol{A}(\omega)$), potential damping coefficient matrices ($\boldsymbol{B}(\omega)$) and first order wave excitation load transfer function ($\boldsymbol{H}_{fw}(\omega)$), and specified forces, moments and restoring stiffness matrix. A finite element model, for which the mooring lines, tower and RNA are modelled as bar and beam elements and coupled to the motion equations of the hull are generated and solved in Riflex [28] with necessary input, e.g. relevant mass and structural properties and drag and added mass coefficients. Aerodyn [32] and a Java controller [31] are coupled to Riflex through a dll file [31] to account for the aerodynamic loads on the RNA and tower, effect of pitch control on aerodynamic loads on the three blades and effect of the generator inside the nacelle on the power production and generator torque. More details are available in the later part of this paper and [47].

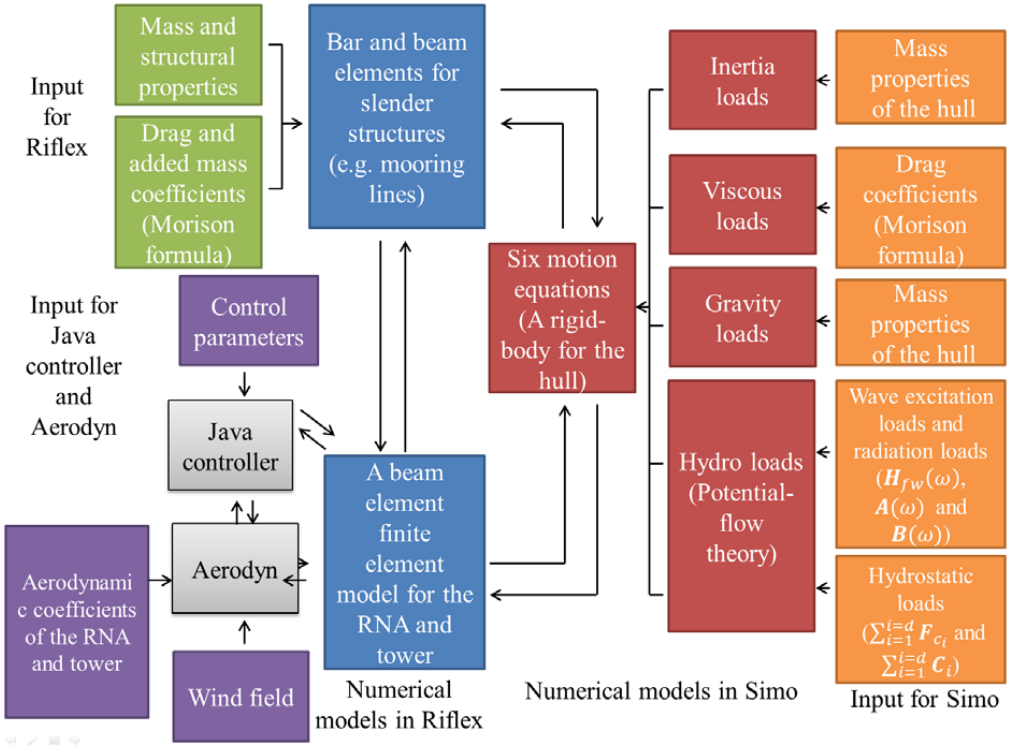

Figure 1 The flow chart of a time-domain numerical model of a generic horizontal axis floating wind turbine developed in Simo/Riflex/Aerodyn (the conventional approach)

The conventional hybrid frequency-time domain approach is considered as the state-of-the-art approach and has been used by researchers, e.g. [21, 43, 46, 47], to analyze responses of floating wind turbines. However, to calculate structural responses of the hull, we must develop a finite element model of the hull rather than a rigid-body formulation; while, to map the loads in the finite element model, we must develop accurate and effective time-domain approach to model the loads on the hull as distributed loads rather than three integrated forces and moments.

This paper addresses a time-domain approach to deal with the challenges mentioned above. The focus is on the modeling of the inertia and external loads on the floating wind turbine hull and the mapping of the loads to the finite element model of the hull. The proposed approach can be easily implemented in various state-of-the-art computer codes, e.g. Simo/Riflex/Aerodyn, OrcaFlex [22] and FAST+CHARM3D [22], to extend their capabilities to analyze global forces and moments in structural components of a generic floater subject to linear and non-linear environmental loads, e.g. wind and waves. Details of the proposed approach and verification are available in the later part of this paper. An application of the proposed approach for ULS design check for the structural design of the hull of a semi-submersible wind turbine is available in [15].

2 The proposed approach

In general, numerical models in finite element codes are developed in an earth fixed coordinate system, such as the global coordinate system (O^g-x^g-y^g-z^g) shown in Figure 2.

In the proposed approach, the hull of floating structures is considered as an assemble of d structural components. d is specified by designer. A beam element finite element model, which includes d nodes (red colored in Figure 2), can be developed in the global coordinate system to represent the global stiffness of the structural components. Each node has 6 d.o.f.s and corresponds to a structural component. The external loads on and inertia loads of each structural component are calculated, integrated and transferred to the node that corresponds to the structural component in the finite element model. In particular, the hydrostatic and the hydrodynamic loads on each structural component are obtained by integrating the hydrostatic and hydrodynamic pressure loads on the wet surface of the structural component. The pressure loads are normally calculated based on a frequency-domain hydrodynamic code using a panel method. Global forces and moments in structural components of the hull can be obtained by carrying out a finite element analysis using a time-domain code. Accurate global forces and moments are given at the cross-sections corresponding to the red dashed lines, see Figure 2. The number of the structural components and quality of the finite element model of the hull affect the accuracy of the global forces and moments. The beam element finite element model of the hull should accurately represent the global stiffness of the hull, in particular for statically indeterminate structures.

The flow chart of a time-domain numerical model of a generic horizontal axis floating wind turbine which implements the proposed approach and is developed in the computer code Simo/Riflex/Aerodyn is given in Figure 3. Comparing to Figure 1 (the hybrid frequency-time domain approach), the proposed approach models the hull as a beam element finite element model while the approaches for modeling the external on and inertia loads of each structural component are illustrated in the following part of this section together with the limitations of the approaches.

The approaches are developed by extending the conventional approaches used in the state-of-the-art computer codes. Therefore, the proposed approach can be easily implemented in various state-of-the-art computer codes to extend their capabilities.

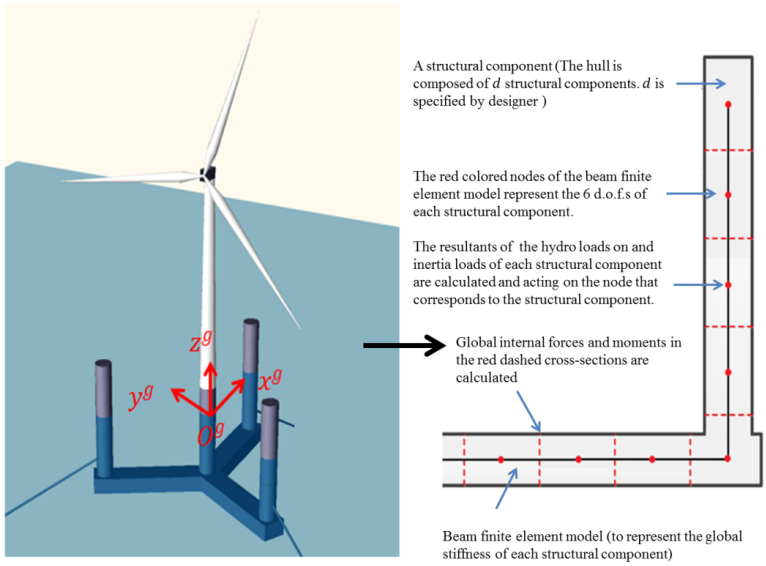

Figure 2 Definition of a finite element model of the hull

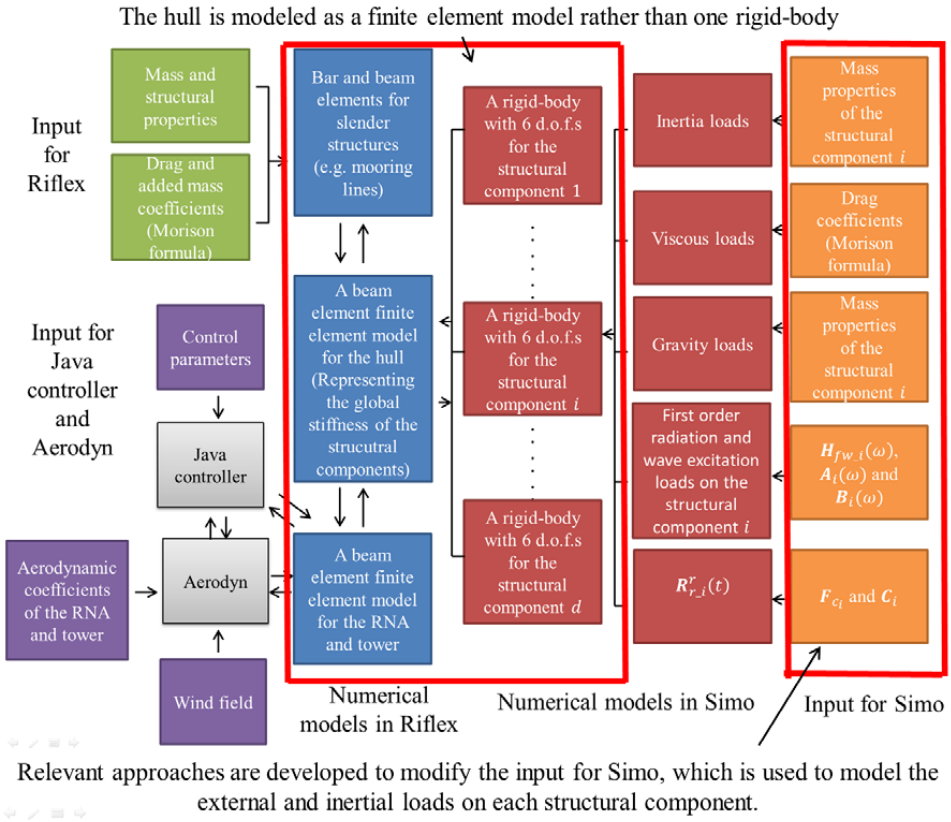

Figure 3 The flow chart of a time-domain numerical model of a generic horizontal axis floating wind turbine developed in Simo/Riflex/Aerodyn (the proposed approach)

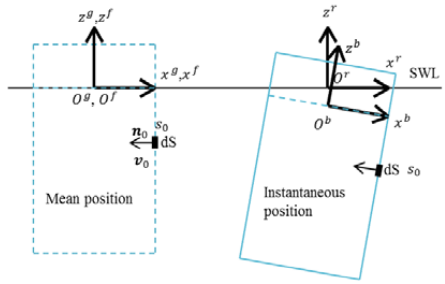

Figure 4 Definition of the coordinate systems for a floating body

Generating and solving time-domain motion equations for a rigid-body oscillating with respect to its mean position in waves is a fundamental feature in some of the state-of-the-art computer codes used in the offshore wind and offshore oil and gas industry. In these computer codes, usually, three coordinate systems, i.e. O^b-x^b-y^b-z^b, O^r-x^r-y^r-z^r and O^f-x^f-y^f-z^f coordinate systems, are established. As shown in Figure 4, the O^f-x^f-y^f-z^f coordinate system is an earth fixed coordinate system located at the mean position of the geometrical center of the water plane area of the floater. The O^b-x^b-y^b-z^b coordinate system is a body-fixed coordinate system. The position of O^b and the orientation of the coordinate system rigidly follow rigid-body motions of the floater. The O^r-x^r-y^r-z^r coordinate system is a body-related coordinate system. O^r rigidly follows horizontal movements of O^b (the hull) but the orientation of the body-related coordinate system and vertical position of the O^r are fixed (as the same as the body-related coordinate system when the hull is located at its initial position in time-domain simulation). When the floater is located at its mean position, the O^f-x^f-y^f-z^f, O^b-x^b-y^b-z^b and O^r-x^r-y^r-z^r coordinate systems are coincident. In the motion equations, the hybrid frequency-time domain approach is implemented to account for the wave excitation load effects and radiation load effects on the rigid-body motions. Hydrodynamic coefficients, i.e. the added-mass coefficient matrices ($\boldsymbol{A}(\omega)$), potential damping coefficient matrices ($\boldsymbol{B}(\omega)$) and first order wave excitation load transfer function ($\boldsymbol{H}_{fw}(\omega)$) must be calculated by 1) solving the potential-flow boundary value problem with the assumption that the hull of the floater is a rigid-body in the O^f-x^f-y^f-z^f coordinate system, 2) calculating pressure forces on the mean wet surface of the hull based on the Bernoulli's equation and corresponding velocity potential, 3) integrating the pressure on the wet surface of the hull using the coordinate system O^f-x^f-y^f-z^f to obtain the integrated forces and moments acting on O^f, and 4) derive the hydrodynamic coefficients based on the corresponding resultant forces and moments on the O^f in the O^f-x^f-y^f-z^f coordinate system.

In the proposed approach to calculate external and inertial loads on each structural component, we assumes that 1) the atmospheric pressure inside the hull is constantly equal to the atmosphere pressure at the still water plane and 2) the ballast fluid inside the hull is considered as ballast mass which introduce inertia loads on the hull rather than hydro pressure forces on the corresponding inner surface of the hull; while, in the boundary value problem for solving the hydrodynamic loads on each structural component, the hull is considered as a rigid-body. The second order and higher order terms of the hydro loads on the hull, except for the drag forces induced by viscous effect, and hydroelasticity effects are not included in the approaches discussed in the present paper, but they can be further included. The two assumptions are used to simplify the numerical models for the loads on the structural components. The second assumption can be implemented since the focus of the proposed approach is on capturing the global forces and moments in the structural components.

Details of the approaches for modeling inertial and external loads on each structural component are illustrated as follows.

For each structural component, a body-related coordinate system and a body-fixed coordinate system are established. We denote the origins of the body-related and body-fixed coordinate systems for the structural component i as $O^{r,i}$ and $O^{b,i}$ respectively. When the floating wind turbine is located at its mean position, the body-related and body-fixed coordinate systems for each structural component and the O^f-x^f-y^f-z^f coordinate system are coincident. The body-fixed coordinate system of the structural component i rigidly follows the motion of the corresponding node of the structural component i in the finite element

model in the O^g-x^g-y^g-z^g coordinate system. In the O^f-x^f-y^f-z^f coordinate system, the motion of the $O^{b,i}$ and the orientation of the body-fixed coordinate system are described by $\boldsymbol{\eta}^i(t) = [\eta_1^i, \eta_2^i, \eta_3^i, \eta_4^i, \eta_5^i, \eta_6^i]^T$. η_4^i, η_5^i and η_6^i are three Euler angles about x^f, y^f and z^f axis.

The gravity loads of the structural component i can be modelled as constant force acting on the centre of gravity of the structural component i in the body-fixed coordinate system of the structural component i and pointing to the negative direction of the vertical axis of the global coordinate system. Inertial loads of and viscous loads on the structural component i can be calculated in the body-fixed coordinate system. A body mass matrix of each structural component with respect to the origin of the corresponding body-fixed coordinate system can be specified. The viscous loads can be accounted for by the drag term of the Morison formula.

The resultants of the first order radiation and wave excitation loads on the structural component i are represented by $\boldsymbol{L}_{external,i}^t$, see Eq.(1). $\boldsymbol{L}_{external,i}^t$ is described in the body-related coordinate system of the structural component i and acting on the $O^{r,i}$.

$$\boldsymbol{L}_{external,i}^t = \boldsymbol{R}_{potential\_wave\_i}(t) - \int_{-\infty}^{+\infty} \boldsymbol{k}_i(t-\tau)\dot{\boldsymbol{\eta}}^i(\tau)d\tau - \boldsymbol{A}_i^{\infty}\ddot{\boldsymbol{\eta}}^i(t) \quad (1)$$

In the $\boldsymbol{L}_{external,i}^t$, $\boldsymbol{R}_{potential\_wave\_i}(t)$ is the resultants of the wave excitation loads on the structural component i obtained by applying inverse Fourier transform on $\boldsymbol{R}_{wave\_i}(\omega)$. $\boldsymbol{R}_{wave\_i}(\omega)$ is frequency dependent first order wave excitation vector for the structural component i. We have $\boldsymbol{R}_{wave\_i}(\omega) = \boldsymbol{H}_{fw\_i}(\omega) * Amp_{\omega}$. Amp_{ω} is determined by a spectrum of incident waves. For a sinusoidal wave with a given frequency ω, Amp_{ω} is the amplitude of the sinusoidal wave. $\boldsymbol{H}_{fw\_i}(\omega)$ is first order wave excitation load transfer function for the structural component i. $\boldsymbol{k}_i(t)$ is known as retardation or memory function for the structural component i and determined by $\boldsymbol{A}_i(\omega)$ or $\boldsymbol{B}_i(\omega)$. $\boldsymbol{A}_i^{\infty}$ is $\boldsymbol{A}_i(\omega)$ corresponding to the high-frequency limit. $\boldsymbol{A}_i(\omega)$ and $\boldsymbol{B}_i(\omega)$ are frequency dependent added mass coefficient matrix and potential damping coefficient matrix for the structural component i.

$\boldsymbol{H}_{fw\_i}(\omega)$, $\boldsymbol{A}_i(\omega)$ and $\boldsymbol{B}_i(\omega)$ are obtained by the following steps, 1) solving the boundary value problem in the O^f-x^f-y^f-z^f coordinate system with the rigid-body assumption for the hull, 2) calculating pressure forces on the mean wet surface of the structural component i ($S_{wet,i}^0$) based on the Bernoulli's equation and corresponding velocity potential, 3) integrating the pressure on the wet surface of the component i (on the $S_{wet,i}^0$) using the coordinate system O^f-x^f-y^f-z^f to obtain the integrated forces and moments acting on O^f, and 4) derive the hydrodynamic coefficients based on the corresponding resultant forces and moments on the O^f in the O^f-x^f-y^f-z^f coordinate system. $\boldsymbol{H}_{fw\_i}(\omega)$, $\boldsymbol{A}_i(\omega)$ and $\boldsymbol{B}_i(\omega)$ include hydrodynamic interactions.

$\boldsymbol{R}_{r\_i}^r(t)$ represents the resultant forces and moments of the hydrostatic pressure forces on the outer surface and the atmospheric pressure forces on the inner surface of the structural component i when the structural component is located at the instantaneous position described by $\boldsymbol{\eta}^i(t) = [\eta_1^i, \eta_2^i, \eta_3^i, \eta_4^i, \eta_5^i, \eta_6^i]^T$ in the O^f-x^f-y^f-z^f coordinate system. $\boldsymbol{R}_{r\_i}^r(t)$ is a 6×1 vector, acting on $O^{r,i}$ and described in the body-related coordinate system.

Neglecting the second order and higher order terms, the expression of the $\boldsymbol{R}_{r\_i}^r(t)$ is derived as:

$$\boldsymbol{R}_{r\_i}^r(t) = \boldsymbol{F}_{c_i} + (-1) * \boldsymbol{C}_i\boldsymbol{\eta}^i(t) \quad (2)$$

$\boldsymbol{F}_{ci}$ is a 6×1 vector. $\boldsymbol{C}_i$ is a 6×6 matrix with real coefficients. The expressions of $\boldsymbol{F}_{ci}$ and $\boldsymbol{C}_i\boldsymbol{\eta}^i(t)$ are available in Eq. (3-8).

The coefficients in the $\boldsymbol{C}_i$ and $\boldsymbol{F}_{c_i}$ are expressed by parameters that are defined in the O^f-x^f-y^f-z^f coordinate system with respect to the mean wet surface whereas $\boldsymbol{R}_{r\_i}^r(t)$ represents forces and moments acting on $O^{r,i}$ in the body-related coordinate system. We assume that the mean outer wet surface of the structural component i and the corresponding inner surface are identical and are denoted as $S_{wet,i}^0$ in the O^f-x^f-y^f-z^f coordinate system. s_0 is a point on the wet surface of the hull. The normal vector and position vector of s_0 at the mean position are denoted as $\boldsymbol{n}_0 = [n_1, n_2, n_3]^T$ and $\boldsymbol{v}_0 = [v_1, v_2, v_3]^T$. $\boldsymbol{n}_0$ is pointing away from the fluid field. Hydrostatic pressure on the s_0 ($P_{s_0,hydro\_sta}^0$) is given by applying Bernoulli's equation. P_0 represents the atmosphere pressure at the still water plane. $Z_0 = 0$ since the O^f-x^f-y^f-z^f coordinate system is located at the still water plane. ρ_f is density of sea water, taken as 1.025 tonnes/m^3. g is gravity acceleration, 9.81 m/s^2. We denote the atmospheric pressure inside the hull as $P_{inner,atm}$. We assume $P_{inner,atm}$ is constantly equal to P_0 . $P_{s_0,net}^0$ denotes the net pressure on the s_0 at the mean

position. $P^0_{s_0,net}$ is the difference between the hydrostatic pressure on the outer surface of the s_0 and the atmospheric pressure on the inner surface of the s_0.

$$P^0_{s_0,hydro\_sta} = P_0 + \rho_f g Z_0 - \rho_f g v_3 \qquad (3)$$

$$P^0_{s_0,net} = P^0_{s_0,hydro\_sta} - P_{inner,atm} \qquad (4)$$

$$\boldsymbol{F}_{c_i} = \begin{bmatrix} \iint\limits_{S^0_{wet,i}} \begin{bmatrix} n_1 \\ n_2 \\ n_3 \end{bmatrix} P^0_{s_0,net} ds \\ \iint\limits_{S^0_{wet,i}} \begin{bmatrix} v_1 \\ v_2 \\ v_3 \end{bmatrix} \times \begin{bmatrix} n_1 \\ n_2 \\ n_3 \end{bmatrix} P^0_{s_0,net} ds \end{bmatrix} \qquad (5)$$

$$\boldsymbol{C}_i \boldsymbol{\eta}^i(t) = \begin{bmatrix} \boldsymbol{D}_1 \\ \boldsymbol{D}_2 \end{bmatrix} \qquad (6)$$

$$\boldsymbol{D}_1 = \rho_f g \iint\limits_{S^0_{wet,i}} \begin{bmatrix} n_1 \\ n_2 \\ n_3 \end{bmatrix} \left(\eta^i_3 + \eta^i_4 v_2 - \eta^i_5 v_1\right) ds - \iint\limits_{S^0_{wet,i}} \begin{bmatrix} \eta^i_4 \\ \eta^i_5 \\ \eta^i_6 \end{bmatrix} \times \begin{bmatrix} n_1 \\ n_2 \\ n_3 \end{bmatrix} P^0_{s_0,net} ds \qquad (7)$$

$$\boldsymbol{D}_2 = \rho_f g \iint_{S^0_{wet,i}} \begin{bmatrix} v_1 \\ v_2 \\ v_3 \end{bmatrix} \times \begin{bmatrix} n_1 \\ n_2 \\ n_3 \end{bmatrix} \left(\eta^i_3 + \eta^i_4 v_2 - \eta^i_5 v_1\right) ds - \iint_{S^0_{wet,i}} \begin{bmatrix} 0 \\ 0 \\ \eta^i_3 \end{bmatrix} \times \begin{bmatrix} n_1 \\ n_2 \\ n_3 \end{bmatrix} P^0_{s_0,net} ds - \iint_{S^0_{wet,i}} \begin{bmatrix} \eta^i_4 \\ \eta^i_5 \\ \eta^i_6 \end{bmatrix} \times \left(\begin{bmatrix} v_1 \\ v_2 \\ v_3 \end{bmatrix} \times \begin{bmatrix} n_1 \\ n_2 \\ n_3 \end{bmatrix} \right) P^0_{s_0,net} ds \qquad (8)$$

Flexibility effects of the hull on the hydro loads are not accounted for. The hydrodynamic loads on each structural component are derived from the velocity potential that are obtained by solving the boundary value problems with the assumption that the hull is a rigid-body. The kinematics of different structural components is constrained by the rigid-body assumption. Consequently, the hydrodynamic interaction effects between the structural components are included in the hydrodynamic loads on each structural component. However, the proposed approach may not be able to well model the hydroelasticity effect. Therefore, it is not recommended to be applied on floating structures with relatively large flexibility, for which hydroelasticity effect can be important.

The expressions of $\boldsymbol{L}^t_{external,i}$ and $\boldsymbol{R}^r_{r\_i}(t)$ can be further modified. For example, additional terms can be included to account for second order and/or higher order hydro loads on each structural component, while the load effects of the ballast fluid can be modeled as pressure forces on the inner surface of each structural component.

3 Verification of the proposed approach

The proposed approach is implemented in Simo/Riflex/Aerodyn [29-32] to calculate global forces and moments of the 5-MW-CSC [15]. The layout of the semi-submersible floater is given in Figures 5 and 6. The O^g-x^g-y^g-z^g and O^f-x^f-y^f-z^f coordinate systems are established at the mean position of the geometrical centre of the water plane area.

Five numerical models have been developed. Three comparisons, i.e. Comparison A, Comparison B and Comparison C, have been carried out to verify the proposed approach step by step. These numerical models and the comparisons are briefly explained below and illustrated in Figure 7 and Figure 8, respectively. Detailed descriptions for the numerical models are available in the later part of this paper. A summary of the features of the time-domain models is available in Table 3.

FDM is a frequency-domain model of the 5-MW-CSC developed in WADAM [26] to calculate wave induced global forces and moments by implementing a standard procedure used in the offshore oil and gas industry [26].

TDM-2B-L is a time-domain model of the 5-MW-CSC developed in Simo/Riflex [27, 28]. The proposed approach is implemented to calculate wave induced global forces and moments in the cross-section as shown by the dashed line in Figure 5. Aerodynamic loads are not available in the TDM-2B-L.

TDM-1B-C is a time-domain model developed in Simo/Riflex/Aerodyn. Aerodynamic loads on the RNA and tower are appropriately accounted for in the TDM-1B-C, while the conventional hybrid frequency-time domain approach is implemented to model the hydro loads on the semi-submersible hull. The modeling approach implemented in the TDM-1B-C is considered as the state-of-the-art approach that has been used by researchers, e.g. [21, 43, 46, 47], to analyze responses of floating wind turbines in wind and waves except for the global forces and moments in the hull since the approach models the hull as one rigid-body with 6 d.o.f.s.

TDM-2B-N is an extension of the TDM-1B-C. The proposed approach is implemented to calculate global forces and moments in the hull (in the cross-section as shown by the dashed line in Figure 5). The TDM-1B-C and TDM-2B-N are identical except for the finite element model of the hull and method for modeling the external and inertial loads on the hull.

TDM-29B-N is an extension of the TDM-2B-N. The TDM-2B-N includes two rigid-bodies for the hull, while, the TDM-29B-N includes twenty-nine rigid-bodies for the hull. The TDM-29B-N model is developed and compared to the TDM-2B-N model in order to show that the proposed method can be generalized to a model consisting of any number of structural components. From the practical use point of review, it is convenient to use the TDM-29B-N model to obtain the dynamic responses at any critical position of the hull by just one time-domain model. While, using the TDM-2B-N approach, many different numerical models need to be built and analyzed.

It is expected that the time-domain model TDM-2B-N can calculate the global forces and moments in the cross-section as shown by the dashed line in Figure 5 while the time-domain model TDM-29B-N can calculate the global forces and moments in the same cross-section and the other twenty-seven cross-sections.

As far as the authors know, there is no published experimental data for the global forces and moments in the hull of floating wind turbines in wind and waves. In addition, the state-of-the-art time-domain computer codes cannot accurately calculate the global forces and moments in the hull [22].

The accuracy of the calculated responses is related to two modeling issues: 1) whether or not the computer codes can accurately calculate the wind and waves induced external and inertial loads on the floating wind turbines and map the loads to the generated finite element models of the floating wind turbines; and 2) whether or not the finite element models generated in the computer codes can accurately represent the global stiffness of the floating wind turbines and calculate the structural responses for given loads. These two features are coupled.

The hull of the 5-MW-CSC is a statically determinate structure. For a statically determinate structure, in general, the accuracy of the responses in the structure is purely determined by the accuracy of the external loads acting on the structural components, like aerodynamic loads on the blades and the tower and hydrodynamic loads on the floater and mooring lines and the inertial loads.

In linear theory, hydrodynamic and hydrostatic loads on structural components of the hull are determined by two issues. We denote these issues as ISA and ISB respectively.

ISA: The configuration and shape of the mean wet surfaces of the structural components.

ISB: The motion responses of the structural components.

The accuracy of the global forces and moments in the hull calculated by the TDM-2B-N is indicated by the results of Comparison A and Comparison B. Comparison A focuses on verifying that the influence of the ISA on the hydro loads on the structural components can be accurately modeled in finite element codes which implement the proposed approach. Comparison B focuses on verifying that finite element codes which implement the proposed approach can accurately predict the motion responses of the structural components and responses of the RNA, tower and mooring lines of the reference semi-submersible wind turbine in wind and waves. Comparison C is carried out, to some extent, to address that the proposed approach can be applied to generic floating wind turbines, for which the hull may need to be modeled by any number of structural components. The proposed approach is not necessarily limited to two rigid-bodies for the hull. Due to the limitation of the proposed approach, we do not account for the hydroelasticity effect in the comparisons discussed in the present paper.

In Comparison A, the FDM is used as a reference model for the transfer functions of wave to global forces and moments in the hull. While the transfer functions can also be derived from structural responses of the hull calculated by carrying out regular

and/or irregular wave analysis in time-domain numerical models that implement the proposed approach, e.g. TDM-2B-L, TDM-2B-N and TDM-29B-N. The FDM is a linear system and does not account for non-linear effects on the global forces and moments, while TDM-2B-L is developed to be, as much as possible, a linear system and equivalent to the FDM. The agreement in the transfer functions calculated in the FDM and TDM-2B-L is expected to be good if the proposed approach accurately models the hydro pressure forces on the structural components of the hull and maps the forces on the finite element model of the hull.

TDM-2B-L models the 5-MW-CSC as two structural components connected by three artificial beam elements. Aerodynamic loads are not accounted for in the TDM-2B-L. In contrast, aerodynamic loads are accounted for in the TDM-2B-N while the TDM-2B-N models the hull of the 5-MW-CSC as two structural components connected by three artificial beam elements and the mooring lines, tower and blades as beam elements. The mean wet surfaces of the two structural components of the TDM-2B-L are identical to the mean wet surfaces of the two structural components of the TDM-2B-N correspondingly and respectively. Consequently, if the influence of the ISA on the hydro loads on the structural components can be accurately modeled in TDM-2B-L, the influence can be accurately modeled in the TDM-2B-N.

The motions of the hull and responses of the RNA, tower and mooring lines predicted by TDM-2B-N and TDM-1B-C are compared in Comparison B. TDM-1B-C is used as a reference model except for the global forces and moments in the hull. TDM-1B-C and TDM-2B-N are identical except for the finite element model of the hull and method for modeling the external and inertial loads on the hull. Therefore, agreement in the compared responses is expected to be good.

Since the hull of the 5-MW-CSC is a statically determinate structure, it is expected that the global structural stiffness of the hull does not affect the global forces and moments in the structural components of the hull except for the inertia loads and hydro loads induced by the flexible modes of the hull. The global structural stiffness of the hull is determined by properties of the equivalent cross-sections of the pontoons and columns and material properties, e.g. Young's modulus and modulus of rigidity. In Comparison C, artificial material properties are implemented to make the global structural stiffness of the hull of the TDM-29B-N to be of the same magnitude as the one of the TDM-2B-N. Consequently, the global forces and moments calculated by the TDM-2B-N and TDM-29B-N are expected to be identical. Research on the importance of the influence of the inertia loads and hydro loads induced by the flexible modes of the hull is interesting and will be investigated in future.

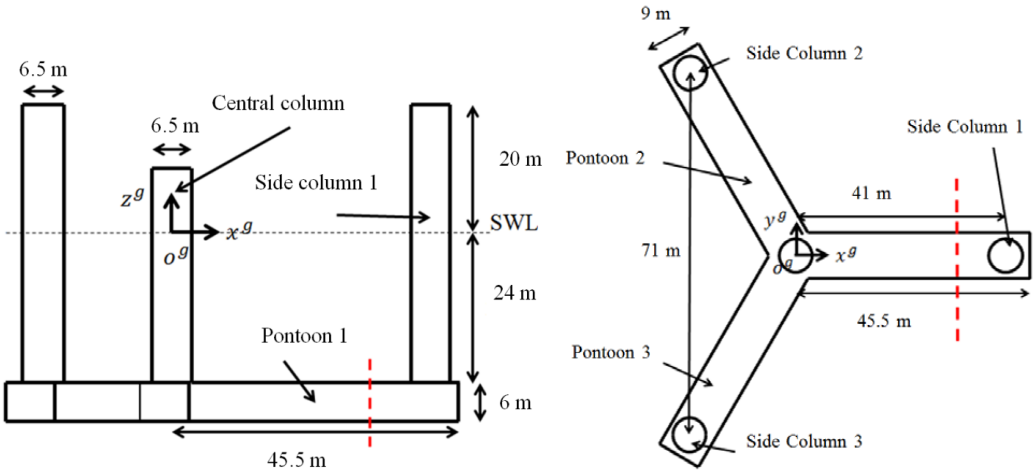

Figure 5 Side (left) and top (right) views of the semi-submersible hull of 5-MW-CSC

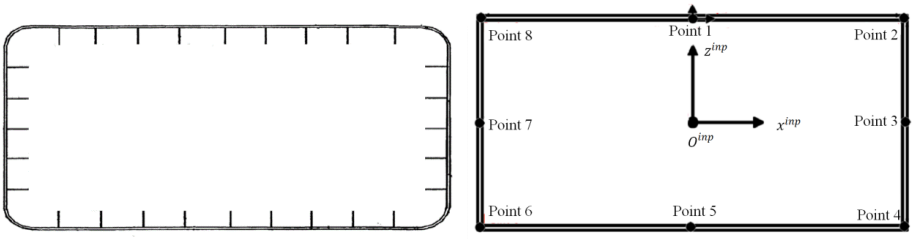

Figure 6 A realistic cross-section (left) and simplified box-shape cross-section with equivalent thickness (right)

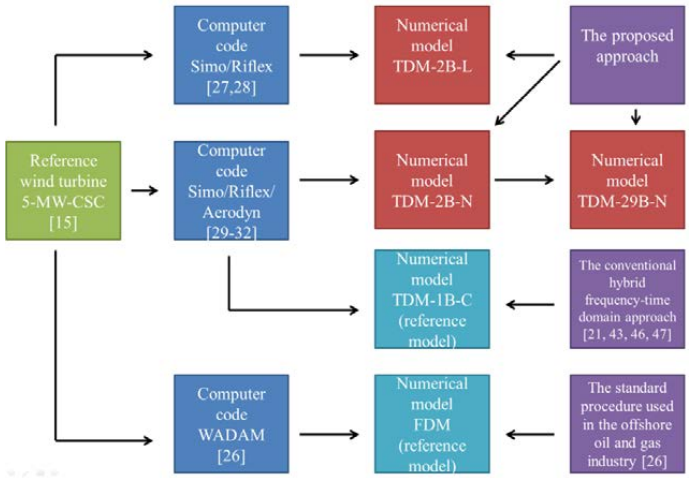

Figure 7 Numerical models

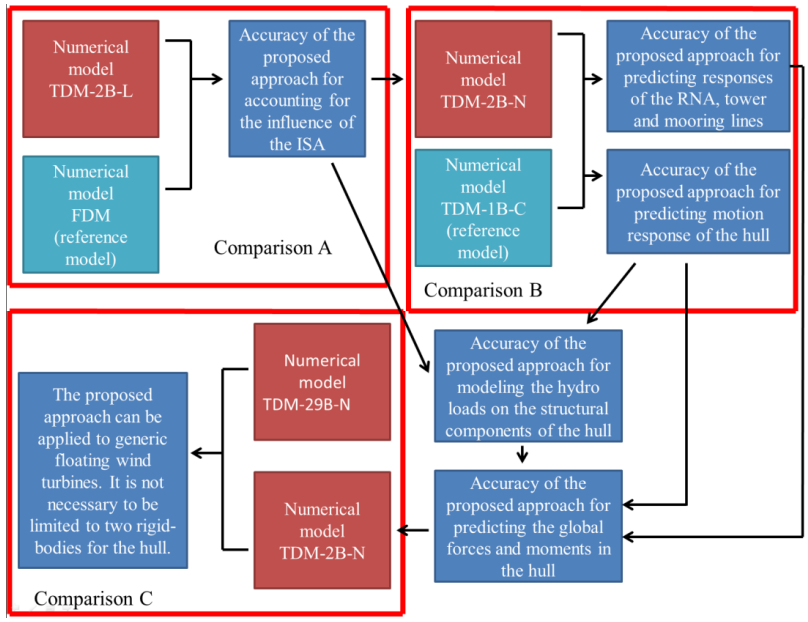

Figure 8 Verification procedure

3.1 FDM

The FDM is a frequency-domain model developed in WADAM [26] to calculate wave induced global forces and moments in a cross-section as shown by the dashed line in Figure 5. Only wave loads are considered here. A realistic cross-section of the pontoon of the hull may be composed of stiffened plates, stiffeners and girders. As shown in Figure 6, in global analysis, the realistic cross-section can be simplified as a box-shape cross-section with equivalent thickness. The mean position of the geometrical center of the box-shape cross-section in the O^f-x^f-y^f-z^f coordinate system is (31.5, 0, -27). The cross-section divides the semi-submersible wind turbine into two parts: "Part A" and "Part B". The wind turbine is included in the "Part B". The global forces and moments in the cross-section are derived based on the fact that the global forces and moments in the cross-section and inertial and external loads on the "Part A" (as well as on Part B) must be in equilibrium. The standard procedure used in the offshore oil and gas industry [26] is implemented in WADAM to calculate the inertial and external loads on the "Part A".

The inertial loads on the "Part A" are determined by the mass and acceleration of the "Part A". Motion equations are generated and solved in frequency domain to derive the acceleration. In the motion equations, the RNA, tower and hull are modeled as a single rigid-body with 6 d.o.f.s. Structural flexibility of the floating wind turbine is neglected. The mooring lines are not included in the rigid-body formulation. Instead, a 6×6 restoring stiffness matrix ($C_{mooring}$) is introduced in the motion equations to represent the restoring effect of the mooring lines on the motions. Hydrodynamic coefficients used in the motion equations are calculated by solving the potential-flow boundary value problem with the rigid-body assumption. The motion equations do not include viscous effect. The external loads on the "Part A" are composed of the first order hydrodynamic loads and the fluctuations of hydrostatic pressure forces and gravity loads.

$$C_{mooring} = \begin{bmatrix} 114\ kN/m & 0 & 0 & 0 & -2052\ KN & 0 \\ 0 & 114\ kN/m & 0 & 2052\ KN & 0 & 0 \\ 0 & 0 & 0 & 0 & 0 & 0 \\ 0 & 2052\ KN & 0 & 149669\ kN*m & 0 & 0 \\ -2052\ KN & 0 & 0 & 0 & 149669\ kN*m & 0 \\ 0 & 0 & 0 & 0 & 0 & 204628\ kN*m \end{bmatrix} \quad (9)$$

3.2 TDM-2B-L

The TDM-2B-L is a time-domain model developed in Simo/Riflex [27,28] and implements the proposed approach. We intend to make it be, as much as possible, equivalent to the FDM. That means, in the TDM-2B-L, the "Part A" and "Part B" are modeled as two rigid-bodies. Each rigid-body has 6 d.o.f.s. The origins of the body-fixed and body-related coordinate systems for the two rigid-bodies are denoted as $O^{b,PA}$ and $O^{r,PA}$and $O^{b,PB}$ and $O^{r,PB}$ respectively. When the floating wind turbine is located at its mean position, the body-fixed and body-related coordinate systems are coincident to the O^f-x^f-y^f-z^f coordinate system. The positions and orientations of the $O^{b,PA}$ and $O^{b,PB}$ are described by $\boldsymbol{\eta}^{PA}(t)$ and $\boldsymbol{\eta}^{PB}(t)$ in the O^f-x^f-y^f-z^f coordinate system. In the frequency-domain model, the global forces and moments in the cross-section are derived from the equilibrium between the relevant external and inertial loads and the global forces and moments. However, to calculate the global forces and moments in a straight-forward manner in Simo/Riflex, we must have a finite element model. Consequently, the two rigid-bodies are connected by three artificial beam elements. The mean positions of the end nodes of the artificial beams in the O^f-x^f-y^f-z^f coordinate system are tabulated in Table 1. Each end node rigidly follows the motions of its corresponding rigid-body ($\boldsymbol{\eta}^{PA}(t)$ or $\boldsymbol{\eta}^{PB}(t)$). The artificial beam elements are massless. There are no external loads on the artificial beam elements. Each artificial beam element only has axial and torsional stiffness. Artificial Young's modulus and modulus of rigidity are specified to make the artificial beams be stiff. For each beam element, the product of the Young's modulus and cross-section area is specified as 10^9 kN, while, the product of the torsional rigidity and modulus of rigidity are specified as 10^9 kNm^2/rad. The proposed approach is implemented to calculate the first order hydrodynamic loads, gravity and hydrostatic pressure forces on the "Part A" and "Part B" and map the loads on the end nodes of the artificial beam elements. Viscous loads on the hull are not included. The mooring lines induced forces and moments on the floating wind turbine are accounted for by $(-1) * C_{mooring} * \boldsymbol{\eta}^{PB}(t)$, which are acting on $O^{r,PB}$ and described in the body-related coordinate system of the rigid-body that corresponds to the "Part B".

Table 1 Positions of end nodes of three artificial beams in the body-fixed coordinate system (Units in meter)

	End 1	End 2
Artificial beam 1	(31.4,0,-27)	(31.6,0,-27)
Artificial beam 2	(31.5,-0.1,-27)	(31.5,0.1,-27)
Artificial beam 3	(31.5,0,-27.1)	(31.5,0,-26.9)

3.3 TDM-1B-C

The TDM-1B-C is a time-domain model developed in Simo/Riflex/Aerodyn. The time-domain model implements the conventional hybrid frequency-time domain approach. The hull is modeled as a rigid-body with 6 d.o.f.s in Simo. The conventional hybrid frequency-time domain approach is used to account for the first order wave excitation and radiation loads on the hull. The blades, shaft of the drive train inside the nacelle, tower and mooring lines are modeled as beam elements in Riflex. The motions of the lower end node of the tower and the upper nodes of the mooring lines rigidly follow the motions of the hull. The hub and nacelle are modeled as rigid mass points attached on the shaft and top of the tower. Aerodynamic loads on the blades and tower are calculated in Aerodyn [32]. A dll file [31] is used to account for the effect of pitch control on aerodynamic loads on the three blades and the effect of the generator inside the nacelle on the power production and generator torque. The torque of the generator is calculated by the dll file based on the rotational speed of the shaft. The shaft is rotational about its longitudinal axis. The rotational d.o.f. is achieved by applying a flex joint [28] on the beam element of the shaft. The blades are connected to the tower through the shaft. Loads on the blades, hub, shaft and generator torque are transferred through the flex joint to the beam element of the tower. Hydrodynamic loads on the mooring lines are accounted for by the Morison formula. The drag term of the Morison formula is used to account for the viscous loads on the hull. The non-dimensional drag coefficients (C_d) are specified in DNV[33]. C_d for the width and height of the pontoons of the 5-MW-CSC is 1.95. C_d for the central column is 0.8. C_d for the side columns is 0.64. The work-flow chart is available in Figure 1.

3.4 TDM-2B-N

The TDM-1B-C and TDM-2B-N are identical except for the finite element model of the hull and method for modeling the external and inertial loads on the hull. The cross-section, as shown by the dashed line in Figure 5, discretizes the hull into two components. The two components of the hull are modeled as two rigid-bodies: "Body1" and "Body2". The wind turbine is mounted on the "Body 2". Each rigid-body has 6 d.o.f.s. The origins of the body-fixed and body-related coordinate systems for the "Body1" and "Body2" are denoted as $O^{b,B1}$ and $O^{r,B1}$and $O^{b,B2}$ and $O^{r,B2}$ respectively. When the floating wind turbine is located at its mean position, the body-fixed and body-related coordinate systems are coincident to the O^f-x^f-y^f-z^f coordinate system. The positions and orientations of the $O^{b,B1}$ and $O^{b,B2}$ are described by $\boldsymbol{\eta}^{B1}(t)$ and $\boldsymbol{\eta}^{B2}(t)$ in the O^f-x^f-y^f-z^f coordinate system. The two rigid-bodies are connected by the artificial beam elements used in the TDM-2B-L. Each end node of the artificial beam element rigidly follows the motions of its corresponding rigid-body ($\boldsymbol{\eta}^{B1}(t)$ or $\boldsymbol{\eta}^{B2}(t)$). The proposed approach is implemented to calculate the first order hydrodynamic loads, gravity and hydrostatic pressure forces on the "Body1" and "Body2" and map the loads on the end nodes of the artificial beam elements. The drag term of the Morison formula is used to account for the viscous loads on the hull. The non-dimensional drag coefficients used in TDM-2B-L and TDM-2B-N are identical. The work-flow chart is available in Figure 3.

3.5 TDM-29B-N

The TDM-29B-N is an extension of the TDM-2B-N. Numerical models for the RNA, tower and mooring lines of the TDM-2B-N and TDM-29B-N are identical. In the TDM-29B-N, we consider that the hull is composed of twenty-nine structural components. For example, the blue colored parts in the Figure 9 are the structural components named "ICP_S1" and "SP3_2" respectively. Each structural component corresponds to a reference node (the brown colored circle). Each reference point represents 6 d.o.f.s of the corresponding structural component. The reference points are connected by beam elements that represent the flexibility of the hull. The beam elements are massless and there are no external loads on the beam elements. The viscous drag is accounted for by the drag term of the Morison formula and being integrated and transferred to the corresponding reference nodes. The end nodes of beam elements rigidly follow the motions of the corresponding reference node. In the 5-MW-CSC, there are four interfaces between the columns and pontoons. The ICP_S1 represents an interface between the side column 1 and the pontoon 1. For the TDM-29B-N, the stiffness of the interfaces is not modeled since the interfaces are modeled as rigid-bodies. The stiffness of the beam elements are determined by properties of the equivalent cross-sections of the pontoons and columns and material properties, e.g. Young's modulus and modulus of rigidity. In the Comparison C, artificial material properties are implemented to make the global structural stiffness of the hull of the TDM-29B-N be in the same level as the one of the TDM-2B-N. The specified stiffness properties of the beam elements are tabulated in Table 2. $\mathrm{E}A_g$ represents the product of the Young's modulus and cross-section area. EI_g represents the product of the Young's modulus and the second moment of the area of the cross-section. GJ_g represents the product of the torsional rigidity and modulus of rigidity. The work-flow chart is available in Figure 3.

Table 2 Specified stiffness properties of the beam elements used in TDM-29B-N

	$\mathrm{E}A_g$ [kN]	EI_g [kNm^2]	GJ_g [kNm^2/rad]
Column	$1.29 * 10^{10}$	$6.79 * 10^{10}$	$5.11 * 10^{10}$
Pontoon	$1.89 * 10^{10}$	$6.27 * 10^{10}$	$2.00 * 10^{10}$

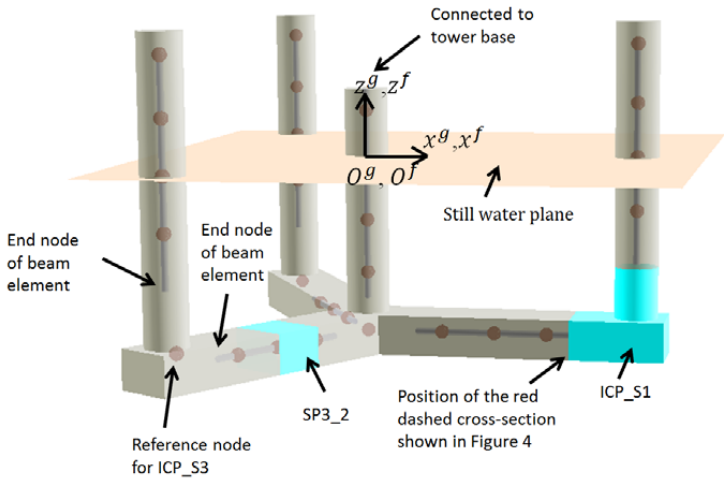

Figure 9 The finite element model of the hull with twenty-nine bodies

Table 3 Summary of the features of the time-domain models

<table>
<tr><th>Mass and structural models</th><th>TDM-2B-L</th><th>TDM-1B-C</th><th>TDM-2B-N/ TDM-29B-N</th></tr>
<tr><td>The hull</td><td>The floating wind turbine is divided into two parts: “Part A” and “Part B”. The two parts are modeled as two rigid-bodies. Each rigid-body has 6 d.o.f.s. The two rigid-bodies are connected by three artificial beam elements. Integrated mass (corresponding to each rigid-body).</td><td>The hull is modeled as one rigid-body with 6 d.o.f.s. Integrated mass.</td><td>The hull is discretized as two rigid-bodies: “Body1” and “Body2” / twenty-nine rigid-bodies. Each rigid-body has 6 d.o.f.s. The two rigid-bodies are connected by three artificial beam elements / The twenty-nine rigid-bodies are connected by beam elements. Integrated mass (corresponding to each rigid-body)</td></tr>
<tr><td>Nacelle</td><td rowspan="5">Rigid-bodies with integrated mass (Included in the rigid-body for the “Part B”).</td><td>Mass point attached to tower top</td><td rowspan="6">Identical to TDM-1B-C</td></tr>
<tr><td>hub</td><td>Mass point attached to shaft</td></tr>
<tr><td>Tower</td><td rowspan="4">Flexible bodies
Beam elements
Distributed mass</td></tr>
<tr><td>Blades</td></tr>
<tr><td>Shaft</td></tr>
<tr><td>Mooring lines</td><td>The finite element model of the mooring lines is not developed.</td></tr>
<tr><th>External load model</th><th>TDM-2B-L</th><th>TDM-1B-C</th><th>TDM-2B-N/ TDM-29B-N</th></tr>
<tr><td>The hull</td><td>1) Gravity loads
2) Extended hybrid frequency-time domain approach
3)Hydrostatic pressure force
4) Rayleigh damping (the part that is proportional to the structural stiffness)
5) Linearized restoring forces and moments provided by the mooring lines.</td><td>1) Gravity loads
2) Conventional hybrid frequency-time domain approach
3) Viscous force (Drag term of the Morison formula)
4) Hydrostatic pressure force</td><td>1) Gravity loads
2) Extended hybrid frequency-time domain approach
3) Viscous force (Drag term of the Morison formula. The drag coefficients are identical to TDM-1B-C)
4) Hydrostatic pressure force
5) Rayleigh damping (the part that is proportional to the structural stiffness)</td></tr>
<tr><td>Nacelle</td><td rowspan="5">1) Gravity loads</td><td rowspan="2">1) Gravity loads
2) Rayleigh damping (the part that is proportional to the structural stiffness)</td><td rowspan="5">Identical to TDM-1B-C</td></tr>
<tr><td>hub</td></tr>
<tr><td>Tower</td></tr>
<tr><td>Blades</td><td>1) Gravity loads
2) Aerodynamic loads (Aerodyn)
3) Rayleigh damping (the part that is proportional to the structural stiffness)</td></tr>
<tr><td>Shaft</td><td>1)Generator torque</td></tr>
<tr><td>Mooring lines</td><td>None</td><td>1) Gravity and Buoyancy loads
2) Morison formula</td><td></td></tr>
</table>

4 Results and discussions

4.1 Comparison A

F_x, F_y, F_z, M_x, M_y, and M_z denote the wave induced global forces and moments in the cross-section shown by the dashed line in Figures 5 and 6. The global forces and moments are acting on the origin of the O^{inp}-x^{inp}-y^{inp}-z^{inp} coordinate system and described in the O^{inp}-x^{inp}-y^{inp}-z^{inp} coordinate system. The O^{inp}-x^{inp}-y^{inp}-z^{inp} coordinate system is a body-fixed coordinate system. When the 5-MW-CSC is located at its mean position, the body-fixed coordinate system is coincident to the O^f-x^f-y^f-z^f coordinate system except that the origin of the body-fixed coordinate system is located at the geometrical center of the cross-section which is (31.5, 0, -27) in the O^f-x^f-y^f-z^f coordinate system.

For a given point on the cross-section, axial stress (σ_x) and shear stress (τ) are calculated by Eqs.(10,11).

$$\sigma_x = \frac{F_x}{A} + \frac{M_y}{w_{y\_inp}} + \frac{M_z}{w_{z\_inp}} \qquad (10)$$

$$\tau = \frac{M_x}{2A_0 t_c} + \frac{F_y S_{z\_inp}}{I_{z\_inp} t_c} + \frac{F_z S_{y\_inp}}{I_{y\_inp} t_c} \qquad (11)$$

A is the area of the cross-section. w_{y_inp} and w_{z_inp} are the section moduli corresponding to the y_inp and z_inp axes and the position of the point on the cross-section. A_0 is the circumscribed area of the cross-section. t_c is the equivalent thickness of the cross-section. S_{y_inp} and S_{z_inp} are static moments corresponding to the y_inp and z_inp axes and the position of the point on the cross-section. I_{y_inp} and I_{z_inp} are the second moments of area of the cross-section.

For the TDM-2B-L, transfer function moduli for wave induced global forces and moments and axial and shear stresses can be obtained by carrying out irregular wave analysis or regular wave analysis.

Regular wave analysis can directly give the moduli and phase angles of the transfer functions; however, the phase angles are very sensitive to numerical issues. The transfer functions corresponding to 19 different wave directions and 58 different frequencies are calculated. The wave direction varies from 0 degrees to 180 degrees with 10-degree intervals. The frequencies are distributed in the range from 0.3 rad/s to 2.2 rad/s. The amplitude of each regular wave is specified as 0.1 m.

Alternatively, transfer function moduli can be derived from the spectral densities of the incident waves and global forces and moments. For each wave direction, a 10-hour realization of wave elevation is generated from a white noise spectrum. The frequency range of the spectrum is from 0.3 rad/s to 2.2 rad/s. Significant wave height of the spectrum is specified as 1.233m (H_s=4$\sqrt{m_0}$, m_0 denotes the variance-area under the spectral density function). The wave induced motions and global forces and moments are calculated by the TDM-2B-L. The spectral densities are obtained by applying inverse Fourier transform, with a fixed smoothing parameter, of the autocorrelation function of the incident wave and global forces and moments.

The relative difference (R_b) in the obtained transfer function is employed to show the difference in two groups of data. R_b is used to address the relative difference with respect to the corresponding maximum value in the entire wave frequency range (from 0.35 rad/s to 2 rad/s). For example,$\mathrm{e}(\omega) = \{\mathrm{e}(\omega_1), \mathrm{e}(\omega_2), \ldots \mathrm{e}(\omega_i), \ldots\}$ and $\mathrm{f}(\omega) = \{\mathrm{f}(\omega_1), \mathrm{f}(\omega_2), \ldots \mathrm{f}(\omega_i), \ldots\}$ represent transfer function moduli for wave induced axial force ($|H_{F_x}|$). The transfer function moduli are calculated by carrying out irregular wave analysis and regular wave analysis respectively. ω_i is a given frequency.

$$R_b(\omega_i) = \left| \mathrm{e}(\omega_i) - \mathrm{f}(\omega_i) \right| \Big/ \max\{\mathrm{e}(\omega), \mathrm{f}(\omega)\} \times 100\% \qquad (12)$$

Transfer function moduli for wave induced global forces and moments and axial and shear stresses obtained by carrying out regular and irregular wave analysis in the TDM-2B-L are compared. The agreement is good. The largest R_b for the transfer function moduli for axial and shear stresses is less than 6%. For most of the transfer function moduli, R_b is less than 3%. Therefore, for the TDM-2B-L, in the following, the transfer function moduli are obtained by carrying out irregular wave analysis.

The transfer function moduli given by the FDM and TDM-2B-L are compared. Some selected results are shown in the present paper. Note that the trend of the transfer function moduli for the sectional forces and moments are not necessary to be the same as that of the total integrated wave excitation loads or motions. The sectional forces and moments are resultants of the difference between the effects of these two on the structure.

The main observations are discussed as follows:

The agreement in transfer function moduli for the global forces and moments and stresses given by the FDM and TDM-2B-L is very good. The relative differences (R_b) vary with respect to the wave frequency and wave direction. In general, peak values of R_b may appear at frequencies nearby troughs of the transfer function modulus curves. However, the effect of the peak values of R_b on the accuracy of the global forces and moments calculated by the TDM-2B-L is very limited. This is because, in the

frequency range from 0.35 rad/s to 2 rad/s, for most of the transfer function moduli, R_b is less than 2.5%. The maximum value of R_b for the transfer function moduli for stresses and for global forces and moments is no more than 8% and 5.9% respectively. Two examples are available in Figure 10 and 11. Position of the points on the cross-section is shown in Figure 6.

The difference between the FDM and TDM-2B-L is induced by: 1) inherent difference between frequency-domain and time-domain models; 2) accuracy limitation for the numerical solver and other numerical issues.

Detailed discussions are as follows:

- Transfer function moduli for the global forces and moments and stresses subjected to the white noise irregular wave analysis with $H_s = 1.233$ m and $H_s = 12.33$ m are compared. For wave directions, where yaw motion is very small due to the shape of the wet surface of the hull, i.e. 0-degree-wave, 60-degree-wave and 120-degree-wave, R_b for the transfer function moduli is close to zero and indicates that the difference is negligible. In the rest wave directions, the difference is significant. In the frequency range from 0.85 rad/s to 2 rad/s, R_b for the transfer function moduli for the stresses can be up to 28% (in the area around 1.85 rad/s). In the frequency range from 0.35 rad/s to 0.85 rad/s, R_b for the transfer function moduli for the stresses is less than 5%. An example is shown in Figure 12.
- Transfer function moduli for the responses are calculated by the TDM-2B-L based on two groups of random seed. R_b for the transfer function moduli for the stresses is in the range of 0% to 2.2%. The difference may be induced by stochastic uncertainties, non-linear effect and/or numerical errors.
- The mooring lines, tower and blades are flexible slender structures, while the hull and shaft are very stiff. For a large volume structure, such as the 5-MW-CSC, the integrated hydrodynamic loads on the hull can be much larger than the integrated aerodynamic loads on the blades or hydrodynamic loads on the mooring lines. The large variations in the generalized stiffness matrix and external load vectors of the finite element model of the floating wind turbine may, numerically, result in an accuracy limitation and/or numerical errors.
- In Simo/Riflex, global shear forces in the beam elements are calculated by the Euler–Bernoulli beam theory. If the three artificial beam elements of the TDM-2B-L are replaced by a very short (0.1 m) beam element with very large axial, torsional and bending stiffness, the shear forces calculated by the TDM-2B-L are strange and wrong until the bending stiffness of the beam element is reduced and/or the length of the beam element is increased.
- The TDM-2B-L does not have viscous damping. Therefore, very limited wave energy at the resonant frequencies can result in very large resonant motions. The amplitude of the resonant motions could be much larger than the amplitude of the motions in the wave frequency range. The very large resonant motions can introduce strong numerical noise on the realizations of the motions in the wave frequency range. Therefore, the lower limit of the frequency range of the white noise spectrum used in the irregular wave analysis is specified as 0.3 rad/s to keep the wave energy be away from the resonant frequencies, avoid very large resonant motions and limit the numerical noise. Alternatively, the numerical noise can be moderated by introducing viscous effect into the numerical model.
- In the TDM-2B-L, the first order wave excitation loads on the hull are generated from the corresponding spectral densities of the wave excitation loads. “WETFF59” and “WETFF199” represent wave to wave excitation load transfer functions that correspond to a set of 59 selected frequencies and a set of 199 selected frequencies respectively. If the TDM-2B-L use the “WETFF59” and is subjected to 80-degree-wave, 90-degree-wave or 100-degree-wave, the TDM-2B-L will give strange results in the transfer functions for the global forces and moments. The strange results will disappear if the “WETFF59” is replaced by “WETFF199”. Figure 13 shows the transfer function modulus curves for the global lateral shear force (F_y) given by the FDM and TDM-2B-L, which use the “WETFF59” and is subjected to 90-degree-wave, as an example. Compare to the FDM, the TDM-2B-L gives strange transfer function moduli (“an impulse”) in the frequency range from 0.79 rad/s to 0.89 rad/s. We can observe similar strange results in the spectral densities for the global forces and moments given by the TDM-2B-L that implements the “WETFF59” rather than the “WETFF199”. Figure 14 shows the spectral densities for the global lateral shear force (F_y) given by the TDM-2B-L that implements the “WETFF59” and “WETFF199” respectively. The circles and squares on the curves represent the set of the 59 selected frequencies and set of the 199 selected frequencies respectively. The spectral densities are generated based on the same smoothing factor for the inverse Fourier transform. The realizations of the global forces and moments are calculated based on the same realization of the wave elevation. In the frequency range from 0.79 rad/s to 0.89 rad/s, the set of the 59 selected frequencies for the “WETFF59” has two frequencies (0.797 rad/s and 0.877 rad/s). These two frequencies are nearby the boundary of the range and sufficient to represent the wave excitation transfer functions in the range. The set of the 199 selected frequencies for the “WETFF199” has 12 frequencies uniformly distributed in the range. The “WETFF59” agree with the “WETFF199”, while, the “WETFF199” are smoother since the “WETFF199” include more frequencies. Figure 15 shows the transfer function curves for the lateral wave excitation force on the “PartA” in 90-degree-wave, as an example. We do not observe similar strange results in the “WETFF59” and “WETFF199”. We can conclude that the strange results are related to the selected frequencies for the wave excitation transfer functions. However, the reason is not clear yet. In this paper, the numerical models, which implement the proposed method, utilize the “WETFF199”. In general, a refined frequency resolution should be considered when using irregular wave analysis to obtain the transfer function.

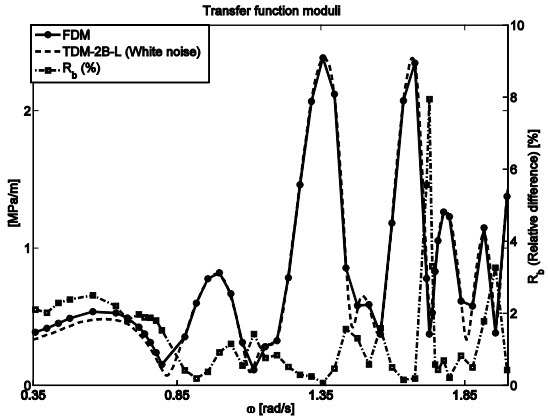

Figure 6 Comparison of transfer function modulus curves for the axial stress at the point 6 given by the FDM and TDM-2B-L subjected to 120-degree-wave

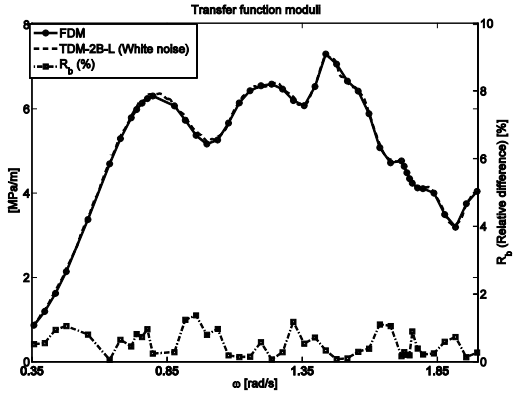

Figure 11 Comparison of transfer function modulus curves for the axial stress at the point 1 given by the FDM and TDM-2B-L subjected to 10-degree-wave

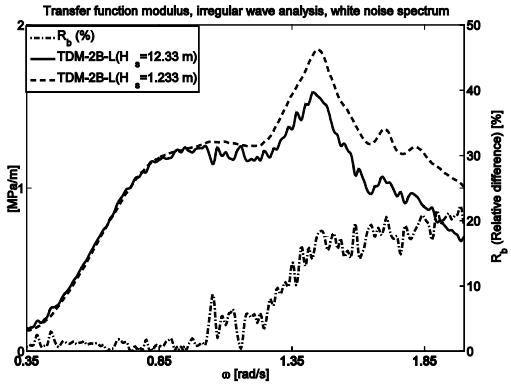

Figure 12 Comparison of transfer function modulus curves for the axial stress at the point 3 given by the TDM-2B-L subjected to 80-degree-wave and different significant wave heights

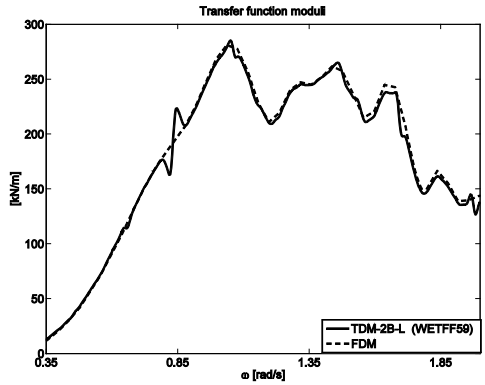

Figure 13 Comparison of transfer function modulus curves for the global lateral shear force (F_y) given by the FDM and TDM-2B-L (based on the "WETFF59"), subjected to 90-degree-wave

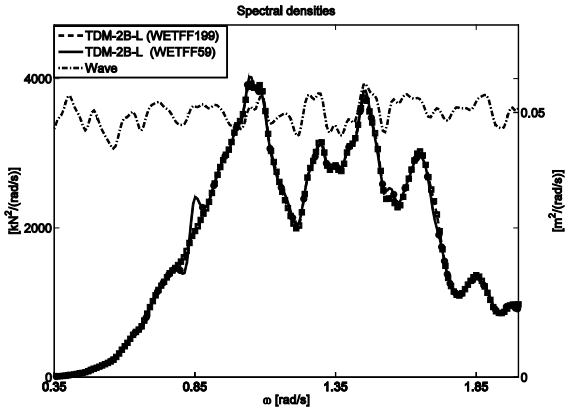

Figure 14 Spectral densities of the global lateral shear force (F_y) calculated by the TDM-2B-L based on the "WETFF59" and "WETFF199". Wave direction is 90-degree. The circles and squares on the curves represent the set of the 59 selected frequencies and set of the 199 selected frequencies respectively.

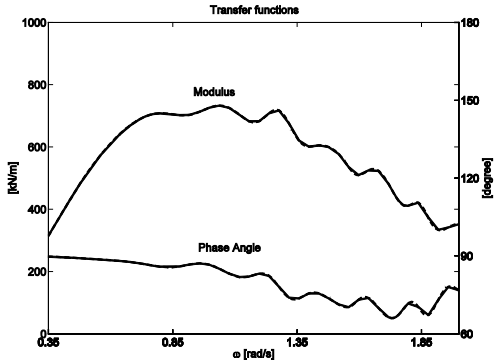

Figure 15 Moduli and phase angles of transfer functions of wave to lateral wave excitation force on the "PartA", subjected to 90-degree-wave. The solid lines represent the moduli and phase angles corresponding to the set of the 59 selected frequencies. The dashed lines represent the moduli and phase angles corresponding to the set of the 199 selected frequencies.

4.2 Comparison B and Comparison C

Ten combined wind and wave conditions are selected from a site in northern North Sea [34] and tabulated in Table 4. The combined wind and wave conditions are composed of five different mean wind speeds covering the below rated, at rated, above rated and parked wind speed and two wave directions. In addition, we also looked at wave only conditions by removing the winds from the combined conditions. For each condition, one 1-hour time-domain simulation is carried out in the TDM-1B-C, TDM-2B-N and TDM-29B-N respectively. Identical random seeds are used to eliminate stochastic uncertainties. Responses, i.e. the pitch angle of each blade, azimuth angle and rotational speed of the rotor, aerodynamic forces and moments on the rotor, torque on the rotational shaft of the drive train, generator torque, generated power, global forces and moments in a given cross section of the tower, global rigid-body motions of the hull and mooring line tension at the top end (fairlead) of each mooring line, are calculated and compared.

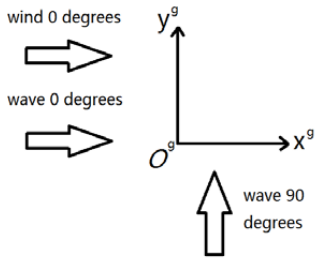

Figure 16 Definition of the directions of wind and waves.

Table 4 Environmental conditions

Environmental conditions	Mean wind speed at nacelle height [m/s]	Turbulence intensity [%]	H_s [m]	T_p [s]	Wave direction [degree]	Note
EC01000	4.9	23	4.6	8	0	Wind turbine in operation; Two-parameter JONSWAP spectrum
EC01090	4.9	23	4.6	8	90	
EC02000	8.0	17	5.2	8	0	
EC02090	8.0	17	5.2	8	90	
EC03000	11.0	15	5.7	8	0	
EC03090	11.0	15	5.7	8	90	
EC04000	16.5	13	6.5	8	0	
EC04090	16.5	13	6.5	8	90	
EC05000	34.6	11.1	8.7	9	0	Wind turbine parked; Two-parameter JONSWAP spectrum
EC05090	34.6	11.1	8.7	9	90	

Results and discussions with respect to the Comparison B are given as follows:

The responses of the TDM-1B-C and TDM-2B-N subjected to the wave only conditions are firstly compared. We find that the responses are identical to each other (the difference is negligible). Part of the realization of the fore-aft bending moment at the tower base, in EC02000 (wave only), is given as an example, see Figure 17.

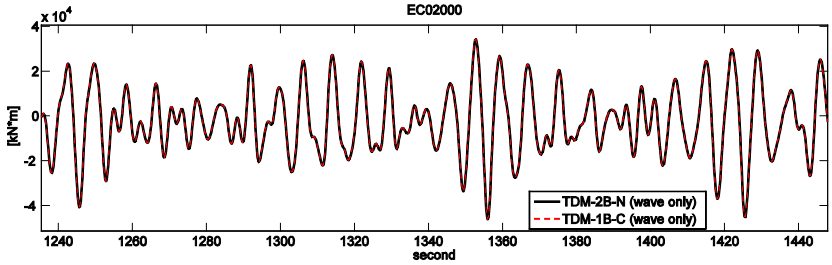

Figure 17 An example of the time series of the fore-aft bending moment at the tower base of the TDM-1B-C and TDM-2B-N, EC02000 (wave only)

Then, the responses of the TDM-1B-C and TDM-2B-N subjected to the combined wind and wave conditions are compared. When the relative wind speed at the hub is below the rated speed, the generator torque and rotational speed of the rotor will be adjusted by the controller to optimize the power generation. A slightly numerical difference in the TDM-1B-C and TDM-2B-N can result in slightly differences (phase shift) in the azimuth angle and rotational speed of the rotor. The differences will be accumulated with development of simulation time and result in developing differences in the aerodynamic loads on the rotor, global forces and moments at the tower base and mooring line tensions at the fairleads. As shown in Figures 18 and 19, the realizations of the azimuth angle of the TDM-1B-C and TDM-2B-N are identical at the beginning but the phase shift is accumulated with the development of the simulation time. The differences induced by the phase shift have very limited effects on the realizations of the rigid-body motions of the hull and spectra of the global forces and moments at the tower base, mooring line tensions and rigid-body motions. Spectral densities of the fore-aft bending moment at the tower base of the TDM-1B-C and TDM-2B-N are given in Figure 20 as an example.

For EC04000 and EC04090, the relative wind speed at nacelle is always above the rate speed. Therefore, the generator torque is constant and azimuth angles of TDM-1B-C and TDM-2B-N are in phase. Very slightly difference exists in the responses, see Figure 21 as an example. The difference is induced by very slightly numerical difference in pitch actuator control. Identical responses can be obtained if the control model is removed from the TDM-1B-C and TDM-2B-N. In EC05000 and EC05090, where the wind turbine is parked, identical responses are observed.

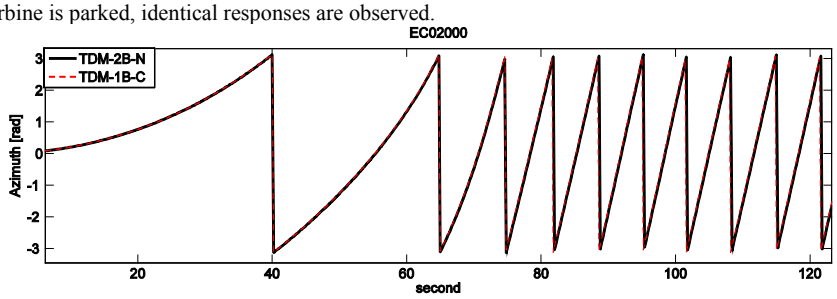

Figure 18 An example of the time series of the azimuth angle of the TDM-1B-C and TDM-2B-N, EC02000

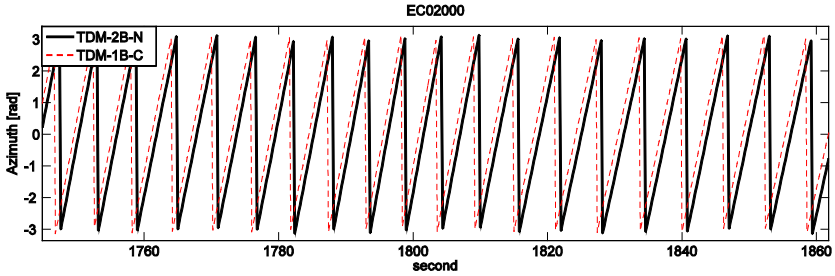

Figure 19 An example of the time series of the azimuth angle of the TDM-1B-C and TDM-2B-N, EC02000

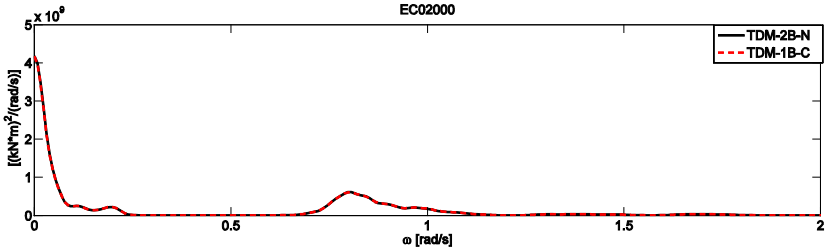

Figure 20 Spectral densities of the fore-aft bending moment at the tower base of the TDM-1B-C and TDM-2B-N, EC02000

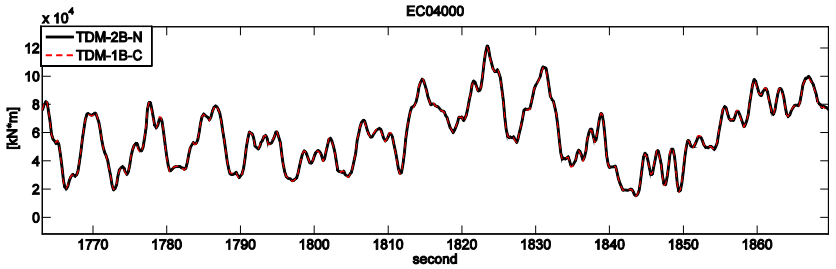

Figure 21 An example of the time series of the fore-aft bending moment at the tower base of the TDM-1B-C and TDM-2B-N, EC04000

Results and discussions with respect to the Comparison C are given as follows:

We compare the responses of the TDM-2B-N and TDM-29B-N in wave only and in combined wind and wave conditions. Observations of the comparisons of the responses of the RNA, tower and mooring lines of the TDM-2B-N and TDM-29B-N are similar to the observations of the comparison of the TDM-1B-C and TDM-2B-N which have been illustrated in above.

Therefore, we focus on discussions with respect to the global forces and moments in the cross-section shown in the Figure 5. As mentioned in above, the global forces and moments in the cross-section (the dashed line) are described in the O^{inp}-x^{inp}-y^{inp}-z^{inp} coordinate system and are denoted as F_x, F_y, F_z, M_x, M_y, and M_z. For each condition, time realizations of the global forces and moments of the TDM-2B-N and TDM-29B-N are in phase and almost identical. An example is given in Figure 22.

When the floating wind turbine is located in calm water without wind loads, the global forces and moments in the hull are static and are determined by the gravity and hydrostatic pressures forces on the floating wind turbine. We find the difference in the static loads calculated by the TDM-2B-N and TDM-29 and the analytical solution is less than 1%.

Figure 23 and 24 show the spectral densities of the M_y (bending moment) of the TDM-2B-N and TDM-29B-N in EC01000, EC02000, EC03000, EC04000 and EC05000. We do not observe any high frequency responses (in the frequency range 2 rad/s to 4 rad/s). The peaks of the density curves in the frequency range 0.5 rad/s to 2rad/s correspond to the T_p of the wave spectrum, while, in the operational conditions, considerable low-frequency (from 0 rad/s to 0.3 rad/s) components can be observed. The standard deviation of the M_y, for example, in EC03000 with combined wind and waves is 21.4 MN*m, while the standard deviation of the M_y in EC03000 with waves only is 15.2 MN*m. The relative difference is 41%.

In the low frequency range, the global forces and moments in the structural components of the hull are sensitive to fluctuations of the hydrostatic pressure forces on the structural components. This is because: 1) the aerodynamic loads on the RNA and tower can excite significant rotational motions (e.g. roll and pitch) in particular in the low frequency range comparing to the motions excited by the wave excitation loads on the hull, while the first order terms of the fluctuations of the hydrostatic pressure forces are proportional to the motions; 2) wave excitation loads are expected to be small since wave energy is expected to be very limited (except for swell) in the low-frequency range; and 3) inertia and radiation loads are proportional to the first order derivative (velocity) and second order derivative (acceleration) of the motions and are expected to be small in the low-frequency range.

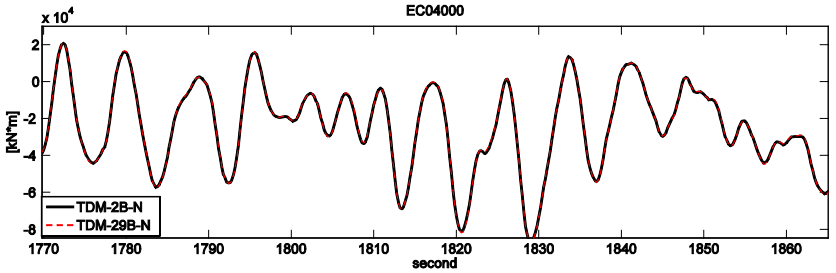

Figure 22 An Example of the time series of the M_y (bending moment) of the TDM-2B-N and TDM-29B-N, EC04000

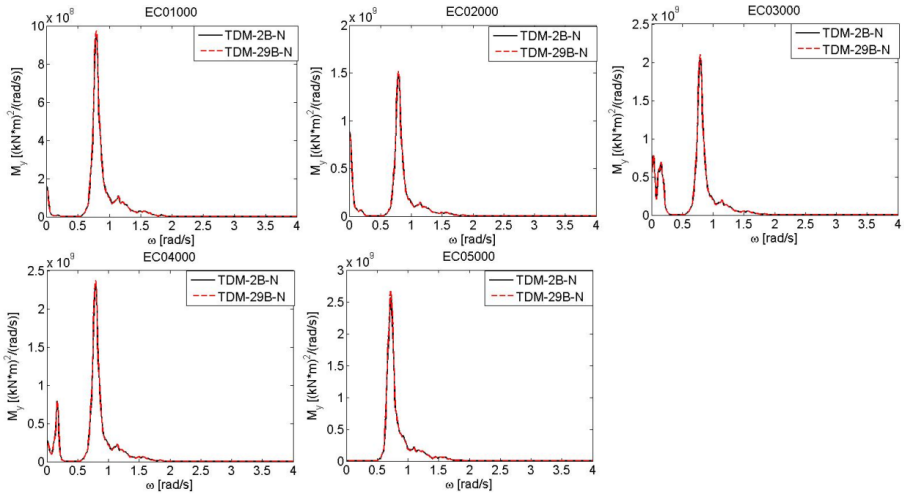

Figure 23 Spectral densities of the M_y (bending moment) of the TDM-2B-N and TDM-29B-N in EC01000, EC02000, EC03000, EC04000 and EC05000

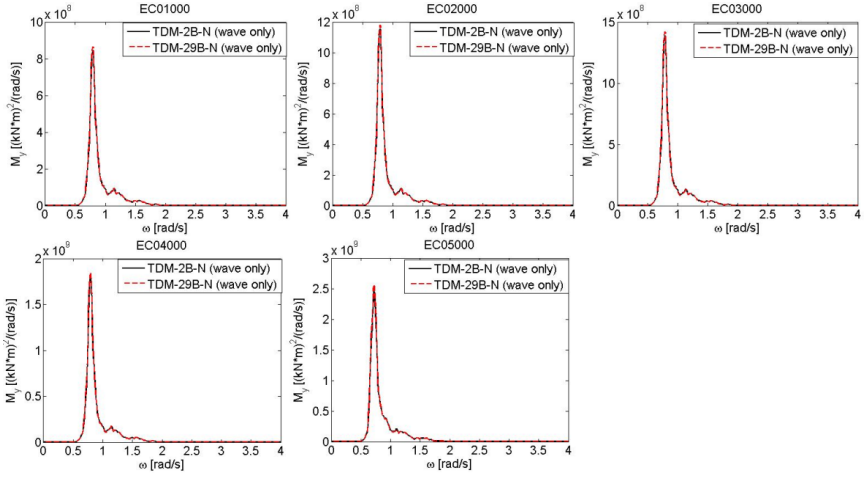

Figure 24 Spectral densities of the M_y (bending moment) of the TDM-2B-N and TDM-29B-N in EC01000, EC02000, EC03000, EC04000 and EC05000 (wave only)

5 Conclusions

The present paper deals with the development and verification of a time-domain approach that can be easily implemented in various state-of-the-art computer codes to extend their capabilities to analyze global forces and moments in structural components of a generic floater subject to linear and non-linear environmental loads from wind and waves. The global forces and moments in the structural components might be used as inputs of design formulas for structural strength design checks and/or used as boundary conditions in a sub-model finite element analysis to determine structural responses such as stresses, etc.

The proposed approach focuses on the modeling of the inertia and external loads on the hull and the mapping of the loads in the finite element model of the hull. In the proposed approach, floating wind turbines are considered as an assemblage of several structural components. The conventional hybrid frequency-time domain approach is extended to model the external loads on and inertia loads of each structural component. Hydrodynamic loads on each structural component are obtained by integrating the pressure loads that are obtained by solving the linear hydrodynamic problem with the assumption that the hull is a rigid-body. The kinematics of different structural components is constrained by the rigid-body assumption. The proposed approach does not account for hydroelasticity effects. The expressions of the hydro loads on each structural component can be further modified to

account for, for example, second order and/or higher order hydro loads on each structural component. Beam elements are used to represent the global stiffness of the structural components but the proposed approach can be further extended to use other finite element models to represent the stiffness of the structural components.

So far, the proposed approach has been implemented in the computer code Simo/Riflex/Aerodyn to analyze global forces and moments in the hull of a semi-submersible wind turbine. Responses calculated by the numerical models that implement the proposed approach and obtained by the reference models are compared step by step. The agreements are very good. Accuracy of the proposed approach needs to be further checked by sensitivity studies and by comparison to the model test data.

In the operational conditions, considerable low-frequency components can be observed in the spectra of the obtained global forces and moments in the pontoons of the reference floating wind turbine. The results indicate that the low-frequency aerodynamic loads, the fluctuations of the hydrostatic pressure forces and the fluctuations of the gravity loads of floating wind turbines are important contributions to the structural responses, in particular, in the low-frequency range. This feature needs to be further investigated by experimental studies.

ACKNOLEDGEMENT

The authors acknowledge the financial support provided by the Research Council of Norway through the Centre for Ships and Ocean Structures; the Norwegian Research Centre for Offshore Wind Technology (NOWITECH), NTNU; and the Centre for Autonomous Marine Operations and Systems (AMOS), NTNU.

REFERENCE

[1] Jonkman J., (2010), "Definition of the Floating System for Phase IV of OC3", NREL/TP-500-47535, National Renewable Energy Laboratory, Golden, CO, USA.

[2] Nielsen, F. G., Hanson, T. D., and Skaare, B., (2006), "Integrated Dynamic Analysis of Floating Offshore Wind Turbines," Proceedings of the 25th International Conference on Offshore Mechanics and Arctic Engineering, OMAE2006-92291, Hamburg, Germany.

[3] Bachynski EE, Moan T., (2012), "Design considerations for tension leg platform wind turbines.", Marine Structures, Vol 29, pp 89-114.

[4] Matha, D., (2009), "Model development and loads analysis of an offshore wind turbine on a tension leg platform, with a comparison to other floating turbine concepts". Master's thesis, University of Colorado-Boulder, April.

[5] Moon III, W. L., and Nordstrom, C. J., (2010), "Tension leg platform turbine: A unique integration of mature technologies", In Proceedings of the 16th Offshore Symposium, Texas Section of the Society of Naval Architects and Marine Engineers, pp. A25-A34.

[6] Henderson, A. R., Argyriadis, K., Nichos, J., and Langston, D., (2010), "Offshore wind turbines on TLPs - assessment of floating support structures for offshore wind farms in German waters". In 10th German Wind Energy Conference, Bremen, Germany.

[7] Sclavounos, P., Tracy, C., and Lee, S., (2007), "Floating offshore wind turbines: responses in a seastate; Pareto optimal designs and economic assessment", Tech. rep., Department of Mechanical Engineering, Massachusetts Institute of Technology.

[8] Botta, G., Casale, C., Lembo, E., Serri, L., and Viani, S., (2009), "Resource and technology assessment for evaluating Italy's offshore wind energy potential", In 2009 International Conference on Clean Electrical Power, Capri, Italy, pp. 507 -513.

[9] Stewart, G., Lackner, M., Robertson, A., Jonkman, J., and Goupee, A., (2012), "Calibration and validation of a FAST floating wind turbine model of the DeepCwind scaled tension-leg platform", In Twenty-Second International Offshore and Polar Engineering Conference, Rhodes, Greece, Vol. 1, pp. 380-387, no. NREL/CP-5000-54822.

[10] Roddier, D., Cermelli, C., Aubault, A., and Weinstein, A., (2010), "WindFloat: A floating foundation for offshore wind turbines", Journal of Renewable and Sustainable Energy 2, 033104, doi:10.1063/1.3435339.

[11] Roddier, D., Peiffer, A., Aubault, A., and Weinstein, J., (2011), "A generic 5 MW WindFloat for numerical tool validation & comparison against a generic spar", In 30th International Conference on Ocean, Offshore and Arctic Engineering, no, OMAE2011-50278, Rotterdam, the Netherlands.

[12] Robertson, A., Jonkman, J., Masciola, M., Song, H., Goupee, A., Coulling, A., and Luan C., (2012), "Definition of the Semisubmersible Floating System for Phase II of OC4", Offshore Code Comparison Collaboration Continuation (OC4) for IEA Task 30.

[13] Huijs, F., Mikx, J., Savenije, F., and Ridder, E., (2013), "Integrated design of floater, mooring and control system for a semisubmersible floating wind turbine", European Wind Energy Association (EWEA) Offshore, Frankfurt.

[14] Dr.techn.Olav Olsen AS, (2016), http://www.olavolsen.no/en/node/17, accessed 2nd.May.2016.

[15] Luan, C., Gao, Z., and Moan, T., (2016). "Design and analysis of a braceless steel 5-mw semi-submersible wind turbine". Proceedings of the 35th International Conference on Ocean, Offshore and Arctic Engineering, OMAE2016-54848, Busan, Korea, June 19–24.

[16] Viselli, A. M., Goupee, A. J., and Dagher, H., (2014), "Model Test of a 1:8 Scale Floating Wind Turbine Offshore in the Gulf of Maine", In 33th International Conference on Ocean, Offshore and Arctic Engineering, no, OMAE2014-23639, San Francisco, CA, USA.

[17] The HiPRWind project, (2016), http://hiprwind.eu/, accessed 2nd.May.2016.
[18] Amlashi, H. K.K., and Moan, T, (2008), "Ultimate Strength Analysis of a Bulk Carrier Hull Girder under Alternate Hold Loading—A Case Study, Part 1: Nonlinear Finite Element Modeling and Ultimate Hull Girder Capacity," Marine Structures, Vol 21, pp 327–352.
[19] DNV, (2010), "Recommended Practice – Buckling strength of plated structures", DNV-RP-C201, Det Norske Veritas.
[20] Standards Norway, (2004), "Design of steel structures", NORSOK STANDARD N-004, Standards Norway.
[21] Nejad, A.R., Bachynski, E.E., Kvittem, M.I., Luan, C., Gao, Z. and Moan, T., (2015), "Stochastic Dynamic Load Effect and Fatigue Damage Analysis of Drivetrains in Land-based and TLP, Spar and Semi-Submersible Floating Wind Turbines", Marine Structures, Vol 42, pp 137–153.
[22] Robertson, A., Jonkman, J. Qvist, J.,Chen, X., Armendariz,J.A., Soares, C.G., Luan, C., Huang, Y., Yde, A.,Larsen, T., Nichols, J., Lei, Liu, Maus, K.J., Godreau, C., Heege, A., Vatne, S.R., Manolas,D., Qin, H., Riber, H., Abele, R., Yamaguchi, A., Pham,A. Alves,M., Kofoed-Hansen,H., (2014), " Offshore code comparison collaboration, continued: phase II results of a floating semisubmersible wind system", In Proceedings of the 33rd International Conference on Ocean, Offshore and Arctic Engineering, no. OMAE2014-24040, San Francisco, USA, 2014.
[23] Faltinsen, O.M., (1990), "*Sea loads on ships and offshore structures*", Cambridge University Press, UK.
[24] Kvittem, M.I., Bachynski, E.E. and Moan, T., (2012), "Effects of Hydrodynamic Modelling in Fully Coupled Simulations of a Semi-Submersible Wind Turbine", Energy Procedia. 2012; 24: 351-362. doi:10.1016/j.egypro.2012.06.118.
[25] Naess, A. and Moan, T., (2013), "*Stochastic dynamics of marine structures*", Cambridge University Press, UK.
[26] DNV, (2013), SESAM User Manual HydroD.
[27] MARINTEK, (2011). SIMO User's Manual.
[28] MARINTEK, (2013). RIFLEX User's Manual.
[29] Ormberg, H., Passano, E., and Luxcey, N., (2011), "Global analysis of a floating wind turbine using an aero-hydro-elastic model. Part 1: Code development and case study". In 30th International Conference on Ocean, Offshore, and Arctic Engineering,no, OMAE2011-50114, Rotterdam, Netherlands.
[30] Luxcey, N., Ormberg, H., and Passano, E., (2011), "Global analysis of a floating wind turbine using an aero-hydro-elastic numerical model. Part 2: Benchmark study". In 30th International Conference on Ocean, Offshore, and Arctic Engineering,no, OMAE2011-50088, Rotterdam, Netherlands.
[31] Ormberg, H., and Bachynski, E. E., (2012). "Global analysis of floating wind turbines: Code development, model sensitivity and benchmark study". In 22nd International Ocean and Polar Engineering Conference, Vol. 1, pp. 366–373.
[32] Moriarty, P. J., and Hansen, A. C., (2005), AeroDyn theory manual, Tech. Rep, NREL/TP-500-36881.
[33] DNV, (2010), "Recommended Practice - Environmental Conditions and Environmental Loads", DNV-RP-C205, Det Norske Veritas.
[34] Li, L., Gao, Z., Moan, T., (2015), "Joint Distribution of Environmental Condition at Five European Offshore Sites for Design of Combined Wind and Wave Energy Devices", Journal of Offshore Mechanics and Arctic Engineering. 137(3), 031901 (16 pages). doi: 10.1115/1.4029842.
[35] Cordle, A., and Jonkman, J., (2011), "State of the art in floating wind turbine design tools", Proceedings of the 21st International Offshore and Polar Engineering Conference, Maui, Hawaii, USA. Vol. 1, pp. 367–374.
[36] Matha, D., Schlipf, M., Cordle, A., Pereira, R., and Jonkman, J., (2011), "Challenges in Simulation of Aerodynamics, Hydrodynamics, and Mooring-Line Dynamics of Floating Offshore Wind Turbines," Proceedings of the 21st International Offshore and Polar Engineering Conference, Maui, Hawaii, USA, Vol. 1, pp. 421–428.
[37] Kvittem, M.I.and Moan, T., (2015). "Time domain analysis procedures for fatigue assessment of a semi-submersible wind turbine". Marine Structures. Vol 40, pp 38–59.
[38] IEC, (2005), "Wind turbines – Part 1: Design requirements", IEC-61400-1, International Electrotechnical Commission.
[39] IEC, (2009), "Wind turbines: Part 3: Design requirements for offshore wind turbines", IEC-61400-3, International Electrotechnical Commission.
[40] Karimirad, M., and Moan, T., (2012),"Wave and wind induced dynamic response of a spar-type offshore wind turbine", J. Waterw. Port Coast Ocean Eng, 138 (1) , pp. 9–20
[41] Bae, Y.H. and Kim, M.H. (2014), "Coupled dynamic analysis of multiple wind turbines on a large single floater", J. Ocean Eng., 92, 175-187.
[42] Bagbanci, H. , Karmakar, D. , and Guedes Soares, C. , (2015), " Comparison of Spar-Type and Semi-Submersible Type Floaters Concepts of Offshore Wind Turbines Using Long-Term Analysis," ASME J. Offshore Mech. Arct. Eng., 137(6), p. 061601.
[43] Moan, T., (2015), "Recent development of analysis and design of offshore wind turbines for deep water". Renewable Energies Offshore - 1st International Conference on Renewable Energies Offshore, RENEW 2014,
Lisbon, Portugal.
[44] Debruyne, Y., Alves, M., and Sarmento, A., (2015), "Efficient time-domain simulation of the performances of a floating offshore wind farm", Renewable Energies Offshore - 1st International Conference on Renewable Energies Offshore, RENEW 2014, Lisbon, Portugal.

[45] Mazarakos, T.P., Manolas, D.I., Grapsas, T., Mavrakos, S.A., Riziotis, V.A., and Voutsinas, S.G., (2015), "Conceptual design and advanced hydro-aero-elastic modeling of a TLP concept for floating wind turbine applications", Renewable Energies Offshore - 1st International Conference on Renewable Energies Offshore, RENEW 2014, Lisbon, Portugal.
[46] Bachynski, E.E., Etemaddar, M., Kvittem, M.I., Luan, C., Moan, T., (2013) "Dynamic analysis of floating wind turbines during pitch actuator fault, grid loss, and shutdown", Energy Procedia vol. 35, 210-222. doi:10.1016/j.egypro.2013.07.174
[47] Bachynski, E.E., (2014). "Design and Dynamic Analysis of Tension Leg Platform Wind Turbines", Ph.D thesis, Norwegian University of Science and Technology, Trondheim, Norway

A.2 Paper A2

Paper A2:

Experimental validation of a time-domain approach for determining sectional loads in a floating wind turbine hull subjected to moderate waves

Chenyu Luan, Valentin Chabaud, Erin E. Bachynski, Zhen Gao and Torgeir Moan

Published in Energy Procedia, Volume 137, Pages 366-381,
https://doi.org/10.1016/j.egypro.2017.10.361

Available online at www.sciencedirect.com

ScienceDirect

Energy Procedia 00 (2017) 000–000

Energy Procedia

www.elsevier.com/locate/procedia

14th Deep Sea Offshore Wind R&D Conference, EERA DeepWind'2017, 18-20 January 2017, Trondheim, Norway

Experimental validation of a time-domain approach for determining sectional loads in a floating wind turbine hull subjected to moderate waves

Chenyu Luan[a,b,c,*], Valentin Chabaud[d], Erin E. Bachynski[b,c,d], Zhen Gao[b,c,d], Torgeir Moan[a,b,c,d]

a Norwegian Research Centre for Offshore Wind Technology, Norway
b Centre for Ships and Ocean Structures, NTNU, Otto Nielsens veg 10, Trondheim, Norway, NO-7491
c Centre for Autonomous Marine Operations and System, NTNU, Otto Nielsens veg 10, Trondheim, Norway, NO-7491
d Department of Marine Technology, Norwegian university of science and technology (NTNU), Otto Nielsens veg 10, Trondheim, Norway, NO-7491

Abstract

To achieve cost-effective and reliable structural design of floating wind turbines, efficient and accurate time domain numerical approaches are required to analyse structural responses in design conditions, e.g. wind and waves. This paper focuses on validation of a time-domain numerical approach for determining forces and moments in structural components of floaters. The approach considers floating wind turbines as a system of several structural components, e.g. blades, rotational shaft, nacelle, tower, mooring lines, columns, pontoons and braces. A finite element model is developed to represent global stiffness of the structural components. The external and inertia loads on the structural components are modelled as distributed loads. Hydrodynamic loads on each structural component are derived from the corresponding hydrodynamic coefficients obtained by solving the first order boundary value problem using WAMIT. A 1:30 scaled braceless semi-submersible model test which implements the ReaTHM® testing approach was done by SINTEF Ocean, formerly MARINTEK, in its ocean basin. Measurements of the global forces and moments at the base of a side column of the model and rigid-body motions of the model are compared to the corresponding simulations. This paper focuses on responses in moderate waves for which linear hydrodynamic loads are applicable. Differences in the corresponding simulations and measurements are found to be small, while possible reasons, e.g. synchronizations, non-linear effects, and uncertainties in the measurements and simulations, for the differences are analysed. Essential information about the model test, descriptions of the numerical models, calibrations and results and discussions of the validation are given in this paper.

Peer-review under responsibility of SINTEF Energi AS.

Keywords: Semi-submersible wind turbine; Sectional loads; Experimental validation; Numerical simulation; Moderate waves

* Corresponding author. Tel.: +47-73595513
E-mail address: Chenyu.luan@ntnu.no

1. Introduction

Innovative floating wind turbine concepts are considered an attractive solution for harvesting offshore wind energy in relatively deep water, e.g. deeper than 80 m. The offshore wind industry is moving from pilot prototype field tests to pilot commercial size floating wind farms while structural optimization for cost reduction is a focus of these pilot projects [1, 2].

In general, a floating wind turbine is composed of a rotor nacelle assembly (RNA), a tower, a hull, and a mooring system. Many concepts, e.g. [3-9], have been proposed. These concepts can be classified as spar [3, 4], TLP [5, 6] and semi-submersible wind turbines [7-9].

Floating wind turbines operate in wind, current and waves which result in dynamic motions around mean offsets and structural responses. Limit states with respect to the motions and structural responses are specified in design standards of floating wind turbines, e.g. DNV-OS-J103, ABS #195 and ClassNK guideline [10-12], to make sure that the developed designs will have acceptable stability and structural strength. Consequently, designers must implement appropriate approaches, e.g. numerical simulations and/or model tests, to demonstrate that the designs satisfy the specified requirements and criteria.

Frequency-domain computer codes, e.g. WADAM [25], are widely used in the offshore oil and gas industry to efficiently analyse wave induced rigid-body motions and hydro-pressure forces on mean wetted body surface of a floating unit. The hydro-pressure forces can be used in a finite element analysis [25] to efficiently determine structural responses such as stresses, etc. If the unit has a hull, which is a statically determinate structure, global forces and moments in the hull can be obtained by integrating external and inertia loads which are acting on the corresponding structural components of the hull. Meanwhile, frequency-domain computer codes, e.g. Turbu Offshore [30], are capable of efficient optimizations for designs of offshore bottom-fixed wind turbines. However, validity of the linearized approximations used in the frequency-domain codes must be appropriately checked, in particular for novel designs of floating wind turbines. While we still need to use time-domain simulations and model tests to shed more light on the aero-hydro-servo-elastic feature [13]. Another limitation is that frequency-domain models cannot be used to account for transient loading events, e.g. wind turbine faults. Kvittem and Moan [31] studied a frequency-domain method for estimating short-term tower base bending moments and tower fatigue damage of a semi-submersible wind turbine. In the frequency-domain method, responses to combined wind and wave loads are obtained by superposing responses to separated wind and wave loads. The frequency-domain method was used in a case study to predict bending moments and fatigue damage in tower base of a reference semi-submersible wind turbine in combined wind and wave loads. Predicted results given by carrying out a fully coupled, nonlinear time-domain analysis are considered as reference values. Comparing to the reference values, the fatigue damage predicted by the frequency-domain method were underestimated by 0-60%, corresponding to discrepancies in standard deviations of stress in the order of 0–20%.

Conventional time-domain computer codes [14] focus on simulating global responses of the RNA, tower, and mooring system, and rigid-body motions of floating wind turbines. Finite element models for floating wind turbines are generated and solved in these computer codes. A review of conventional approaches for modelling aerodynamic loads on the RNA and tower and hydro loads on the hull and mooring lines is available in [15]. Morison formula and/or the conventional hybrid frequency-time domain approach [16] are used to model hydro loads on the floating wind turbine's hull. The hull is modelled as a rigid-body with 6 d.o.f.s in the time-domain finite element model, while the conventional hybrid frequency-time domain approach gives integrated forces/moments in 6 d.o.f.s rather than distributed forces and moments. Consequently, sectional forces and moments in the hull cannot be captured in a straightforward manner. A straightforward manner means that the sectional forces and moments can be directly obtained from time-domain simulations and used for design check. This is in contrast to the approach for which a global motion response analysis must be carried out first and then the external aero- and hydro- dynamic loads as well as the inertial loads are applied in a structural analysis of the floater for design check.

Luan et al [16] developed an approach for determining forces and moments in floaters. The approach can be easily implemented in various state-of-the-art computer codes for wind turbine analysis, e.g. Simo/Riflex/Aerodyn, OrcaFlex and FAST+CHARM3D, to extend their capabilities to analyse sectional forces and moments in structural components of a generic floater. The sectional forces and moments in the structural components might be used as input to design formulas for structural strength design checks and/or used as boundary conditions in a sub-model finite element analysis. More details with respect to the difference between the developed approach and conventional approaches, as well features and limitations, can be found in [16].

We intend to, step by step, validate the approach of Luan et al [16] by using measurements of a 1:30 model test of a braceless semi-submersible wind turbine [9] which has been tested in the ocean basin of MARINTEK, now SINTEF Ocean.

In this paper, we focus on comparisons of the responses of the semi-submersible wind turbine in moderate waves with less non-linear effects for which frequency-domain commercial computer codes, e.g. WAMIT, WADAM, can be used as a reference model. Wave-induced transfer functions for rigid-body motions and fore-aft and side-to-side bending moments in base of a side column derived from time-domain and frequency-domain simulations and measurements are compared. The developed time-domain model is expected to give the same results as the commercial computer codes, while the time-domain model can be further used to analyze the sectional forces and moments in the hull in combined wind and wave loads in a straightforward manner but the frequency-domain codes cannot.

The "model-the-model" principle, which means to simulate the actual model tests as closely as possible [17, 18], is used. Uncertainties exist in the measurements, e.g. mass matrices, position of centre of gravity of each component and positions of the anchors. Consequently, necessary calibrations with respect to some inputs of the numerical models are carried out. All numerical results are given by the numerical models with calibrated inputs.

Essential information of the model test, i.e. coordinate systems, measured model properties, environmental conditions and post-processing approach for the measurements, is given in section 2. More details with respect to the model test are referred to [19-21]. The developed numerical models are described in section 3. Calibrations are presented in section 4. Analyses and discussions of the results are available in section 5.

2. The floating wind turbine concept and model test

A layout of the experimental model and definitions of the direction of the wind and waves are shown in Figure 1 in a global Earth-fixed coordinate system (O^g-x^g-y^g-z^g). O^g is at the geometrical center of the water plane area when the model is in calm water. Mass properties and dimensions of the semi-submersible wind turbine are described in a body-fixed coordinate system (O^b-x^b-y^b-z^b) The O^b-x^b-y^b-z^b coordinate system is coincident to the global coordinate system when the model is in calm water. Note that all the data and results presented and discussed in this paper are given in full scale and in the corresponding coordinate systems described in this paper. A linear scaling factor of $\lambda = 30$ and the Froude scaling law are used to scale the original data measured from the model test.

The specified dimensions of the semi-submersible hull are tabulated in Table 1 and shown in Figure 2. As shown in Figure 2, a column which includes two flanges is used to connect "Side column 1" to "Pontoon 1". Fore-aft and side-to-side bending moments in a cross section of the column are measured by strain gauges. The geometric centre of the cross section is (41, 0, -27) in the body-fixed coordinate system. The cross section splits the model into two parts. The part which includes the "Side column 1" is denoted as Part A while the rest is denoted as Part B. Measured mass properties are given in Table 2.

The mooring system is composed of three catenary chain mooring lines with lead wires added for weight correction. Distributions of mass and buoyancy of the mooring lines are made according to a design of the mooring system for which each line has two segments from the fairlead to anchor with constant solid circular cross-section. The design parameters are given in Table 3 and 4. According to the Froude scaling law, the scaled value of the Young's modulus of the mooring lines of the experimental model is $6.3 * 10^9$ kN/m^2.

Environmental conditions of the model tests, for which the results are discussed in this paper, are tabulated in Table 5. In addition, some model tests, e.g. the pull-out tests, decay tests and turbulent wind only tests, are used to calibrate the numerical models.

In the tests with the experimental model, wave elevation at Pos1, see Table 6, was measured and denoted as WAVE1 while in the calibration tests (without the experimental model) wave elevations at Pos1, Pos2 and Pos3 were measured and denoted as WAVE1c, WAVE2c and WAVE3c, respectively. Full-scale horizontal locations of the wave probes in the global coordinate system are given in Table 6.

Table 1. Specified dimensions of the semi-submersible hull (Full-scale)

Central column diameter [m]	6.5
Side column diameter [m]	6.5

Pontoon height [m]	6
Pontoon width [m]	9
Central column freeboard [m]	10
Side column freeboard [m]	20
Centre-to-centre (central to side column) [m]	41
Centre-to-edge (central column to pontoon end) [m]	45.5
Operating draft [m]	30
Displacement [tonne]	10,555

Table 2 Measured mass properties of the experimental model. The center of gravity is described in the body-fixed coordinate system with respect to O^b. The moments of inertia are about the center of gravity.

	Mass [tonnes]	Centre of gravity [m]			Moments of inertia [tonnes*m^2]					
		x^b	y^b	z^b	I_{xx}	I_{yy}	I_{zz}	I_{xy}	I_{xz}	I_{yz}
Complete model	9,730	0	0	-19.05	10297582	10297582	7641621	0	0	0
Part A	456.7	41	0	-12.93	96093	96093	2193	0	0	0

Table 3. Design parameters of a single mooring line

Segment	Length (m)	Mass per length (kg/m)	Wet weight (kN/m)	Specified diameter (m)
Upper	240.00	235.0	2.005	0.195
Lower	367.55	446.0	3.804	0.269

Table 4. Arrangement of the mooring line anchors and fairleads described in the global coordinate system

Fairlead	x^g	y^g	z^g	Anchor	x^g	y^g	z^g
1	45.95	0	-27	1	603	0	-200
2	-22.98	39.8	-27	2	-301.5	522.2	-200
3	-22.98	-39.8	-27	3	-301.5	-522.2	-200

Table 5 Environmental conditions of selected model tests

Reference No.	H_s [m]	[s]	Wave direction [degree]	Model test duration [hour]	Note
2310	2	Period range:3.5-22	0	3	Pink noise tests
2321	4	Period range: 4.5-22			
2420	3.6	T_p: 10.2	0	3	JONSWAP spectrum

Table 6 Wave probe position in calibration (in the O^g-x^g-y^g-z^g coordinate system)

	x^g (m)	y^g (m)
Pos1	-187.5	-94.2
Pos2	0	0
Pos3	0	-94.2

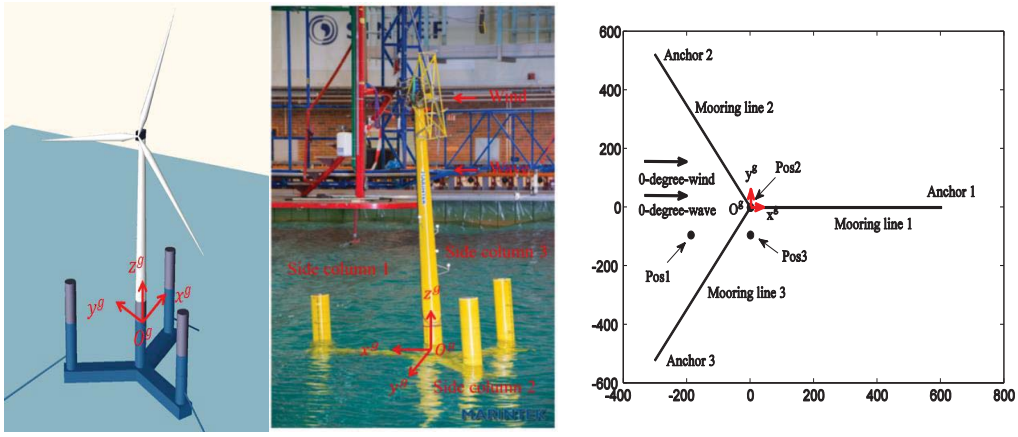

Figure 1 Layout of the experimental model

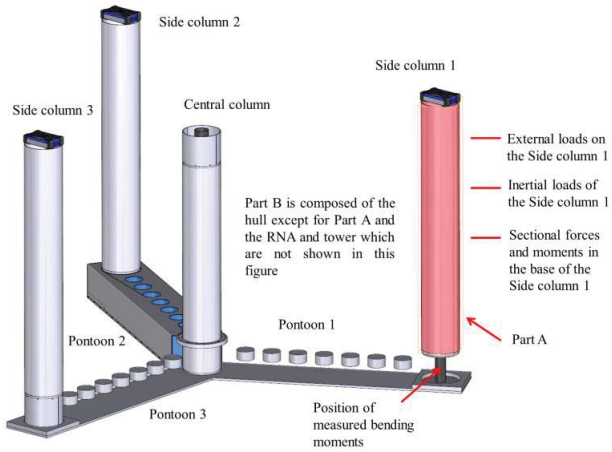

Figure 2 A layout of the hull of the experimental model, courtesy of Fredrik Brun (SINTEF Ocean). Note that the configurations of the three pontoons are identical. Some parts of the configurations of Pontoon 1 and 3 are not shown.

3. Numerical methods and models

A time-domain model (TDM) and a frequency-domain model (FDM) are developed to calculate the forces and moments in the aforementioned cross section for which the geometric center of the cross section is (41, 0, -27) in the O^b-x^b-y^b-z^b coordinate system. The forces and moments are denoted as F_x, F_y, F_z, M_x, M_y, and M_z and described in a body-fixed coordinate system (O^{inp}-x^{inp}-y^{inp}-z^{inp}) with respect to O^{inp}. The O^{inp}-x^{inp}-y^{inp}-z^{inp} and O^b-x^b-y^b-z^b coordinate systems are coincident except that O^{inp} is located at (41, 0, -27) in the O^b-x^b-y^b-z^b coordinate system. M_x and M_y correspond to the side-to-side and fore-aft bending moments, respectively.

3.1. TDM

We denote the Simo/Riflex [43, 44] time-domain finite element model for calculating sectional forces and moments in the cross-section between Parts A and B as TDM.

The finite element model is generated in Riflex in the global coordinate system. The model is composed of 183 truss elements for modelling the three mooring lines, three artificial beam elements for capturing the sectional forces and moments in the cross-section and two control nodes for modelling external and inertial loads on the Parts A and B.

The approach, which is initially described in [16], is used in Simo to calculate the external and inertial loads on Parts A and B. The loads given by Simo are described in the corresponding body-related coordinate systems ($O^{r,A}$-$x^{r,A}$-$y^{r,A}$-$z^{r,A}$ and $O^{r,B}$-$x^{r,B}$-$y^{r,B}$-$z^{r,B}$) respectively and transferred to the control nodes of the finite element model. Each control node has 6 d.o.f.s. Each of the end nodes of the artificial beam elements and the top end nodes of the mooring lines (the fairleads) rigidly follows the motions of the corresponding control node. The O^b-x^b-y^b-z^b and body-related coordinate systems are coincident when the model is located at its mean position in calm water. $O^{r,A}$ and $O^{r,B}$ rigidly follow rigid-body motions of the O^b but the orientation of the body-related coordinate systems and vertical position of the $O^{r,A}$ and $O^{r,B}$ are fixed (as the same as the body-related coordinate systems when the model is located at its initial position in time-domain simulation). To obtain the first order hydro loads, boundary value problem in an earth-fixed coordinate system (e.g. O^g-x^g-y^g-z^g) with assumption that the hull is a rigid-body needs to be solved to derive the corresponding coefficient vectors and matrices. Note that the derived coefficient vectors and matrices include hydrodynamic interactions. Second order and higher order hydrodynamic loads and hydroelastical effects are not included. More details are available in [16].

Morison's formula is used to model the hydrodynamic loads on the mooring lines, while the drag term of the Morison's formula is use to model the drag forces on Parts A and B. A discussion with respect to selection of the corresponding drag coefficients (C_d) and added mass coefficients (C_a) is given in section 4.

Young's modulus of mooring lines of the numerical model is specified as $2.1 * 10^8$ kN/m^2 rather than the value of the experimental test ($6.3 * 10^9$ kN/m^2) to avoid numerical problems. In theory, effects of this difference on mooring line tensions and global responses of the model are negligible.

In Riflex, the time-domain finite element model is solved by using the Newmark-β numerical integration ($\beta = 3.9$ and $\gamma = 0.505$). Time step is set to be 0.05 seconds. Rayleigh damping, which is a linear combination of the Riflex generated global mass and stiffness matrices, is used for modelling effect of structural damping. The corresponding mass and stiffness proportional coefficients are set to be 0 and 0.005, respectively. More explanations are given in [24].

3.2. FDM

WADAM implements a function for which a specified plane, e.g. the y-z plane at x=5, automatically divides the hull into two parts, and calculates sectional forces and moments that are in equilibrium to inertial and external hydro-loads on each part. However, we cannot use this function to calculate the forces and moments in the base of the side column of our model since the specified plane in WADAM is infinite. If we specified an x-y plane at z=-24, one of the parts divided by the specified plane would be composed of the wetted surface of the three side columns and the central column. Consequently, the FDM, which implements the same principle as WADAM for calculating wave induced transfer functions for rigid-body motions and sectional forces and moments but is more flexible for users to divide the wetted surface into user specified parts, is developed in Matlab [22] and validated by using WADAM. Note that the FDM implements linear theory [25]. Viscous drag forces on the hull and hydroelastic effects are not included.

The implemented principle is described as follows:

The transfer functions for the sectional forces and moments ($\boldsymbol{R}^s\ (\omega)$) can be derived from $\boldsymbol{R}^s\ (\omega, t) = \mathcal{R}\{\boldsymbol{R}^s\ (\omega)e^{-i\omega t}\}$. $\boldsymbol{R}^s\ (\omega, t)$ denotes the global forces and moments induced by a unit-amplitude regular wave for which second order and higher order terms with respect to amplitude of the regular wave are removed. The hull of the experimental model is a statically determinate structure. As a result, the global forces and moments ($\boldsymbol{R}^s\ (\omega, t)$) are in equilibrium with inertia loads ($\boldsymbol{R}^i\ (\omega, t)$) and external loads ($\boldsymbol{R}^e\ (\omega, t)$) on the Part A, see Figure 2 and Eq. (1). $\boldsymbol{R}^i\ (\omega, t)$ is determined by the mass matrix of Part A and acceleration ($\ddot{\boldsymbol{Y}}(\omega, t)$). $\ddot{\boldsymbol{Y}}(\omega, t)$ is obtained by solving the equations of motion in the the O^g-x^g-y^g-z^g coordinate system, see Eq. (2). Rigid-body motions are denoted as $Y(\omega) = [Y_1, Y_2, Y_3, Y_4, Y_5, Y_6]$. $\boldsymbol{Y}(\omega, t) = \mathcal{R}\{\boldsymbol{Y}(\omega)e^{-i\omega t}\}$ denotes the 6 d.o.f. rigid-body motions induced by a unit-amplitude regular wave. $\mathcal{R}\{\}$ denotes the real part of the complex value inside the bracket. Approaches for generating and solving the equations of motion are well known and referred to [26]. In Eq. (1), $\boldsymbol{M}^g$, $\boldsymbol{A}^g(\omega)$, $\boldsymbol{B}^g(\omega)$, $\boldsymbol{C}^g$and $\boldsymbol{H}^g\ (\omega)$ are the mass matrix, added mass coefficient matrix, potential damping coefficient matrix, restoring coefficient matrix and first order wave excitation load transfer function. The $\boldsymbol{R}^e\ (\omega, t)$ is composed of wave excitation loads ($\boldsymbol{R}^{waex}(\omega, t)$), added mass forces ($\boldsymbol{R}^{add}(\omega, t)$), potential damping forces ($\boldsymbol{R}^{pd}(\omega, t)$) and $\boldsymbol{R}^{flu}(\omega, t)$. $\boldsymbol{R}^{waex}(\omega, t)$, $\boldsymbol{R}^{add}(\omega, t)$, and $\boldsymbol{R}^{pd}(\omega, t)$ can be obtained by 1) solving the potential-flow boundary value problem with the assumption that the hull of the model is a rigid-body; 2) calculating the corresponding pressure forces on the mean wetted body surface of the Part A based on the Bernoulli's equation and the corresponding velocity potential, and 3) integrating the pressure forces and transfer the integrated forces and moments to the corresponding coordinate system. $\boldsymbol{R}^{flu}(\omega, t)$ is the resultant forces and moments of gravity, hydrostatic pressure forces on the outer surface and the atmospheric pressure forces on the inner surface of the Part A when the model is located at an instantaneous position. Note that second and higher order terms with respect to amplitude of the regular wave are not included in the $\boldsymbol{R}^i\ (\omega, t)$ and $\boldsymbol{R}^e\ (\omega, t)$ as well.

$$\boldsymbol{R}^s\ (\omega, t) + \boldsymbol{R}^i\ (\omega, t) + \boldsymbol{R}^e\ (\omega, t) = 0 \quad (1)$$

$$\mathcal{R}\{\big(\boldsymbol{M}^g + \boldsymbol{A}^g(\omega)\big)\ddot{\boldsymbol{Y}}(\omega, t) + \boldsymbol{B}^g(\omega)\dot{\boldsymbol{Y}}(\omega, t) + \boldsymbol{C}^g\boldsymbol{Y}(\omega, t)\} = \mathcal{R}\{\boldsymbol{H}^g\ (\omega)e^{-i\omega t}\} \quad (2)$$

4. Calibration of numerical model

The "model-the-model" principle, which means to simulate the actual model tests as closely as possible [18], is used. A rational calibration procedure for the mooring system is available in [27] and implemented in this paper. C_d and C_a for the segments of each mooring line are specified as 1.4 and 1.0 respectively. The anchors of the mooring lines are moved 1.5 meters away along the radial direction to increase the simulated pretension of each mooring line in calm water from 1,517 kN to 1,597 kN. As discussed in [27], the deviation can be attributed to small inaccuracies in the setup of the model test, e.g. the actual positions of anchors deviated from the specified positions and the actual lengths of the mooring lines were slightly shorter than the specified values.

The mass of the experimental model can be estimated based on the draft, configuration of the hull and resultant force of the vertical components of the mooring line tensions at the fairleads. Comparing the estimated mass to the measured mass (which is tabulated in Table 2), a 4.7% deviation is observed. Meanwhile there are discrepancies between the simulated and measured roll/pitch natural periods (obtained from decay tests) and mean heeling angle and fore-aft and side-to-side bending moment in turbulent wind-only conditions. As discussed in [27], deviations may exist in the measurements of the position of the centre of gravity and moment of inertia.

Consequently, a constant force which is acting on the $O^{r,Part\ B}$ and pointed to the negative axis of $z^{r,Part\ B}$ is added in the TDM model to compensate the 4.7% difference and make the numerical model float at the same draft as the experimental model in calm water while the vertical position of the centre of gravity and mass matrix of Part A and B are calibrated.

The centre of gravity of the Part A is adjusted to (41, 0, -15.3) in the body-fixed coordinate system to give the TDM the same mean bending moments as the measurements when the experimental and numerical models are subjected to the same static tilt angle. The centre of gravity of the Part B is adjusted to (-2.019, 0, -20.6) so that the TDM and experimental model have the same title angle under the same overturning moment. Adjustment of the centre of gravity of the Part A has limited effects on the centre of gravity of the whole model. The relative difference between the adjusted and original vertical positions of the centre of gravity of Part B is 6% (compared to [27]).

Three forces and moments are used to adjust the inertial loads of Part B and denoted as $\boldsymbol{M}_{ad}^{B}\ddot{\boldsymbol{\eta}}^{B}(t)$. The $\boldsymbol{M}_{ad}^{B}$ is a 6×6 matrix. The $\ddot{\boldsymbol{\eta}}^{B}(t)$ is the simulated motions of Part B. The $\boldsymbol{M}_{ad}^{B}$, $\ddot{\boldsymbol{\eta}}^{B}(t)$ and $\boldsymbol{M}_{ad}^{B}\ddot{\boldsymbol{\eta}}^{B}(t)$ are described in the $O^{r,B}$-$x^{r,B}$-$y^{r,B}$-$z^{r,B}$ coordinate system with respect to the $O^{r,B}$. According to the results of a parametric study with respect to the effect of each term in the $\boldsymbol{M}_{ad}^{B}$ on the motion responses and bending moments, all the terms in the $\boldsymbol{M}_{ad}^{B}$ are zero except for $m_{11} = m_{22} = 571$ tonnes and $m_{24} = m_{42} = 5690$ tonnes*m^2. Relative differences between the adjusted terms and the corresponding terms in the original measured mass matrix of Part B are less than 6%.

Adjustments with respect to the terms in the mass matrix of the Part A are not considered since a parametric study shows that reasonable variations, e.g. in a range from -10% to 10%, have very limited effects on the motion responses and bending moments.

The non-dimensional drag coefficients (C_d) for the width and height of the pontoons and the columns are specified as 2.1, 1.7 and 0.5, respectively, according to [28]. Results of a sensitivity study show that the effect of the drag coefficients on the simulated global forces and moments and rigid-body motions are negligible in the wave frequency range, i.e. from 0.3 rad/s to 1.4 rad/s.

5. Results and discussions

In this section we intend to compare the simulated and measured responses, i.e. the fore-aft and side-to-side bending moments and rigid-body motions, of the model in moderate wave-only conditions.

5.1. General

WAVE2c are the measurements of undisturbed waves at Pos2 in wave calibration tests (without the experimental model). WAVE2c were synchronized with the measurements of the model tests by comparing the WAVE1 and WAVE1c from the time 0 to 100 seconds (full-scale) since the WAVE1 and WAVE1c were measured by the same wave probe at the same position in the model tests and wave calibration tests, and radiation and diffraction effects of

the experimental model on the wave elevations at the Pos1 are expected to be negligible in the first 100 seconds. The synchronized WAVE2c are considered as measurements of incident waves of the corresponding model tests (with the experimental model) and were used as input to the TDM.

Lowpass Butterworth filter [22] and zero-phase digital filtering are used to remove high frequency components in the measurements. The cutoff frequency, which is the frequency where the magnitude responses of the filter is $\sqrt{1/2}$, is specified as 0.5 Hz. Then, the measurements are downsampled from 111.11 Hz to 5 Hz without risk of aliasling.

Skewness and kurtosis [29] of the measured and simulated responses and waves are around 0 and 3, respectively and indicate that, in moderate waves, the experimental model and TDM are linear systems with respect to waves (input, denoted as x) and the corresponding response (output, denoted as y). Therefore, wave induced transfer function ($H_{xy}(\omega)$), which is composed of the response amplitude operator (RAO) and phase angle (α), are derived by using Eq. (3, 4). G_{xy} and G_{xx} are one-side spectra that are derived from the corresponding cross-correlation and autocorrelation with respect to the realizations of x and y, respectively [29]. $H_{xy}(\omega)$ is a complex number. Real and imaginary parts are denoted as Re and Im respectively. The phase angle (α) is derived based on the corresponding values of Re and $-Im$. A negative phase angle (α) means the y lags the x. Note that computation of the phase angle of the $H_{xy}(\omega)$ derived from measurements of the incident waves and corresponding responses is very sensitive to the synchronization in particular for high-frequency components of the transfer functions. For example, a 0.4 seconds mismatch means a 9-degree-shift and a 32-degree-shift of the phase angle for the wave components for which the frequency is 0.4 rad/s and 1.4 rad/s, respectively.

$$H_{xy}(\omega) = \frac{G_{xy}(\omega)}{G_{xx}(\omega)} = Re + iIm \tag{3}$$

$$\text{RAO} = \sqrt{Re^2 + Im^2} \tag{4}$$

The linear characteristic of the system can also be checked by calculating the corresponding coherence function $\gamma_{xy}^2(\omega)$, see Eq. (5), [29]. The values of γ_{xy}^2 will always satisfy $0 \leq \gamma_{xy}^2 \leq 1$. The γ_{xy}^2 will equal to one for an ideal constant parameter linear system. G_{yy} is one-side spectrum that is derived from the corresponding autocorrelation with respect to the realizations of y.

$$\gamma_{xy}^2(\omega) = \frac{|G_{xy}(\omega)|^2}{G_{xx}(\omega)G_{yy}(\omega)} \tag{5}$$

5.2. Comparisons of transfer functions

Transfer functions are derived from 1-hour measurements of the pink noise and Jonswap spectrum model tests, i.e. model test 2310, 2321 and 2420, and the corresponding simulations. Reasonably good agreement between the RAOs of the experimental and numerical models is observed, see Figure 3-6. In the comparisons, we focus on frequency ranges where majority of the wave energy is distributed (from 0.4 rad/s to 1.4 rad/s for the pink noise model tests and from 0.5 rad/s to 1 rad/s for the Jonswap spectrum model test). Spectral densities of the waves are given in Figure 7. In addition, the work of Bachynski et al [19] shows that the RAOs which are derived from the pink noise and regular wave model tests are consistent.

Peaks at 0.8 and 1.25 rad/s and trough at 1 rad/s are observed in the RAO for the fore-aft bending moment, see Figure 3. The peaks and trough are attributed to inertial loads and added mass forces which are related to second derivatives of surge and pitch motions (accelerations). Two troughs nearby 0.8 and 1.25 rad/s and a peak nearby 1 rad/s can be observed in the RAO for surge motion.

More significant discrepancies are in comparisons of the phase angles of the transfer functions, in particular for frequencies that are higher than 0.9 rad/s. For the fore-aft bending moments in Figure 3, absolute value of the difference between the phase angle given by the FDM and the phase angle given by experimental measurements or simulations is less than 10 degrees at 0.4 rad/s (the frequency), but up to 50 degrees at 1.4 rad/s. For surge, heave

and pitch motions, large differences between the phase angle given by the FDM and the phase angle given by experimental measurements or simulations are in frequency ranges where amplitudes of the corresponding RAOs are very small (close to zero).

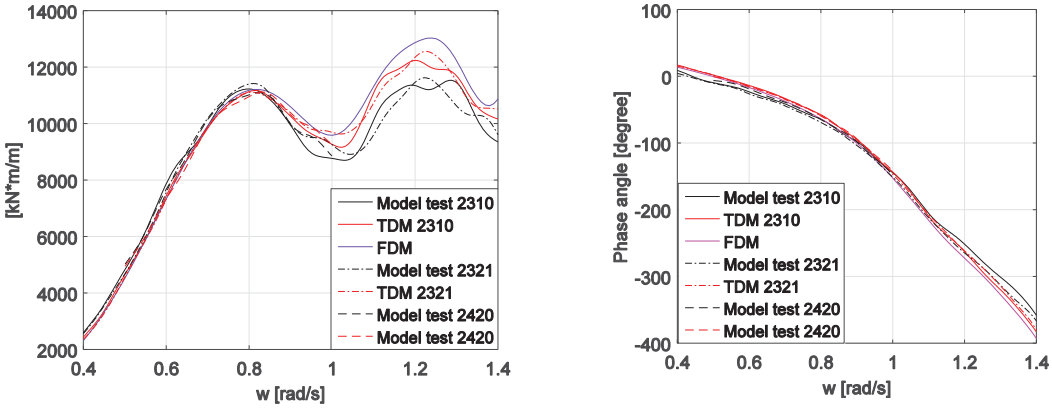

Figure 3 Transfer function for the fore-aft bending moment, derived from 1-hour realizations, pink noise, $H_s = 2$ m (2310) and $H_s = 4$ m (2321), and Jonswap spectrum, $H_s = 3.6$ m and $T_p = 10.2$ seconds (2420)

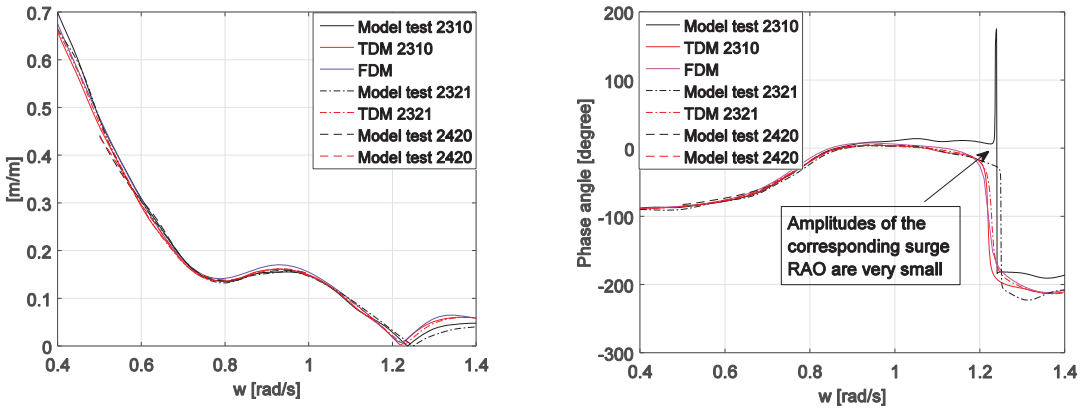

Figure 4 Transfer function for surge, derived from 1-hour realizations, pink noise, $H_s = 2$ m (2310) and $H_s = 4$ m (2321), and Jonswap spectrum, $H_s = 3.6$ m and $T_p = 10.2$ seconds (2420)

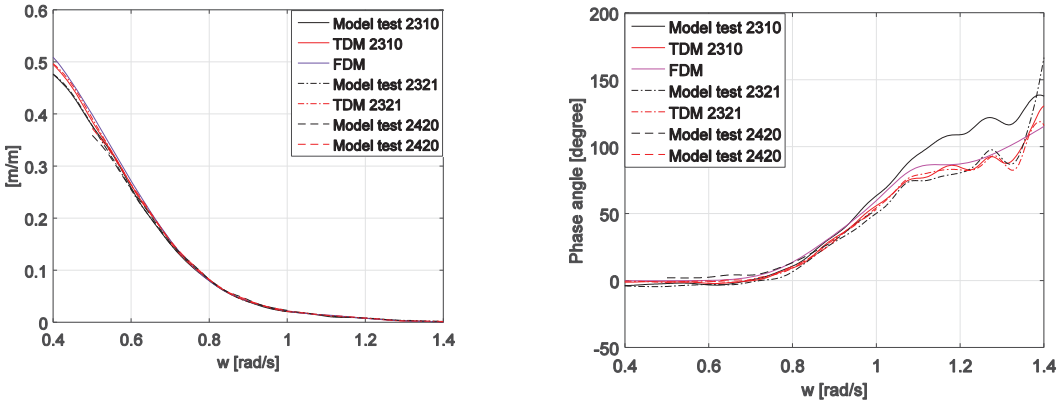

Figure 5 Transfer function for heave, derived from 1-hour realizations, pink noise, $H_s = 2$ m (2310) and $H_s = 4$ m (2321), and Jonswap spectrum, $H_s = 3.6$ m and $T_p = 10.2$ seconds (2420)

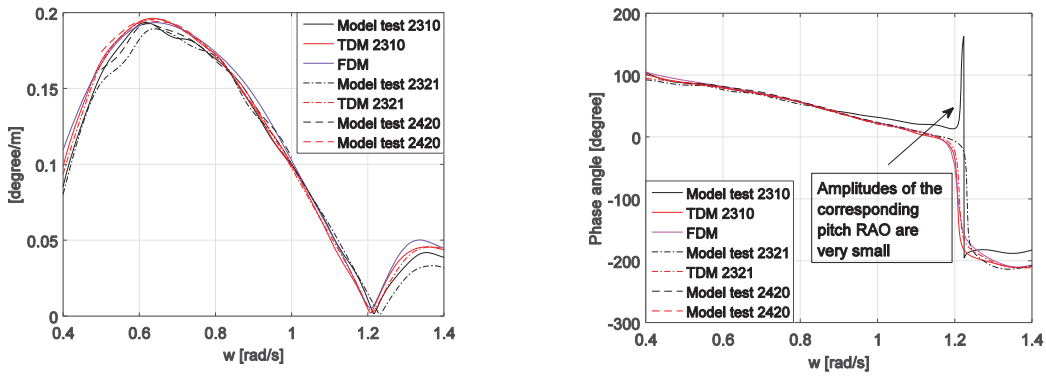

Figure 6 Transfer function for pitch, derived from 1-hour realizations, pink noise, $H_s = 2$ m (2310) and $H_s = 4$ m (2321), and Jonswap spectrum, $H_s = 3.6$ m and $T_p = 10.2$ seconds (2420)

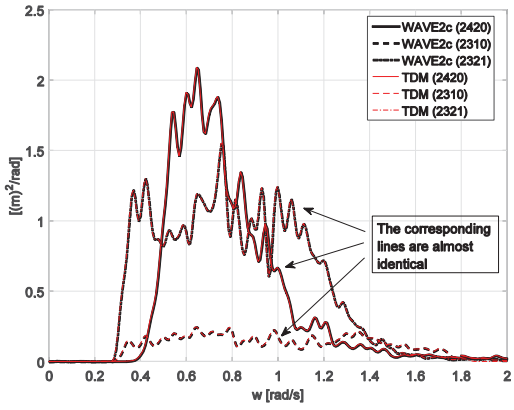

Figure 7 Spectral densities of measured and simulated wave elevations at Pos2 (WAVE2c), derived from 1-hour realizations

5.3. Investigation of differences between simulation and experiment

Some explanations for differences in the transfer functions between the TDM and experimental model are 1) some non-linear effects, e.g. second and higher order hydrodynamic loads and non-linear wave kinematics, which inherently exist in the model tests but are not modelled numerically, and 2) uncertainties, noise and unknown errors in the measurements. Some relevant observations are discussed as follows.

Coherence functions are expected to equal to one when the TDM and experimental model are subject to small incident waves, e.g. the pink noise model test 2310. However, as shown in Figure 8, significant deviations can be observed in the coherence function of the measurements in the frequency range from 1 rad/s to 1.4 rad/s. The deviations indicate that one or more of three possible physical situations exist. The three possible situations are 1) extraneous noise is present in the measurements; 2) the system relating the incident wave (input) and the corresponding response (output) is not linear; and 3) the response is an output due to an input of the wave elevation as well as to other inputs.

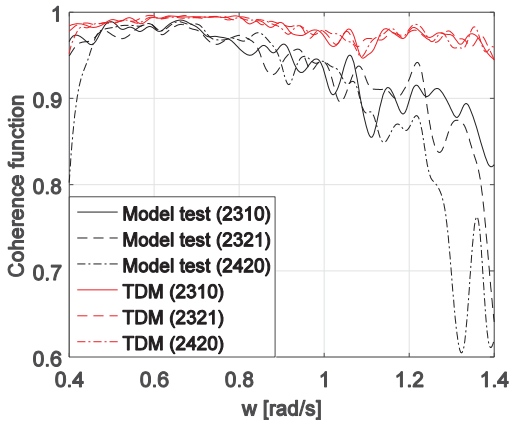

Figure 8 Coherence functions between incident waves (input) and the fore-aft bending moment (output), derived from 1-hour realizations, pink noise, $H_s = 2$ m (2310) and $H_s = 4$ m (2321), and model test 2420, $H_s = 3.6$ m and $T_p = 10.2$ s

Statistical moments, i.e. skewness and kurtosis, are used to analyse characteristics of probability distributions of the measurements with and without implementing a highpass Butterworth filter [22]. The cutoff frequency [22] is 1.2 rad/s. The use of the highpass filter removes the frequency components below 1 rad/s. The results, see Table 7, show that 1) in full frequency range (without filter) the skewness and kurtosis of the measurements are close to 0 and 3, respectively, and indicate that Gaussian distribution can be used to model the probability distribution of the measurements; 2) measurements of the responses are dominated by components that are linearly proportional to the corresponding components of the measured incident waves since in the full frequency range the measured waves and responses can be described by Gaussian distributions; and 3) non-Gaussian components exist in the measurements in particular for the low frequency range due to slow varying drift force on the model and frequency range above 1 rad/s where the corresponding coherence functions significantly deviate from 1. For example, the kurtosis of the measured pitch motion in the model 2321 is 3.68 and 2.99, with and without filter respectively. The kurtosis of the measured wave elevation in the model test 2321 is 3.05 and 6.01, with and without filter respectively.

Some statistical values of the measured and simulated wave elevations are tabulated in Table 8. Airy wave theory is implemented in the TDM. The spectral densities and standard deviations of the simulated and measured wave elevations are almost identical, see Figure 7. However the relevant difference between the maximum values of 1-hour wave elevation of the simulation and measurement can be more than 19% (in the Pink noise model test 2321), also see Figure 9.

Table 7 Skewness and kurtosis of measurements with and without filter

		Measurements	Wave	M_y	Surge	Heave	Pitch
Skewness	2420	Full frequency range	0.09	0.02	-0.10	0.08	0.24
		Above 1 rad/s (after filtering)	0.38	0.00	-0.11	0.96	0.02
	2310	Full frequency range	0.13	0.08	-0.08	0.07	-0.03
		Above 1 rad/s (after filtering)	0.34	-0.02	-0.02	-0.87	0.01
	2321	Full frequency range	0.15	0.04	-0.05	0.03	0.03
		Above 1 rad/s (after filtering)	0.78	0.06	-0.12	2.49	-0.04
Kurtosis	2420	Full frequency range	3.00	3.08	3.05	2.93	3.14
		Above 1 rad/s (after filtering)	3.64	3.14	8.21	56.72	3.06
	2310	Full frequency range	3.17	3.02	2.53	2.97	3.19
		Above 1 rad/s (after filtering)	3.90	3.00	3.14	32.70	3.21
	2321	Full frequency range	3.05	2.99	2.77	2.92	3.68
		Above 1 rad/s (after filtering)	6.01	3.87	5.17	233.01	2.99

Table 8 Statistical values of simulated and measured wave elevations

Unit [m]		2310	2321	2420
Std	Model test	0.47	1.00	0.92
	TDM	0.47	0.99	0.92
Max	Model test	1.89	3.89	4.00
	TDM	1.78	3.15	3.89
Min	Model test	-1.62	-3.08	-3.03
	TDM	-1.63	-3.33	-3.02
Skewness	Model test	0.13	0.15	0.09
	TDM	0.11	0.02	0.10
Kurtosis	Model test	3.17	3.05	3.00
	TDM	3.12	2.92	2.99

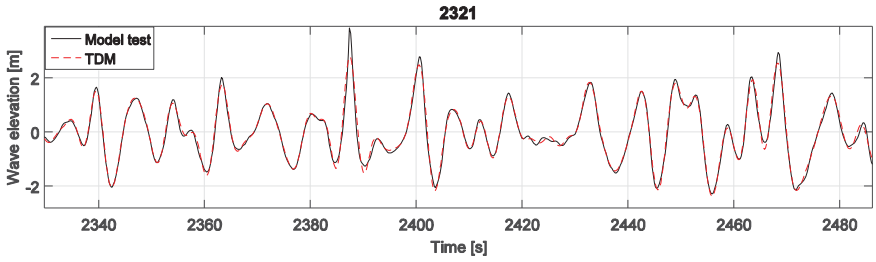

Figure 9 Comparisons of measured and simulated wave elevation realizations. Pink noise model test 2321

Incident wave elevations are measured at the Pos2. However, there is a difference between the mean position of the experimental model, which is induced by mean drift forces on the model, and the Pos2. Fortunately, the difference is negligible since, in moderate wave conditions, the mean offset of the model is relatively small compared to wave length of the incident waves. For instance, the mean offset is less than 0.2 meters (in full-scale) while the wave length of a 4-second-period wave, approximately, is 25 meters.

Transfer functions that are derived from different sets of 1-hour simulations subjected to different moderate

waves are more consistent than the transfer functions derived from different sets of 1-hour measurements, see Figure 10 as an example. To quantify uncertainties in the measurements, well designed and systematical repeat-model tests are needed and should be analysed in future.

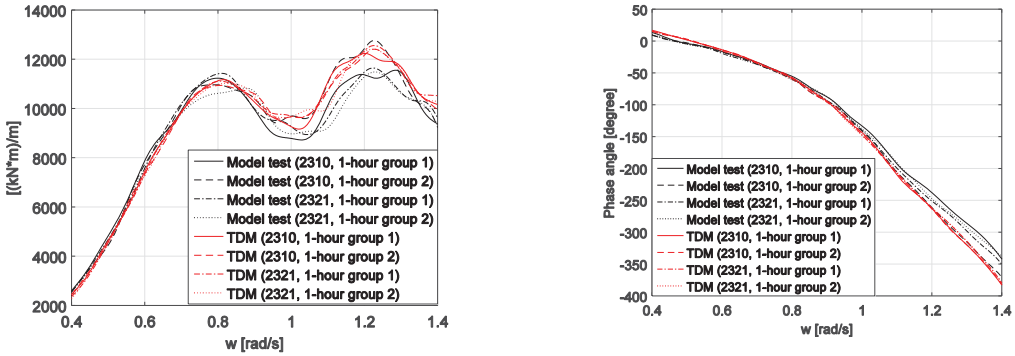

Figure 10 Transfer functions of the fore-aft bending moment, derived two sets of 1-hour realizations

5.4. Simulations and measurements in a moderate Jonswap wave-only condition

Spectral densities and realizations of the simulated and measured responses, i.e. the fore-aft and side-to-side bending moments and rigid-body motions, of the model in a moderate wave-only condition (model test 2420) are compared. The difference in the standard deviation of the simulated and measured fore-aft bending moment is 1.4% and good agreement is seen in the spectrums and realizations, see Figure 11 and 12. In wave frequency range (from 0.4 rad/s to 1.4 rad/s), good agreement is seen in spectrums of measured and simulated rigid-body motions. Motions induced by the slow varying drift force on the experimental model can be observed in the low frequency range in the spectrums of the measurements, while second and higher order hydrodynamic loads, expect for viscous drag forces, are not included in the TDM.

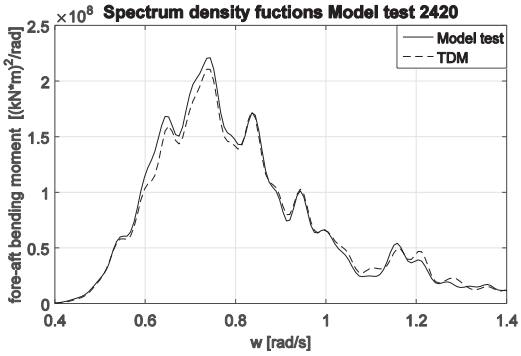

Figure 11 Spectral density functions of the fore-aft bending moment, derived from 1-hour realizations, moderate wave only, $H_s = 3.6$ m and $T_p = 10.2$ s

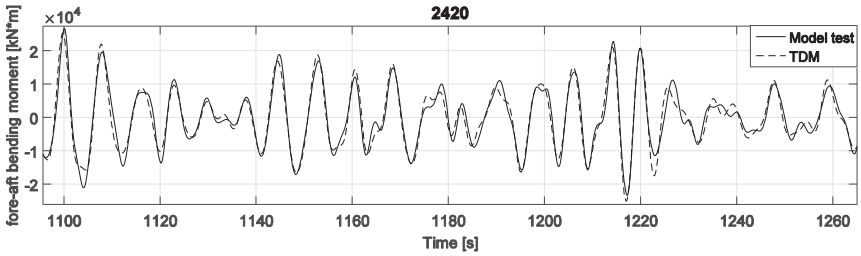

Figure 12 Part of measured and simulated fore-aft bending moment, moderate wave only, $H_s = 3.6$ m and $T_p = 10.2$ s

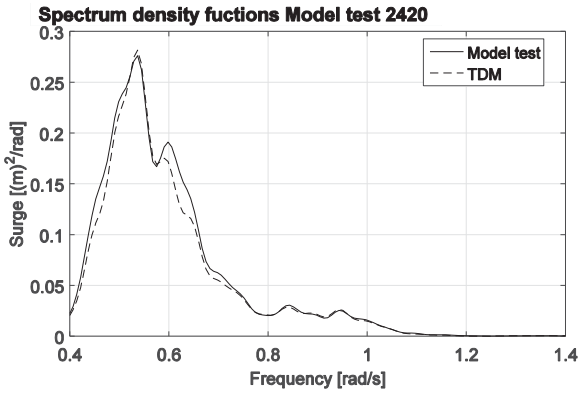

Figure 13 Spectral density functions of surge, derived from 1-hour realizations, moderate wave only, $H_s = 3.6$ m and $T_p = 10.2$ s

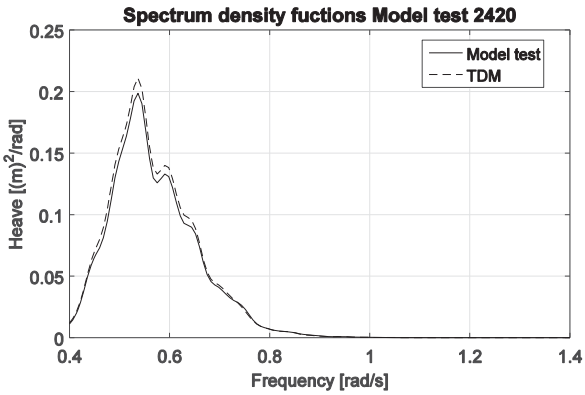

Figure 14 Spectral density functions of heave, derived from 1-hour realizations, moderate wave only, $H_s = 3.6$ m and $T_p = 10.2$ s

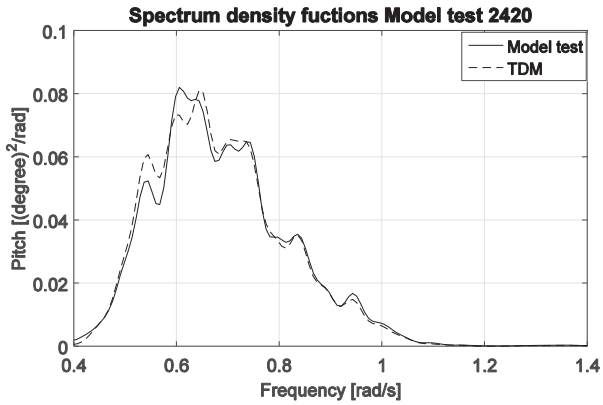

Figure 15 Spectral density functions of pitch, derived from 1-hour realizations, moderate wave only, $H_s = 3.6$ m and $T_p = 10.2$ s

6. Conclusions

Measurements of a 1:30 scaled braceless semi-submersible model test which implements the ReaTHM™ testing approach are used to validate a recently developed time-domain numerical approach for determining forces and moments in floaters. The focus of this paper is on responses in moderate waves. Second order wave loads are expected to be negligible in moderate waves. Statistical values, kurtosis and skewness, for the wave elevations and responses measured in the model test show that the incident waves and corresponding responses are Gaussian-distributed and indicate that the model is linear system with respect to the incident wave (input) and responses (output). Therefore, measurements of the global forces and moments in the base of the side column of the experimental model are compared to the corresponding simulations given by a frequency-domain model (the FDM) and a time-domain model (the TDM). Necessary calibrations with respect to some measured data, i.e. mass matrices, position of centre of gravity and positions of the anchors of the experimental model and drag and added mass coefficients for the hydrodynamic loads on the mooring lines and drag forces on the hull of the model have been carried out according to a rational procedure. The measured wave elevations were synchronized.

Reasonably good agreements are observed in the comparisons between the transfer functions for wave induced rigid-body motions and bending moments at the base of the side column, which are directly given in the FDM and derived from the corresponding simulations and measurements, and comparisons between the corresponding response spectral densities. More differences are observed in comparisons of phase angles of the transfer functions, in particular in frequencies that are higher than 0.9 rad/s. Phase angles of the transfer functions are very sensitive to the synchronizations of the measured data in particular for the higher frequency components of the waves. Due to mean drift forces on the experimental model, there is a difference between the mean position of the experimental model and the Pos2. Fortunately, the difference is negligible in moderate waves. Viscous drag forces have limited effects on the transfer functions. Transfer functions that are derived from different sets of 1-hour simulations subjected to different moderate waves are more consistent than the transfer functions derived from different sets of 1-hour measurements.

The differences in the transfer functions may be arbitrated to 1) some non-linear effects, e.g. second and higher order hydrodynamic loads and non-linear wave kinematics, inherently exist in the model tests but are not modelled numerically; and 2) uncertainties, noise and unknown errors exist in the measurements. Relevant observations in term of coherence functions, statistical properties and realizations are analysed. To quantify the uncertainties in the measurements, well designed and systematical repeat-model tests are needed and should be analysed in future.

Analysis for the comparisons between the simulated realizations and measurements in extreme waves, for which the second-order effects and maybe also high-order effects are critical, will be given in future. Simo/Riflex can account for the second-order wave loads as long as the hull is modelled as one rigid-body. However, to capture the sectional forces and moments in a straightforward manner, the hull needs to be modelled at least as two rigid-bodies.

Therefore, additional efforts are needed to develop modelling approaches to address this problem. At the moment, the second-order wave loads are not modelled in the estimation of the cross-sectional loads.

Acknowledgements

The authors acknowledge the financial support provided by the Research Council of Norway through the Centre for Ships and Ocean Structures; the Norwegian Research Centre for Offshore Wind Technology (NOWITECH), NTNU; and the Centre for Autonomous Marine Operations and Systems (AMOS), NTNU.

References

[1] Statoil AS, (2017), http://www.statoil.com/en/TechnologyInnovation/NewEnergy/RenewablePowerProduction/Offshore/HywindScotland/Pages/default.aspx?redirectShortUrl=http%3a%2f%2fwww.statoil.com%2fHywindScotland, accessed 12.January.2017

[2] Principle Power, Inc., (2017), http://www.principlepowerinc.com/, accessed 12.January.2017

[3] Jonkman J., (2010), "Definition of the Floating System for Phase IV of OC3", NREL/TP-500-47535, National Renewable Energy Laboratory, Golden, CO, USA.

[4] Nielsen, F. G., Hanson, T. D., and Skaare, B., (2006), "Integrated Dynamic Analysis of Floating Offshore Wind Turbines," Proceedings of the 25th International Conference on Offshore Mechanics and Arctic Engineering, OMAE2006-92291, Hamburg, Germany.

[5] Bachynski EE, Moan T., (2012), "Design considerations for tension leg platform wind turbines.", Marine Structures, Vol 29, pp 89-114.

[6] Sclavounos, P., Tracy, C., and Lee, S., (2007), "Floating offshore wind turbines: responses in a seastate; Pareto optimal designs and economic assessment", Tech. rep., Department of Mechanical Engineering, Massachusetts Institute of Technology.

[7] Roddier, D., Cermelli, C., Aubault, A., and Weinstein, A., (2010), "WindFloat: A floating foundation for offshore wind turbines", Journal of Renewable and Sustainable Energy 2, 033104, doi:10.1063/1.3435339.

[8] Robertson, A., Jonkman, J., Masciola, M., Song, H., Goupee, A., Coulling, A., and Luan C., (2012), "Definition of the Semisubmersible Floating System for Phase II of OC4", Offshore Code Comparison Collaboration Continuation (OC4) for IEA Task 30.

[9] Luan, C., Gao, Z., and Moan, T., (2016). "Design and analysis of a braceless steel 5-mw semi-submersible wind turbine". Proceedings of the 35th International Conference on Ocean, Offshore and Arctic Engineering, OMAE2016-54848, Busan, Korea, June 19–24.

[10] DNV, (2013), "Offshore standard – Design of Floating Wind turbine Structures", DNV-OS-J103, Det Norske Veritas.

[11] ABS, (2013), "Guide for Building and Classing Floating Offshore Wind Turbine Installations", American Bureau of Shipping.

[12] ClassNK, (2012), "Guidelines for Offshore Floating Wind Turbine Structures", Nippon Kaiji Kyokai.

[13] Cordle, A., and Jonkman, J., (2011), "State of the art in floating wind turbine design tools", Proceedings of the 21st International Offshore and Polar Engineering Conference, Maui, Hawaii, USA. Vol. 1, pp. 367–374.

[14] Robertson, A., Jonkman, J. Qvist, J.,Chen, X., Armendariz,J.A., Soares, C.G., Luan, C., Huang, Y., Yde, A.,Larsen, T., Nichols, J., Lei, Liu, Maus, K.J., Godreau, C., Heege, A., Vatne, S.R., Manolas,D., Qin, H., Riber, H., Abele, R., Yamaguchi, A., Pham,A. Alves,M., Kofoed-Hansen,H., (2014), " Offshore code comparison collaboration, continued: phase II results of a floating semisubmersible wind system", In Proceedings of the 33rd International Conference on Ocean, Offshore and Arctic Engineering, no. OMAE2014-24040, San Francisco, USA, 2014.

[15] Matha, D., Schlipf, M., Cordle, A., Pereira, R., and Jonkman, J., (2011). "Challenges in Simulation of Aerodynamics, Hydrodynamics, and Mooring-Line Dynamics of Floating Offshore Wind Turbines," Proceedings of the 21st International Offshore and Polar Engineering Conference, Maui, Hawaii, USA, Vol. 1, pp. 421–428.

[16] Luan, C., Gao, Z. and Moan, T., (2017), "Development and verification of a time-domain approach for determining forces and moments in structural components of floaters with an application to floating wind turbines". Marine Structures. vol. 5 pp 87-109.

[17] Aksnes, V., Berthelsen, P. A., and Da Fonseca, N. M. M. D., (2015). "On the need for calibration of numerical models of large floating units against experimental data". In Proceedings of 25th Int Offshore and Polar Eng Conf, ISOPE-2015, Kola, Hawaii, USA, June 21–26.

[18] Ormberg, H., Baarholm, R., and Stansberg, C.T., (2003). "Time-domain coupled analysis of deepwater TLP, and verification against model tests". Proc. 13th ISOPE Conf., Honolulu, Hawaii, USA.

[19]Bachynski, E. E., Thys, M., Chabaud, V., and Sauder, T., (2016). "Realtime Hybrid Model Testing of a Braceless Semi-submersible Wind turbine. Part II: Experimental Results". In 35th International Conference on Ocean, Offshore and Arctic Engineering, no OMAE2016-54437.

[20]Sauder, T., Chabaud, V., Thys, M., Bachynski, E. E., and Sæther, L. O., (2016). "Real-time hybrid model testing of a braceless semi-submersible wind turbine: Part I: The hybrid approach". In 35th International Conference on Ocean, Offshore and Arctic Engineering, no. OMAE2016-54435.

[21] Chabaud, V., (2016), "*Real-Time Hybrid Model Testing of Floating Wind Turbines*". Ph.d thesis, ISBN 978-82-326-2083-8., NTNU, Norway.

[22] MathWorks, Inc., (2010), MATLAB: The Language of Technical Computing. Natick, MA: MathWorks.

[23] MARINTEK, (2011). SIMO User's Manual.

[24] MARINTEK, (2013). RIFLEX User's Manual.

[25] DNV, (2013), SESAM User Manual HydroD, Det Norske Veritas.

[26] Faltinsen, O.M., (1990), "*Sea loads on ships and offshore structures*", Cambridge University Press, UK.

[27] Berthelsen, P. A., Bachynski, E. E., Karimirad, M., and Thys, M., (2016). “Real-time hybrid model testing of a braceless semi-submersible wind turbine. Part III: Calibration of a numerical model”. In 35th International Conference on Ocean, Offshore and Arctic Engineering, no. OMAE2016-54640.

[28] DNV, (2010), “Recommended Practice - Environmental Conditions and Environmental Loads”, DNV-RP-C205, Det Norske Veritas.

[29] Bendat, J. S., and Piersol, A. G., (2010). “*Random Data: Analysis and Measurement Procedures, 4th Edition*”. John Wiley & Sons, Inc. ISBN: 978-0-470-24877-5, page 180.

[30] van Engelen, T.G., and Braam, H., (2004). “TURBU Offshore, Computer Program for Frequency Domain Analysis of Horizontal Axis Offshore Wind Turbines; Implementation”, ECN-C--04-079, Dutch Ministry of Economic Affairs, Netherlands.

[31] Kvittem, M. I., and Moan, T.,(2015), "Frequency versus time domain fatigue analysis of a semi-submersible wind turbine tower", Journal of Offshore Mechanics and Arctic Engineering, 137(1):011901.

A.3 Paper A3

Paper A3:
Comparisons and analysis of simulated and measured motions and sectional loads in a floating wind turbine hull subjected to combined wind and waves
Chenyu Luan, Zhen Gao and Torgeir Moan
Submitted for review at Engineering Structures

Comparisons and analysis of numerical simulated and experimental measured motions and sectional loads in a floating wind turbine hull subjected to combined wind and waves

Chenyu Luan*

Email: chenyu.luan@ntnu.no

PhD Candidate
Norwegian Research Centre for Offshore Wind Technology (NOWITECH)
Centre for Ships and Ocean Structures (CeSOS), NTNU
Centre for Autonomous Marine Operations and Systems (AMOS), NTNU
NO-7491 Trondheim, Norway

Zhen Gao
Email: zhen.gao@ntnu.no
PhD, Professor
CeSOS and AMOS, NTNU
Department of Marine Technology, NTNU
NO-7491 Trondheim, Norway

Torgeir Moan
Email: torgeir.moan@ntnu.no
PhD, Professor
CeSOS and AMOS, NTNU
NOWITECH
Department of Marine Technology, NTNU
NO-7491 Trondheim, Norway

ABSTRACT

Multi-body time-domain finite element models, which implement a recently developed numerical approach for determining forces and moments in floaters, are developed to simulate rigid-body motions and sectional forces and moments of a reference 5-MW braceless semi-submersible wind turbine in turbulent winds and irregular waves corresponding to below rated, at rated and above rated conditions. The simulated responses are compared with measurements of a 1:30 scaled model test using a real-time hybrid testing approach. In general, agreement between simulations and measurements are very good. Differences in spectral densities of the measurements and simulations have been quantified while the reasons for the differences have been thoroughly analyzed and discussed based on comparisons of measurements in different conditions and numerical parametrical study. Effects of non-linear wave excitation loads and drag forces on the rigid-body motions and sectional forces and moments are analyzed while dominant load components in fore-aft bending moments in five cross-sections in the hull of the reference model are identified. The interface between the pontoons and central column of the reference model is identified as the most critical part. Both low frequency and wave frequency load effect should be accounted for. Mean forces and moments from wind and waves result in a change in configuration of mean wetted body surface of the hull when compared to its configuration in calm water. This may result in a considerable change in resultant sectional forces and moments even though change in resultant of the hydro pressure forces on whole of the wetted body surface could be very limited. For the analyzed model, simulated fore-aft bending moments of the model in wind and waves could be obtained by superimposing the results for wind only condition, and wave only condition except that the corresponding averaged wind induced forces and moments should be applied on the numerical model. This simplification can significantly reduce number of cases of short-term analysis required in long-term analysis. However, applicability of the simplification should be analyzed case by case in particular for a blunt structure with relatively large volume of displaced water in waves with relatively small wave length. Analysis and discussions given in this paper are based on available measurements of the model test. Hydroelastisity and structural vibration of the columns and pontoons of the hull are not accounted for by the numerical and experimental models. Suggestions for design of future model tests are given in this paper.

1 Introduction

Floating wind turbines are considered an attractive solution for harvesting offshore wind energy in relatively deep water, e.g. deeper than 80 m. In general, a floating wind turbine is composed of a Rotor Nacelle Assembly (RNA), a tower, a hull and a mooring system.

As required by relevant standards and guidelines for offshore wind turbines, e.g. [1-5], global responses, in terms of motions and sectional forces and moments, should be appropriately analyzed for limit state design checks. As the development of floating wind turbines is at an early stage, numerical simulations and model tests for analyzing the global responses of floating wind turbines in wind and waves are hot research topics.

Computer codes for analyzing floating wind turbines have been developed by combining the knowledge and computer codes for modelling hydro loads on offshore platforms and aerodynamic loads on land-based wind turbines for decades [6]. A review of conventional approaches for modelling aerodynamic loads on the RNA and tower, hydro loads on the hull and mooring lines of floating wind turbines is available in [7]. Features of some conventional time-domain computer codes are tabulated in [8]. Global responses of the RNA, tower, and mooring system, and rigid-body motions of a given floating wind turbine can be simulated in these codes by generating and solving finite element model for the floating wind turbine, while Morison formula and/or the conventional hybrid frequency-time domain approach [9] is used to model hydro loads on the hull of the floating wind turbine. Morison formula is an empirical formula and, in general, applicable when wave length is larger than five times the diameter of the slender structure's cross-section [10]. The computer codes which implement the conventional hybrid frequency-time domain approach cannot capture the sectional forces and moments in the hull since the hull is modelled as a rigid-body with 6 d.o.f.s in the finite element model. Luan et al [9] recently developed an approach based on an extension of the conventional hybrid frequency-time domain approach, for which the hull is modelled as multi-bodies. The developed approach can be easily implemented in various state-of-the-art time-domain computer codes for floating wind turbines, e.g. Simo/Riflex/Aerodyn, OrcaFlex and FAST+CHARM3D, to extend their capabilities to analyze sectional forces and moments in structural components of a generic floater. A moderate wave-only experimental validation for this approach is made in [11].

Global responses of floating wind turbines in wind and waves can be measured (and analyzed) by carrying out model tests. Conventional model tests for measuring wave induced responses of a floating unit are designed to satisfy geometrical and kinematic similarities and equality according to Froude number ensure similarity between inertia and gravity forces of the experimental and actual models. However, similarity between inertia and viscous forces of the models cannot be achieved since, in practice, equality in Reynolds number cannot be satisfied at the same time. Different Reynolds number may indicate different patterns of fluid flows around the experimental and actual models. Necessary corrections are needed if the measurements are sensitive to the viscous forces. Due to the same reason, similarity between inertia and aerodynamic loads on the RNA, which are important to responses of floating wind turbines, cannot be achieved either, see [12-14]. To solve this problem, various forms of "non-geometrical scaling" of the wind turbine rotor have been developed to improve the aerodynamic load modeling in wind-wave model tests. For example, one form of non-geometrical scaling is to replace the wind turbine rotor with a drag disk, e.g. [15, 16]. A more sophisticated method of non-geometrical scaling is to modify the wind turbine airfoil shape and chord length to

obtain improved performance at low Reynolds numbers [17-20]. These non-geometrical scaled wind turbines can be designed to achieve the same non-dimensional thrust coefficient as the reference full scale wind turbine in a specified steady condition (calm water, constant wind speed, and fixed rotational speed and pitch angle of the blades). Therefore, the "non-geometrical scaled" wind turbines can be used to physically analyze static response of the experimental model of floating wind turbines in steady conditions. However, it is still a challenge, which has not been solved yet, to make a performance-matched wind turbine model, which means to use the non-geometrical scaled wind turbines in model tests to accurately mimic Froude scaled actual aerodynamic loads on the rotor of the corresponding full scale reference wind turbine in dynamic conditions (turbulent winds, and/or regular or irregular waves, and/or with or without controller for blade pitch angle and rotational speed). This is because it is a challenge to design a non-geometrical scaled wind turbine for which the non-dimensional thrust coefficient is always identical to the corresponding coefficient of the reference full scale wind turbine in an arbitrary steady condition. As shown in [17], the non-dimensional thrust coefficient versus tip speed ratio curves of the non-geometrical scaled wind turbines can be very sensitive to the wind speed (the Renolds number). It is also a challenge to generate and/or measure constant and turbulent wind fields in a classical towing tank or ocean basin [21] as well. Implementation of real-time hybrid model testing approach, e.g. ReaTHM® [22], and reference [23], is a recent development for accurate modelling the actual aerodynamic loads in ocean basin. ReaTHM® relies on the assumption that actual aerodynamic loads on the full scaled reference wind turbine can be captured by the state-of-the-art aerodynamic computer codes, e.g. Aerodyn [24]. A numerical finite element model for the RNA and control system of the full scale reference wind turbine and numerical model of wind field are generated in a computer code which implements the state-of-the-art aerodynamic computer code to calculate the aerodynamic loads on the RNA in the wind field. The resultants of the calculated aerodynamic loads are down scaled (based on Froude scale) and physically applied on a Froude scaled model of the floating wind turbine, while in the computer code the hub of the RNA rigidly follows the measured rigid-body motions, which has been up scaled (based on Froude scale), of the experimental model. A 1:30 scaled braceless semi-submersible model test which implements the ReaTHM® testing approach was done by SINTEF Ocean in its ocean basin [25]. Sectional forces and moments in base of a side column and tower base of the model in different combined wind and wave conditions have been measured. ReaTHM® can appropriately address effects of the control system on the aerodynamic loads while the actual loaded forces can be measured in a straight-forward manner. A detailed description of the approach and its feasibility is available in [22, 26].

This paper intends to shed more light on sectional forces and moments in the hull of semi-submersible wind turbines submitted to combined wind and wave loads by thoroughly analyzing the measurements of the 1:30 scaled model test in SINTEF Ocean and corresponding numerical simulations. A Simo/Riflex model which implements the approach presented by Luan et al [9] has been generated. Sectional forces and moments in five cross-sections of the hull of the braceless semi-submersible wind turbine are analyzed. The hull of the braceless semi-submersible wind turbine is a static determinate structure. The external load on the hull is composed of wave excitation loads, added mass forces, potential damping forces, gravity, hydrostatic forces, and drag forces. Configurations of mean wetted body surface of the model in wind and waves and in wave only are different due to mean components of the wind loads on the rotor, tower and hull of the model. The difference means that hydrodynamic coefficients that are calculated for modeling hydro loads on the hull are different since values and distributions of hydro pressure forces on the hull are changed. Numerical sensitivity study and comparisons of measurements in different conditions are used to analyze effects of each component of the external loads, and inertial load on the sectional bending moments in different cross-sections of the hull. Simplifications for the numerical modelling are discussed based on the results of the parametric analysis. Sectional forces and moments in different cross-sections are compared. To quantify the differences between the numerical model and the experimental model, the simulated and measured fore-aft bending moments in the bases of the side column and tower are compared. The agreement is reasonably good.

In previously, comparisons of simulated and measured responses of floating wind turbines have been analyzed by some researchers, e.g. [27]. Geometrical scaled or non-geometrical scaled wind turbine, which cannot correctly mimic the Froude scaled aerodynamic loads on the corresponding full scale reference wind turbine in dynamic condition, are used in the model tests mentioned by the researchers in their publications, while these model tests are not designed for capturing sectional forces and moments in hull of floating wind turbines. For each model test, the wind turbine of the experimental model is modelled in its corresponding numerical model to simulate aerodynamic loads on the wind turbine while numerical wind field is generated based on measured wind speed at one specified fixed position in the model test. Consequently, the differences between the measurements and simulations are due to the differences between 1) the numerical wind field and actual wind field in the model test, 2) performance of the numerical and experimental models of the wind turbine and 3) mass properties of the numerical and experimental models and 4) hydro loads on the hull of the numerical and experimental models. These differences are mixed and make it difficult to analyze reasons for the differences between the measurements and simulations in quantity. To avoid this difficult situation, the aerodynamic loads which are actually loaded on the 1:30 scaled model analyzed in this paper are measured and loaded on their corresponding numerical model to ensure identical aerodynamic loads. As analyzed in detail later in this paper, although the aerodynamic loads are loaded as prescriptive loads the differences between the measurements and simulations only indicate differences in the hydro loads on the hull and the mass properties of the numerical and experimental models. The differences in the mass properties can be reduced to a negligible level by carrying out quality control and calibrations. The differences in each component of the hydro loads are analyzed in this paper.

2 Model tests

A layout of the experimental model, the Earth-fixed coordinate system (O^g-x^g-y^g-z^g) and load directions are shown in Figure 1. O^g is at geometrical center of water plane area when the model is in calm water. The specified dimensions of the semi-submersible hull are tabulated in Table 1 and shown in Figure 2. The mooring system is composed of three catenary chain mooring lines. Each mooring line has two segments from fairlead to anchor with constant solid circular cross-section. Design parameters are given in Table 2 and 3. The scaled value of the Young's modulus of the mooring lines of the experimental model is $6.3 * 10^9$ kN/m^2. Measured mass properties of the hull are given in [25]. However, as analyzed in [11], calibrated rather than measured mass properties are eventually used in development of numerical models due to the "model-the-model" principle which means to simulate the actual model tests as closely as possible [28]. The calibrated mass properties are given in Section 3, describing the numerical models used in this paper. Note that all the data and results presented and discussed in this paper are given in full scale and in the corresponding coordinate systems described in this paper. A linear scaling factor of $\lambda = 30$ and the Froude scaling law are used to scale the original data measured from the model test. Environmental conditions of the model tests are tabulated in Table 4. Fore-aft bending moments in the base of the side column 1 and tower are measured. A more detailed description of the model tests is found in [11, 25].

Table 1. Specified dimensions of the semi-submersible hull (Full-scale)

Central column diameter [m]	6.5
Side column diameter [m]	6.5
Pontoon height [m]	6
Pontoon width [m]	9
Central column freeboard [m]	10
Side column freeboard [m]	20
Center-to-center (central to side column) [m]	41
Center-to-edge (central column to pontoon end) [m]	45.5
Operating draft [m]	30
Displacement [tonne]	10,555

Table 2. Design parameters of a single mooring line (Full-scale)

Segment	Length (m)	Mass per length (kg/m)	Wet weight (kN/m)	Specified diameter (m)
Upper	240.00	235.0	2.005	0.195
Lower	367.55	446.0	3.804	0.269

Table 3. Arrangement of the mooring line anchors and fairleads described in the global coordinate system (Full-scale)

Fairlead	x^g	y^g	z^g	Anchor	x^g	y^g	z^g
1	45.95	0	-27	1	603	0	-200
2	-22.98	39.8	-27	2	-301.5	522.2	-200
3	-22.98	-39.8	-27	3	-301.5	-522.2	-200

Table 4 Environmental conditions of selected model tests (Full-scale)

Reference No.	H_s [m]	T_p [s]	Mean wind speed at nacelle [m/s]	Turbulence intensity factor [%]	Direction of waves [degree]	Direction of winds [degree]	Model test duration [hour]	Note
2410	15.3	14	None	None	0	None	3	Irregular wave only condition. JONSWAP wave spectrum
2420	3.6	10.2	None	None	0	None	3	
1713	None	None	11	17.0	None	0	3	Turbulent wind only condition. Kaimal wind spectrum
1733	None	None	25	13.2	None	0	3	
4121	5.9	11.3	25	13.2	0	0	3	Turbulent wind and irregular waves. JONSWAP wave spectrum and Kaimal wind spectrum. In operation
4132	5.9	11.3	25	13.2	0	0	3	
4310	3.6	10.2	11	17.0	0	0	3	
4410	5.2	8	8	19.5	0	0	3	

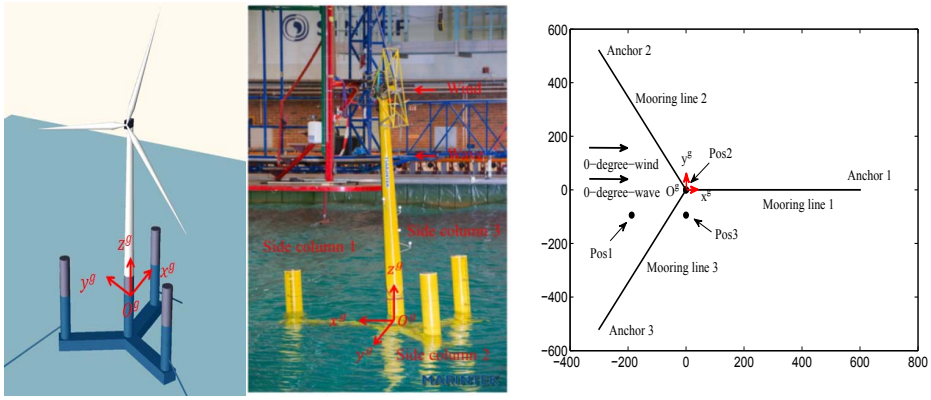

Figure 1 Layout of the experimental model

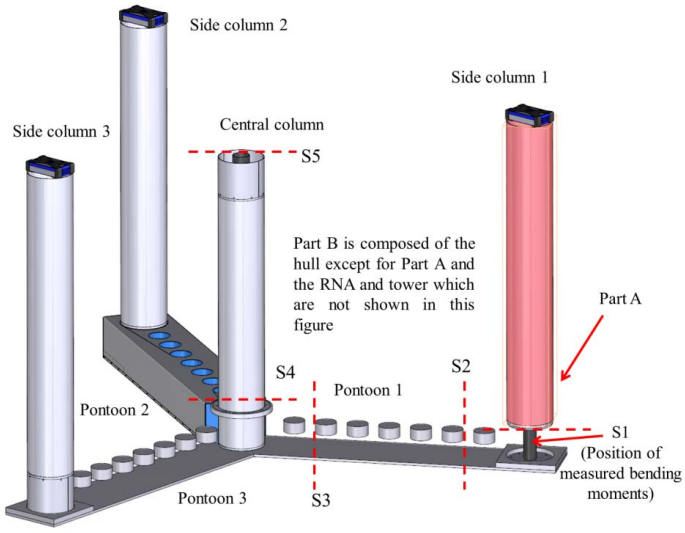

Figure 2 A layout of the hull of the experimental model, courtesy of Fredrik Brun (SINTEF Ocean). Note that the configurations of the three pontoons are identical. Some parts of the configurations of Pontoon 1 and 3 are not shown.

3 Numerical models and calibrations

3.1 Numerical models

Simo and Riflex [29, 30] are used to simulate sectional forces and moments in five cross-sections (denoted as SX, X=1, 2,…,5) in the hull of the semi-submersible wind turbine. S1 represents a horizontal cross-section on the base of side column 1. S2 and S3 are vertical cross-sections on Pontoon 1. S4 is a horizontal cross-section on base of central column. S5 is a horizontal cross-section on the base of tower, see Figure 2. The geometrical center of the cross-sections are tabulated in Table 5 in a body-fixed coordinate system (denoted as O^b-x^b-y^b-z^b) which coincides with the global coordinate system (O^g-x^g-y^g-z^g) when the wind turbine is located in calm water. Each cross-section divides the model into two part: Part A and B. We denote the part which includes the tower and RNA as Part B, see Figure 2 for an example.

Key features and limitations of the developed numerical models are highlight as follows:

- A time-domain finite element model is generated to simulate sectional forces and moments
- Effect of flexible modes of the hull and tower on motions and sectional forces and moments (effect of hydroelasticity) is negligible as the hull and tower of the experimental model is stiff.
- Wave excitation and radiation loads on Parts A and B are modelled by using hydrodynamic coefficients that are obtained by solving a first order boundary value problem based on corresponding mean wetted body surface of the hull with rigid-body assumption for the hull. The second and higher order wave loads on the hull are not modelled except for the drag forces which are modelled by the drag term of Morison formula
- The measured aerodynamic loads are applied on Part B as prescriptive loads. The differences between the measurements and simulations only indicate the differences in the hydro loads on the hull and the mass properties of the numerical and experimental models.
- Necessary calibrations are carried out to reduce uncertainties between the numerical and experimental models.
- Luan et al's approach is available to a generic floater (with a static determinate or indeterminate structure). The numerical models used in this paper are its specific applications. More detailed descriptions and limitations of the approach are referred to [9]

A detailed description of the developed numerical models is given as follows:

To simulate sectional forces and moments in a given cross-section, a time-domain finite element model is generated and solved in Riflex in the global coordinate system. The model is composed of 183 truss elements for modelling the three mooring lines, three artificial beam elements for capturing sectional forces and moments in the corresponding cross-section and two control nodes for modelling external and inertial loads on the corresponding Parts A and B.

If we denote location of geometrical center of SX as $(x_{SX}^b, y_{SX}^b, z_{SX}^b)$ in the O^b-x^b-y^b-z^b coordinate system, positions of end nodes of the corresponding artificial beams are given in Table 6. The artificial beam elements are massless. There are no external loads on the artificial beam elements. Each artificial beam element only has axial and torsional stiffness. The columns and pontoons of the experimental model are designed to have sufficient stiffness to make hydroelasticity effects on the model negligible. Therefore, for each artificial beam element, the product of the Young's modulus and cross-section area is specified as 10^9 kN, while, the product of the torsional rigidity and modulus of rigidity are specified as 10^9 kNm^2/rad.

The external and inertial loads on Parts A and B are modelled in Simo by using the Luan et al's approach which is initially described in [9] and applied on the control nodes in the finite element model generated in Riflex. Each control node has 6 d.o.f.s. Each of the end nodes of the artificial beam elements and the top end nodes of the mooring lines (the fairleads) rigidly follows the motions of the corresponding control node.

We denote position of the control nodes corresponding to the corresponding Parts A and B for the cross-section SX in the global coordinate system as $\boldsymbol{\eta}^{SX,A}(t)$ and $\boldsymbol{\eta}^{SX,B}(t)$, respectively. $\boldsymbol{\eta}^{SX,A}(t)$ and $\boldsymbol{\eta}^{SX,B}(t)$ are 6×1 vectors and used to represent motions of the Parts A and B. When the floating wind turbine is in calm water, the control nodes are located at the origin of the global coordinate system while all of the terms in $\boldsymbol{\eta}^{SX,A}$ and $\boldsymbol{\eta}^{SX,B}$ are zero.

Body related coordinate systems for Parts A and B corresponding to cross-section SX are generated in Simo and denoted as $O^{r,A,SX}$-$x^{r,A,SX}$-$y^{r,A,SX}$-$z^{r,A,SX}$ and $O^{r,B,SX}$-$x^{r,B,SX}$-$y^{r,B,SX}$-$z^{r,B,SX}$, respectively. The O^b-x^b-y^b-z^b and body-related coordinate systems are coincident when the model is located at its mean position in calm water. $O^{r,A,SX}$ and $O^{r,B,SX}$ rigidly follow rigid-body motions of the O^b but the orientation of the body-related coordinate systems and the vertical position of the $O^{r,A,SX}$ and $O^{r,B,SX}$ are fixed (as the same as the body-related coordinate systems when the model is located at its initial position in time-domain simulation).

Applying Luan et al's approach, the first order wave excitation and radiation loads are modeled as forces and moments acting on the $O^{r,A,SX}$ and $O^{r,B,SX}$, while the forces and moments are determined by corresponding hydrodynamic coefficients and first and second derivative of $\boldsymbol{\eta}^{SX,A}(t)$ and $\boldsymbol{\eta}^{SX,B}(t)$ and wave elevation of incident waves.

The hydrodynamic coefficients are obtained by the following steps, 1) generating and solving a boundary value problem based on corresponding mean wetted body surface in O^f-x^f-y^f-z^f coordinate system (an earth fixed coordinate system) with rigid-body assumption for the hull, 2) calculating pressure forces on the mean wetted body surface based on the Bernoulli's equation and corresponding velocity potential, 3) integrating the pressure on the wetted body surface of the corresponding Part A or B using the coordinate system O^f-x^f-y^f-z^f to obtain the integrated forces and moments acting on the O^f, and 4) derive the

hydrodynamic coefficients based on the corresponding resultant forces and moments on the O^f in the O^f-x^f-y^f-z^f coordinate system.

Wind and wave loads on floating wind turbines have a steady (constant) component. The component is composed of constant forces and moments and results in a mean horizontal offset and title angle. Phase angle of each frequency component of incident wave should be updated based on the mean horizontal offset in particular for high frequency components which can be very sensitive to the mean horizontal offset. The configuration of the mean wetted body surface in the O^f-x^f-y^f-z^f coordinate system should be updated based on the mean title angle. The mean wetted body surfaces of the hull corresponding to 0-degree and α-degree tilt angles in the O^f-x^f-y^f-z^f coordinate system are shown in Figure 3.

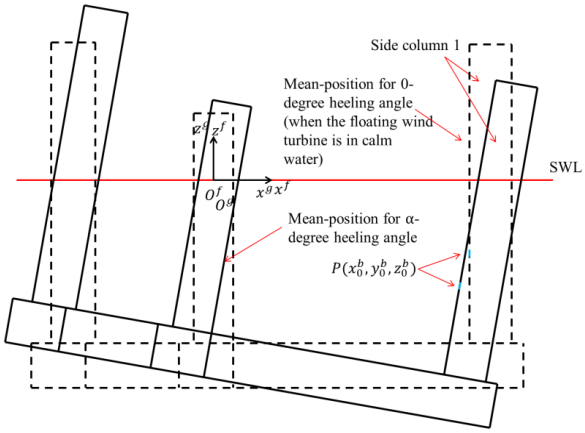

Figure 3 Configuration of mean wetted body surface of the hull subjected to different title angles

Morison's formula is used to model the hydrodynamic loads on the mooring lines, while the drag term of the Morison's formula is use to model the drag forces on the hull components. Non-dimensional drag and mass coefficients (C_d and C_a) for the segments of each mooring line are specified as 1.4 and 1.0 respectively, while C_d for width and height of the pontoons and columns are specified as 2.1, 1.7 and 0.5, respectively, according to [31]. Young's modulus of mooring lines of the numerical model is specified as $2.1 * 10^8$ kN/m^2 rather than $6.3 * 10^9$ kN/m^2, which is obtained by upscaling the measured value of the experimental model, to avoid numerical problems. In theory, the effect of this difference on mooring line tension and global responses of the model are negligible.

Aerodynamic loads which were applied on the experimental model were measured. The measured aerodynamic loads are applied on the control node for Part B to model the aerodynamic loads.

The numerical models do not include the second order and higher order hydrodynamic loads and hydroelastical effects except for the viscous drag forces, while the numerical models include hydrodynamic interactions between Parts A and B.

In Riflex, the time-domain finite element model is solved by using Newmark-β numerical integration ($\beta = 3.9$ and $\gamma = 0.505$). Time step is set to be 0.05 seconds. Rayleigh damping, which is a linear combination of the Riflex generated global mass and stiffness matrices, is used for modelling effect of structural damping. The corresponding mass and stiffness proportional coefficients are set to be 0 and 0.005, respectively. More explanations are given in [30].

Table 5 Positions of geometrical center of the five cross-sections in the body fixed coordinate system

	S1	S2	S3	S4	S5
x_{SX}^b	41	31.5	7.5	0	0
y_{SX}^b	0	0	0	0	0
z_{SX}^b	-27	-27	-27	-22	10

Table 6 Positions of end nodes of the three artificial beams that correspond to the SX in the body-fixed coordinate system (Units in meter)

	End 1	End 2
Artificial beam 1	(x_{SX}^b-0.1, y_{SX}^b, z_{SX}^b)	(x_{SX}^b+0.1, y_{SX}^b, z_{SX}^b)
Artificial beam 2	(x_{SX}^b, y_{SX}^b-0.1, z_{SX}^b)	(x_{SX}^b, y_{SX}^b+0.1, z_{SX}^b)
Artificial beam 3	(x_{SX}^b, y_{SX}^b, z_{SX}^b-0.1)	(x_{SX}^b, y_{SX}^b, z_{SX}^b+0.1)

Table 7 Mass properties of the numerical models. The center of gravity is described in the body-fixed coordinate system with respect to O^b. The moments of inertia are about the center of gravity.

	Mass [tonnes]	Centre of gravity [m]			Moments of inertia [tonnes*m^2]					
		x^b	y^b	z^b	I_{xx}	I_{yy}	I_{zz}	I_{xy}	I_{xz}	I_{yz}
Complete model	9,730.0	0	0	-20.35	10,308,320	10,293,841	7,637,715	0	20,759	0
Part A for S1	456.7	41	0	-12.93	96,093	96,093	2,193	0	0	0
Part A for S2	1,422.7	37.6	0.0	-24.6	170,571	193,411	27,594	0.0	0.0	-25,754
Part A for S3	2,574.7	29.5	0.0	-26.7	187,382	474,115	295,068	0.0	0.0	-79,897
Part A for S4	8,712.0	0.0	0.0	-27.9	4,009,202.0	4,080,202.0	7,638,356.0	0.0	0.0	19,947.0
Part A for S5	8,873.2	0.0	0.0	-27.5	4,105,877.0	4,173,877.0	7,640,000.0	0.0	0.0	19,947.0

3.2 Calibrations

The "model-the-model" principle, which means to simulate the actual model tests as closely as possible [18], is used. As discussed in [11, 32], the anchors of the mooring lines are moved 1.5 meters away along the radial direction. The mass of the experimental model can be estimated based on the draft, configuration of the hull and resultant force of the vertical components of the mooring line tensions at the fairleads. Comparing the estimated mass to the measured mass, a 4.7% deviation is observed (Note that the difference due to the weight of the mooring lines has already been considered). Meanwhile there are discrepancies between the simulated and measured roll/pitch natural periods (obtained from decay tests) and mean heeling angle and fore-aft and side-to-side bending moment in turbulent wind-only conditions. As discussed in [32], deviations may exist in the measurements of the position of the center of gravity and moment of inertia. Consequently, a constant force is added to compensate the 4.7% difference and make the numerical model float at the same draft as the experimental model in calm water while the vertical position of the center of gravity and mass matrix of the corresponding Parts A and B are calibrated. Mass properties used in the numerical models are tabulated in Table 7. The procedure for calibrating the mass properties of the whole model and Parts A and B corresponding to S1 has been presented in [11]. Note that three forces and moments were used to adjust the inertial loads of Part B (corresponding for S1) and denoted as $-\boldsymbol{M}_{mass}^{addi}\ddot{\boldsymbol{\eta}}^{S1,B}(t)$. The $\boldsymbol{M}_{mass}^{addi}$ is a 6×6 matrix. The $\ddot{\boldsymbol{\eta}}^{S1,B}(t)$ is the second derivative of the $\boldsymbol{\eta}^{S1,B}(t)$. The three forces and moments are described in the $O^{r,B,S1}$-$x^{r,B,S1}$-$y^{r,B,S1}$-$z^{r,B,S1}$ coordinate system with respect to the $O^{r,B,S1}$. According to the results of a parametric study with respect to the effect of each term in the $\boldsymbol{M}_{mass}^{addi}$ on the motion responses and bending moments, all the terms in the $\boldsymbol{M}_{mass}^{addi}$ are zero except for $M_{mass,11}^{addi} = M_{mass,22}^{addi} = 571$ tonnes and $M_{mass,24}^{addi} = M_{mass,42}^{addi} = 5{,}690$ tonnes*m^2. Relative differences between the adjusted terms and the corresponding terms in the original measured mass matrix of Part B are less than 6%. As shown in [11], agreement between measured and simulated rigid-body motions and fore-aft bending moments in cross-section S1 of the semi-submersible wind turbine in moderate wave-only conditions is very good. Therefore, the same calibrated mass properties are used in the present paper while the same procedure is used to calibrate mass properties of Parts A and B corresponding to S5. We do not have any measurements to calibrate mass properties of Parts A and B corresponding to cross-section S2, S3 and S4. Therefore, these mass properties are reasonably estimated by the authors according to the calibrated mass properties and mass distribution of the original design described in [33].

In numerical models for simulating sectional forces and moments in S1, S2 and S3, an inertial load vector ($-\boldsymbol{M}_{mass}^{addi}\ddot{\boldsymbol{\eta}}^{SX,B}$), a quadratic damping force vector ($-\boldsymbol{D}_{Q}^{addi}|\dot{\boldsymbol{\eta}}|^{SX,B}\dot{\boldsymbol{\eta}}^{SX,B}$) and a restoring load vector ($-\boldsymbol{K}_{rest}^{addi}\boldsymbol{\eta}^{SX,B}$), $\boldsymbol{X}$=1, 2, or 3, are added on the control node corresponding to the corresponding Part B. Forces and moments presented by the vectors are described in the $O^{r,B,SX}$-$x^{r,B,SX}$-$y^{r,B,SX}$-$z^{r,B,SX}$ coordinate system with respect to the $O^{r,B,SX}$, $\boldsymbol{X}$=1, 2, or 3. $\boldsymbol{D}_{Q}^{addi}$ and $\boldsymbol{K}_{rest}^{addi}$ are 6×6 matrixs. All terms in $\boldsymbol{K}_{rest}^{addi}$ are zero except for $K_{rest,11}^{addi} = -8$ kN/m and $K_{rest,15}^{addi} = K_{rest,51}^{addi} = -80$ kNm/m. All terms in $\boldsymbol{D}_{Q}^{addi}$ are zero except for $D_{Q,55}^{addi} = 40{,}013{,}494$ kNms^2/rad^2 for model tests 4410 and 4310. Note that the quadratic damping force vector is not added on the numerical models for test 4121. Similarly, $-\boldsymbol{M}_{mass}^{addi}\ddot{\boldsymbol{\eta}}^{SX,A}$, $-\boldsymbol{D}_{Q}^{addi}|\dot{\boldsymbol{\eta}}|^{SX,A}\dot{\boldsymbol{\eta}}^{SX,A}$ and $-\boldsymbol{K}_{rest}^{addi}\boldsymbol{\eta}^{SX,A}$, $\boldsymbol{X}$=4 or 5, is added on the control node corresponding to the corresponding Part A in the numerical models corresponding for S4 and S5.

These added forces and moments, to some extent, affect rigid-body motions of the model, in particular for low frequency components of the motions. Consequently, components of sectional forces and moments in the cross-sections that are related to motions, velocities and accelerations are affected by these added forces and moments. While, comparing to forces and moments in the specified cross-sections, the added forces and moments are negligible.

4 Comparisons for measured and simulated responses in operational conditions

Simulated and measured rigid-body motions and fore-aft sectional bending moments of the model in combined wind and wave conditions, i.e. model test 4410, model test 4310 and model test 4121, are compared.

The differences between the measurements and simulations are related to uncertainties in the measurements and the differences between the actual and simulated inertial and external loads on the semi-submersible wind turbine. In another word, the simulated and measured responses, e.g. rigid-body motions and sectional forces and moments, will be identical, if the simulated and actual inertial and external loads are identical, and the actual responses can be accurately measured. The external

loads are composed of aerodynamic loads, hydro loads and gravity forces. We can assume that the differences between the simulated and actual aerodynamic loads are negligible since the measured aerodynamic loads are applied on the numerical model as prescriptive loads. While, as analyzed by [25, 26], we can assume that sensors used in the model test can accurately measure the rigid-body motions, fore-aft sectional bending moments, wave elevation and the actual applied aerodynamic loads on the experimental model.

Consequently, differences in simulated and measured responses indicate differences between simulated and actual inertial loads, gravity forces and hydro loads.

The differences between simulated and actual inertial loads and gravity forces are related to uncertainties in the mass properties and the differences in measured and simulated rigid-body motions. As analyzed in [11, 32] and Section 3.2 of this paper, measurements of the mass properties and configurations of the mooring lines and hull of the experimental model may be uncertain. Therefore, essential calibrations are carried out to reduce these uncertainties, see Section 3.2.

Objective of this section is to identify differences between the simulated and actual hydro loads via comparing the simulated and measured responses.

Note that the developed numerical models cannot completely account for all the components of the second and higher order hydro loads however these loads inherently exist in the experimental tests. In addition, the drag term of Morison formula [31] is used to model the viscous drag forces on the hull and mooring lines. This is an empirical formula. While, the coefficients for simulating the viscous drag forces are determined according to the Reynolds number, Keulegan-Carpenter numbers and surface roughness which correspond to the full size model rather than the Froude law scaled model. Consequently, the drag coefficients need to be appropriately calibrated, see Section 3.2. The hydro loads can be further classified as wave excitation loads, radiation loads, and hydrostatic pressure forces, see [9]. Note that these loads are related to the configuration of the wetted body surface of the hull. The sensitivity study and comparisons of measurements in different conditions are used to analyze effects of these components on rigid-body motions and sectional bending moments, see Section 5. The effect of these components is used to identify reasons for the differences between the measurements and simulations presented in this section.

In this section, the measurements correspond to three different turbulent wind conditions, which includes turbulent winds with mean wind speed below (8 m/s), at (11 m/s) and above (25 m/s) the rated wind speed of the 5-MW wind turbine. 3-hour realizations of wave elevation are generated in the time-domain models according to the corresponding 3-hour realizations of the measured wave elevations; while the measured aerodynamic loads are loaded on the time-domain models, correspondingly. 1-hour realizations of rigid-body motions and bending moments are selected from the 3-hour simulated realizations by neglecting transient processes (first 1,000 seconds of each realization).

Spectral density functions are obtained by applying inverse Fourier transform, with a fixed smoothing parameter, of the autocorrelation function of the 1-hour realizations. Regarding the spectral density functions, we focus on spectral densities in frequency range of 0 rad/s to 2 rad/s. Major parts of areas under spectral density curves of incident wave-elevations and thrust forces and moments applied on the rotor are in wave-frequency-range (defined as from 0.3 rad/s to 2 rad/s) and low frequency-range (defined as from 0 rad/s to 0.3 rad/s), respectively, see Figure 4. The turbine is in operational condition in these model tests.

Relative difference (n_r) of standard deviations of simulations and measurements are calculated based on the area under the corresponding spectral density curves in the corresponding specified frequency range, see Eq. (1) and [34]. In Eq. (1), $m_{0,s}$ represents the area of the part under the spectral density curve of a simulated response in a specified frequency range, i.e. full frequency-range, low frequency-range and wave-frequency-range. Similarly, $m_{0,m}$ represents the area of the part under the spectral density curve of a measured response in a specified frequency range.

$$n_r = \frac{\sqrt{m_{0,s}} - \sqrt{m_{0,m}}}{\sqrt{m_{0,m}}} * 100\% \qquad (1)$$

We denote a simulated and a measured response as x and y, respectively. Transfer function between x and y can be calculated by using Eq. (2). G_{xy} and G_{xx} are one-side spectra that are derived from corresponding cross-correlation and autocorrelation with respect to the realizations of x and y, respectively [35]. $H_{xy}(\omega)$ is a complex number. Real and imaginary parts are denoted as Re and Im respectively. Phase angle (α) between x and y is derived based on the corresponding values of Re and Im.

$$H_{xy}(\omega) = \frac{G_{xy}(\omega)}{G_{xx}(\omega)} = Re + Im * i \qquad (2)$$

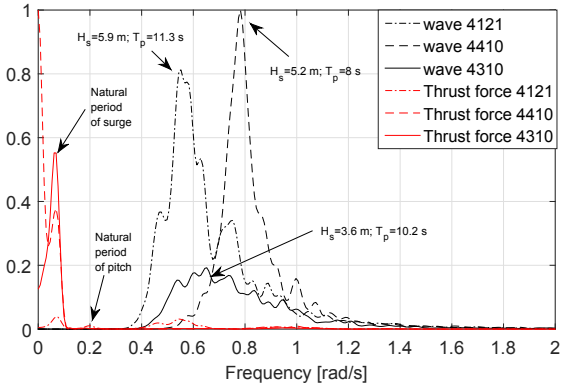

Figure 4 Normalized spectral densities of wave elevations and thrust forces applied on the rotor.

4.1 Comparisons of measured and simulated rigid-body motions in operational conditions

In general, agreement between simulated and measured rigid-body motions, in terms of spectral densities and phase angle, is very good. Relative difference of standard deviations of simulated and measured pitch in full frequency-range is less than 4%. Differences in phase angle between simulated and measured motions are no more than 20 degrees, see Figure 8. For the phase angles, we focus on the differences in frequency range from 0 rad/s to 1 rad/s since the responses in the rest frequency range are very limited.

Wave-frequency components in the surge and pitch motions are limited when compared to the corresponding low frequency components, see Figures 5 and 6. As analyzed later in this paper, the difference between simulated and measured wave-frequency components in the surge and pitch motions could be induced by the second and higher order wave excitation loads which are inherently exist in the model tests but are not modelled in the numerical models and/or differences between the simulated and actual first order wave excitation loads on the hull. The agreement between wave-frequency components of the heave motion of the numerical and experimental models is very good.

Low frequency responses of the model with frequency components around its natural frequencies (0.073rad/s for surge, 0.21 rad/s for pitch and 0.246 rad/s for heave) are sensitive to the second and higher order hydro loads (potential loads and viscous drags) and restoring stiffness, while low frequency responses of the model with frequency components less than 0.05 rad/s are sensitive to the restoring stiffness. As analyzed later in this paper, the differences between the measured and simulated heave motions with frequency components from 0.2 rad/s to 0.3 rad/s, and the surge motions with frequency components from 0 rad/s to 0.1 rad/s are due to differences in the second and higher order hydro loads of the numerical and experimental models. When the effect of the second and higher order hydro loads on the low frequency surge and pitch motions are relatively small (i.e. low frequency surge motion of model test 4310, and pitch motions of model test 4310, 4410 and 4121), very good agreement between simulated and measured surge and pitch motions can be achieved by adjusting (calibrating) restoring stiffness of the numerical mooring lines and quadratic damping coefficients. n_r for standard deviations of the simulated and measured pitch motion in low frequency-range is less than 3%, while n_r for standard deviations of the simulated and measured surge motion of the model test 4310 in the low frequency-range is less than 0.34%.

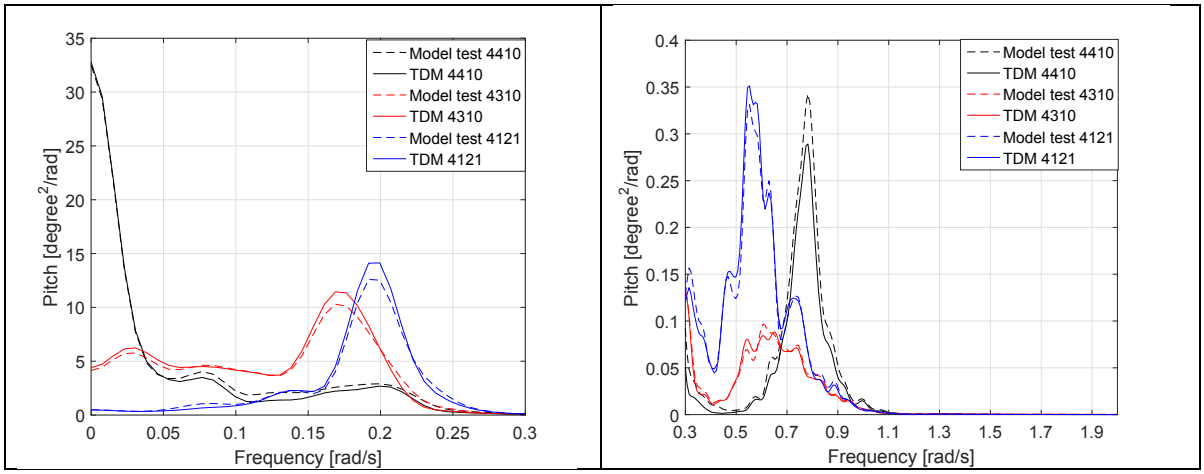

Figure 5 Comparisons of spectral densities of simulated and measured pitch motions in operational conditions

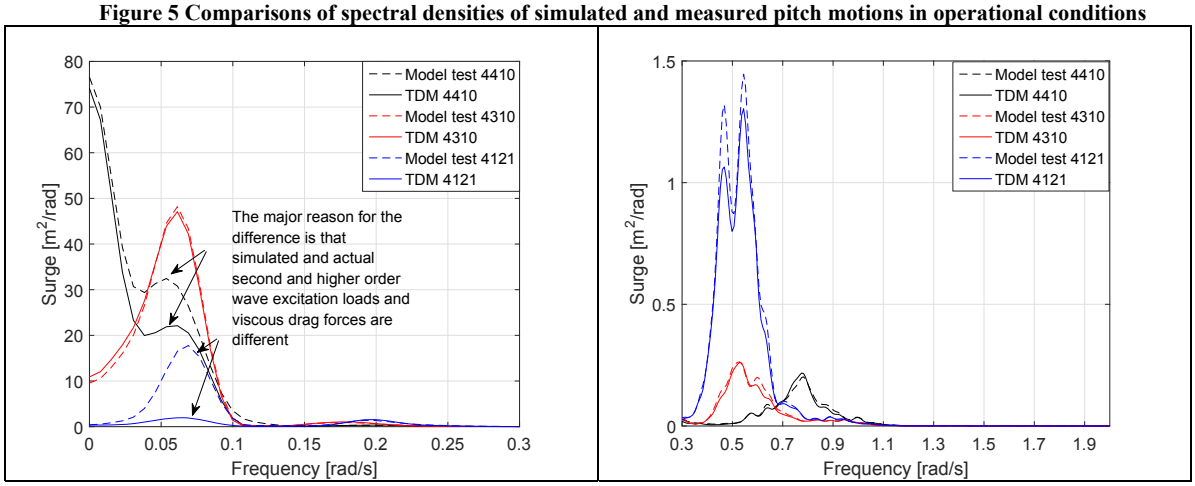

Figure 6 Comparisons of spectral densities of simulated and measured surge motions in operational conditions

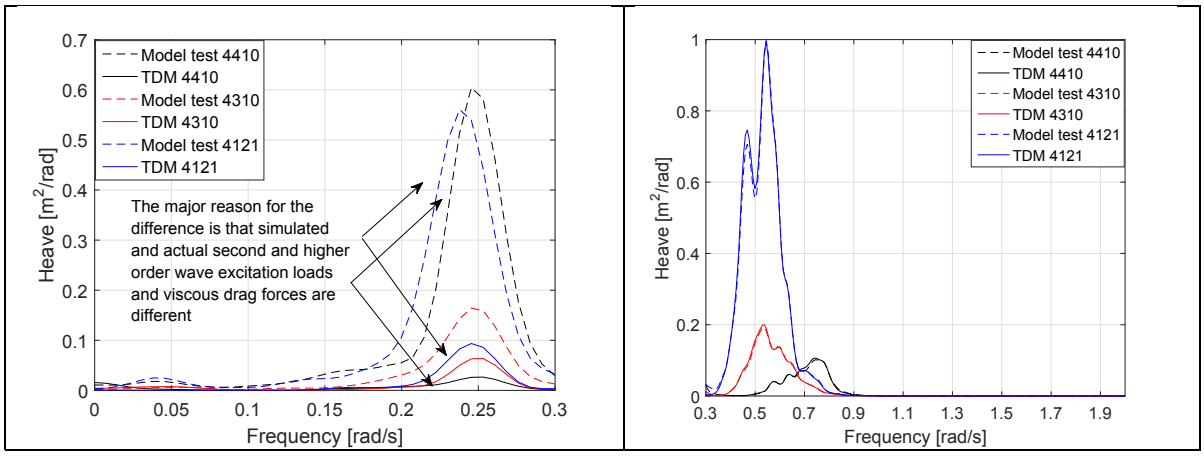

Figure 7 Comparisons of spectral densities of simulated and measured heave motions in operational conditions

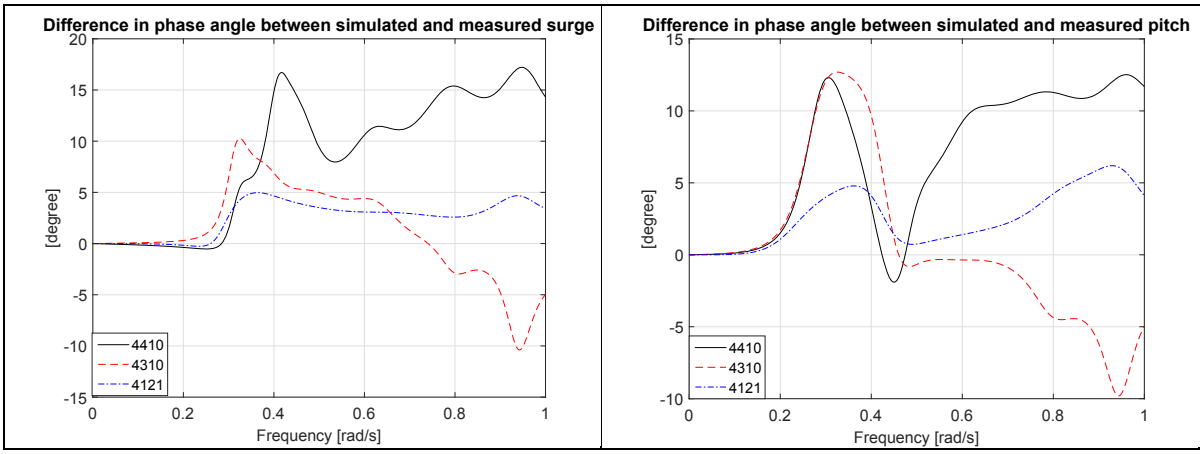

Figure 8 Difference in phase angle between simulated and measured surge (Left Figure) and pitch (Right Figure) motions in operational conditions

Note that, as shown in Section 3.2, we did not make calibrations with respect to quadratic damping coefficients for the surge motions. This is because that the model tests were not designed for distinguishing the second and higher order wave excitation loads and viscous drag forces from the measured responses. Fortunately, the differences in the surge motions have very limited effects on sectional bending moments.

Comparisons of measured and simulated bending moments are given as follows. More detailed analysis is available later in this paper.

4.2 Comparisons of measured and simulated bending moments in operational conditions

In general, agreement between simulated and measured fore-aft bending moments, in terms of spectral densities and phase angle, is very good. $|n_r|$ for standard deviations of simulated and measured fore-aft bending moments in full frequency-range in the tower base and base of the side column 1 are less than 4% and 10%, respectively. While differences in phase angle between simulated and measured bending moments are no more than 25 degrees, see Figure 9-13. Mean values of the fore-aft bending moments in the base of the side column (S1) and base of the tower in difference environmental conditions can be significantly different. For instance, mean value of the measured fore-aft bending moment in S1 in the model tests 4121 and 4310 are -2,885 kN*m and -10,050 kN*m. To highlight differences in variations of the measured and simulated fore-aft bending moments in different model tests with respect to time, mean values of realizations presented in Figures 12 and 13 have been removed. In general, agreement between the simulated and measured mean values of the fore-aft bending moments in S1 and S5 is good and reasonable. For example, relative difference between the simulated and measured mean values of the fore-aft bending moment in S5 is less than -1.3% (the relative difference is only -0.19% in the model test 4310). Mean values of the fore-aft bending moments in S1 are affected by mean components of the second and higher order hydrodynamic loads on the side column 1, e.g. mean wave (drift) forces and moments, which inherently exist in the experimental model test but are not modelled in the numerical models. However, absolute values of the differences between the mean values of simulated and measured fore-aft bending moments in S1 are small and have very limited effect on extreme responses while, roughly speaking, fatigue damage is related to the variations rather than the mean values of the bending moments. The differences between the mean values of the simulated and measured fore-aft bending moments in S1 in the model tests 4121, 4410 and 4310 are -649 kN*m, -714 kN*m and -331 kN*m, respectively, while simulated 1 hour maximum fore-aft bending moments in S1 in these model tests are 51,338 kN*m, 49,658 kN*m and 29,487 kN*m, correspondingly and respectively.

Therefore, in this section, we focus on comparing the differences in standard deviations and spectral densities of the simulations and measurements.

As analyzed in [26], we expect that the differences between the applied aerodynamic loads on the numerical and experimental model are negligible. Major reasons for the difference between wave-frequency components of the simulated and measured bending moments are identified as:

- Differences in the modelled and actual wave excitation loads and radiation loads.
- Differences in the rigid-body motions.

The major reasons for the difference between low frequency components of the simulated and measured bending moments are identified as:

- Differences in the modelled and actual fluctuations of hydrostatic pressure forces and viscous drag forces.
- Differences in the rigid-body motions.

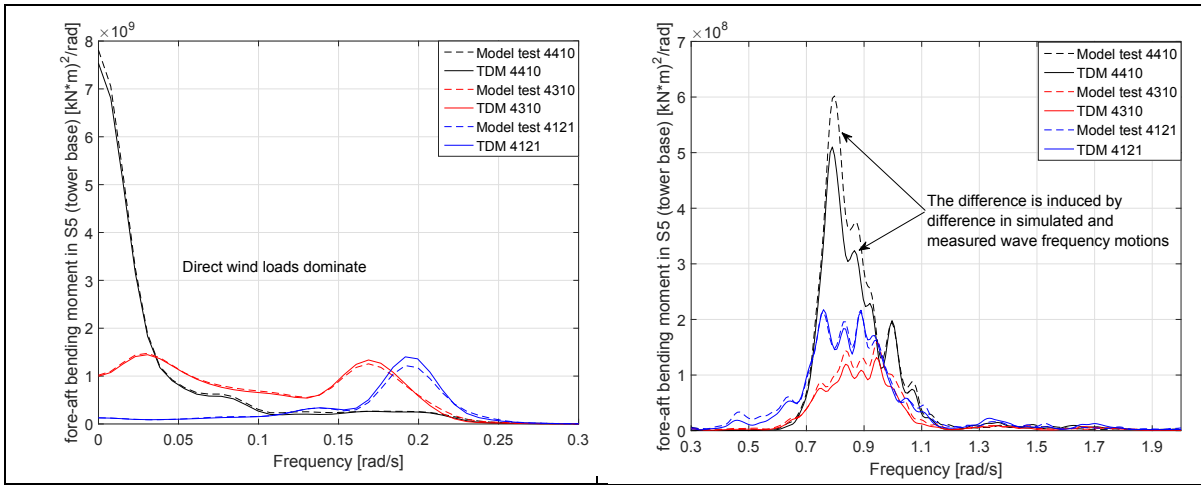

Figure 9 Comparisons of spectral densities of the simulated and measured fore-aft bending moments in the tower base (S5)

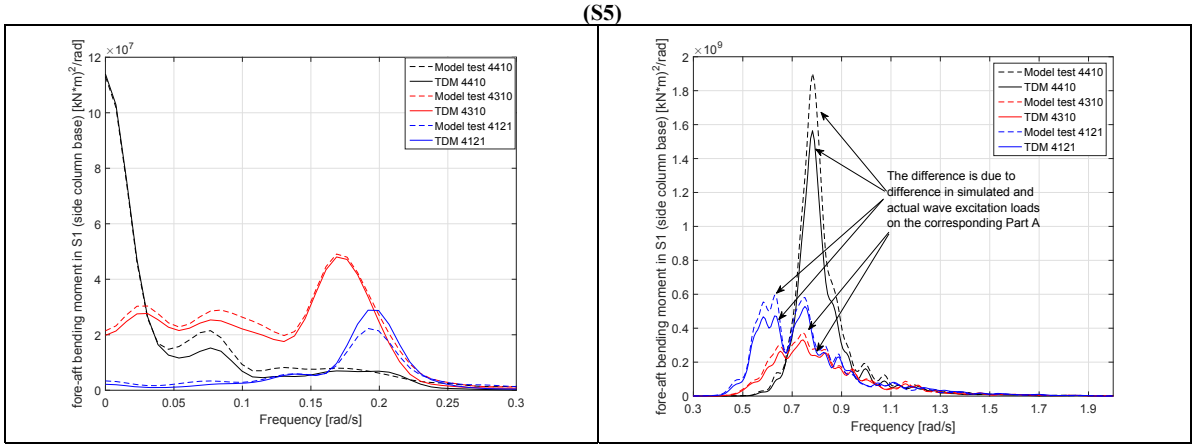

Figure 10 Comparisons of spectral densities of the simulated and measured fore-aft bending moments in the base of side column 1(S1)

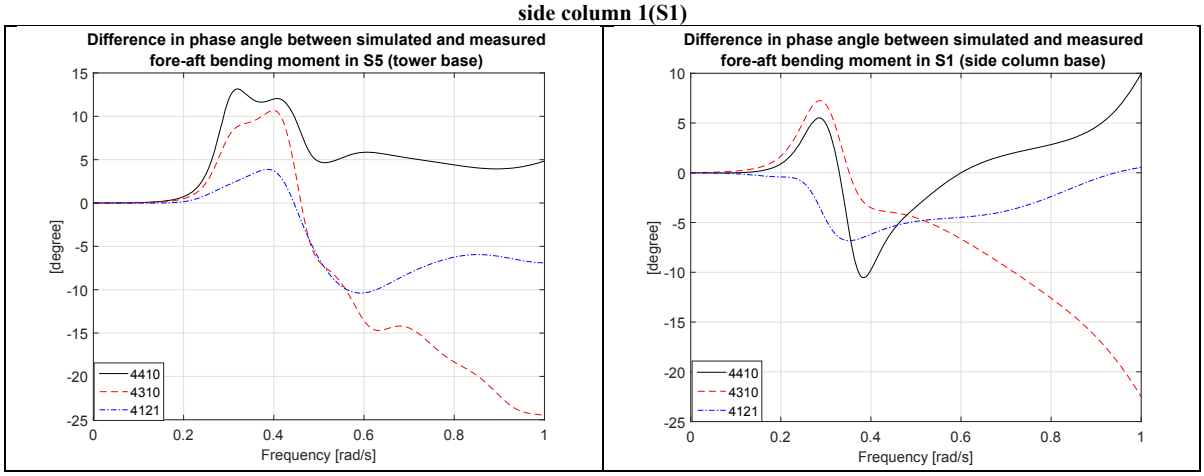

Figure 11 Differences in the phase angle between simulated and measured fore-aft bending moments in S1 and S5

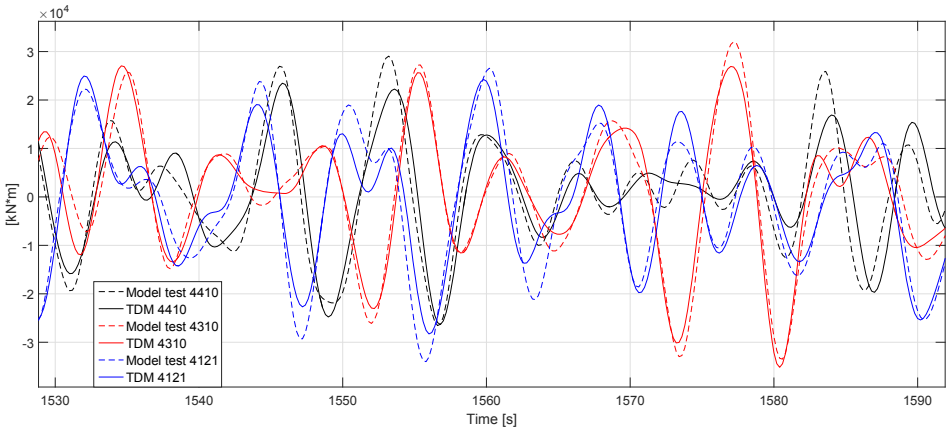

Figure 12 Comparisons of the simulated and measured realizations of fore-aft bending moments in the base of side column 1(S1) (mean values have been removed)

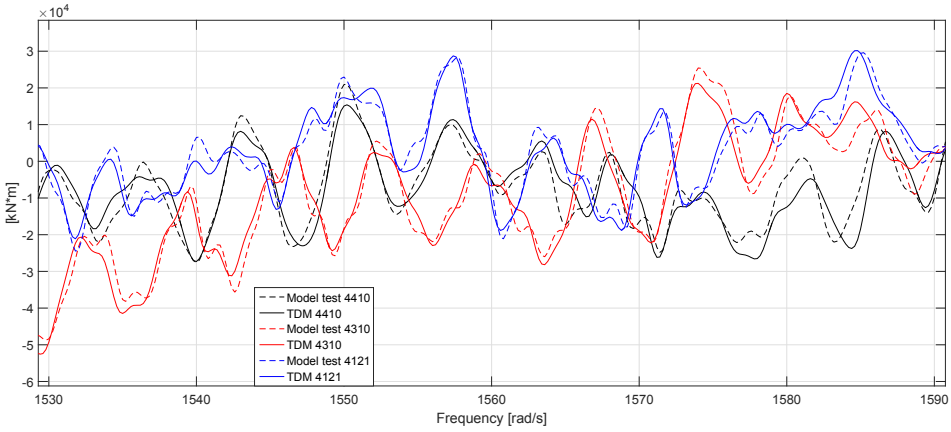

Figure 13 Comparisons of the simulated and measured realizations of fore-aft bending moments in the base of tower (S5) (mean values have been removed)

Table 8 Relative difference of standard deviations of the simulated and measured fore-aft bending moments in S1 and S5

n_r of Std. of the fore-aft bending moment [%]		Full frequency range	Wave frequency range, in range from 0.3 rad/s to 2 rad/s	Low frequency range, below 0.3 rad/s
S1	4121	-4.6	-4.5	2.8
	4410	-10.2	-10.1	-5.7
	4310	-5.3	-5.2	-4.9
S5	4121	-0.2	-2.2	3.0
	4410	-4.1	-6.8	-2.4
	4310	-2.2	-9.1	-0.3

The differences in the rigid-body motions result in differences in the gravity forces and inertial loads on the tower, and the inertial loads and fluctuated hydrostatic pressure forces on the side column 1. To eliminate these differences, the simulations can be modified by regenerating the simulated gravity forces, inertial loads and fluctuated hydrostatic pressure forces by using the measured rigid-body motions instead of using the simulated rigid-body motions.

Comparisons of spectral densities of the simulations with and without the modification and measurements of the fore-aft bending moment in S5 and S1 are given in Figures 14 and 15, respectively.

In Figure 14, spectral densities of the simulations with modification are almost identical to the spectral densities of the corresponding measurements. This fact indicates that the differences in the rigid-body motions are the major reason for the differences in simulated and measured fore-aft bending moments in the base of the tower, while the differences in the calibrated and actual moment of inertial of the tower with respect to the tower base is negligible.

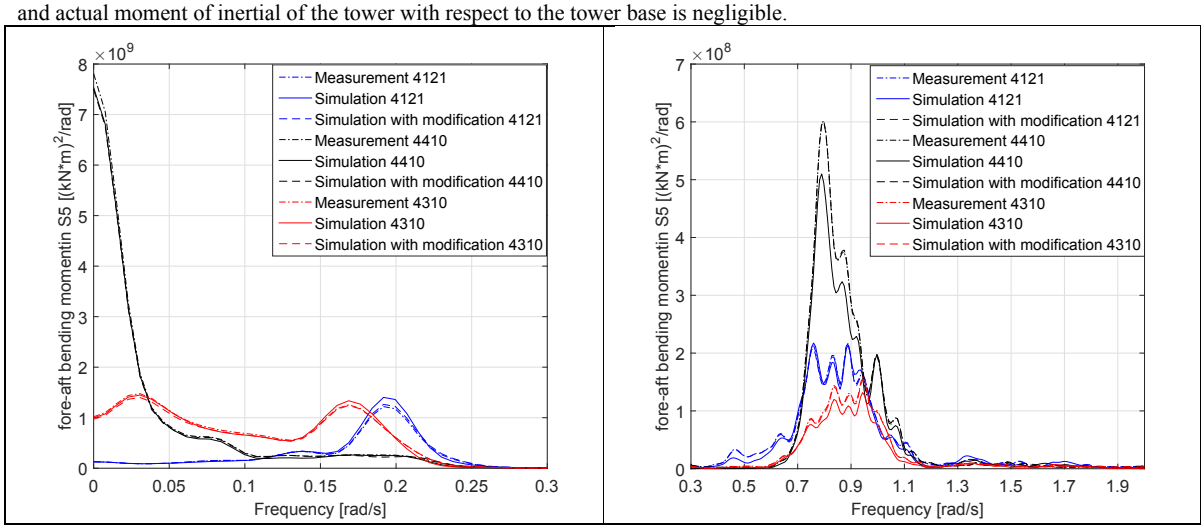

Figure 14 Comparisons of spectral densities of the simulated and measured fore-aft bending moments in the tower base (S5) with and without the modifications

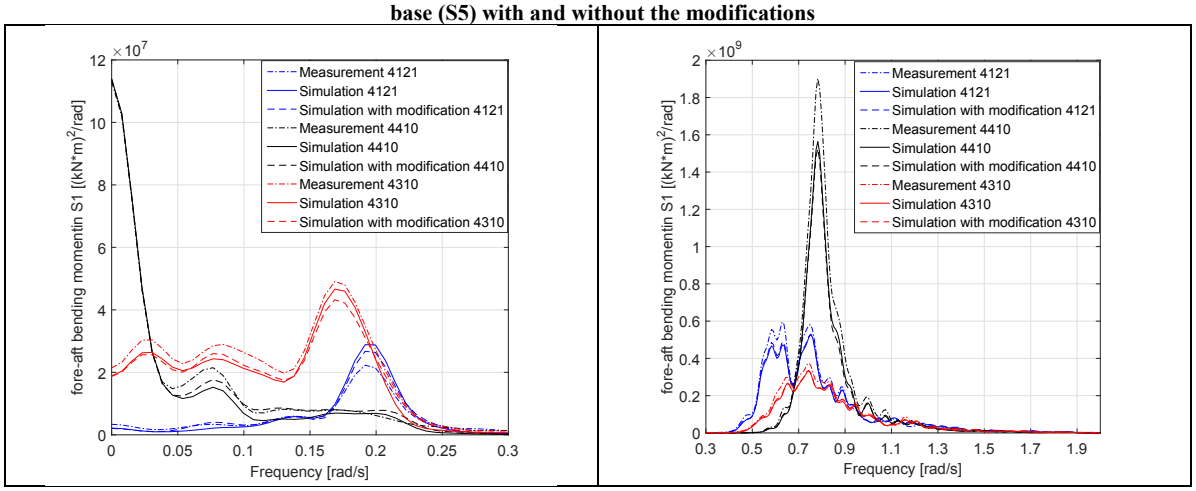

Figure 15 Comparisons of spectral densities of the simulated and measured fore-aft bending moments in the base of the side column 1 (S1) with and without the modifications

In Figure 15, differences in wave-frequency components of the spectral densities of the simulations with and without the modification are negligible. This indicates that differences exist in the modeled and actual wave excitation loads and radiation loads on the model since these loads dominate the fore-aft bending moments in S1, see discussions in Section 5.2. It should be kept in mind that the second and higher order hydro loads are not completely modeled in the numerical model, however the loads are inherently exist in the experimental model. Sclavounos et al [36] analyzed non-linear wave excitation loads on a fixed column in a sea state for which the significant wave height is 10.71 m and peak period of the wave spectrum is 15 seconds. Diameter of the column is 6 meters, which is close to the diameter of the columns of the reference semi-submersible wind turbine. Sclavounos et al show that the standard deviation of the second order wave excitation loads on the column in surge direction can be approximately 10% of the standard deviation of the first order wave excitation loads. Analyses in Section 5.1 confirm that the experimental model in model tests 4121 and 4410, for which the significant wave heights are 5.9 meters and 5.2 meters respectively, are subjected to considerable non-linear wave excitation loads. The differences in the simulated and actual wave excitation loads agree with, and explain the reason for, the differences observed in the simulated and measured rigid-body motions, see Figures 5, 6, and 8.

Analysis in Section 5.1 shows that the second and higher order wave excitation loads on the experimental model in the model test 4310, for which the significant wave height is 3.6 meters, are negligible. Consequently, the differences in the simulated and measured results of the model test 4310 are due to the differences in the modeled and actual first order wave excitation loads and radiation loads, and uncertainties and noises in the measurements. Some analysis with respect to the uncertainties and noises are referred to [11] for which the simulated and measured responses of the model in moderate waves, e.g. model test 2420, are analyzed. Note that elevation of incident waves in each model test is measured from its corresponding calibration test which is a repeated test without the experimental model. The model tests 2420 and 4310 correspond to the same calibration test since the incident waves in these model tests are designed to be identical. Differences between measured wave elevations in the calibration test and wave elevations of the actual incident waves in the model tests 2420 and 4310 can be quantified by comparing measurements of these model tests and their repeated tests. The model test 4132 is a repeated test for the model test 4121. Relative difference of standard deviations of measurements of the fore-aft bending moments in full frequency-range in S1of the model tests 4121 and 4132 is 2.48%. Note that repeated tests for the model tests 2420 and 4310, and calibration tests were not carried out. The relative difference of standard deviations of the simulated and measured fore-aft bending moment in the full frequency-range in S1 of the model subjected to environmental conditions of the model tests 4310 and 2420 are 5.3% and 1.4%, respectively. Accounting for the relative difference quantified by the repeated test, the authors feel that the agreements between the measured and simulated fore-aft bending moments in S1 for the model subject to environmental conditions of the model tests 2420 and 4310, respectively, are consistent to each other and acceptable. In addition, note that different sets of coefficients for modeling the first order wave excitation loads and radiation loads are used in the numerical models corresponding to the model tests 4310 and 2420. This is because, from the model test 2420 to the model test 4310, mean configuration of the wetted body surface of the experimental model changes with respect to the mean aerodynamic loads on the tower of the model. More analysis is referred to Section 5.4.

In Figure 15, for the model test 4310, the differences between the low frequency components of the spectral densities of the simulations with the modification and measurements indicate the differences in the modelled and actual hydrostatic pressure forces on the hull of the model, while the differences in the modelled and actual radiation loads also contribute to the differences in the components with frequencies around the natural frequency of the pitch motion. The differences in the hydrostatic pressure forces are also related to the changes in the mean wetted body surface. More explanation is referred to Section 5.4.

For the model tests 4121 and 4410, some differences in the low frequency components are due to the second and higher order wave excitation loads on the experimental model.

5 Analysis for effect of components on rigid-body motions and sectional bending moments

In this section, effect of the non-linear wave excitation loads, drag forces, each load component, and steady wind and wave loads induced changes with respect to the mean wetted body surface on the rigid-body motions and sectional bending moments are analyzed by comparing the measurements in different conditions and carrying out numerical sensitivity study.

As mentioned in Sections 3.1 and 4, the measured aerodynamic loads are applied on the numerical models. This ensures that the simulated and actual applied aerodynamic loads on the corresponding numerical and experimental models are identical. The differences between the simulated and measured responses are induced by the differences between simulated and actual hydrodynamic loads. As shown in Section 4, in general, agreements between the simulations and measurements are good. This indicates that differences between simulated and actual hydrodynamic loads are small. Consequently, in general, the aerodynamic loads and hydrodynamic loads on the experimental models can be reasonable accounted for in the numerical models. Therefore, the numerical models could be used to analyze the effect of the components on rigid-body motions and sectional bending moments of the 5-MW-CSC.

5.1 Analysis for the effect of the non-linear wave excitation loads and drag forces

Velocity potential can be used to describe unsteady, irrotational and inviscid fluid motion, for which the only external force field is gravity. Consequently, we can consider that the hydro loads are composed of the drag forces due to viscous effects of fluid and potential loads. The potential loads are resultants of pressure forces on the wetted body surface of the hull. We denote position of an arbitrary point on the wetted body surface of the hull in the global coordinate system as (x,y,z). The hydro pressure at the point follows from Bernoulli's equation, see Eq. (3).

$$p = C - \rho g z - \rho \frac{\partial \phi}{\partial t} - \frac{\rho}{2} \nabla\phi \cdot \nabla\phi \qquad (3)$$

where ϕ is time dependent velocity potential. C is a constant value related to the atmospheric pressure on free-surface. ρ is density of the sea. g is gravity acceleration.

ϕ is obtained by solving the corresponding boundary value problem [37]. Note that the positions of free-surface and the wetted body surface of the hull in the global coordinate system, and body-velocity are related to the motions of the hull. We define that the wave excitation loads as the potential loads which include ϕ but are independent to the motions of the hull. Rest part of the potential loads is related to the motions of the hull (including first and second derivative of the motions with respect to time).

The drag force on a 2-D cross-section of a structural component, e.g. column, and pontoon, is expressed by Eq. (4), see [5]. v and $\dot{r}$ are corresponding velocities of the fluid and cross-section. $\dot{r}$ can be derived from the motions of the hull. We can see that

$L_{drag}^{2D}(v,\dot{r})$ is composed of terms that are related to v^2, $\dot{r}^2$, and $v\dot{r}$. The terms related to v^2 behave as excitation forces while the terms related to $\dot{r}^2$ and $v\dot{r}$ behave as damping forces.

$$L_{drag}^{2D}(v,\dot{r}) = \frac{1}{2}\rho C_D D(v-\dot{r})|v-\dot{r}| \qquad (4)$$

Natural periods of the motions of the semi-submersible wind turbine are designed in the low frequency-range to avoid resonances excited by the first order wave excitation loads, while, resonances could be excited by the second and higher order wave excitation loads, excitation loads included in the drag forces, and aerodynamic loads. For wind waves in open sea, significant wave height tends to increase with increase of mean wind speed. This means wave load effect could be more and more important, e.g. effect of the second order wave loads on the motions in the low frequency-range could be more important than the effect of aerodynamic loads. Spectral density curves of the motions and fore-aft bending moments of the experimental model in the extreme and moderate wave only conditions are given in Figures 16 and 17 and serve as reference values for the motions and sectional forces and moments excited by the second order wave excitation loads in the low frequency-range. The second order wave loads affect the amplitudes and phase angles of the responses of the model.

Measurements in different wind-only and wind and waves conditions are compared as well, see Figures 16 and 17. Spectral density curves of measurements in the model test 4310 and its corresponding wind-only model test (model test 1713) are almost identical. This indicates that in operational conditions with moderate waves, e.g. the model test 4310, the second and higher order wave excitation loads and drag excitation forces are negligible.

Increased second and higher order wave excitation loads are expected in the model tests 4121 and 4410 as the significant wave height increases. As observed in Figure 16 the experimental model in the model test 4121 has more low frequency dynamic motions in the surge and heave motions than the one in the corresponding wind-only model test. Another evidence is the differences in spectral densities of the measured fore-aft bending moments in S1 of the model tests 4121 and 1733 (in frequency range from 0 rad/s to 0.15 rad/s).

Note that wave steepness and ratio between water depth and wave length of the measured incident waves in the model tests 4121, 4410 and 4310 indicate that wave crest kinematics of some measured waves are recommended to be modelled by Stokes 2nd order or Stokes 3rd order wave theory [46]

In addition to the low frequency excitation loads, the resonant responses are sensitive to the damping level of the model. Eq. (4) shows that the drag forces on the model include a force that is related to the first derivative of the motions of the hull and fluid velocity ($v\dot{r}$). This indicates that the damping level of the model is related to the incident waves.

The motions of the model in the wind-wave and wind-only conditions are simulated and compared in Figure 18. The numerical model does not include low frequency wave excitation loads but includes the drag forces. Comparisons of the low frequency components of the simulated motions of the model in the wind-waves and wind-only conditions show that the incident waves result in increase of the damping level of the model, while, as a result, the low frequency motions in the frequency ranges around the model's natural frequencies of the surge, heave and pitch motions can be significantly reduced. The observations in Figure 18 are supported by observations in comparisons of simulations of the conventional numerical models used in [9] for which aerodynamic loads (including aerodynamic damping effect) are accounted for by Aerodyn based on blade element momentum theory.

The differences in spectral densities of measured fore-aft bending moments in S5 and S1 of the model tests 4121 and 1733 (in the frequency range from 0.15 rad/s to 0.25 rad/s) are results of the differences in the pitch motions which are affected by the differences in the damping level and differences in low frequency excitation loads, i.e. 2nd and higher order wave loads and aerodynamic loads, see more discussions in Section 5.2. Effect of the wave excitation loads can be quantified in a straight-forward manner by carrying out a corresponding wave-only model test which is similar as the model tests 2410 and 2420. However, the wave-only model test was not carried out in the laboratory. Analysis and discussions given in this paper are based on available measurements. More systematical model tests are welcome in future.

As shown in Figure 15 and Table 8, the numerical model based on linear potential-flow theory underestimates the standard deviations of wave-frequency components of the fore-aft bending moments in S1 by 5% to 10%. The differences in the simulated and actual excitation loads are considered as the major reason for the differences. More experimental tests designed for distinguishing linear and non-linear hydro loads are recommended to be considered in future.

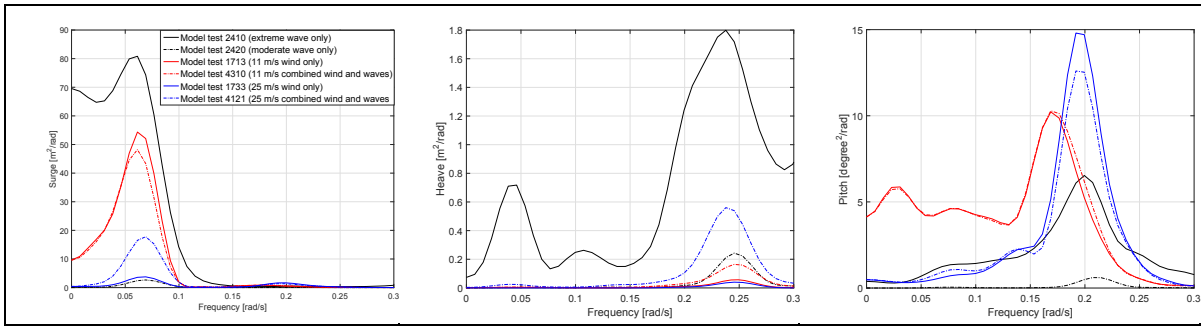

Figure 16 Comparisons of spectral densities of the measured surge, heave and pitch motions in the wind-only, wave-only and wind-wave conditions

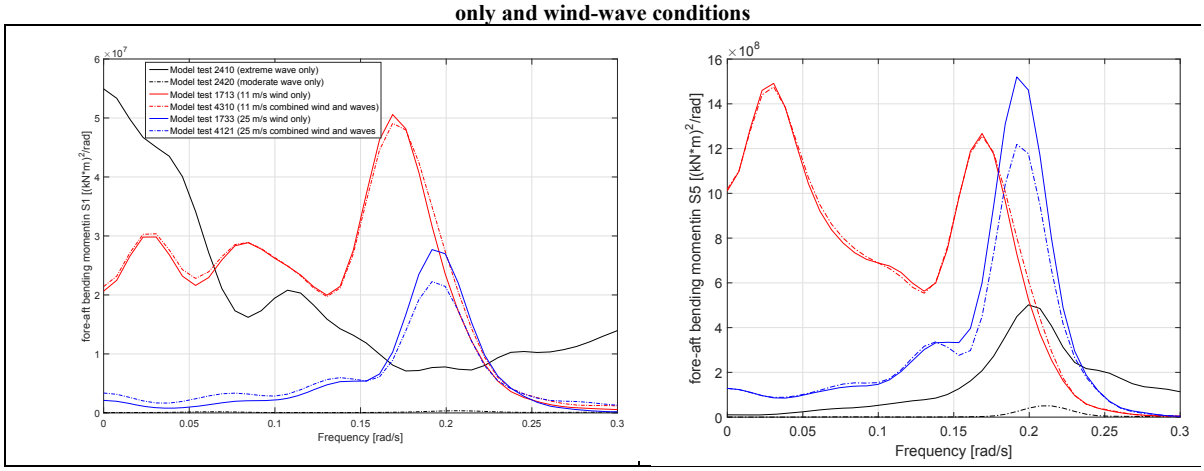

Figure 17 Comparisons of spectral densities of the measured fore-aft bending moments in S1 and S5 in the wind-only, wave-only and wind-wave conditions

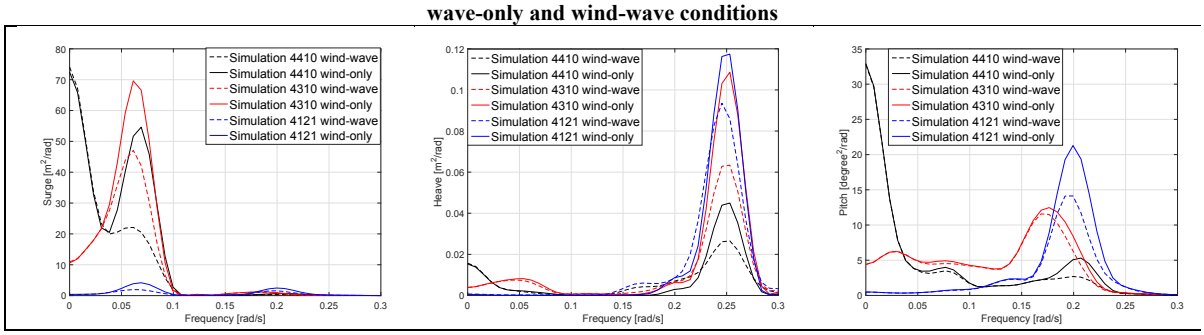

Figure 18 Comparisons of spectral densities of the simulated surge, heave and pitch motions in the wind-only and wind-wave conditions. Note that the only difference between the numerical model for a wind-wave condition and its corresponding wind-only condition is that the model for the wind-only condition is in calm water

5.2 Dominant components in the fore-aft bending moments in five cross-sections

We denote simulated realizations of sectional forces and moments in cross-section SX as $\boldsymbol{R}^{s,SX}(t) = [R_1^{s,SX}, R_2^{s,SX}, R_3^{s,SX}, R_4^{s,X}, R_5^{s,SX}, R_6^{s,SX}]^{\mathrm{T}}$. $\boldsymbol{R}^{s,SX}(t)$ are described in a body-fixed coordinate system ($O^{b,SX}$-$x^{b,SX}$-$y^{b,Sx}$-$z^{b,SX}$) that is identical to the body-fixed coordinate system except that the $O^{b,SX}$ is located at geometrical center of the cross-section SX.

The sectional forces and moments are in equilibrium to external and inertial loads on the corresponding Part A or B. As classified in [9], components of the external loads on Parts A and B are tabulated in Table 9.

Table 9List of the components of external loads on Parts A and B

Components (Each component is 6 × 1 vector including three forces and moments)	On Part A corresponding to SX	On Part B corresponding to SX
Drag forces	$\boldsymbol{L}^{e,vis,SX,A}(t)$	$\boldsymbol{L}^{e,vis,SX,B}(t)$
Gravity loads	$\boldsymbol{L}^{e,gra,SX,A}(t)$	$\boldsymbol{L}^{e,gra,SX,B}(t)$
First order wave excitation loads	$\boldsymbol{L}^{e,waex,SX,A}(t)$	$\boldsymbol{L}^{e,waex,SX,B}(t)$
First order radiation loads	$\boldsymbol{L}^{e,rad,SX,A}(t)$	$\boldsymbol{L}^{e,rad,SX,B}(t)$
Resultant forces and moments of hydrostatic pressure forces on the outer surface and the atmospheric pressure forces on the inner surface of the corresponding part (the corresponding Part A or B) at instantaneous position	$\boldsymbol{L}^{e,sta,SX,A}(t)$	$\boldsymbol{L}^{e,sta,SX,B}(t)$
Applied thrust forces and moments	Not applicable	$\boldsymbol{L}^{e,thrust,SX,B}(t)$

Each of the radiation loads ($\boldsymbol{L}^{e,rad,SX,A}(t)$ and $\boldsymbol{L}^{e,rad,SX,B}(t)$, see Table 9) can be expressed as a superposition of a convolution term and a term that is proportional to acceleration associated with the rigid-body motions, see Eq. (5) as an example. In Eq. (5), rigid-body motions are denoted as $\boldsymbol{\eta}^{SX,A}(t)$, $\dot{\boldsymbol{\eta}}^{SX,A}$ and $\ddot{\boldsymbol{\eta}}^{SX,A}$ are first order derivative (velocity) and second order derivative (acceleration) of $\boldsymbol{\eta}^{SX,A}$, respectively. $\boldsymbol{k}_i(t)$ is known as retardation or memory function for Part A and determined by $\boldsymbol{A}_{SX,A}(\omega)$ or $\boldsymbol{B}_{SX,A}(\omega)$. $\boldsymbol{A}_{SX,A}^{\infty}$ is $\boldsymbol{A}_{SX,A}(\omega)$ corresponding to the high-frequency limit. $\boldsymbol{A}_{SX,A}(\omega)$ and $\boldsymbol{B}_{SX,A}(\omega)$ are frequency dependent added mass coefficient matrix and potential damping coefficient matrix for Part A. More details are referred to [9].

$$\boldsymbol{L}^{e,rad,SX,A}(t) = -\int_{-\infty}^{+\infty} \boldsymbol{k}_i^{SX,A}(t-\tau)\dot{\boldsymbol{\eta}}^{SX,A}(\tau)d\tau - \boldsymbol{A}_{SX,A}^{\infty}\ddot{\boldsymbol{\eta}}^{SX,A}(t) \tag{5}$$

Consequently, each realization of simulated sectional forces and moments in the specified cross-sections can be expressed as a superposition of realizations tabulated in Table 10. Expression of the superposition is given in Eq.s (6) and (7).

Table 10 List of decomposed realizations of the simulated sectional forces and moments. All the terms in Eq.s (6 and 7) are described in the body-fixed coordinate system ($O^{b,SX}$-$x^{b,SX}$-$y^{b,Sx}$-$z^{b,SX}$) with respect to $O^{b,SX}$.

Realizations in Eq. (6)	Definition
$\boldsymbol{R}^{waex,SX,A}$	Simulated realizations of three forces and moments that are in equilibrium to $\boldsymbol{L}^{e,waex,SX,A}$.
$\boldsymbol{R}^{flu,SX,A}$	Simulated realizations of three forces and moments that are in equilibrium to $\boldsymbol{L}^{e,gra,SX,A}$ and $\boldsymbol{L}^{e,sta,SX,A}$.
$\boldsymbol{R}^{Inertia,SX,A}$	Simulated realizations of three forces and moments that are in equilibrium to inertial loads of corresponding Part A
$\boldsymbol{R}^{add\_inf,SX,A}$	Simulated realizations of three forces and moments that are in equilibrium to $-\boldsymbol{A}_{SX,A}^{\infty}\ddot{\boldsymbol{\eta}}^{SX,A}$
$\boldsymbol{R}^{Retard,SX,A}$	Simulated realizations of three forces and moments that are in equilibrium to the convolution term $(-\int_{-\infty}^{+\infty} \boldsymbol{k}_i^{SX,A}(t-\tau)\dot{\boldsymbol{\eta}}^{SX,A}(\tau)d\tau)$.
$\boldsymbol{R}^{Res,SX,A}$	Simulated realizations of three forces and moments that are in equilibrium to the rest external loads on the corresponding Part A, e.g. $\boldsymbol{L}^{e,vis,SX,A}$.
Realizations in Eq. (7)	Definition
$\boldsymbol{R}^{Thrust,SX,B}$	Simulated realizations of three forces and moments that are in equilibrium to $\boldsymbol{L}^{e,thrust,SX,B}$.
Similarly, $\boldsymbol{R}^{waex,SX,B}$, $\boldsymbol{R}^{flu,SX,B}$, $\boldsymbol{R}^{Inertia,SX,B}$, $\boldsymbol{R}^{add\_inf,SX,B}$, $\boldsymbol{R}^{Retard,SX,B}$ and $\boldsymbol{R}^{Res,SX,B}$ are in equilibrium to the corresponding loads on the corresponding Part B.	

$$\boldsymbol{R}^{s,SX}(t) = \boldsymbol{R}^{waex,SX,A} + \boldsymbol{R}^{flu,SX,A} + \boldsymbol{R}^{Inertia,SX,A} + \boldsymbol{R}^{add\_inf,SX,A} + \boldsymbol{R}^{Retard,SX,A} + \boldsymbol{R}^{Res,SX,A}(t), SX = 1,2\ or\ 3 \tag{6}$$

$$\boldsymbol{R}^{s,SX}(t) = \boldsymbol{R}^{waex,SX,B} + \boldsymbol{R}^{flu,SX,B} + \boldsymbol{R}^{Inertia,SX,B} + \boldsymbol{R}^{add\_inf,SX,B} + \boldsymbol{R}^{Retard,SX,B} + \boldsymbol{R}^{Thrust,SX,B} + \boldsymbol{R}^{Res,SX,B}(t)\ , SX = 4\ or\ 5 \tag{7}$$

$\boldsymbol{R}^{s,SX}(t)$ and all of the other terms shown in Eq.s (6 and 7) are simulated in the time-domain model. We focus on fore-aft bending moments ($R_5^{s,SX}$) which are the sectional bending moments with respect to axis $y^{b,Sx}$ and intend to identify dominant terms in the fore-aft bending moment.

Spectral density functions of $R_5^{s,SX}$ and different combinations of the corresponding terms are compared.

For example, according to Eq. (7), we have Eq. (8). As shown in Figure A4, the spectral density curves of $R_5^{s,S5}$ and $R_5^{flu,S5,B} + R_5^{Thrust,S5,B}$ are almost identical in the frequency-range from 0 rad/s to 0.1 rad/s. This indicates that effects of $R_5^{Inertia,S5,B}$ on $R_5^{s,S5}$ are negligible in this frequency-range.

Note that $\boldsymbol{R}^{flu,S5,B}$, gravity forces and hydrostatic pressure forces on the Part B (the tower and RNA) corresponding to the cross-section S5 (the tower base) are in equilibrium. Similarly, $\boldsymbol{R}^{Thrust,S5,B}$ and $\boldsymbol{R}^{Inertia,S5,B}$ are in equilibrium to the applied thrust forces and moments (aerodynamic loads) and inertia loads on the corresponding Part B, respectively. For S5, there are no hydro pressure forces on the Part B since the Part B is out of the sea. Consequently, $\boldsymbol{R}^{flu,S5,B}$ is, actually, in equilibrium to the gravity forces. Meanwhile, $\boldsymbol{R}^{waex,S5,B}$, $\boldsymbol{R}^{add\_inf,S5,B}$ and $\boldsymbol{R}^{Retard,S5,B}$, which are in equilibrium to hydrodynamic pressure forces on the corresponding Part B are not exist. Except for the external and inertia loads on the Part B discussed in above the numerical models do not have any other external and/or inertial loads on the Part B. Consequently, $\boldsymbol{R}^{Res,S5,B}$ does not exist.

$$R_5^{s,S5}(t) = R_5^{flu,S5,B} + R_5^{Inertia,S5,B} + R_5^{waex,S5,B} + R_5^{add\_inf,S5,B} + R_5^{Retard,S5,B} + R_5^{Thrust,S5,B} + R_5^{Res,S5,B}$$
$$= R_5^{flu,S5,B} + R_5^{Inertia,S5,B} + R_5^{Thrust,S5,B} \quad (8)$$

Using this approach, dominant components in the fore-aft bending moments in five cross-sections are analysed. Results are summarized in Table 11.

Table 11 Summary of dominant load components in the fore-aft bending moments in the five cross-sections

<table>
<tr><td></td><td colspan="3">Low frequency-range</td><td rowspan="2"></td><td>Wave-frequency-range</td></tr>
<tr><td></td><td></td><td>Around surge natural frequency</td><td>Around pitch natural frequency</td><td></td></tr>
<tr><td></td><td>0-0.05 rad/s</td><td>0.05-0.15 rad/s</td><td>0.15-0.25 rad/s</td><td>0.25-0.3 rad/s</td><td>0.3-2 rad/s</td></tr>
<tr><td>S1</td><td colspan="2" rowspan="2">$R_5^{flu,SX,A}, X = 1,2 \text{ or } 3$</td><td rowspan="3">$R_5^{flu,SX,A} + R_5^{Inertia,SX,A} + R_5^{add\_inf,SX,A}, X = 1,2 \text{ or } 3$</td><td rowspan="4">Components of $R_5^{s,SX}, X = 1,2,3,4 \text{ or } 5$ in this range are negligible since excitations and rigid-body motions in this range are very limited.</td><td>$R_5^{waex,S1,A} + R_5^{Inertia,S1,A} + R_5^{add\_inf,S1,A}$</td></tr>
<tr><td>S2</td><td rowspan="2">$R_5^{waex,SX,A} + R_5^{Inertia,SX,A} + R_5^{add\_inf,SX,A} + R_5^{flu,SX,A}, X = 2 \text{ or } 3$</td></tr>
<tr><td>S3</td></tr>
<tr><td>S4</td><td colspan="2" rowspan="2">$R_5^{flu,SX,B} + R_5^{Thrust,SX,B}, X = 4 \text{ or } 5$</td><td rowspan="2">$R_5^{flu,SX,B} + R_5^{Thrust,SX,B} + R_5^{Inertia,SX,B} + R_5^{add\_inf,SX,B}, X = 4 \text{ or } 5$</td><td>$R_5^{waex,S4,B} + R_5^{Inertia,S4,B} + R_5^{add\_inf,S4,B} + R_5^{Thrust,S4,B} + R_5^{flu,S4,B}$</td></tr>
<tr><td>S5</td><td>$R_5^{flu,S5,B} + R_5^{Inertia,S5,B} + R_5^{Thrust,S5,B}$</td></tr>
</table>

In the numerical models, $\boldsymbol{R}^{Thrust,SX,B}$, $\boldsymbol{R}^{waex,SX,B}$ and $\boldsymbol{R}^{waex,SX,A}$ are prescriptive since the thrust forces and moments applied on the numerical models are identical to the measurements of the thrust forces and moments applied on the experimental model during the model tests, while the first-order wave loads are generated based on the corresponding hydrodynamic coefficients, which are related to configuration of the mean wetted body surface of the hull and obtained by solving the corresponding boundary value problem [9] and measured wave elevations of incident waves.

$\boldsymbol{R}^{Inertia,SX,A}$ and $\boldsymbol{R}^{Inertia,SX,B}$ are related to mass distributions of the hull and the acceleration associated with rigid-body motions. $\boldsymbol{R}^{add\_inf,SX,A}$ and $\boldsymbol{R}^{add\_inf,SX,B}$ are related to the acceleration associated with the rigid-body motions and configuration of the mean wetted body surface of the hull.

$\boldsymbol{R}^{flu,SX,A}$ and $\boldsymbol{R}^{flu,SX,B}$ are related to rigid-body motions, distribution of the vertical position of the mass of the hull and configuration of the mean wetted body surface of the hull.

In the numerical models, the dynamic motions and sectional forces and moments in the hull are excited by the first-order wave loads and thrust forces and moments, which are dominant excitations for the wave frequency responses and low frequency responses, respectively. Components of the fore-aft bending moments with oscillating frequencies in range from 0.25 rad/s to 0.3 rad/s are negligible since excitations and rigid-body motions in this range are very limited.

For a model oscillating with frequency ω_0, inertial loads of the model are proportional to ω_0^2. Therefore, effects of $\boldsymbol{R}^{Inertia,SX,A}$, $\boldsymbol{R}^{Inertia,SX,B}$, $\boldsymbol{R}^{add\_inf,SX,A}$ and $\boldsymbol{R}^{add\_inf,SX,B}$ on components of the fore-aft bending moments with very small oscillating frequencies, e.g. below 0.05 rad/s, are negligible when compared to the corresponding $\boldsymbol{R}^{Thrust,SX,B}$, $\boldsymbol{R}^{flu,SX,A}$ and $\boldsymbol{R}^{flu,SX,B}$ even though in nature large low-frequency motions, e.g. the surge and pitch motions, may be excited by wind loads on the RNA and tower, and second and higher order wave excitation loads on the hull. For the reference semi-submersible wind turbine, we observe that components of the fore-aft bending moments with oscillating frequencies in the low frequency-range are dominated by $R_5^{flu,SX,A}$ or $R_5^{flu,SX,B} + R_5^{Thrust,SX,B}$ except that inertial related terms, e.g. $R_5^{Inertia,SX,A}$ and $R_5^{add\_inf,SX,A}$, can affect the components of the fore-aft bending moments with oscillating frequencies that are around pitch and surge natural frequencies since 1) amplitudes of rigid-body motions are amplified as the resonant motions are excited, and 2) $R_5^{flu,SX,A}$, $R_5^{flu,SX,B}$, $R_5^{Thrust,SX,B}$ and the terms related to the acceleration associated with the rigid-body motions are not uncorrelated.

The resonant rigid-body motions are sensitive to the level of the damping forces. Consequently, rigid-body-motion related terms of $\boldsymbol{R}^{s,SX}$, e.g. $\boldsymbol{R}^{flu,SX,A}$, $\boldsymbol{R}^{Inertia,SX,A}$ and $\boldsymbol{R}^{add\_inf,SX,A}$, are sensitive to the level of the damping forces. While, a numerical

sensitivity analysis shows that the fore-aft bending moments, which are in the five cross-sections and in equivalent to the corresponding damping forces on the corresponding Part A or B, are negligible when compared to $\boldsymbol{R}^{s,SX}$. It should be noted that, as discussed in Section 5.1, the damping forces and moments are affected by incident waves via the term $v\dot{r}$.

Relative importance of load components on the fore-aft bending moments depends on wind and wave conditions, location of the cross-section in the hull, amplitudes and phase angles of the rigid-body motions, and configuration of corresponding wetted body surface of the hull, as well. Effect of these issues is analyzed in Sections 5.3-5.5.

5.3 Comparisons of the simulated fore-aft bending moments in the specified five cross-sections

Spectral densities of the fore-aft bending moments in the five cross-sections for the model in the three wind-wave environmental conditions are compared, see Figure 19. The interface between the pontoons and central column is identified as the most critical structural component. Ratio between square root of area under low frequency-range and wave-frequency-range of each spectral density curve is calculated. We find the ratio varies from 0.1, which means the corresponding fore-aft bending moment is dominated by wave frequency components (see the bending moment in S1), to 2.3, which means the corresponding bending moment is dominated by low frequency components (see the bending moment in S5 in the model tests 4310 and 4410). The ratio is around 1 for the corresponding bending moment in S5 in the model test 4121, S2, S3 and S4. This indicates that both of the low frequency and wave frequency components are important.

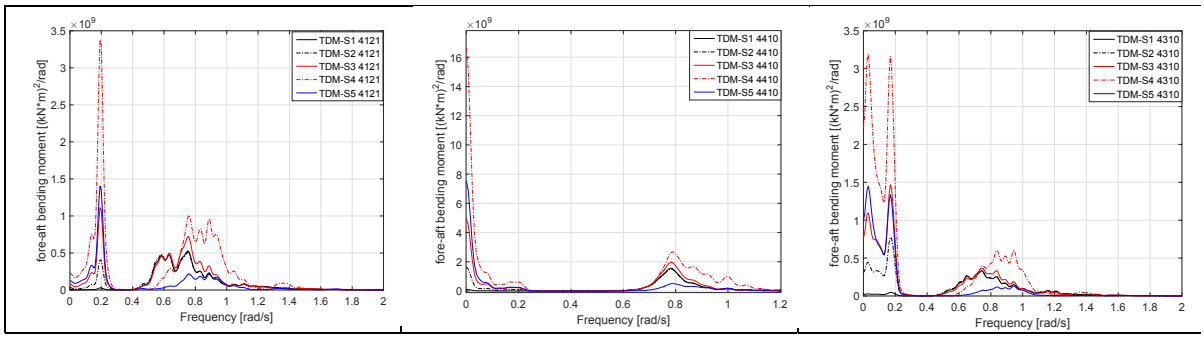

Figure 19 Comparisons of spectral densities of the simulated fore-aft bending moments in the five cross-sections in the three wind-wave conditions

Spectral densities of $R_5^{waex,SX,A}$, $(R_5^{Inertia,SX,A} + R_5^{add\_inf,SX,A})$ and $R_5^{flu,SX,A}$, $X = 1, 2$ or 3, $R_5^{waex,S4,B}$, and $(R_5^{Inertia,SX,B} + R_5^{add\_inf,SX,B})$ and $R_5^{flu,SX,B}$ are compared. See Figure 20 for example. From S1 to S3, value of standard deviation of the corresponding first order wave excitation load induced fore-aft bending moment increases. Effects of fluctuation of hydrostatic pressure forces on wetted body surface of the hull and fluctuation of gravity forces are important to fore-aft bending moments in cross-sections in the tower and central column and in cross-sections that are on the pontoons and close to the central column.

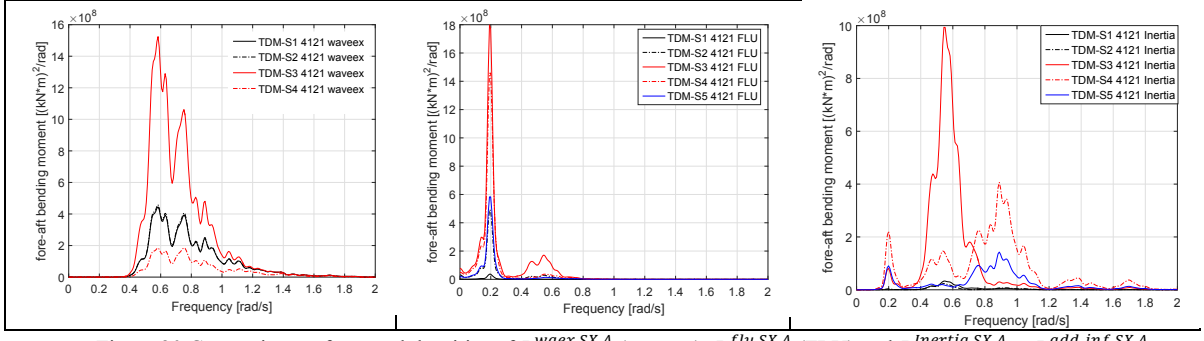

Figure 20 Comparisons of spectral densities of $\boldsymbol{R}^{waex,SX,A}$ (waveex), $\boldsymbol{R}^{flu,SX,A}$ (FLU) and $\boldsymbol{R}^{Inertia,SX,A} + \boldsymbol{R}^{add\_inf,SX,A}$ (Inertia), $X = 1,2\ or\ 3$, and $\boldsymbol{R}^{waex,SX,B}$, $\boldsymbol{R}^{flu,SX,B}$ and $\boldsymbol{R}^{Inertia,SX,B} + \boldsymbol{R}^{add\_inf,SX,B}$, $X = 4\ or\ 5$

The inertial loads induced fore-aft bending moments in the tower base and base of the central column are dominated by the inertial loads that are proportional to the acceleration associate with the surge and pitch motions. Spectral densities of the fore-aft bending moments in the tower base, which are in equilibrium to the components of the inertial loads on the tower that are associated to acceleration in surge only, acceleration in pitch only and acceleration in combined surge and pitch, are given in the

left figure of Figure 21. A cancellation effect between the bending moments induced by the inertial loads that are associated to acceleration in surge and pitch can be clearly observed in frequency range from 0.4 rad/s to 0.6 rad/s. The cancellation is due to, as shown by the right figure given in Figure 21, the fact that phase difference between simulated surge and pitch motions is close to 180 degrees in this frequency range.

By using the same analysis approach, we find that the inertial loads induced fore-aft bending moments in S3 are dominated by the inertial loads that are proportional to the acceleration associate with the heave motions.

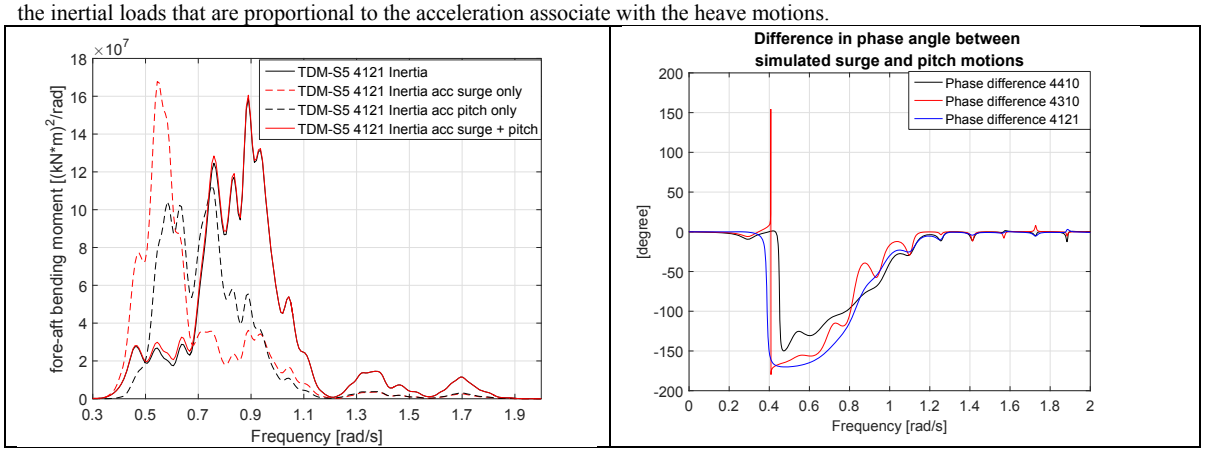

Figure 21 left: comparisons of spectral densities of the simulated fore-aft bending moments in S5 which are in equivalent to different components of the inertial loads of the RNA and tower; right: differences in phase angle between simulated surge and pitch motions

5.4 Analysis for effects of changes in the mean-offset and mean-heeling-angle of the hull on rigid-body motions and sectional bending moments

As mentioned in Section 3, floating wind turbines are subjected to constant forces and moments from wind and waves. These constant forces and moments can result in a mean horizontal offset and title angle. The horizontal offset results in a change in restoring stiffness of the mooring lines due to change in configuration of the mooring lines and a change in phase angle of each frequency component of the incident waves. As shown in Figure 3, the tilt angle means a change in configuration of mean wetted body surface of the hull which results in a change in corresponding velocity potential and a change in value and distribution of hydro pressure forces on the wetted body surface. This may result in a considerable change in resultant sectional forces and moments even though change in resultant of the hydro pressure forces on whole of the wetted body surface could be very limited. This statement is substantiated by comparisons of the measurements and simulations of the platform in a combined wind-wave condition (the model test 4310), its corresponding wave only condition (model test 2420), and a model for which averaged wind induced forces and moments are applied, see Figure 22.

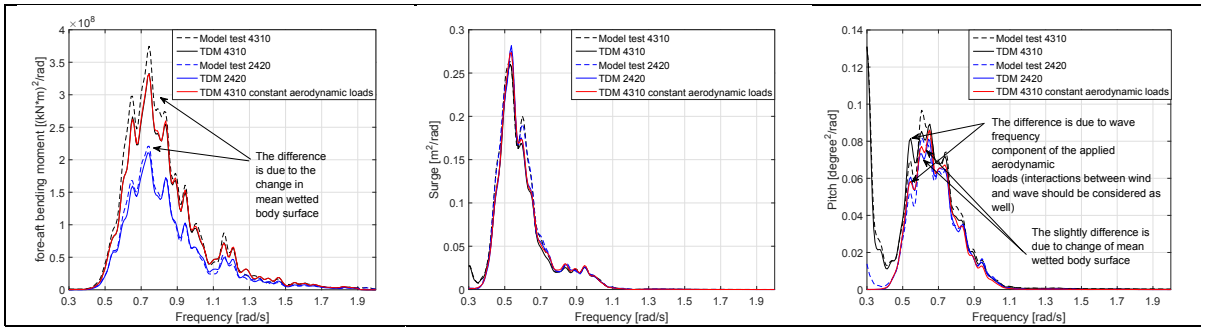

Figure 22 Comparison of spectral densities of the simulated and measured fore-aft bending moments in S1, and the surge and pitch motions. The model test 4310 is a combined wind-wave condition, while the model test 2420 is its corresponding wave only condition.

5.5 Convolution terms in expressions of the radiation loads

It is of great interesting to analyze load effects of the convolution terms shown in the expressions of $\boldsymbol{L}^{e,rad,SX,A}$ and $\boldsymbol{L}^{e,rad,SX,B}$ since computational cost and complexity of the numerical models can be significantly reduced if the convolution terms can be neglected. $\boldsymbol{R}^{Retard,SX,A}$ and $\boldsymbol{R}^{Retard,SX,B}$ are in equilibrium to the corresponding convolution terms, respectively. Comparisons of the numerical results presented in Section 5.2 show that $R_5^{Retard,SX,B}, X = 4$ or 5, and $R_5^{Retard,SX,A}, X = 1,2$ or 3, are negligible for the analyzed model.

Spectral densities of the rigid-body motions and fore-aft bending moments in the five cross-sections given by numerical models with and without the convolution terms in the expressions of radiation loads on each part of the hull are compared, see Appendix B. Numerical model without the convolution terms means that 1) the potential damping forces are not modelled, and 2) the frequency dependent added mass coefficients are replaced by added mass coefficients that corresponding to the high-frequency limit. Components of the potential damping forces with oscillating frequencies in the low frequency range are expected to be negligible. We find that effect of the convolution terms on the motions and fore-aft bending moments of the present model in the analyzed environmental conditions are negligible. This is agreed by the measured responses and indicates that, for the analyzed environmental conditions, Morsion formula with calibrated coefficients could be available to reasonably account for the hydro dynamic loads on the hull. However, this should be validated in future. By now, computer codes which implement Morison formula focus on rigid-body motions while thorough validation with respect to sectional forces and moments in semi-submersible wind turbine hulls is very limited. In addition, as addressed in [8], hydro pressure forces on end surface of each structural component of floating wind turbine hulls need to be appropriately accounted for in the computer codes which implement Morison formula

Note that importance of the convolution terms is related to configurations of the wetted body surface, and amplitudes and frequencies of the motions of the hull. According to potential flow theory, it is expected that the effect of the convolution terms on the dynamic responses of the 5-MW-CSC could be more important when the model is subjected to waves with smaller periods, e.g. below 8 seconds. This effect needs to be considered in design of model test in future. It is also of great interest to apply the Luan et al's approach on numerical and experimental analysis of a floater with large water plane area for which the convolution terms could be important.

In contrast to using Morison formula to model the hydrodynamic loads on floaters, hydrodynamic coefficients used in the Luan et al's approach are obtained by solving the corresponding boundary value problem (there is no need to calibrate the hydrodynamic coefficients). While, the Luan et al's approach is expected to be available in situations for which the diffraction and radiation effects are important, e.g. for waves with relatively small periods.

6 Simplification of numerical modelling for global dynamic analysis

Interaction effect between wind and wave loads may be very limited while the interaction effect on the sectional forces and moments may be negligible.

For example, as shown in Figure 17, the low frequency components of spectral densities of the measured fore-aft bending moments in the tower base (S5) and base of the side column 1 (S1) in the model test 4310, for which the model is subjected to turbulent winds and moderate irregular waves, are almost identical to the low-frequency components of spectral densities of the corresponding measurements in the model test 1713 which is a wind-only model test corresponding to the model test 4310. While the interaction effect can be observed from the differences between the wave frequency components of spectral densities of simulated pitch motions in environmental condition of the model test 4310 and the model test for which the model is subjected to the same condition as the model test 4310 except that the corresponding applied aerodynamic load, which include wave frequency components, are replaced by three constant forces and moments that are averaged wind induced forces and moments (constant steady wind loads), see Figure 22. However, as shown in Figure 22, the differences between the wave frequency components of the spectral densities of the simulated fore-aft bending moment in S1 in these two conditions are negligible. This is because that the wave frequency components of the fore-aft bending moments in S1 are dominated by the wave excitation loads and inertial and radiation loads which are related to wave induced motions.

These facts encourage the idea that the fore-aft bending moments of the model in wind and waves could be approximately but effectively simulated by superimposing the corresponding simulations of the model subjected to its corresponding wind only condition and wave only condition with the corresponding averaged wind induced forces and moments. If the simplification is applicable, the number of cases of short-term analysis required in long-term analysis can be significantly reduced. In addition, based on the results discussed in Section 5.5, we suggest that the convolution terms could be excluded from the numerical model to reduce real-time-computational effort and modelling complexity for each short-term analysis. Consequently, the computational time for a 4,600-second-simulation can be reduced from 1,253 seconds to 638 seconds (for a 2.30GHz CPU). Note that effect of the convolution terms on responses of a generic floater could be important if the floater has relatively large volume of displaced water and/or is subjected to waves with relatively small wave length.

Applicability of the simplification should be analyzed case by case. Spectral densities of the simulated fore-aft bending moments in the five cross-sections of the models with and without the simplification in conditions of the model tests 4310 and 4121 have been compared. Typical results are shown in Figure 23. As expected, these results substantiate that the simplification could be used to simulate the fore-aft bending moments in the hull. Relative difference between square root of area of

corresponding spectral density curves with and without the simplification under the low frequency-range and wave-frequency-range are no more than 2.5% and 5%, respectively. We also find that fore-aft bending moments in cross-sections in the tower could be sensitive to the difference in the simulated pitch motion and thrust force on the rotor with and without the simplification but could be insensitive to the difference in the simulated surge motion. Fore-aft bending moments in cross-sections in the side columns could be insensitive to the difference in the simulated motions and thrust force on the rotor since the fore-aft bending moments are dominated by wave excitation loads, and inertial and radiation loads which are related to wave induced motions.

Note that the simulated model responses in the frequency-range around surge and pitch natural frequencies are very sensitive to damping level of the numerical model. In the numerical models, the damping forces and moments in the low frequency-range come from 1) drag forces on the mooring lines and hull and 2) the quadratic damping matrix. Morison formula, which is an empirical formula, is used to model the drag forces. The coefficients implemented in the formula are selected according to [31] based on Reynolds number, Keulegan–Carpenter number and surface roughness of the model in full size. As shown in Section 5.1, due to implementation of the Morison formula, incident waves can introduce a considerable effect on the damping level of the numerical model in the low frequency-range. Consequently, drag coefficients calibrated by using measured responses in decay tests and/or selected according to standards, e.g. [31], may failed to accurately model the actual drag forces (value and distribution) on the hull and mooring lines. In practice, a quadratic damping matrix is used to compensate the difference between the model and actual damping forces and moments. However, calibration for coefficients in the quadratic damping matrix is needed case by case. Future work for improving the modelling approach for the drag forces is highly recommended. In addition, the second and higher order hydro loads are not completely included in the numerical models but are inherently included in nature. Effect of the second and higher order wave excitation loads on the resonant motions should be kept in mind. As shown by the measured responses of the model test 4310, in moderate waves, effect of the second and higher order hydro loads is very limited.

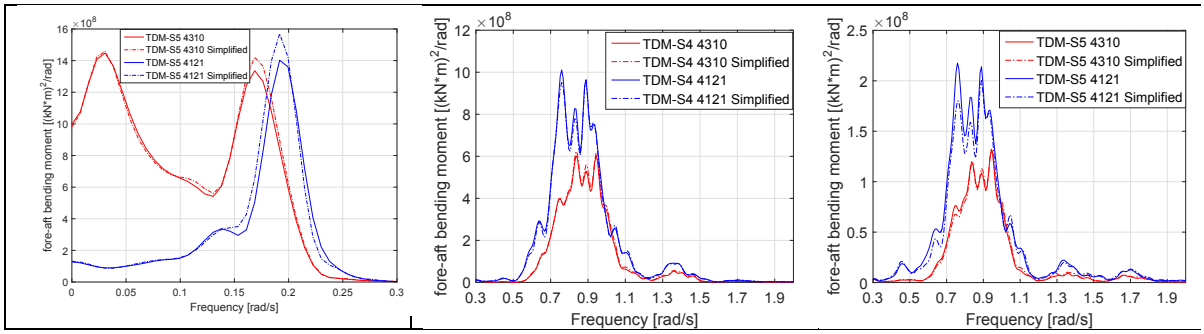

Figure 23 Comparisons of spectral densities of simulated fore-aft bending moments with and without the simplification for two operational conditions

7 Conclusions and future work

Multi-body time-domain finite element models, which implement a recently developed numerical approach for determining forces and moments in floaters, are developed to simulate rigid-body motions and sectional forces and moments of a reference 5-MW braceless semi-submersible wind turbine in turbulent winds and irregular waves corresponding to below rated, at rated and above rated conditions. The simulated responses are compared with measurements with a 1:30 scaled model test. In general, the agreement between the simulations and measurements is very good. The differences in the spectral densities of the measurements and simulations have been quantified while the reasons for the differences have been thoroughly analyzed and discussed based on the comparisons of measurements in the different conditions and numerical parametrical study.

The low frequency rigid-body motions are dominated by the wind loads, second and higher order wave excitation loads, and restoring stiffness while the resonant motions are sensitive to the damping forces and moments that are empirically modeled by the drag terms of the Morison formula in the developed numerical models and are affected by incident waves via the term $v\dot{r}$. In practice, a quadratic damping matrix is used to compensate for the difference between modelled and actual damping forces and moments while the coefficients in the matrix need to be calibrated case by case. Future work for improving numerical model of the drag forces, which able to model the drag forces with an acceptable accuracy in blind tests, is highly recommended.

The uncertainties in the simulated and measured low frequency surge and heave motions have negligible effects on the fore-aft bending moments in the five cross-sections in the hull. The low frequency fore-aft bending moments are dominated by the wind loads, and pitch motion related fluctuations of gravity forces and hydrostatic pressure forces. The inertial load effect on the low frequency responses is limited except for responses with frequency components around the pitch natural frequency. Effect of the second and higher order wave excitation loads on the fore-aft bending moments is observed from the measurements and discussed. In general the effect is relatively limited in the analyzed operational conditions but can be critical in extreme conditions.

The differences in the simulated and measured wave-frequency rigid-body motions and fore-aft bending moments, for which the relative difference for standard deviation of the corresponding measurements and simulations is no more than 10%, are due to the difference between the simulated and actual first order and higher order wave excitation loads. Note that the second and higher

order wave excitation loads are not included in the numerical models. The level of relative difference, which is due to uncertainties and noises in measurements, of standard deviations of the corresponding measurements and simulations could be around 2.48%. To further analyze the reason of the differences in the simulated and actual wave excitation loads on the hull, numerical modelling approach for full second order wave excitation loads should be developed, while the wave excitation loads on the hull, when the hull is fixed at its mean position in wind and waves, should be measured in future test programs. A preliminary comparison, which is scheduled to be published with a more comprehensive analysis in future, with respect to the simulated and measured responses in a 1-hour extreme condition (the model test 2410) shows that the relative difference of the standard deviation and maximum value of the simulated and measured fore-aft bending moment are in the level of 7.3% and 55%, respectively. Note that more efforts are needed to quantify uncertainties in the measurements in the extreme condition, in particular for the 1-hour maximum value.

The mean forces and moments from wind and waves result in a change in the configuration of the mean wetted body surface of the hull when compared to the configuration in calm water. This may result in a considerable change in the resultant sectional forces and moments even though the change in resultant of the hydro pressure forces on the whole wetted body surface could be very limited.

A summary of important load components on the simulated fore-aft bending moments in the five cross-sections is available in Table 11. Relative importance of load components on the fore-aft bending moments depends on wind and wave conditions, location of the cross-section in the hull, amplitudes and phase angles of rigid-body motions, and configuration of corresponding wetted body surface of the hull. The interface between the pontoons and central column is identified as the most critical part. Both the low frequency and wave frequency components of load effects could be important. From S1 to S3, value of standard deviation of the first order wave excitation load induced fore-aft bending moment increases. The effect of the fluctuation of the hydrostatic pressure on the wetted body surface of the hull and the fluctuation of the gravity forces are important to the fore-aft bending moments in the cross-sections in the tower and central column and in the cross-sections that are on the pontoons and close to the central column. The phase difference between the simulated surge and pitch motions can be close to 180 degrees in the frequency range from 0.4 rad/s to 0.6 rad/s and means a cancellation effect for the bending moments induced by the inertial loads which are associated to acceleration in surge and pitch. The inertial loads induced fore-aft bending moments in S3 are dominated by the inertial loads that are proportional to acceleration associated with heave motions.

In the analyzed environmental conditions, the convolutional terms have very limited effect on the simulations and could be removed from the numerical models to significantly reduce modelling complexity and computational cost for short-term analysis. The applicability of this simplification should be analyzed case by case since the importance of the convolution terms is related to configurations of the wetted body surface, and amplitudes and frequencies of the motions of the hull. This issue should be kept in mind in design of model tests in future.

Analysis presented in this paper substantiates that the simulated fore-aft bending moments of the model in wind and waves could be obtained by superimposing the corresponding simulations of the model subjected to its corresponding wind only condition, and wave only condition except that three constant forces and moments which are the corresponding averaged wind induced forces and moments are applied if the interaction effect between wind and wave loads and/or the interaction effect on the sectional forces and moments are limited. The simplification can significantly reduce computational cost but applicability of the simplification should be analyzed case by case.

Analysis and discussions given in this paper are based on available measurements. More systematical and step by step model tests for quantifying and minimizing uncertainties in measurements and identifying the first order and higher order wave excitation loads are welcome in future. While, the frequency dependent radiation and diffraction hydrodynamic loads are expected to be relatively more significant when volume in water and water plane area of the experimental model are relatively large and the experimental model is subjected to irregular waves for which major wave energy is in frequency range from 1 rad/s to 2 rad/s. Numerical and experimental analysis for the model in extreme conditions and fault conditions as described for example in [38-40] is scheduled as a future work.

The aerodynamic loads applied on the numerical models are prescriptive loads measured from the model tests. Analysis shows that the actual aerodynamic loads on the experimental model can be accurately measured. Consequently, the difference between the measurements and simulations only indicate differences in the hydro loads on the hull and the mass properties of the numerical and experimental models. If the deviation between the simulated and measured rigid-body motions is large, the prescriptive loads will fail to represent the right dependency of the aerodynamic loads with respect to the rigid-body motions. Fortunately, the agreement between the simulated and measured rigid-body motions is very good. This limitation can be avoided by developing a numerical model for the wind turbine of the experimental model to simulate the aerodynamic loads in the time-domain simulations based on numerical wind field and the simulated rigid-body motions. However, increase of uncertainties due to the differences between the numerical and actual wind fields, and the differences between performance of the numerical and experimental models of the wind turbine must be considered.

The time-domain approach used for developing numerical models analyzed in this paper is a generic approach that is applicable for static determinate and indeterminate structures. The approach could be used for long-term extreme load prediction and fatigue damage analysis while the understanding with respect to the wind and wave load effects on the sectional loads could be helpful for structural optimization and control for the hull of floating wind turbines, for example, similar work with respect to the work presented in [42-45] could be done in future. According to the approach, a genetic structure can be discretized into several bodied for modeling hydro loads, which are based on coefficients that are obtained by solving the first order boundary

value problem with the rigid-body assumption, in time-domain on each body while global flexibility of the structure can be modelled by using beam elements. Extension for accounting for hydroelastisity, e.g. [41], is scheduled as future work for development of the approach.

ACKNOWLEDGEMENT

The authors acknowledge Mr. Fredrik Brun from SINTEF Ocean (formerly MARINTEK) for providing Figure 2 and the financial support provided by the Research Council of Norway through the Centre for Ships and Ocean Structures; the Norwegian Research Centre for Offshore Wind Technology (NOWITECH), NTNU; and the Centre for Autonomous Marine Operations and Systems (AMOS), NTNU.

REFERENCES

[1] IEC, (2005), "Wind turbines – Part 1: Design requirements", IEC-61400-1, International Electrotechnical Commission.
[2] IEC, (2009), "Wind turbines: Part 3: Design requirements for offshore wind turbines", IEC-61400-3, International Electrotechnical Commission.
[3] DNV, (2013), "Offshore standard – Design of Offshore Wind Turbine Structures", DNV-OS-J101, Det Norske Veritas.
[4] GL, (2010), "Guideline for the certification of Wind Turbines". Germanischer Lloyd, Hamburg, Germany
[5] DNV, (2013), "Offshore standard – Design of Floating Wind turbine Structures", DNV-OS-J103, Det Norske Veritas.
[6] Cordle, A., and Jonkman, J., (2011), "State of the art in floating wind turbine design tools", Proceedings of the 21st International Offshore and Polar Engineering Conference, Maui, Hawaii, USA. Vol. 1, pp. 367–374.
[7] Matha, D., Schlipf, M., Cordle, A., Pereira, R., and Jonkman, J., (2011). "Challenges in Simulation of Aerodynamics, Hydrodynamics, and Mooring-Line Dynamics of Floating Offshore Wind Turbines," Proceedings of the 21st International Offshore and Polar Engineering Conference, Maui, Hawaii, USA, Vol. 1, pp. 421–428.
[8] Robertson, A., Jonkman, J. Qvist, J.,Chen, X., Armendariz,J.A., Soares, C.G., Luan, C., Huang, Y., Yde, A.,Larsen, T., Nichols, J., Lei, Liu, Maus, K.J., Godreau, C., Heege, A., Vatne, S.R., Manolas,D., Qin, H., Riber, H., Abele, R., Yamaguchi, A., Pham,A. Alves,M., Kofoed-Hansen,H., (2014), " Offshore code comparison collaboration, continued: phase II results of a floating semisubmersible wind system", In Proceedings of the 33rd International Conference on Ocean, Offshore and Arctic Engineering, no. OMAE2014-24040, San Francisco, USA, 2014.
[9] Luan, C., Gao, Z. and Moan, T., (2017), "Development and verification of a time-domain approach for determining forces and moments in structural components of floaters with an application to floating wind turbines". Marine Structures. vol. 5 pp 87-109.
[10] Kvittem, M.I., Bachynski, E.E. and Moan, T., (2012), "Effects of Hydrodynamic Modelling in Fully Coupled Simulations of a Semi-Submersible Wind Turbine", Energy Procedia. 2012; 24: 351-362. doi:10.1016/j.egypro.2012.06.118.
[11] Luan, C., Chabaud, V., Bachynski, E., Gao, Z., and Moan, T., "Experimental validation of a time-domain approach for determining sectional loads in a floating wind turbine hull subjected to moderate waves", accepted for publication at Energy Procedia
[12] A. J. Goupee, B. J. Koo, K. Lambrakos, and R. W. Kimball, "Model tests for three floating wind turbine concepts," in Proceedings of the 2012 Offshore Technology Conference, Houston, Texas, USA, 30 April 2012–3 May 2012.
[13] A. J. Goupee, B. Koo, R. W. Kimball, K. F. Lambrakos, and H. J. Dagher, "Experimental comparison of three floating wind turbine concepts," in Proceedings of the 31st ASME International Conference on Offshore Mechanics and Arctic Engineering, Rio de Janeiro, Brazil, 1–6 July 2012.
[14] B. Koo, A. J. Goupee, K. Lambrakos, and R. W. Kimball, "Model tests for a floating wind turbine on three different floaters," in Proceedings of the 31st ASME International Conference on Offshore Mechanics and Arctic Engineering, Rio de Janeiro, Brazil, 1–6 July 2012.
[15] Roddier, D., Cermelli, C., Aubault, A., and Weinstein, A., (2010), "WindFloat: A floating foundation for offshore wind turbines", Journal of Renewable and Sustainable Energy 2, 033104, doi:10.1063/1.3435339.
[16] Wan, L., Gao, Z., and Moan, T., (2015). "Experimental and numerical study of hydrodynamic responses of a combined wind and wave energy converter concept in survival modes". Coastal Engineering, 104, pp. 151 – 169.
[17] Kimball, R., Goupee, A. J., Fowler, M. J., de Ridder, E.-J., and Helder, J., (2014). "Wind/wave basin verification of a performance-matched scale-model wind turbine on a floating offshore wind turbine platform". In Proceedings of the ASME 2014 33rd International Conference on Ocean, Offshore and Arctic Engineering, no. OMAE2014-24166.
[18] Fowler, M. J., Kimball, R. W., Thomas, D. A., and Goupee, A. J., (2013). "Design and testing of scale model wind turbines for use in wind/wave basin model tests of floating offshore wind turbines". In 32nd International Conference on Ocean, Offshore and Arctic Engineering, no. OMAE2013- 10122.
[19] Bottasso, C. L., Campagnolo, F., and Pectrovic, V., (2014). "Wind tunnel testing of scaled wind turbine models: Beyond aerodynamics". Journal of Wind Engineering and Industrial Aerodynamics, 127, pp. 11–28.
[20] Fernandes, G., Make, M., Gueydon, S., and Vaz, G., (2014). "Sensitivity to aerodynamic forces for the accurate modelling of floating offshore wind turbines". In RENEW2014, G. Soares, ed., no. ISBN: 978-1-138-02871-5.
[21] Helder, J., and Pietersma, M., (2013), "UMAINE-DEEPCWIND/OC4 SEMIFLOATING WIND TURBINE", 27005-1-OB. Wageningen, NL:MARIN.

[22]Sauder, T., Chabaud, V., Thys, M., Bachynski, E. E., and Sæther, L. O., (2016). "Real-time hybrid model testing of a braceless semi-submersible wind turbine: Part I: The hybrid approach". In 35th International Conference on Ocean, Offshore and Arctic Engineering, no. OMAE2016-54435.
[23] Hall, M., Goupee, A., and Jonkman, J., (2017), "Development of performance specifications for hybrid modeling of floating wind turbines in wave basin tests", Journal of Ocean Engineering and Marine Energy.
[24] Laino, D., and Hansen, C., (2002), "User's guide to the wind turbine aerodynamics computer software Aerodyn", Windward Engineering, Prepared for the National Renewable Energy Laboratory under Subcontract No. TCX-9-29209-01.
[25]Bachynski, E. E., Thys, M., Chabaud, V., and Sauder, T., (2016). "Realtime Hybrid Model Testing of a Braceless Semi-submersible Wind turbine. Part II: Experimental Results". In 35th International Conference on Ocean, Offshore and Arctic Engineering, no OMAE2016-54437.
[26] Chabaud, V., (2016), "*Real-Time Hybrid Model Testing of Floating Wind Turbines*". Ph.d thesis, ISBN 978-82-326-2083-8., NTNU, Norway.
[27] Wendt, F., Robertson, A., and Jonkman, J., (2017), "FAST model calibration and validation of the OC5-DeepCwind floating offshore wind system against wave tank test data", the 27th International Ocean and Polar Engineering Conference, San Francisco, California, U.S.A..
[28] Ormberg, H., Baarholm, R., and Stansberg, C.T., (2003). "Time-domain coupled analysis of deepwater TLP, and verification against model tests". Proc. 13th ISOPE Conf., Honolulu, Hawaii, USA.
[29] MARINTEK, (2011). SIMO User's Manual.
[30] MARINTEK, (2013). RIFLEX User's Manual.
[31] DNV, (2010), "Recommended Practice - Environmental Conditions and Environmental Loads", DNV-RP-C205, Det Norske Veritas.
[32] Berthelsen, P. A., Bachynski, E. E., Karimirad, M., and Thys, M., (2016). "Real-time hybrid model testing of a braceless semi-submersible wind turbine. Part III: Calibration of a numerical model". In 35th International Conference on Ocean, Offshore and Arctic Engineering, no. OMAE2016-54640.
[33] Luan, C., Gao, Z., and Moan, T., (2016). "Design and analysis of a braceless steel 5-mw semi-submersible wind turbine". Proceedings of the 35th International Conference on Ocean, Offshore and Arctic Engineering, OMAE2016-54848, Busan, Korea, June 19–24.
[34] Naess, A. and Moan, T., (2013), "*Stochastic dynamics of marine structures*", Cambridge University Press, UK.
[35] Bendat, J. S., and Piersol, A. G., (2010). "*Random Data: Analysis and Measurement Procedures, 4th Edition*". John Wiley & Sons, Inc. ISBN: 978-0-470-24877-5, page 180.
[36] Sclavounos, P., Zhang, Y., Ma, Y., and Larson, D., (2017), "Offshore wind turbine nonlinear wave loads and their statistics", In 36th International Conference on Ocean, Offshore and Arctic Engineering, no. OMAE2017-61184.
[37] Faltinsen, O.M., (1990), "*Sea loads on ships and offshore structures*", Cambridge University Press, UK.
[38] Jiang, Z., Moan, T. and Gao, Z., (2015). "A comparative study of shutdown procedures on the dynamic responses of wind turbines". Journal of Offshore Mechanics and Arctic Engineering, 137(1), p.011904.
[39] Jiang, Z., Karimirad, M. and Moan, T., (2013). "Response Analysis of Parked Spar-Type Wind Turbine Considering Blade-Pitch Mechanism Fault". International Journal of Offshore and Polar Engineering, 23(02).
[40] Jiang, Z., Karimirad, M. and Moan, T., (2014). "Dynamic response analysis of wind turbines under blade pitch system fault, grid loss, and shutdown events". Wind Energy, 17(9), pp.1385-1409.
[41] Watanabe, E., Utsunomiya, T., Wang, C., and Hang, L., (2006), "Benchmark hydroelastic responses of a circular VLFS under wave action". Engineering Structures, Vol.28, pp 423-430.
[42] Colwell, S., and Basu, B., (2009), "Tuned liquid column damper in offshore wind turbines for structural control". Engineering Structures, Vol.31, pp 358-368.
[43] Agarwal, P., and Manuel, L., (2009), "Simulation of offshore wind turbine response for long-term extreme load prediction". Engineering Structures, Vol.31, pp 2236-2246.
[44] Dong, W., Moan, T., and Gao, Z., (2011), "Long-term fatigue analysis of multi-planar tubular joints for jacket-type offshore wind turbine in time domain". Engineering Structures, Vol.33, pp 2002-2014.
[45] Si, Y., Karimi, H., and Gao, H., (2014), "Modelling and optimization of a passive structural control design for a spar-type floating wind turbine". Engineering Structures, Vol.69, pp 168-182.
[46] Le Méhauté, B., (1969). "An introduction to hydrodynamics and water waves". Technical Report ERL 118-POL-3-2. U.S. Department of Commerce, Washington DC.

APPENDIX A

Detailed observations of comparisons for identifying the dominant load components listed in Table 11 in section 5.2 are analysed and described as follows:

- Components of $R_5^{s,S1}$ (realization of the fore-aft bending moment in base of side column 1) with oscillating frequencies in the low frequency-range are dominated by $\boldsymbol{L}^{e,gra,S1,A}$ and $\boldsymbol{L}^{e,sta,S1,A}$. Effects of the inertial loads and added mass loads with a constant coefficient matrix corresponding to infinite frequency of the corresponding Part A on $R_5^{s,S1}$ are negligible except for components of $R_5^{s,S1}$ with oscillating frequencies in frequency-range nearby natural frequencies of surge and pitch. Note that effects of second and higher order wave excitations are not included in the numerical models. Components of first-order wave excitations in the low frequency-range are negligible. Spectral densities of incident waves are given in Figure 4. Components of $R_5^{s,S1}$ with oscillating frequencies in the wave-frequency-range are dominated by $\boldsymbol{L}^{e,waex,SX,A}$ and inertial loads and added mass loads with a constant coefficient matrix corresponding to infinite frequency of the corresponding Part A. See Figure A1.

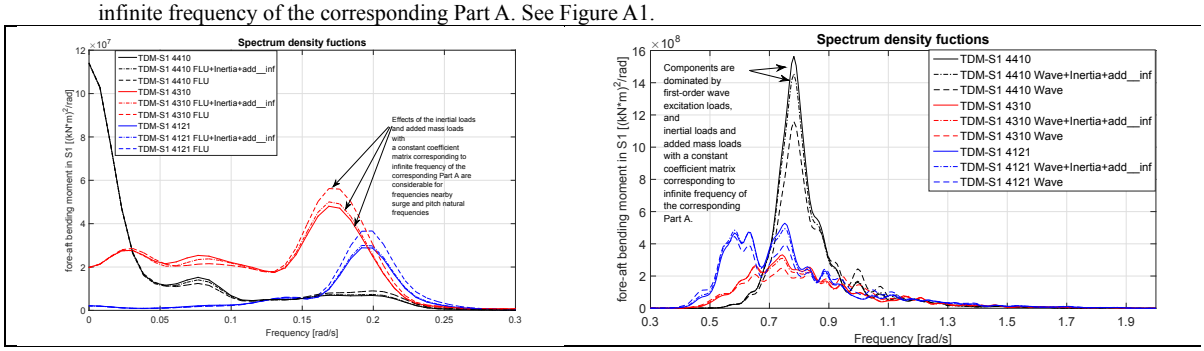

Figure A1 Comparisons of spectral densities of simulated fore-aft bending moments in S1. Note that "Wave+Inertia+add__inf" corresponding to $\boldsymbol{R}^{waex,S1,A}+\boldsymbol{R}^{Inertia,S1,A}+\boldsymbol{R}^{add\_inf,S1,A}$ while "Wave" corresponding to $\boldsymbol{R}^{waex,S1,A}$

- Observations for components of $R_5^{s,S2}$ are similar to the observations for components of $R_5^{s,S1}$ as described in above except that effects of $\boldsymbol{L}^{e,gra,S2,A}$ and $\boldsymbol{L}^{e,sta,S2,A}$ on components of $R_5^{s,S2}$ with oscillating frequencies in the wave-frequency-range are not negligible. Note that $\boldsymbol{L}^{e,sta,S2,A}$ is related to rigid-body motions and configuration of the wetted body surface of the corresponding Part A. See Figures A1 and A2.

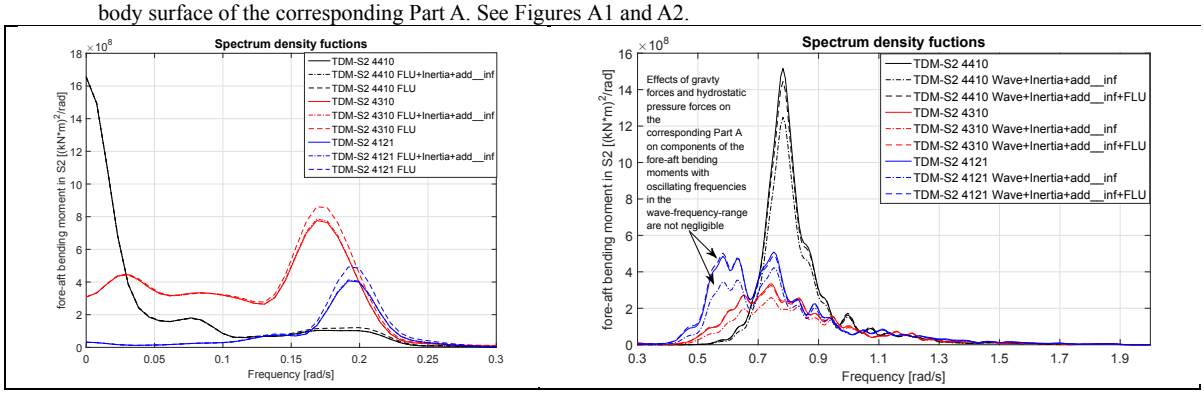

Figure A2 Comparisons of spectral densities of simulated fore-aft bending moments in S2. Note that "Wave+Inertia+add__inf" corresponding to $\boldsymbol{R}^{waex,S2,A}+\boldsymbol{R}^{Inertia,S2,A}+\boldsymbol{R}^{add\_inf,S2,A}$ while "FLU" corresponding to $\boldsymbol{R}^{flu,S2,A}$

- Observations for components of $R_5^{s,S3}$ are similar to the observations for components of $R_5^{s,S2}$ as described in above. See Figures A2 and A3.

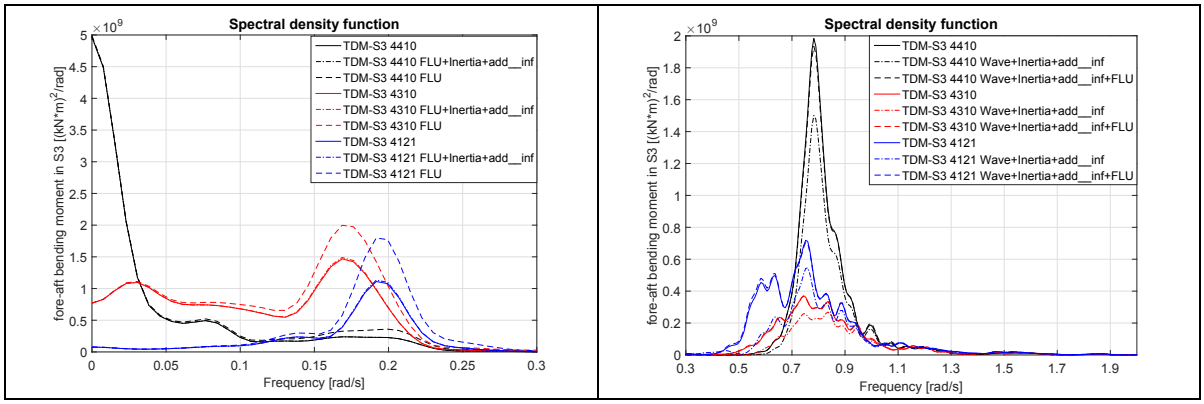

Figure A3 Comparisons of spectral densities of simulated fore-aft bending moments in S3. Note that "Wave+Inertia+add__inf" corresponding to $\boldsymbol{R}^{waex,S3,A}$+$\boldsymbol{R}^{Inertia,S3,A}$ + $\boldsymbol{R}^{add\_inf,S3,A}$ while "FLU" corresponding to $\boldsymbol{R}^{flu,S3,A}$

- The expression of equilibrium for $R_5^{s,S5}$ is given in Eq. (8). Inertial loads on the RNA and tower affect components of $R_5^{s,S5}$ with oscillating frequencies that are around pitch natural frequency, e.g. from 0.15 rad/s to 0.25 rad/s. Components of $R_5^{s,S5}$ with very small oscillating frequencies, e.g. below 0.15 rad/s, are dominated by wind loads on and gravity forces of the RNA and tower. The inertial loads of the RNA and tower strongly affect components of $R_5^{s,S5}$ with oscillating frequencies that are in the wave-frequency-range. While, effects of the wind loads on and gravity forces of the RNA and tower on these components are not negligible.

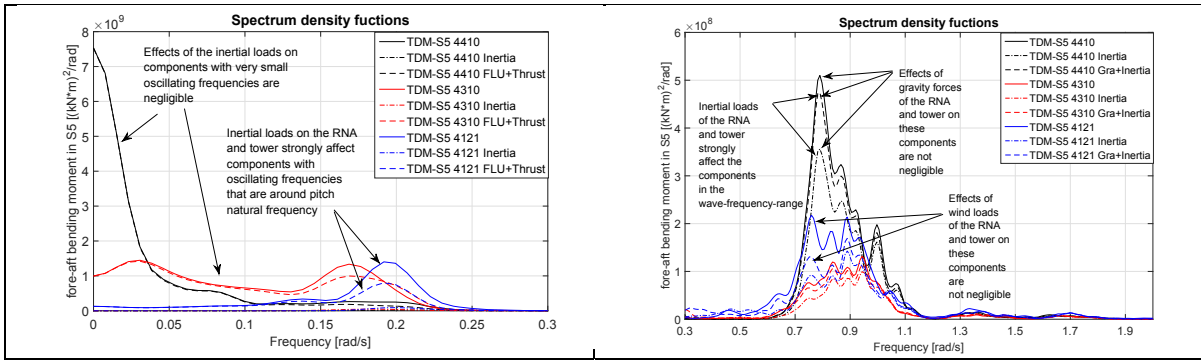

Figure A4 Comparisons of spectral densities of simulated fore-aft bending moments in S5. Note that "Inertia" corresponding to $\boldsymbol{R}^{Inertia,S5,B}$ while "Gra" corresponding to $\boldsymbol{R}^{flu,S5,B}$

- Observations for components of $R_5^{s,S4}$ (realization of the fore-aft bending moment in base of the central column) with oscillating frequencies in the low frequency-range are similar to the observations for the corresponding components of $R_5^{s,S5}$. Observations for components of $R_5^{s,S4}$ with oscillating frequencies in the wave-frequency-range are similar to the observations for components of $R_5^{s,S2}$ except that effects thrust forces on the RNA and tower on the components of $R_5^{s,S4}$ with oscillating frequencies in the wave-frequency-range are not negligible. See Figures A2, A4 and A5.

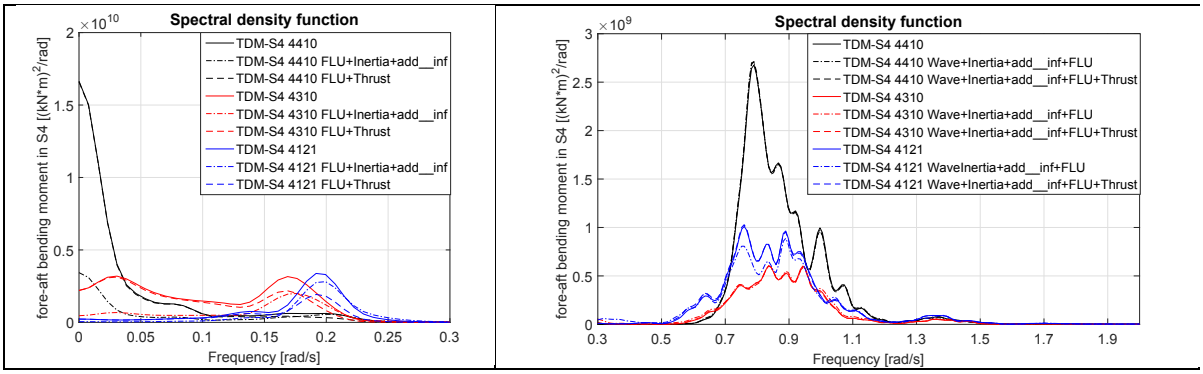

Figure A5 Comparisons of spectral densities of simulated fore-aft bending moments in S4. Note that "Wave+Inertia+add__inf+FLU" corresponding to $\boldsymbol{R}^{waex,S4,B}$+$\boldsymbol{R}^{Inertia,S4,B}$ + $\boldsymbol{R}^{add\_inf,S4,B}$ + $\boldsymbol{R}^{flu,S4,B}$ while "Thrust" corresponding to $\boldsymbol{R}^{Thrust,S4,B}$

APPENDIX B

Spectral densities of rigid-body motions and fore-aft bending moments in the five cross-sections given by numerical models with and without the convolution terms in the expressions of radiation loads on each part of the hull are compared. Numerical model without the convolution term means that 1) the potential damping forces are not modelled, and 2) the frequency dependent added mass coefficients are replaced by added mass coefficients that corresponding to the high-frequency limit.

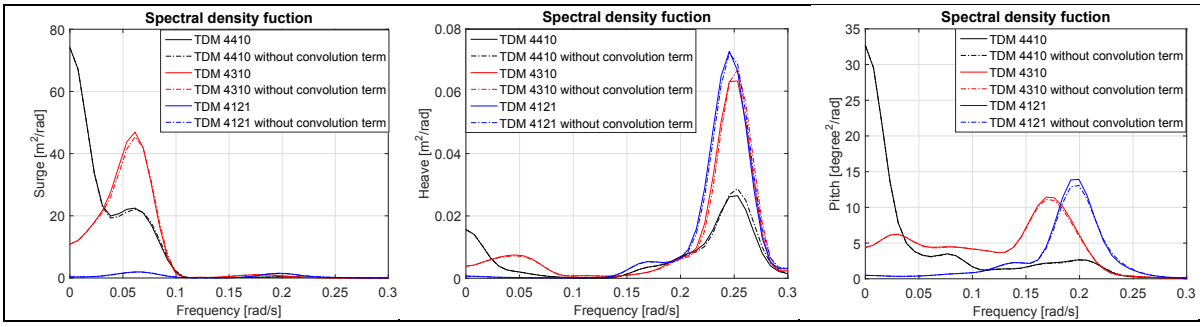

Figure B1 Comparisons of spectral densities of simulated surge, heave and pitch motions with and without the convolution terms in frequency range from 0 rad/s to 0.3 rad/s

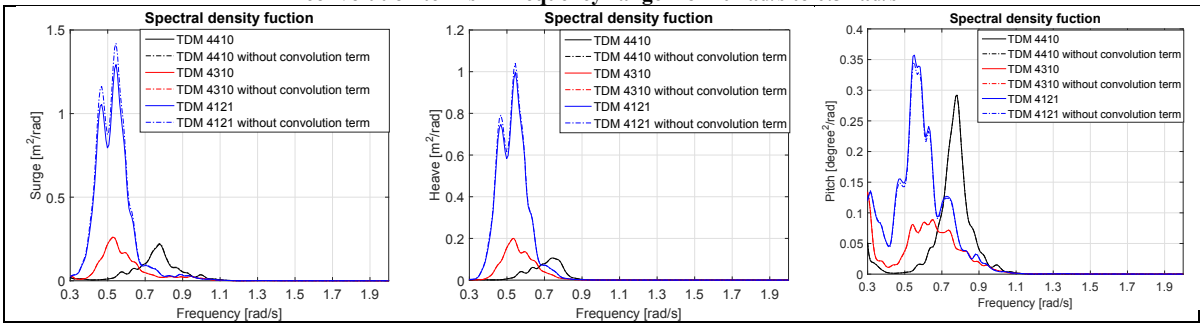

Figure B2 Comparisons of spectral densities of simulated surge, heave and pitch motions with and without the convolution terms in frequency range from 0.3 rad/s to 2 rad/s

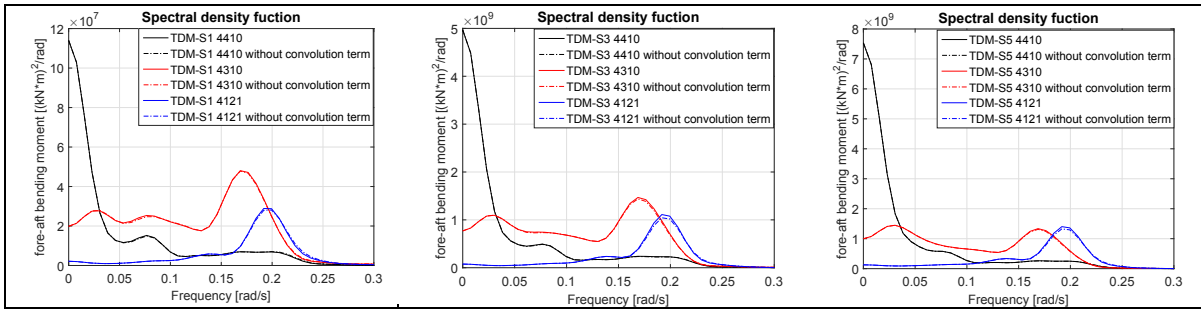

Figure B3 Comparisons of spectral densities of simulated fore-aft bending moment with and without the convolution terms in frequency range from 0 rad/s to 0.3 rad/s

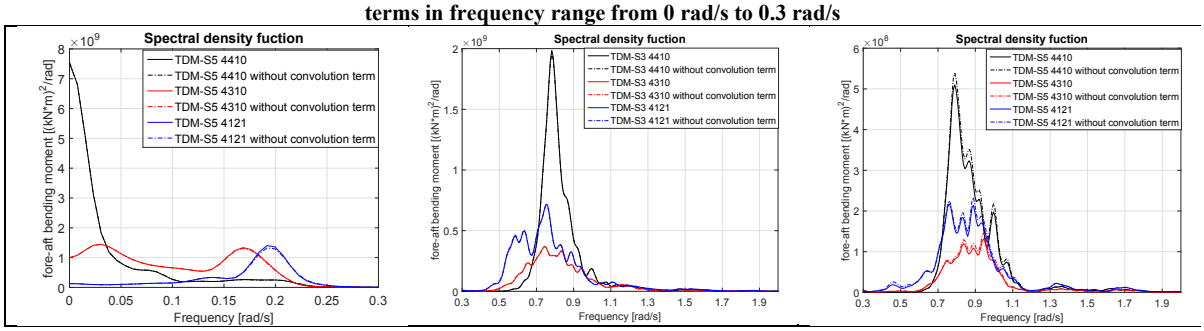

Figure B4 Comparisons of spectral densities of simulated fore-aft bending moment with and without the convolution terms in frequency range from 0.3 rad/s to 2 rad/s

A.4 Paper A4

Paper A4:
Modelling and analysis of a semi-submersible wind turbine with a central tower with emphasis on the brace system
Chenyu Luan, Zhen Gao and Torgeir Moan
Published in 32nd International Conference on Ocean, Offshore and Arctic Engineering, no, OMAE2013-10408, Nantes, France.

MODELLING AND ANALYSIS OF A SEMI-SUBMERSIBLE WIND TURBINE WITH A CENTRAL TOWER WITH EMPHASIS ON THE BRACE SYSTEM

Chenyu Luan
Centre for Ships and Ocean Structures, NTNU
Norwegian Research Centre for Offshore Wind Technology, NTNU
Trondheim, Norway
Chenyu.luan@ntnu.no

Zhen Gao
Centre for Ships and Ocean Structures, NTNU
Trondheim, Norway
Zhen.gao@ntnu.no

Torgeir Moan
Centre for Ships and Ocean Structures, NTNU
Norwegian Research Centre for Offshore Wind Technology, NTNU
Trondheim, Norway
Torgeir.moan@ntnu.no

ABSTRACT

This paper deals with analysis of the OC4 DeepCWind semi-submersible wind turbine, which is provided by NREL through the OC4 project. This concept is a three-column semi-submersible supporting a 5 MW wind turbine on an additional central column.

The fact that the semi-submersible floater needs a large water line restoring moment to achieve sufficient stability and the control of the cost based on the steel weight make the design of braces and pontoons very challenging. Effective methods are needed to check the strength of the brace system based on the response forces and moments in the braces under different design environmental conditions, while the floating wind turbine is needed to be considered as an aero-hydro-servo-elastic system.

A novel modeling methodology based on the code Simo/Riflex is introduced in this paper. Simo/Riflex is a state-of-the-art code that can account for the coupling effect between rigid body motions and slender structures (e.g. mooring lines, braces and blades) in the time-domain. Simo/Riflex can be combined with Aerodyn, which is a state-of-the-art aerodynamic code, to model the floating wind turbine as an aero-hydro-servo-elastic system, as well as be combined with simplified aerodynamic codes (e.g.TDHMILL) to improve the efficiency of the numerical simulation.

The novel modeling method can give the forces and moments in the brace system of the floater under hydrodynamic and aerodynamic loads in the time-domain. In order to get the structural response of the braces, the side columns and the central supporting column are modeled as independent rigid bodies in Simo while the braces are modeled by beam elements in Riflex. Master and slave relationship is applied at the joints in between of the columns and braces.

As an application example, the novel modeling method based on the code Simo/Riflex+TDHMILL, which is capable of modeling the floating wind turbine as an aero-hydro-elastic system, has been used to carry out Ultimate Limit State (ULS) design check for the brace system of the OC4 DeepCWind semi-submersible wind turbine based on relevant standards, i.e. NORSOK N00-3, NORSOK N-004, IEC61400-1, IEC61400-3.

The modeling method can also be used by other codes which have similar features as Simo/Riflex.

INTRODUCTION

The interest in offshore wind energy is increasing since most of easy and good onshore wind fields have been developed. Moreover, offshore has better wind conditions, and offshore has less noise pollution to the local residence. The main challenge of developing offshore wind energy is to reduce the cost per generated power to a competitive level compared to onshore wind energy and other commercial methods for power generation such as hydropower and thermal power.

The substructure of offshore wind turbines makes up a high percentage of the total cost of an offshore wind field. Based on some existing data of monopile wind turbine farms, the percentage may be about 20% or even more [1]. But the cost is sensitive to environmental conditions at the specified field. In general, bottom fixed concepts, e.g. monopile and jacket, are used for shallow water (water depth up to 30-40m for monopile and water depth up to 60-80m for jacket). With the increasing of the water depth, the cost of the monopile or jacket increases significantly. Floating concepts are considered for water depth more than 100m. The experiences in the offshore oil industry have been used to develop floating wind turbines. Several designs with a 5 MW turbine have been proposed, e.g. the OC3-Hywind [2], NREL-MIT TLP [3], and WindFloat [4].

In the present paper, the focus is on the OC4 DeepCWind semi-submersible wind turbine [5], which is a semi-submersible wind turbine provided by NREL for the OC4 project. The OC4 DeepCWind semi-submersible supports the wind turbine by a central column, while WindFloat supports the wind turbine by an offset-column.

The semi-submersible concept mainly uses water line area restoring moment to achieve sufficient stiffness against overturning. On one hand, the large overturning moment due to the aerodynamic loads on the blades forces the designer to obtain sufficient restoring stiffness by increasing the distance between the side columns. On the other hand, the designers have to control the steel weight because of the associated costs. Consequently, the design of the brace system for semi-submersible floating wind turbine is a challenging task. Meanwhile, long-term harsh environmental conditions and wind turbine faults may result in ultimate or fatigue failure. As a result, design checks based on well considered numerical simulations are important for designers to achieve a floating wind turbine design with satisfied reliability and acceptable costs.

The present paper proposes a novel numerical modeling method that can be used to obtain the brace responses due to environmental loads in the time-domain. The method has been applied for ULS design check for the OC4 DeepCWind semi-submersible wind turbine. The environmental data corresponding to an offshore site at the central North Sea has been selected in the design check although the floater is originally designed for Gulf of Maine. Relevant information about model descriptions, modeling method, results and discussions have been presented in the following sections.

WIND TURBINE MODEL

The outline of the OC4 DeepCWind semi-submersible is shown in Figure 1 and Figure 2. Wind turbine is located on the centre column, named as main column (MC). There are three side-columns around the central column. For each of the side-columns, it includes an upper column (UC) and a base column (BC). Braces are used to connect the main column, the upper columns and base column as an integrated body. Relevant geometry information about the columns can be found in Figure 2.

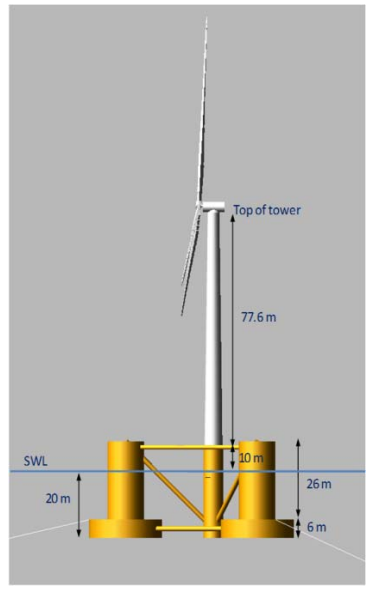

Figure 1Side view of the OC4 DeepCWind semisubmersible wind turbine [5]

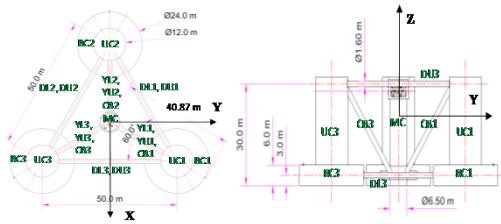

Figure 2 Plan (left) and Side (right) view of the OC4 DeepCWind Semisubmersible [5]

The freeboard of the side-columns is 12m. The distance between the top of the main column and the SWL is 10m. The NREL offshore 5-MW base line wind turbine described in reference [6] is used in the current model. The control system is described in reference [6] is used in the OC4 project. But it is not included in the present model due to the limitation of the applied simplified aerodynamic model which has been described in the following section. The coordinate system is shown in Figure 2. The origin of the coordinate system is at the center of the water line area of the main column.

The names of the columns and braces have been shown in Figure 2. All columns and braces have cylindrical shape. The diameter of all the braces is 1.6m.

Normal steel (Desity=7850 [kg/m^3]; Young's modulus=2.1E+11[Pa]; Yield stress=235[MPa]; Poisson ratio=0.3; Structural damping ratio=1%) is applied to all the braces. The position of each brace is tabulated by Table 1. The coordinate system is the same as the one used in Figure 2.

Table 1 Member Geometry [5]

Name	Abbr.	Start location (X,Y,Z)	End location (X,Y,Z)	Length (m)	Wall Thick. (m)
Main Column	MC	(0, 0,-20)	(0, 0,10)	30	0.03
Upper Column 1	UC1	(14.43, 25, -14)	(14.43, 25, 12)	26	0.06
Upper Column 2	UC2	(-28.87, 0, -14)	(-28.87, 0, 12)	26	0.06
Upper Column 3	UC3	(14.43, -25, -14)	(14.43, -25, 12)	26	0.06
Base Column 1	BC1	(14.43, 25, -20)	(14.43, 25, -14)	6	0.06
Base Column 2	BC2	(-28.87, 0, -20)	(-28.87, 0, -14)	6	0.06
Base Column 3	BC3	(14.43, -25, -20)	(14.43, -25, -14)	6	0.06
Delta Upper Brace 1	DU1	(9.20, 22, 10)	(-23.67, 3, 10)	38	0.0175
Delta Upper Brace 2	DU2	(-23.67, -3, 10)	(9.20, -22, 10)	38	0.0175
Delta Upper Brace 3	DU3	(14.43, -19, 10)	(14.43, 19, 10)	38	0.0175
Delta Lower Brace 1	DL1	(4, 19, -17)	(-18.47, 6, -17)	26	0.0175
Delta Lower Brace 2	DL2	(-18.47, -6, -17)	(4, -19, -17)	26	0.0175
Delta Lower Brace 3	DL3	(14.43, -13, -17)	(14.43, 13, -17)	26	0.0175
Y Upper Brace 1	YU1	(1.625, 2.815, 10)	(11.43, 19.81, 10)	19.62	0.0175
Y Upper Brace 2	YU2	(-3.25, 0, 10)	(-22.87, 0, 10)	19.62	0.0175
Y Upper Brace 3	YU3	(1.625, -2.815, 10)	(11.43, -19.81, 10)	19.62	0.0175
Y Lower Brace 1	YL1	(1.625, 2.815, -17)	(8.4, 14.6, -17)	13.62	0.0175
Y Lower Brace 2	YL2	(-3.25, 0, -17)	(-16.87, 0, -17)	13.62	0.0175
Y Lower Brace 3	YL3	(1.625, -2.815, -17)	(8.4, -14.6, -17)	13.62	0.0175
Cross Brace 1	CB1	(1.625, 2.815, -16.2)	(11.43, 19.81, 9.13)	32.04	0.0175
Cross Brace 2	CB2	(-3.25, 0, -16.2)	(-22.87, 0, 9.13)	32.04	0.0175
Cross Brace 3	CB3	(1.625, -2.815, -16.2)	(11.43, -19.81, 9.13)	32.04	0.0175

It should be noted that the wall thickness in Table 1 is specified by reference [5] with the consideration of achieving the same mass distribution as a scaled model in the laboratory test [7].

The mass of the OC4 DeepCWind semi-submersible has been re-calculated and reformulated for the purpose of applying the novel method described in the next section to do ULS design check.

Table 2 Mass property of columns and braces. The centre of gravity and moments of inertia are referred to the coordinate system described in Figure 2.

Item	Unit	Offset column 1	Offset column 2	Offset column 3	MC	Braces
M	Tonne	4354	4354	4354	152	268
x	m	-14.65	-14.65	29.3	0	0
y		-25.37	25.37	0	0	0
z		-13.78	-13.78	-13.78	-5.77	-1.63
I_x	Tonne *m^2	4.00E+06	4.00E+06	1.20E+06	1.83E+04	6.44E+04
I_y		2.13E+06	2.13E+06	4.94E+06	1.83E+04	6.44E+04
I_z		4.08E+06	4.08E+06	4.08E+06	1.58E+03	4.87E+04
I_xy		1.62E+06	-1.62E+06	0.00E+00	0.00E+00	0.00E+00
I_yz		0.00E+00	0.00E+00	0.00E+00	0.00E+00	0.00E+00
I_xz		0.00E+00	0.00E+00	0.00E+00	0.00E+00	0.00E+00

The mass of the side-column includes the mass of the steel hull of UC and BC and the mass of ballast water in UC and BC. There is no ballast water in MC and braces. The mass of MC only considers the mass of the steel hull. It should be noted that the mass of turbine, tower and mooring lines are not included in Table 2.2, but they are available in [5, 6].

Three catenary mooring lines are used to provide horizontal restoring stiffness. Each of the mooring lines is attached at the upper surface of each base column through the corresponding fairlead. The distance from each fairlead to the centre line of the main column is 40.868m. The anchors are located on flat sea floor which is 200m below the SWL. The distance from each anchor to the centre line of the main column is 837.6m. The unstretched length of each mooring line is 835.5m. The angle in between of the mooring lines is 120 degree. Uniform properties are assumed along the length of the mooring lines. The diameter of each mooring line is 0.0766m. The mass density along the length of each mooring line is 113.35kg/m. The bending stiffness and torsional stiffness are set to be zero. The axial stiffness is 7.536E+8N.

Numerical decay tests have been done by the authors to identify the natural periods the OC4 DeepCWind semi-submersible wind turbine. The results are tabulated as following:

Table 3 Natural periods of the rigid body motions of the OC4 DeepCWind semi-submersible wind turbine based on numerical decay test simulations. The unit is second.

Surge	Sway	Heave	Roll	Pitch	Yaw
115.9	117.3	17.1	26.0	25.8	80.2

NOVEL MODELLING METHOD

The NORSOK standard N004 [8] requires that appropriate models should be developed to verify that the structure can resist relevant actions associated with conditions that may occur during all stages of its life-cycle [8]. In the offshore oil industry, different detailed FEM models have been used to get the responses of the structure under the specified design loads [8]. However, the floating wind turbine is considered as an aero-hydro-servo-elastic system [9]. It means that the aerodynamic loads on blades, as well as the hydrodynamic loads on the floater, are fully coupled with the global motions of the floater. In addition, the aerodynamic control of the wind turbine will change the aerodynamic loads and therefor the floater motions simultaneously. Consequently, it is a big challenge to decide the appropriate design loads. Unfortunately, by now, the experiences are quite limited.

From an engineering point of view, a simple and effective method is needed, especially for preliminary design, to improve the efficiency, reduce the design cost and save the human effort and time. The authors of this paper propose a novel modeling method that makes it possible to obtain the forces and moments in the brace system of a semi-submersible wind turbine based on the time-domain analysis, while considering the floating wind turbine as an aero-hydro-servo-elastic system.

The novel method is developed on the basis of the code Simo/Riflex [10, 11]. Simo/Riflex is a state-of-the-art time-domain code that can well address the hydrodynamic loads and solve the structural dynamic problem in a fully coupled way involving all of rigid body motions and flexible deformations of slender structures (e.g. mooring lines, braces and blades) in the time-domain. The code Simo/Riflex+TDHMILL [12, 13],

which is capable of modeling the floating wind turbine as an aero-hydro-elastic system and Simo/Riflex+Aerodyn [14], which is capable of modeling the floating wind turbine as an aero-hydro-servo-elastic have been used by several researchers to model various floating wind turbines with different types of floaters such as Spar, TLP and semi-submersible [13, 15-17]. In applications that are related to semi-submersible floaters, the floater (including the columns, pontoons and braces) is considered as an integrated rigid body and modeled as a single rigid body system with 6 degrees of freedom of motions. The rigid body motions, in general, can be expressed by Equation (1) and (2). [18]

$$(\boldsymbol{M}+\boldsymbol{A})\ddot{\boldsymbol{x}}+\boldsymbol{C}\dot{\boldsymbol{x}}+\boldsymbol{D_2 f}(\dot{\boldsymbol{x}})+\boldsymbol{K}(\boldsymbol{x})\boldsymbol{x}=\boldsymbol{q}(t,\boldsymbol{x},\dot{\boldsymbol{x}}) \qquad (1)$$

where, $\boldsymbol{M}$ is body mass matrix; $\boldsymbol{A}$ is frequency-dependent added-mass matrix; $\boldsymbol{C}$ is frequency-dependent potential damping matrix; $\boldsymbol{D_2}$ is quadratic damping matrix; $\boldsymbol{f}$ is vector function where each element is given by $f_n = \dot{x}_n|\dot{x}_n|$; $\boldsymbol{K}$ is hydrostatic stiffness matrix; $\boldsymbol{x}$ is position vector; $\boldsymbol{q}$ is external force vector

$$\boldsymbol{q}(t,\boldsymbol{x},\dot{\boldsymbol{x}})=\boldsymbol{q_{WI}}+\boldsymbol{q}_{\boldsymbol{WA}}^{(1)}+\boldsymbol{q}_{\boldsymbol{WA}}^{(2)}+\boldsymbol{q_{CU}}+\boldsymbol{q_{ext}} \qquad (2)$$

where, $\boldsymbol{q_{WI}}$ is wind force; $\boldsymbol{q}_{\boldsymbol{WA}}^{(1)}$ is first order wave excitation force; $\boldsymbol{q}_{\boldsymbol{WA}}^{(2)}$ is second order wave excitation force; $\boldsymbol{q_{CU}}$ is current drag force; $\boldsymbol{q_{ext}}$ any other forces (wave drift damping, specified forces and forces from station-keeping and coupling elements, etc).

$\boldsymbol{X}$, in Equation (1), is 6×1 vector corresponding to 6 degrees of freedom of the rigid-body motions of the floater. $\boldsymbol{A}$ and $\boldsymbol{C}$ are 6×6 frequency dependent added mass and potential damping matrix respectively. They are calculated by the code WAMIT based on Boundary Element Method (BEM) [19]. A panel model corresponding to the whole structure of the floater below water line is needed. The Equation (1) can be further expressed in the form of Cummins equation by doing inverse Fourier transform. The frequency dependent terms are accounted by convolution integrals [20].

The conventional method is not straight-forward to calculate the structural responses of the braces or pontoons since all the braces, columns, pontoons of the floater are modelled as a single body. Instead, the authors propose to model the floater as a multi-body system. Each of the side-columns and the main column is modelled as independent rigid bodies. Meanwhile, each of the braces in between of the columns is modelled as beam element to make it possible to get the brace structure responses under the action effects of the external wave loads and the motions of the side-columns at the ends of the brace. A rigid connection with master and slave relationship is applied at each of the joints between the side-columns and braces. It is used to connect the side-columns with the beam models.

In the novel modelling method, each side-column has 6 degrees of freedom for its rigid-body motion matrix. The motions of the columns can also be solved by Equation (1) except that the matrix and vectors in the Equation (1) should include all degrees of freedom of all columns and the corresponding cross terms which account for the interaction coupling effects between different bodies.

Regarding to the floater of the OC4 DeepCWind semisubmersible wind turbine model, each of the side-columns and main column should be modelled as an independent rigid body. Thus, the floater includes four rigid bodies. Consequently, A(ω) is 24×24 matrix rather than 6×6 matrix. The matrix can be expressed as:

$$A(\omega)=\begin{bmatrix} A^{1,1} & A^{1,2} & A^{1,3} & A^{1,4} \\ A^{2,1} & A^{2,2} & A^{2,3} & A^{2,4} \\ A^{3,1} & A^{3,2} & A^{3,3} & A^{3,4} \\ A^{4,1} & A^{4,2} & A^{4,3} & A^{4,4} \end{bmatrix}_{24\times 24} \qquad (3)$$

$A^{i,j}$ $(i=1,2,3,4; j=1,2,3,4)$ is 6×6 matrix. $A^{i,j}$ expresses the added mass on body i due to 6 degrees of freedom motions of body j. Frequency dependent potential damping matrix is similar to the added mass matrix. These coefficients can be calculated by using multi-body option in WAMIT. However, due to the limitation of the matrix solver, hydrodynamic interaction effect cannot be considered by current version of Riflex. It means, in frequency depended matrix (e.g. Equation (3)) the cross terms are set to be zero, while each of the diagonal terms, e.g. $A^{i,j}$, $i=j$, accounts for the corresponding hydrodynamic load on each body due to the motions of the body in open still sea without the other bodies. Meanwhile, the first order potential wave load on each body does not include hydrodynamic interaction effect. The terms without hydrodynamic interaction effects of each body can be calculated by WAMIT with the panel model corresponding to each body. The second order potential wave loads are not included in current model.

The influence of the hydrodynamic interaction effect on the response of the floater is examined in the next section. The results show that hydrodynamic interaction effect has very limited influence on Response Amplitude Operator (RAO) of the floater, for wave periods (varying from 3 second to 30 second) that are of interest. The hydrodynamic interaction effect will be added by a new version of Riflex in the future.

In addition to the two modelling approaches mentioned in above, each of the columns of the floater could be modelled as beams. Consequently, the floater is treated as a flexible beam element system by which the structural responses of the braces or pontoon can be obtained directly from the time-domain simulation. However the main challenge of this beam element modelling method is how to account for the hydrodynamic loads on the beam model of the columns. Moreover, the beam model may under-estimate the stiffness at the joint between braces and columns, while the local stresses due to stress concentration, which cannot be considered by the beam model, may dominate the stress responses at the joint. The hydrodynamic loads on the columns can be expressed in a practical way by using the Morison formula. It means memory effects due to frequency dependent potential wave loads, added

mass and potential damping have to be neglected. It should be noted that the Morison formula is an empirical formula that is, in general, applicable when the wave length is larger than five times the diameter of the slender structure's cross section [21]. In addition, the Morison formula may not be appropriate to estimate the hydrodynamic loads in the axial directions of the columns. A study presented in [17] concludes that, for a 5 MW semi-submersible wind turbine which is similar to WindFloat, pure Morison model tend to result in overestimation of heave and pitch motions when compared with the potential theory, while diffraction effects became important for heave motions in regular wave analysis with periods below 7 second.

Compared with the conventional method and beam element modelling method used in the offshore oil industry, the proposed approach makes it be capable of accounting for the influence of the hydrodynamic load, aerodynamic load, pitch servo system, and elastic properties of the flexible slender structures on the structural responses of the brace system. The obtained member forces and moments in the brace system can be used for design checks with respect to ULS and Fatigue Limited State (FLS).

The authors apply this method with the code Simo/Riflex+TDHMILL and short term stochastic analysis approach described by NORSOK N003 [22] and NORSOK N004 to obtain the characteristic structural responses in design load conditions. The responses are used to compare with the resistance of the corresponding structure to estimate the safety of the structure. It should be noted that proposed modelling method can also be used in conjunction with other codes, e.g. Simo/Riflex+Aerodyn.

The features of the developed numerical model are summarized in Table 4.

The structure of the 5 MW wind turbine is composed of several systems, i.e. blades, hub, nacelle and tower. The blades, hub and nacelle are modelled as an integrated rigid body attached at the top of the tower. There are no external loads on the rigid body except the gravity and the aerodynamic loads. Aerodynamic load on the blades are simplified as a thrust force acting at the integrated rigid body by TDHMILL. The thrust force and the generated power of the turbine are calculated based on the relative wind speed at the nacelle considering the effect of floater motions and the specified normalized thrust and power coefficients [12]. The gyro moment due to the rotation of the rotor and the global motions of the floater is also considered by TDHMILL.

Each of the columns (side-columns and main column) is modelled as a rigid body with the mass matrix described in Table 2.2. First order wave loads based on the potential theory and drag force based on the Morison formula are used to express the hydrodynamic loads on the columns. The hydrodynamic interaction between the columns is not included in the model.

The tower, mooring lines and braces are modelled as beam elements. The loads on the mooring lines and braces are considered by the Morison formula. The drag coefficient C_d and added mass coefficient C_a in the Morison formula are defined based on the formula described in section 6 of reference [23]. These coefficients depend on Reynolds number, the Keulegan-Carpenter number and the roughness [23]. The drag coefficients used in present model are based on the values specified by [5]. The coefficients have been tabulated in Table 5. The drag coefficients given by reference [5] are selected based on Reynolds number except the base columns since they work as heave plate. Instead, the drag coefficients for base columns are selected based on results of model test [7].

The non-linear hydrodynamic loads (the drag forces on the columns and the hydrodynamic loads on the braces) due to the varying of the wetted surface in the time-domain can be well addressed by Riflex. Riflex provides options that can calculate wave kinematics and wave loads from the sea bed up to the wave surface by stretching the velocity potential of incident wave at the mean surface to the actual wave surface or by keeping the potential being constant from the mean surface to the actual wave surface. In present model, the later one is used. During the time-domain simulation mentioned in the flowing two sections, the relative fluid particle velocity and acceleration at the instantaneous positions of the columns, braces and mooring lines of the OC4 DeepCWind semi-submersible wind turbine and the corresponding Morison loads or viscous loads are calculated by Riflex at each time step.

Table 4 Summary of the features of the developed numerical model

	Mass model	Structure model	Load model
Main column	Integrated mass	Rigid body	1) Gravity/Buoyancy 2) First order wave loads (potential theory) 3) Viscous force (Drag term of the Morison formula)
Side-column 1			
Side-column 2			
Side-column 3			
Nacelle, hub and blades			1) Gravity 2) Aerodynamic loads (TDHMILL)
Mooring lines and braces	Distributed mass	Flexible body, beam element	1) Gravity/Buoyancy 2) Morison formula
Tower		Flexible body, beam element	1) Gravity

Table 5 Drag coefficients and added mass coefficients in the Morison formula [5].

	Braces	Mooring line	MC	UC	BC	BC(axial direction)
C_d	0.63	1.1	0.56	0.61	0.68	4.8
C_a	0.63	1.0				

MODEL VERIFICATION

The influence of hydrodynamic interaction effects on the responses of the floating wind turbine has been investigated.

Two numerical models, Model A and Model B, for the OC4 DeepCWind floating wind turbine have been developed. In Model A, the conventional modeling method with a single body including hydrodynamic interaction effects is used. In Model B, the novel modeling method with a multi-body system but without hydrodynamic interaction effect is used. Regular wave simulations in the time-domain with unit wave amplitude and different wave periods, which are varying from 3 second to 30 second with a step of 0.5 second, have been carried out. The wave direction is pointed to the direction of positive x axis of the coordinate shown in Figure 2. The floating system can be considered as a linear system since the amplitude of each incident regular wave is small (1m) and the aerodynamic loads are not included in the simulations. For each wave period, the motion responses of Model A and Model B are quite sinusoidal. As a result, the response amplitude of the motions are treaded as the motion RAOs, see Figure 3. It should be noted that the motion responses will no longer be sinusoidal due to the non-linear effect when the ratios between the wave height and the diameter of the columns or braces are large, e.g. above 10 [21], in which the drag force dominates.

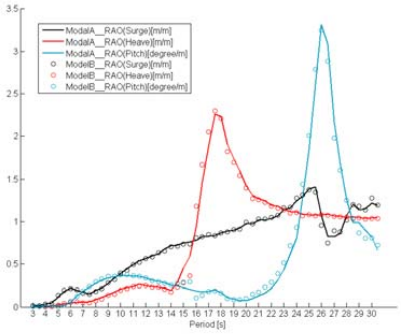

Figure 3 RAOs of surge, heave and pitch motions for Model A and Model B

The motion responses of Model A in Figure 3 refer to the origin of the body related coordinate which is located at the same place as the coordinate system described in Figure 2. Model B includes 4 rigid bodies. The motion responses are referred to origins of the body related coordinate that is similar as the coordinate of Model A except that the positions of the origins are at the intersection of the free surface and the center line of each column. The motion RAOs of Model B shown in Figure 3 are the one of the main column of the floater. The results show that the RAO curves of Model A agree with the curves of Model B quite well, while resonant heave and pitch motions are clearly observed. The results indicate the hydrodynamic interaction effect has very limited influence on the motion responses of the semi-submersible floater described in this paper.

ULS DESIGN CHECK WITH SHORT TERM STOCHASTIC ANALYSIS METHOD

In this section, we address the responses of the braces in 1-hour short term sea states. The main purpose is to give an example of applying the described modeling method and developed numerical model to estimate the responses of the brace system in the environmental conditions corresponding to annual exceedance probability 0.02 (with a return period of 50 years). The responses are further used for ULS design check.

The contour line method [24] is used to predict the long term response by using design environmental conditions. The environmental data at an offshore site at the central North Sea has been used in the example of ULS design check. Information about the chosen site and the corresponding 3-D contour surface have been described in [25]. The water depth of the site is assumed as 200m. Other sites in the northern North Sea, which have more serious sea states, may be applied for future analysis.

135 design environmental conditions along the contour surface of the central North Sea site corresponding to annual exceedance probability 0.02 [26, 27] have been tabulated in Table 6. Five different mean wind speed at the nacelle, including wind speed below rated speed, at rated speed, above rated speed and extreme wind speed have been coved in the specified cases. Kaimal wind spectrums are used to generate turbulent wind. Normal turbulence wind model is used. The turbulent intensity factors given in [26] are applied, while the wind class is assumed as class C (low turbulent wind) due to the fact that offshore wind is less turbulent than onshore wind.

Table 6 Design environmental conditions. Mean wind speed at nacelle: A=9.7m/s; B=11.5 m/s; C=14.69m/s; D=18.3m/s; E=28.65m/s. Turbulence intensity: A=0.16; B=0.15; C=0.14; D=0.13; E=0.11. Hs is significant wave height. Tp is peak period of JONSWAP spectrum.

LC	A		B		C		D		E	
	Hs	Tp	Hs	Tp	Hs	Tp	Hs	Tp	Hs	Tp
1	0.8	23.6	1.1	22.0	1.2	19.7	1.9	16.8	9.2	16.0
2	2.5	17.0	2.8	17.0	2.9	17	5.9	14.7	9.5	12.0
3	4.1	8.5	4.6	8.5	5.5	8.5	6.5	8.5	8.7	10.0
4	4.0	7.5	4.5	7.5	5.3	7.5	6.1	7.5	7.4	8.5
5	4.0	7.0	4.4	7.0	5.2	7	5.8	7.0	6.8	8.0
6	3.8	6.0	4.2	6.0	4.8	6	5.2	6.0	6.1	7.5
7	3.6	5.5	4.0	5.5	4.5	5.5	4.8	5.5	5.4	7.0
8	3.3	4.5	3.5	4.5	3.8	4.5	3.8	4.5	4.5	6.5
9	3.0	4.0	3.2	4.0	3.4	4	3.3	4.0	3.5	6.0

JONSWAP spectrums with peakness factor equal to 3.3 are considered. The Hs, Tp and wave incident directions are chosen based on the results of regular wave analysis [22].

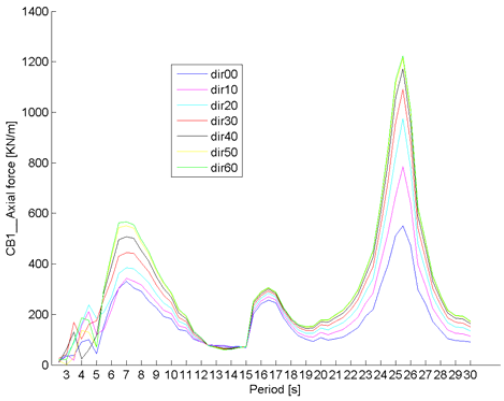

Figure 4 RAO of CB1 axial force based on time-domain regular wave analysis. Dir00, for example, means wave direction is 0 degree.

Similar as what have been shown in previous section, regular wave simulations with unit amplitude have been done by Simo/Riflex to find out structure response RAOs and the critical periods for the brace system. The RAOs of the axial force of CB1 in regular waves with different periods and different incident directions is plotted in Figure 4. The wave period varies from 3 second to 30 second with a step of 0.5 second. The wave direction is defined as the angle from the vector (1,0,0) in the coordinate shown in Figure 2 to the vector of wave propagating direction. Since the wind load effects have not been included in the regular wave analysis, while the hull of the floater and the mass distribution are symmetric, seven different incident directions varying from 0 degree to 60 degree are sufficient to consider effects of waves coming from arbitrary directions. Beside the response RAOs shown in Figure 4, all the other response RAOs have been checked. The results indicate the brace system is sensitive to wave periods around 17s (heave natural period), 26s (pitch natural period) and wave periods from 4s to 8.5 seconds. Consequently, Tp, in Table 6, are chosen to be as close as possible to those critical periods. For each case, Hs is selected as the maximum value on the contour surface corresponding to the chosen mean wind speed and Tp. The incident wave directions in the design environmental conditions are also selected based on the results of regular wave simulations. Wind direction is fixed in the direction of the 0 degree wave direction. For each design cases, three directions of incident wave (0 degree, 30 degree and 60 degree) have been included to consider the effects due to wind and wave misaligned angle. The misaligned wind and wave may be critical to floating wind turbine under certain conditions [3, 13]. A more systematic analysis regarding to the misalign effect on the responses of the brace system should be done in the future work.

It should be noted that, due to the short term response variability, contour line method may, in general, underestimate the responses. The short term response variability can be considered by introducing a correction factor, which depends on the nature of the response model on the expected extreme response or by choosing the extreme maximum value corresponding to a higher percentile of the probability distribution [28]. The correction factor for brace system of semi-submersible floater needs to be calibrated based on full long-term response analysis. Due to the limitation of work scope, the correction based on the consideration of the short term response variability is not included in the work presented in this paper.

The design check of the brace system is carried out by methods and formula specified in NORSOK N004. Utilization ratio (U) is used to express the safety margin of each brace. The brace will fail if U exceed to 1. In general, U can be expressed as [8]:

$$U = {S_d}/{R_d};\ S_d = S_k\gamma_f;\ R_d = {R_k}/{\gamma_M} \qquad (4)$$

where, S_d is design action effect; R_d is design resistance; S_k is characteristic action effect; γ_f is partial factor for actions; R_k is characteristic resistance; γ_M is resulting material factor.

The uncertainty of the material property is reflected in the value chosen for γ_M. It depends on the steel quality. In present study, γ_M is set to be 1.15. γ_f denotes the uncertainty of the action effects, e.g. IEC61400-1 [26] suggests that γ_f could be 1.2 for design wind load. In present study, γ_f is set to be 1.3 to all the action effects for the reason of being conservative. It should be emphasized that the correction factor, which accounts for the short term response variability, mentioned in above is not included since the value of correction factors need to be calibrated based on full long-term response analysis.

The character action effects (force and moment responses) of the brace system are calculated by Simo/Riflex+TDHMILL in time-domain, while the corresponding utilization factors and the characteristic resistances are calculated based on the interaction formulae of the bending moments and the axial forces described in section 6.3.8 of NORSOK N-004. The effects of hydrostatic pressure to structure strength are not included since the design hoop stress is very small compared with design hoop buckling strength. The hydrostatic pressures decrease the characteristic resistances of the structure.

The utilization factor of the interaction formula of tension and bending moment is denoted as U_t. Similarly, U_c denotes the utilization factor of the interaction formula of compression and bending moment. In addition, utilization factor U_r accounts for interaction effects of shear force, bending moment, and torsional moment.

The accuracy of the characteristic load effects depends on mesh density of each brace. Mesh sensitive studies have been done to find out appropriate mesh number for each brace. In addition, it should be noted that design checks have been carried out for braces rather than the joints in between of the braces and columns.

The joints are modeled as rigid. This is because, based on the experience in the offshore oil and gas industry, the bulk head and stiffeners inside the columns lead to high stiffness at the joints. As a result, the effective length factor for calculating

the column slenderness parameter is set to be 0.5 for each of the braces. The effective length factor and the distribution of the bending moments induced by lateral loads depend on the boundary condition at the ends of each brace. The rigid joint assumption will increase the buckling resistance and the bending moments at the ends of each beam.

Selected results are discussed in the following:

Regarding to the static analysis results, the static responses of the forces and moments at the end nodes of each brace in calm water without aerodynamic loads have been checked by hand calculations. The hand calculation results are consistence with the results given by Simo/Riflex+TDHMILL even though, in hand calculation, the braces are simplified as beam with fixed boundary conditions at the ends and unit distributed loads due to the weight and buoyance.

Regarding to the dynamic analysis results, short term 1 hour time-domain simulations corresponding to the design conditions specified in Table 6 have been carried out. According to NORSOK N004, all cross sections along the brace should be checked. In present model, each brace has been discretized as several beam elements. The utilization factors of each brace have been calculated at each time step based on the force and moment responses at the end nodes of each beam element. Then, the maximum utilization factor corresponding to each structure and each design condition can be identified. The value of the maximum utilization factor is a stochastic variable rather than a deterministic value. As a result, the expected value is of interest since it has less variance. For each design condition, 10 1-hour simulations with different random seeds for wind and wave generation have been carried out. For each brace, the average value of the maximum utilization factor of each 10 1-hour simulation is considered as the expected maximum value. Furthermore, for each brace, the largest value of the expected 1-hour maximum utilization factor corresponding to each design condition has been identified and tabulated in Table 7.

The results show that the braces of the OC4 DeepCWind semi-submersible wind turbine have sufficient strength to survive in the specified conditions. It should be emphasized that, as what has been discussed in above, due to the inherent short term stochastic variability, the maximum response in 1-hour simulation corresponding to 50 years return period environmental condition does not necessary mean that the response corresponds to 50 years period probability [24]. A more reliable result is based on the full long term approach.

The results also show that both U_t and U_c are important to design of brace system. DL braces are identified as the most critical braces. The maximum U_c of DL1 in LC3-E30 is 0.91, which is close to 1, while the corresponding U_t is 0.82. Although the utilization factors are not exceeded to the limit, the high values indicate that either the strength of the DL braces may need to be increased or the extreme responses of the braces should be reduced to increase the margin of the floater's safety.

The directions of wind and wave may also be important to brace system design. Figure 5 clearly shows that, for brace DL1, the utilization factors in the cases with 30 degree misaligned angle are much larger, than the one with 0 degree and 60 degree misaligned angles. This is because the wave incident direction is in line with the axial direction of DL1 when the misaligned angle is 30 degree.

The power spectrum of the force and moment responses on DL and DU braces show that the responses of the braces are dominated by wave frequency. In the response spectrum of CB braces, YU and YL braces, low frequency components corresponding to floating wind turbine pitch natural period and slow varying wind speed, wave frequency components and high frequency components corresponding to first eigenperiod can be clearly observed. The results indicate that both the wave induced loads and the loads transferred through the base of the tower are important to the design of YU, YL and CB braces, while DL and DU braces may be more sensitive to wave induced loads.

The torsional moment about the local axial direction along each of the braces is quite limited. As a result, U_r mainly accounts for the combination of shear forces and bending moments.

Table 7 Largest expected utilization factor of each brace. The cases are referred to the design conditions specified in Table 6. LC7-C60, for example, means load condition 7, wind condition "C", wave incident direction is 60 degree.

	Ut		Uc		Ur	
	Value	Case	Value	Case	Value	Case
CB1	0.24	LC3-D60	0.33	LC5-E60	0.20	LC7-C60
CB2	0.17	LC4-E60	0.54	LC5-D00	0.29	LC3-E00
CB3	0.22	LC6-C30	0.34	LC3-E60	0.19	LC6-D30
DL1	0.82	LC3-E30	0.91	LC3-E30	0.52	LC7-D30
DL2	0.60	LC5-D30	0.71	LC6-E30	0.50	LC7-D30
DL3	0.59	LC6-D30	0.77	LC6-D30	0.52	LC6-D30
DU1	0.49	LC6-D30	0.47	LC6-D30	0.39	LC6-D30
DU2	0.48	LC6-D30	0.55	LC6-D30	0.38	LC6-D30
DU3	0.49	LC6-D30	0.57	LC6-D30	0.38	LC6-D30
YL1	0.45	LC5-D30	0.54	LC3-E60	0.46	LC6-D30
YL2	0.45	LC6-D30	0.52	LC3-E00	0.45	LC6-D30
YL3	0.43	LC7-C30	0.40	LC6-D30	0.40	LC7-D30
YU1	0.56	LC6-D30	0.71	LC6-D30	0.59	LC6-D30
YU2	0.61	LC6-D30	0.53	LC6-E30	0.59	LC6-D30
YU3	0.49	LC6-D30	0.59	LC6-D30	0.54	LC6-D30

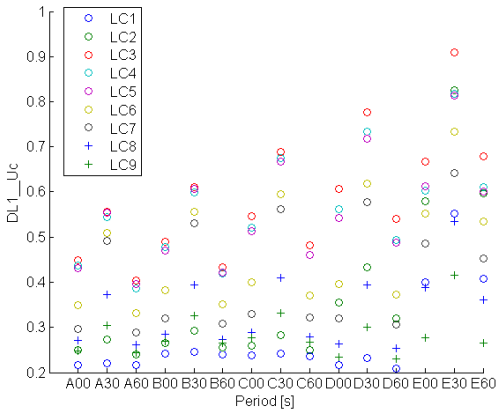

Figure 5 Plot of expected U_c of DL1 for each design condition

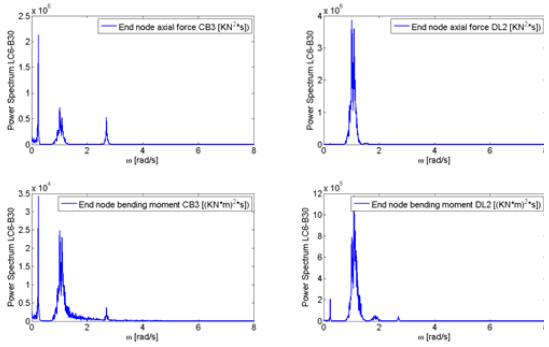

Figure 6 Spectrum plots of axial force and bending moment on end nodes of CB3 and DL2 in sea state LC6-B30 (1-hour simulation)

The application of the proposed novel modeling method makes it possible to get dynamic responses of the braces in short term time-domain analysis. More case simulations have been planned to further release the behaviours of the brace system under the combined wind and wave loads and to improve the current design. Besides the ultimate responses of the brace system, the fatigue problem at the joints may be more critical according to the experience of offshore oil semi-submersible platforms at the North Sea. The brace responses given by proposed method can also be used to do FLS design check. The stress concentrate effect due to the joints can be considered by stress concentration factors based on relevant standards or FEM analysis [29].

CONCLUSIONS

A novel modeling method that can be used to simulate the force and moment responses in the brace system of a semi-submersible wind turbine due to environmental loads and motions in the time-domain while considering the floating wind turbine as an aero-hydro-servo-elastic system has been illustrated.

An example of the ULS design check of the brace system of the OC4 semi-submersible wind turbine with the application of the novel modeling method based on Simo/Riflex+TDHMILL has been shown. The results indicate that the braces have sufficient strength to survive in the design conditions. The utilization factors of the braces are sensitive to misaligned angles of wind and wave. Both U_t and U_c are important to the design of brace system. The DL braces, in specified design conditions, are more critical than other braces.

ACKNOWLEDGMENTS

The authors acknowledge the financial support from the Research Council of Norway granted through the Centre for Ships and Ocean Structures and the Norwegian Research Centre for Offshore Wind Technology (NOWITECH), NTNU. The partial financial support from the EU FP-7 project MARINA Platform project is also acknowledged.

The authors acknowledge the National Renewable Energy Laboratory (NREL) for the close and helpful cooperation. We especially thank Amy Robertson for providing the design data of the OC4 DeepCWind semi-submersible wind turbine.

REFERENCES

[1] Twidell, J. and Gaudiosi, G., (2009), "*Offshore Wind Power*", Multi-Science Publishing Co.Ltd.

[2] Jonkman J., (2010), "Definition of the Floating System for Phase IV of OC3", NREL/TP-500-47535, National Renewable Energy Laboratory, Golden, CO, USA.

[3] Matha, D., Jonkman J., Fischer, T., (2009), "Model Development and Loads Analysis of an Offshore Wind Turbine on a Tension Leg Platform, with a Comparison to Other Floating Turbine Concepts", NREL/SR-500-45891, National Renewable Energy Laboratory, Golden, CO, USA.

[4] Roddier D, Peiffer A, Aubault A, Weinstein J. A Generic, (2011), "5MW WindFloat for Numerical Tool Validation and Comparison Against a Generic Spar", OMAE-2011, Netherlands.

[5] Robertson, A., Jonkman J., Masciola, M., Song, H., A. Goupee, A. Coulling and Luan C., (2012), "Definition of the Semisubmersible Floating System for Phase II of OC4", Offshore Code Comparison Collaboration Continuation (OC4) for IEA Task 30

[6] Jonkman J., Butterfield, S., Musial, W. and Scott, G., (2009), "Definition of a 5-MW Reference Wind Turbine for Offshore System Development", NREL/TP-500-38060, National Renewable Energy Laboratory, Golden, CO, U.S.A.

[7] Andrew G., Bonjun K., Kostas L., Richard K., (2012), " Model Tests for Three Floating Wind Turbine Concepts", Offshore Technology Conference, Houston, Texas, USA, 30 April–3 May 2012

[8] Standards Norway, (2004), "Design of steel structures", NORSOK STANDARD N-004, Standards Norway

[9] Jonkman, J. M. and Matha, D., (2011), “Dynamics of offshore floating wind turbines—analysis of three concepts. Wind Energy”, 14: 557–569. doi: 10.1002/we.442
[10] SIMO project team, (2009), “SIMO - Theory Manual Version 3.7”, REPORT NO.516412.00.04, Norwegian Marine Technology Research Institute, Trondheim, Norway.
[11] MARINTEK, (2011), “RIFLEX User’s Manual”
[12] Yttervik R., (2009), “TDHMILL3D-User documentation”, Statoil, Norway.
[13] Gao, Z., Luan, C., Moan, T., Skaare, B., Solberg, T., and Lygren, J.E., (2011), “Comparative study of wind- and wave-induced dynamic responses of three floating wind turbines supported by spar, semi-submersible and tension-leg floaters”, Proceedings of the 2011 International Conference on Offshore Wind Energy and Ocean Energy, October 31-November 2, Beijing, China.
[14] Ormberg, H. and Bachynski, E.E., (2012), “Global analysis of floating wind turbines: Code development, model sensitivity and benchmark study”, in The 22nd International Ocean and Polar Engineering Conference2012: Rhodes, Greece
[15] Bachynski, E.E. and Moan, T., (2012), “Linear and Nonlinear Analysis of Tension Leg Platform Wind Turbines”, The 22nd International Ocean and Polar Engineering Conference2012, Rhodes, Greece.
[16] Bachynski, E.E. and Moan, T., (2012), “Design Considerations for Tension Leg Platform Wind Turbines”, Marine Structures, 2012. 29: pp. 89-114.
[17] Kvittem, M.I., Bachynski, E.E. and Moan, T., (2012), “Effects of Hydrodynamic Modelling in Fully Coupled Simulations of a Semi-Submersible Wind Turbine”, Energy Procedia. 2012; 24: 351-362. doi:10.1016/j.egypro.2012.06.118
[18] SIMO project team, (2009), “SIMO - Theory Manual Version 3.7”, REPORT NO.516412.00.03, Norwegian Marine Technology Research Institute, Trondheim, Norway.
[19] WAMIT Inc., (2012), “WAMIT User Manual, Version 7.0”, http://www.wamit.com/manual.htm, WAMIT Inc.
[20] Naess, A. and Moan, T., (2013), “*Stochastic dynamics of marine structures*”, Cambridge University Press, UK
[21] Faltinsen, O.M., (1990), “*Sea loads on ships and offshore structures*”, Cambridge University Press, UK
[22] Standards Norway, (2007), “Actions and action effects”, NORSOK STANDARD N-003, Standards Norway.
[23] DNV, (2007), “Recommended Practice - Enivronmental Conditions and Environmental Loads”, DNV-RP-C205, Det Norske Veritas.
[24] Haver, S. and Kleiven G., (2004), “Environmental Contour Lines for Design Purposes- Why and When?”, OMAE-2004, Vancouver, Canada.
[25] Li, L., Gao, Z., Moan, T., (2013), “Joint Environmental Data at Five European Offshore Sites for Design of Combined Wind and Wave Energy Devices”, OMAE2013-10156, Nantes, France.
[26] IEC, (2005), “Wind turbines – Part 1: Design requirements”, IEC-61400-1, International Electrotechnical Commission.
[27] IEC, (2009), “Wind turbines: Part 3: Design requirements for offshore wind turbines”, IEC-61400-3, International Electrotechnical Commission.
[28] Winterstein, S.R., Ude, T.C., Cornell, C.A., Bjerager, P. and Haver, S., 1993. Environmental parameters for the Extreme Response: Inverse FORM with Omission Factors. Proc. ICOSSAR-1993, Balkema, Innsbruck, pp. 551-557.
[29] DNV, (2010), “Recommended Practice - Fatigue Design of Offshore Steel Structures”, DNV-RP-C203, Det Norske Verita

A.5 Paper A5

Paper A5:
Design and analysis of a braceless steel 5-mw semi-submersible wind turbine
Chenyu Luan, Zhen Gao and Torgeir Moan
Published in 35th International Conference on Ocean, Offshore and Arctic Engineering, OMAE2016-54848, Busan, Korea, June 19–24.

DESIGN AND ANALYSIS OF A BRACELESS STEEL 5-MW SEMI-SUBMERSIBLE WIND TURBINE

Chenyu Luan
Norwegian Research Centre for Offshore Wind Technology, (NOWITECH)
Centre for Ships and Ocean Structures (CeSOS)
Centre for Autonomous Marine Operations and Systems (AMOS), NTNU
NO-7491 Trondheim, Norway
Chenyu.luan@ntnu.no

Zhen Gao
CeSOS and AMOS, NTNU
NO-7491 Trondheim, Norway
Zhen.gao@ntnu.no

Torgeir Moan
CeSOS and AMOS, NTNU
NOWITECH
NO-7491 Trondheim, Norway
Torgeir.moan@ntnu.no

ABSTRACT

This paper introduces the design and numerical analysis of a braceless steel semi-submersible wind turbine. The hull of the semi-submersible wind turbine is designed to support a reference 5-MW horizontal axis wind turbine at a site in the northern North Sea. The hull is composed of a central column, three side columns and three pontoons. The side columns and pontoons are arranged radially outward from the central column which is used to support the wind turbine. The side columns form the corners of a triangle on the horizontal plane and are connected by the pontoons to the central column at the bottom to form an integrated structure. Numerical analysis has been carried out to analyze the intact stability, natural periods and modes and structural strength of the design. Results of the numerical analysis show that the design has very good intact stability, well designed natural periods and modes, moderate rigid-body motions in extreme environmental conditions and a reasonable structural design. This paper emphasizes the structural responses of the hull in global and local load effects. The global forces and moments in the hull are calculated by carrying out time-domain global analysis and used as inputs for simplified ultimate limit state design checks for structural strength of the hull. The design can be used as a reference semi-submersible wind turbine. A 1:30 model of the semi-submersible wind turbine has been tested in a hybrid model test by Marintek in October 2015. The model test data will be presented, utilized and discussed in other papers in future.

1 INTRODUCTION

Offshore wind energy has become a significant area of development. Offshore wind power has several advantages over onshore wind power [1]. First, offshore wind sites generally produce stronger winds with less turbulence on average because the sea surface is considerably smoother than the land surface. Second, the effects of noise and visual pollution from these sites on humans are negligible because of their distance from populated areas. Third, in most countries, the sea is owned by the government rather than private landlords, which allows for the development of large offshore wind farms. Finally, good sea transport capabilities allow for the construction of large wind turbines with high rated power (e.g., 5-10 MW).

The potential of offshore wind energy is substantial, particularly in relatively deep water (deeper than 80 m). In deep water, floating platforms might be more economically competitive than bottom fixed structures. As compared to spar-type and TLP wind turbines, the advantages of semi-submersible wind turbines include, but are not limited to, 1) greater flexibility in terms of varying sea bed conditions and drafts and 2) significantly reduced installation costs due to their simpler installation, with full assembly at dock[2].

A design challenge is that semi-submersible wind turbines must have sufficient stability and structural strength while the costs of the produced power must be reduced to a competitive level. Natural periods and modes should be well designed to avoid resonant rigid-body motions and structural vibrations excited by loads such as the 1P and 3P effects and first order wave loads.

Semi-submersible wind turbines mainly use side columns to get sufficient intact stability. To reduce the costs of construction and maintenance, most of the proposed semi-submersible wind turbine concepts feature three side columns. The side columns are arranged radially outward from the geometrical center of the water plane area and form the corners of a triangle on the water plane. A wind turbine could be

mounted on one side column. Alternatively, the wind turbine could be mounted on a central column that is located at the geometrical center of the water plane area.

The 5-MW WindFloat is a well-known three-column semi-submersible wind turbine [2,3], while the OC4-Semi is a four-column semi-submersible wind turbine that includes three side columns and a central column [4]. For each design, the columns are connected by braces to form an integrated structure. At a given joint, a column could be connected by several braces. It can be very complex and expensive to weld the joint. Meanwhile, fatigue life of the joint can be a very critical issue due to stress concentration effect at the joint. In addition, to avoid heave resonant motions excited by first order wave loads, additional heave plates and/or pontoons may be needed. Construction of the additional heave plates can be complex and expensive as well.

Braceless semi-submersible wind turbines, for which the columns are connected by pontoons rather than braces, may be a better solution for reducing design complexity and cost of offshore wind power. Several braceless semi-submersible wind turbine concepts, e.g. the 5-MW GustoMSC Tri-Floater [5], VolturnUS [6] and Dr.techn.Olav Olsen's concept[7], have been proposed. However, discussions on structural behaviors of the pontoons in wind- and wave- induced global and local load effects are very limited.

In present paper, we intend to introduce a design of a braceless steel 5-MW semi-submersible wind turbine. The design is named 5-MW-CSC. The hull of the 5-MW-CSC is designed to support a 5-MW NREL offshore base line wind turbine [8] at a site in the northern North Sea [9]. The hull of the 5-MW-CSC is composed of a central column, three side columns and three pontoons. The side columns are connected by the pontoons to the central column at the bottom to form an integrated structure. The added mass in the heave, roll and pitch is mainly provided by the pontoons. There are no heave plates or braces. The box-shaped cross-section of the pontoons could provide considerable viscous damping at the heave, roll and pitch resonant frequencies.

Numerical analysis has been carried out to analyze the intact stability, natural periods and modes and structural strength of the design. Results of the numerical analysis show that the design has very good intact stability, well designed natural periods and modes, moderate rigid-body motions in extreme environmental conditions and a reasonable structural design. The global forces and moments in the hull are calculated by carrying out time-domain global analysis and used as inputs for simplified ultimate limit state design checks for structural strength of the hull.

The 5-MW-CSC can be used as a reference semi-submersible wind turbine. A 1:30 model of the 5-MW-CSC has been tested in a hybrid model test by Marintek in October 2015. Rigid-body motions, mooring line tensions and global forces and moments in the tower base and the base of a side column, in winds, waves and currents, are measured. The model test data will be presented, utilized and discussed in other papers in future.

2 DESCRIPTION OF THE DEFINITION OF THE 5-MW-CSC

When the 5-MW-CSC is located at its mean positon, the body-fixed coordinate system (x^b-y^b-z^b) of the 5-MW-CSC is coincident to the global coordinate system (x^g-y^g-z^g) shown in Figure 1. The origins of the global and body-fixed coordinate systems (O^g and O^b) are located at the geometrical center of the water plane area. The 0-degree direction of the incident winds and waves is the positive direction of x^g, whereas the 90-degree direction of the incident waves is the positive direction of y^g.

The 5-MW-CSC is composed of a rotor nacelle assembly (RNA), tower, hull and mooring system. The properties of the RNA are described in [8], and the control system and tower are described in [10]. The overall dimensions of the hull are given in Table 1. The diameter of the central column is set to 6.5 m, which is equal to the diameter of the tower base of the wind turbine. The freeboard of the side columns is 20 m. The distance between the top of the central column and SWL is 10 m. The hull is designed to be constructed by steel with the following properties: density=7,850 [kg/m^3]; Young's modulus=$2.1 * 10^{11}$[Pa]; yield stress=235 [MPa]; Poisson's ratio=0.3; and structural damping ratio=1%.

The ratio of the total steel weight to the displacement is approximately 0.17, yielding the equivalent thickness of the hull to be 0.03 m. The global and local load effects at the lower part of the columns, pontoons and joints are more critical than the load effects at the upper part of the columns. The thickness of each component can be adjusted based on a more detailed analysis to improve fatigue life and ultimate strength. Adjustments to the thickness have a negligible effect on the stability, rigid-body motions and global forces and moments in the hull because the displacement is considerably larger than the steel weight.

A ballast distribution for the operating draft is shown in Figure 3. The ballast mass are symmetrically distributed about the central line of the central column. Ballast water is used to achieve the operating draft, and the pontoons are completely filled with ballast water. The pressure head of the ballast water in each side column is 7.7 m as measured from the top of the pontoon. Meanwhile, no ballast water is used in the central column. Mass and moment of inertia of the hull are given in Table 2. The mass properties are calculated by assuming that the ballast water inside the columns and pontoons does not contribute any free surface.

The mooring system is composed of three catenary chain mooring lines. The chain mooring lines are simplified as a uniformly distributed mass with a solid circle cross-section. The design parameters are given in Table 3. The axial stiffness is $3.08 * 10^6$ kN/m. The bending stiffness and torsional stiffness are set to zero.

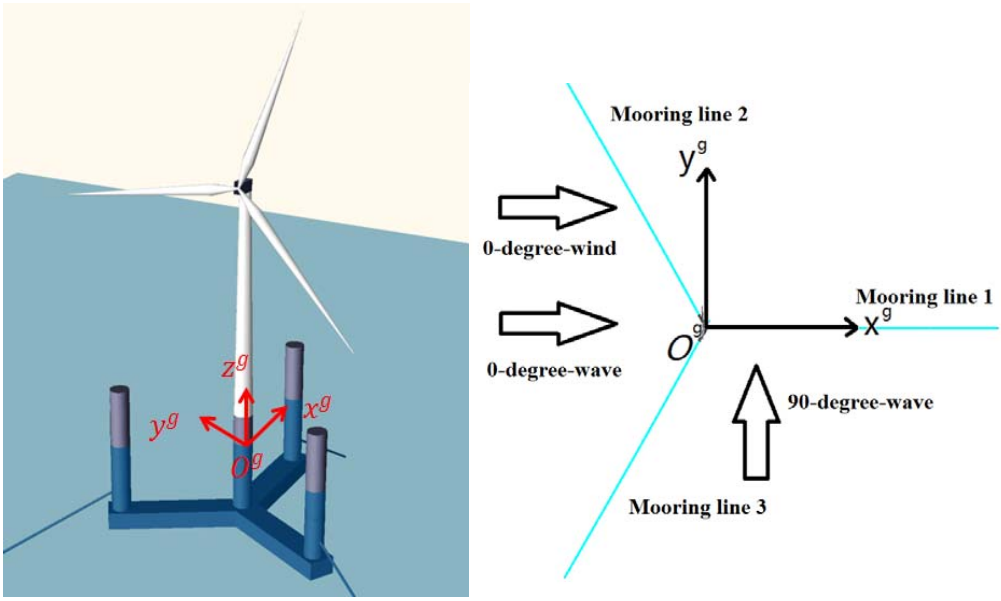

Figure 1 Layout of the 5-MW-CSC

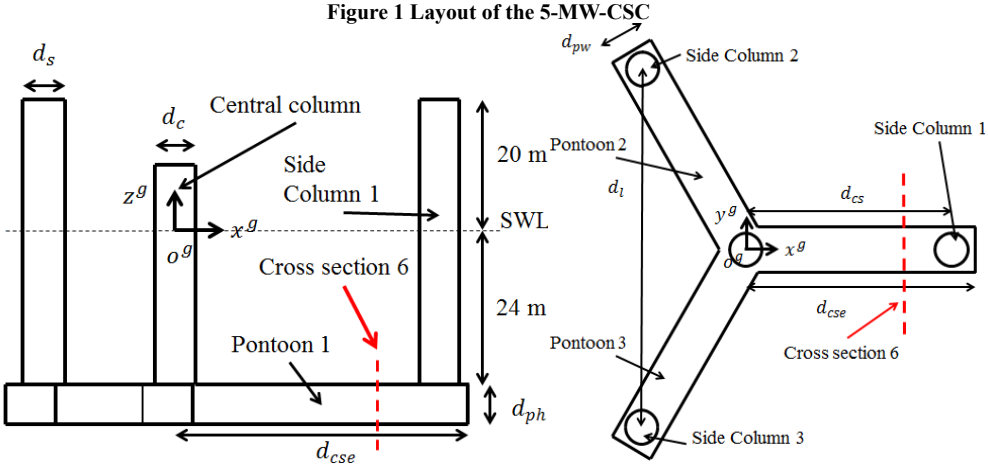

Figure 2 Side (left) and top (right) views of the hull of 5-MW-CSC

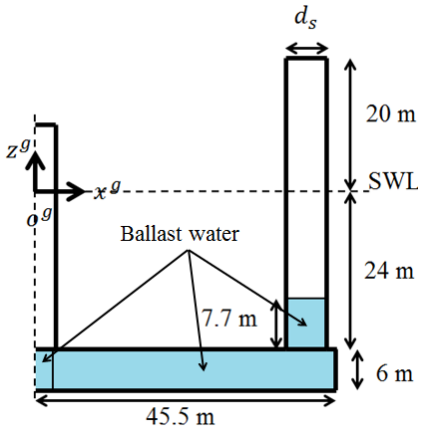

Figure 3 Ballast distribution

Table 1. Dimensions of the hull of the 5-MW-CSC

d_c [m]	6.5
d_s [m]	6.5
d_{ph} [m]	6
d_{pw} [m]	9
d_{cs} [m]	41
d_{cse} [m]	45.5
Operating draft [m]	30
Displacement [tonne]	10,555
Steel weight [tonne] (hull)	1,804
Equivalent thickness [m]	0.03

Table 2 Mass properties of the hull of the 5-MW-CSC (including steel and ballast water). The center of gravity and moments of inertia are described in the body-fixed coordinate system with respect to O^b

Mass [tonnes]	Center of gravity [m]			Moments of inertia [tonnes*m^2]					
	x^b	y^b	z^b	I_{xx}	I_{yy}	I_{zz}	I_{xy}	I_{xz}	I_{yz}
9,738	0	0	-24.36	$1.05 * 10^7$	$1.05 * 10^7$	$8.24 * 10^6$	0	0	0

Table 3. Design parameters of a single mooring line

Mass per unit length (in the air) [tonne/m]	0.115
Pretension at the fairlead [kN]	1,683
Un-stretched mooring line length [m]	1,073
Diameter of the mooring line cross-section [m]	0.137
Density of the material [tonne/m^3]	7.85
Clump weight in water[tonne]	15
Distance from the attachment point of the clump weight to the fairlead (along the mooring line) [m]	240

Table 4. Arrangement of the mooring line anchors and fairleads described in the global coordinate system

Fairlead	x^g	y^g	z^g
1	44.3	0	-18
2	-22.1	38.3	-18
3	-22.1	-38.3	-18
Anchor	x^g	y^g	z^g
1	1,084.4	0	-200
2	-542.2	939.1	-200
3	-542.2	-939.1	-200

3 DESIGN CONDITIONS

Joint probability density function of mean wind speed, significant wave height (H_s) and peak period of wave spectrum (T_p) and a 3-D contour surface of the mean wind speed, H_s and T_p corresponding to the 50-year return period are described in [9]. Two-parameter JONSWAP spectrum is employed to describe the waves, while the winds are described by Kaimal wind spectrum with normal turbulence. Wind class is assumed as class C (low turbulent wind). The turbulent intensity factors are given in [11].

To address motions of the 5-MW-CSC in extreme combined wind and wave conditions, five mean wind speeds (from EC1 to EC5), including a wind speed below the rated speed, a wind speed at the rated speed, two wind speed above the rated speed and an extreme wind speed, are selected and tabulated in Table 5. The mean wind speeds in the table are referred to the position of the nacelle.

The points, which are located on the 3-D contour surface and correspond to a given mean wind speed, can form a closed circle in a 2-D plane with respect to H_s and T_p.

For each mean wind speed, the largest H_s on the corresponding closed circle and the T_p, which corresponds to the largest H_s, are selected. In EC 5, the selected H_s is 0.1 m smaller than the largest H_s of all the points on the 3-D contour surface.

In addition, a simplified ULS design check for the hull is carried out based on 21 design conditions (from U0101 to U0902) selected from the 3-D contour surface. The design conditions are tabulated in Table 5

Table 5. Environmental conditions

Environmental condition	Mean wind speed at nacelle height [m/s]	Turbulence intensity [%]	H_s [m]	T_p [s]	Note
EC1	9.8	16	7.5	14.7	In operation
EC2	11.4	15	7.9	14.4	
EC3	16	13	9.14	15.0	
EC4	20	12	10.3	14.7	
EC5	40.4	11	15.3	14.3	Parked
U0101	4.9	23	4.6	8	In operation
U0102	4.9	23	6.1	18	
U0103	4.9	23	4.7	24	
U0201	8.0	17	5.2	8	
U0202	8.0	17	6.7	18	
U0203	8.0	17	5.3	23	
U0301	11.0	15	5.7	8	
U0302	11.0	15	7.3	18	
U0303	11.0	15	5.5	23	
U0401	16.5	13	6.5	8	
U0402	16.5	13	8.4	18	
U0501	21.3	12	7.1	8	
U0502	21.3	12	10.4	16	
U0601	25.4	11.7	7.5	8	Parked
U0602	25.4	11.7	11.9	15	
U0701	30.0	11.2	8.7	9	
U0702	30.0	11.2	13.3	15	
U0801	34.6	11.1	8.7	9	
U0802	34.6	11.1	14.6	15	
U0901	39.8	11.1	10.5	11	
U0902	39.8	11.1	15.3	14	

4 CASE STUDY FOR THE 5-MW-CSC

4.1 INTACT STABILITY ANALYSIS

The intact stability is checked based on the righting and overturning moment curves. The overturning moments come from aerodynamic loads on the RNA, tower and hull and make the semi-submersible wind turbine rotates with respect to an axis in the water plane area. The geometrical center of the water plane area is always on the axis. For example, the overturning moments induced by constant winds along x^g result in heeling angles with respect to a rotation axis that is in parallel to y^g. Righting moment is generated by hydrostatic pressure forces on the wet surface of the hull and gravity of the semi-submersible wind turbine. To find the most critical situation, righting moment curves corresponding to several different rotational axes need to be calculated and checked. In this paper, we make the rotational axis constantly be in parallel to y^g while the semi-submersible wind turbine is rotated by ϕ degrees with respect to z^g. Since the semi-submersible wind turbine is symmetrical with respect to the $x^g - z^g$ plane, ϕ varies from 0 degrees to 180 degrees with 15-degree intervals. For each righting moment curve, heeling angle varies from 0 degrees to 90 degrees.

Aerodynamic loads on the hull and tower are calculated by Riflex [12]. To simplify the calculation and to be conservative, we neglect the shielding, solidification and finite length effects described in [13] and assume that incident winds are constantly and uniformly distributed from the sea level up to the tower top. The aerodynamic loads on a given cross-section of the tower or a given cross-section of a given column can be expressed by the drag term of the Morison formula [13]. The non-dimensional drag coefficient for the cross-section of the tower or the column is specified as 0.65. Wind loads on the pontoons are not considered even through, under a very large heeling angle, part of the pontoons may be raised from water to air. The aerodynamic loads on the rotor are calculated in Aerodyn [14].

Wind induced forces are in line to the direction of the incident winds. Consequently, for a given ϕ, the maximum overturning moment with respect to the rotational axis is given by the 0-degree-winds, which is project to the rotational axis. Therefore, for each ϕ, overturning moments induced by the 0-degree-winds are calculated. We assume that the rotor plane is always project to the 0-degree-winds and the restoring forces are always acting on (0,0,-18) in the body-fixed coordinate system.

The overturning moments induced by wind loads on the tower and central column are independent to ϕ and proportional to square of cosine of the heeling angle. Due to distribution of the side columns, when the heeling angle is in the range of 0 degrees to 30 degrees, overturning moments induced by wind loads on the side columns are insensitive to ϕ. An example is shown in Figure 4.

Overturning moments induced by wind loads on the rotor in operational and parked conditions and by wind loads on the tower and hull at 0-degree-heeling angle are shown in Figure 5. Aerodynamic loads on the rotor contribute most of the overturning moments in the operational condition. In the parked condition, the overturning moments are proportional to square of mean wind speed and can be critical in extreme winds, e.g. 50 m/s extreme wind at nacelle.

The criterion specified in the DNV-OS-J103 [15] is utilized to check the intact stability of the 5-MW-CSC. We assume that the ballast mass will not introduce a free surface inside the hull. To simplify the calculation and to be conservative, design overturning moment (DOM) is specified as a constant value with respect to the heeling angle. The DOM is independent to Φ and the heeling angle. The constant value is specified as 90,000 kN*m which is obtained by applying a 1.2 safety factor on the most critical overturning moment. The most critical overturning moment is 75,000 kN*m given by the operational condition with 11 m/s mean wind speed. We assume that the hull is an integrated watertight structure without openings on the hull and water will entry to the tower if the central column

is submerged in water. Figure 6 shows that the most critical situation for the intact stability analysis is given by $\phi = 0$. In general, a given righting moment curve and a design overturning moment curve will have two intersections. The ratio of the area under the righting moment curve ($\phi = 0$) from 0 degrees to the second intersection to the corresponding area under the DOM is 1.63, which is larger than 1.3 and satisfies the intact stability criterion. In addition, the DOM inherently includes a large safety margin as well.

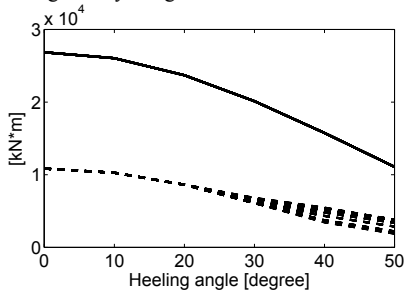

Figure 4. Overturning moment curves induced by 50 m/s constant wind loads on the tower and central column (the solid lines) and on the side columns (the dash lines). ϕ varies from 0 degrees to 180 degrees with 10-degree intervals. Heeling angle varies from 0 degrees to 50 degrees with 10-degree intervals.

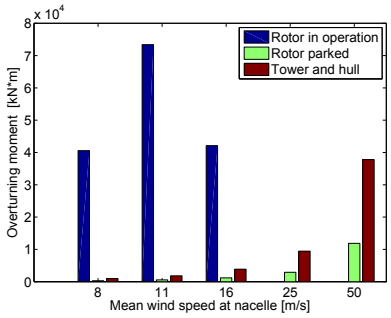

Figure 5 Overturning moments induced by wind loads on the rotor in operational and parked conditions and by wind loads on the tower and hull at 0-degree-heeling angle

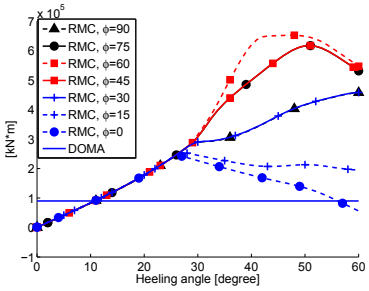

Figure 6 Righting moment curve (RMC) v.s. design overturning moment curve (DOM), intact stability analysis

4.2 NATURAL PERIODS AND MODES

The natural periods of the 6 degrees of freedom rigid-body motions of the 5-MW-CSC are calculated by numerical decay tests and tabulated in Table 6. The numerical model used in the decay tests is denoted as TMD2 and described in the paper [16]. The hull is assumed as a single rigid-body with 6 d.o.f.s. Slender structures, such as blades, shaft of drive train, tower and catenary mooring lines, are modelled by beam elements.

A pure beam model of the 5-MW-CSC (the mooring lines, hull, tower and RNA are modelled by corresponding equivalent beam elements) is developed in Riflex [12] to calculate the other natural periods and modes (structural vibrations). The ballast water inside the pontoons does not contribute to global stiffness. The mass of the beam elements accurately accounts for the mass distribution of the hull (including steel mass and ballast mass). Stiffness of the beam elements for the central column and side columns are calculated based on a circle cross-section with 6.5 m diameter and 0.03 m thickness, while stiffness of the beam elements for the pontoons are calculated based on a box-shape cross-section with 6 m height, 9 m width and 0.03 m thickness. Mooring lines' flexibility is accounted for by using beam elements that do not include bending and torsional stiffness.

The natural periods and modes are calculated based on Lanczos' method. Effects of added mass, gravity, hydrostatic pressure forces on the natural modes are accounted for by the Riflex. The results indicate that the natural periods of the natural modes, which are related to the pontoons and columns, are in the range of 1.6 to 3 seconds, which is beyond the range of the main wave energy. For the 5-MW NREL reference wind turbine, 1P is in the range of 5 to 8.7 seconds, while the 3P is in the range of 1.7 to 2.9 seconds. Due to the shape of the natural modes of the pontoons and columns, the 3P effect excited vibrations of the pontoons and columns are negligible.

Table 6. Natural periods ([s]) of the 6 degrees of freedom rigid-body motions of the 5-MW-CSC

Surge	Sway	Heave	Roll	Pitch	Yaw
79.5	79.5	25.8	31.28	31.32	58.12

4.3 RIGID-BODY MOTIONS

The wave induced transfer functions for rigid-body motions are calculated by WADAM [17]. The transfer functions are related to the wave direction and shape of the hull. Some representative transfer functions are presented in Appendix A. We focus on the transfer functions in the range of 0.314 rad/s to 2 rad/s. The peaks and troughs in the frequency range indicate that the radiation effect and wave diffraction effect are important. Viscous loads on the hull and restoring stiffness of the catenary mooring lines have very limited effects on the transfer functions in the wave frequency range and are not accounted for.

The 5-MW-CSC exhibits relatively small motions under different combined wind and wave conditions, even in extreme wind and wave conditions. This is because that 1) the pontoons of the 5-MW-CSC provide relatively large viscous damping and potential damping, 2) water plane area is relatively small, 3) the

draft of the 5-MW-CSC is relatively deep, and 4) the natural periods are well designed to be away from the wave frequency range.

Time-domain simulations based on the five environmental conditions (from EC1 to EC5) described in the Table 5 are carried out to check the rigid-body motions of the 5-MW-CSC in extreme combined wind and wave conditions. The numerical model employed by these time-domain simulations is identical to the TDM2 [16] except that mean drift forces and slow varying drift forces on the hull are included through the Newman's approximation. In the time-domain simulations, the direction of the incident winds is constantly specified as 0 degrees, while, 19 different wave directions are specified (from 0 to 180 degrees with 10 degrees interval).

Statistical properties of the rigid-body motions, i.e. mean, standard deviation, maximum and minimum, are calculated based on time series in stationary process. To account for statistical uncertainty, in this section, we only discuss the averaged statistical properties. For a given environmental condition with a given wave direction, the averaged statistical properties are calculated based on ten 1-h time-domain simulations with different random seeds. The averaged statistical results are given in Appendix B. The main observations are illustrated as follows.

The 5-MW-CSC has very limited heave motions in most of the operational conditions, where H_s could be less than 4 m. For example, in the EC1, where H_s is 7.5 m and T_p is 14.7 seconds, maximum 1-h heave motion is less than 2.4 m and the standard deviation is 0.7 m. The most critical heave motion is given by the EC5, in which the 1-h heave motion is in range of -5 m to 5.5 m and standard deviation is 1.5 m. The heave motion is independent to directions of winds and waves.

The 1-h pitch motion is in range of -3 degrees to 10 degrees. When the rotor is in operation, the pitch motion is dominated by wind loads. When the rotor is parked, wave loads dominate the pitch motion. The 1-h pitch motion standard deviation is in range of 0.3 degrees to 1.8 degrees. Compared to the statistical properties of the WindFloat given by [18], the 5-MW-CSC has more moderate pitch motions in combined winds and waves. The 1-h roll motion is in range of -4 degrees to 3.2 degrees. The roll motion is dominated by wave loads except that, when the rotor is in operation, the aerodynamic torque on the rotor results in a mean roll motion.

Regarding horizontal motions, 1-h surge, sway and yaw motions are in range of -7 m to 11 m, -5 m to 9 m and -2.25 degrees to 2.5 degrees respectively. Surge and sway motions are referred to the center of the water plane area rather than the center of gravity of the 5-MW-CSC. The moderate horizontal motions could be good for power cable design.

No instable motions, which are induced by the misalignment of the winds and waves, are observed.

4.4 SIMPLIFIED ULS DESIGN CHECK BASED ON A LIMITED NUMBER OF DESIGN CONDITIONS

The pontoons of the 5-MW-CSC are composed of stiffened plates, girders and bulkheads. We focus on buckling strength design check for the stiffened plates of the pontoons.

A stiffened plate is shown in Figure 7. We assume that the stiffened plate is located at bottom of the Pontoon 1 and is nearby a specified cross-section of the Pontoon 1. The specified cross-section is shown by the red dashed line in Figure 2. In addition, the stiffened plate is assumed to be located in between of two transverse girders and the side surfaces of the pontoon. Therefore, the width of the stiffened plate (l_2) is equal to the width of the Pontoon 1 which is 9 m. We assume that the distance between the girders is 3m. Consequently, the length of the plate (l_1) is 3 m.

We assume that the thickness of the plate is 0.016 m, the span (s) for the T stiffeners on the plate is 0.5 m, the web height and flange length of the T stiffeners is 0.5 m and 0.2 m. The web thickness and flange thickness is 0.008 m and 0.016 m. Consequently, the steel weight of the stiffened plate is equal to the steel weight of a plate with the same length and width and 0.0315 m thickness, which is very close to the equivalent thickness of the hull. However, the steel weight of the girders is not included yet. To estimate the steel weight of the girders, at least, a preliminary design for structural details of the pontoons need to be developed in future. The estimated steel weight of the hull can be maintained since the global and local load effects on the upper part of the columns are less critical than the global and local load effects on the lower part of the columns, pontoons and joints. Adjustments to the thickness have a negligible effect on the stability, rigid-body motions and global forces and moments in the hull because the displacement is considerably larger than the steel weight.

The stiffened plate is subjected to σ_{hp}, σ_1, σ_2 and τ_{12}. σ_{hp} represents hydro-pressure on the plate. The hydro-pressure includes hydrostatic pressure and hydrodynamic pressure on the outer surface of the plate and the ballast water induced pressure on the inner surface of the plate. σ_1 represents nominal uniform stress in stiffener direction. σ_2 represents nominal uniform stress in perpendicular to stiffener direction. τ_{12} represents shear stress. σ_1 and τ_{12} can be derived from the global forces and moments in the specified cross-section of the Pontoon 1.

Global time-domain analysis is carried out to calculate the global forces and moments in the combined wind and wave conditions described in Table 5. In the global analysis, the TDM3, which is described in [16], is utilized to calculate the global forces and moments in the specified cross-section.

The cross-section discretizes the hull into two parts. In the TDM3, the hull is modelled as two rigid-bodies connected by three artificial beam elements, while the RNA, tower and mooring lines are modelled as beam elements. A novel method [16] is implemented to accurately account for the inertial and external loads on the hull. Luan et al [16] show that the TDM3 can accurately calculate the global forces and moments in the

hull on the conditions that 1) the hull is a determinate structure, 2) the hull is very stiff, and 3) second and higher order hydrodynamic loads on the hull are not considered.

We assume that global behavior of the pontoons of the hull can be accounted for by Euler-Bernoulli beam theory. The cross-section can be simplified as a thin-wall box-shape cross-section shown in Figure 8. Eight points are specified on the cross-section. F_x, F_y, F_z, M_x, M_y, and M_z denote the global forces and moments in the cross-section in the x_{inp}-y_{inp}-z_{inp}coordinate system. The x_{inp}-y_{inp}-z_{inp}coordinate system is a body-fixed coordinate system. The x_{inp}-y_{inp}-z_{inp} coordinate system is coincident to the body-fixed coordinate system of the 5-MW-CSC (x^b-y^b-z^b) except that the origin of the x_{inp}-y_{inp}-z_{inp} coordinate system is located at (31.5, 0, -27) in the x^b-y^b-z^b coordinate system.

For a given point on the cross-section, normal stress (σ_x) and shear stress (τ) are calculated by Eqs.(1,2).

$$\sigma_x = \frac{F_x}{A} + \frac{M_y}{w_{y_{inp}}} + \frac{M_z}{w_{z_{inp}}} \quad (1)$$

$$\tau = \frac{M_x}{2A_0 t_c} + \frac{F_y S_{z_{inp}}}{I_{z_{inp}} t_c} + \frac{F_z S_{y_{inp}}}{I_{y_{inp}} t_c} \quad (2)$$

A is area of the cross-section. $w_{y_{inp}}$ and $w_{z_{inp}}$ are the section moduli corresponding to the y_{inp} and z_{inp} axes and the position of the point on the cross-section. A_0 is the circumscribed area of the cross-section. $S_{y_{inp}}$ and $S_{z_{inp}}$ are static moments corresponding to the y_{inp} and z_{inp} axes and the position of the point on the cross-section. $I_{y_{inp}}$ and $I_{z_{inp}}$ are the second moments of area of the cross-section.

To calculate A, $w_{y_{inp}}$ and $w_{z_{inp}}$, the thickness of the thin-wall of the box-shape cross-section is specified as 0.03 m, which is slightly smaller than the equivalent thickness estimated based on the steel weight of the stiffened plate (0.0315 m) and on the safe side.

In the global analysis, torsional stiffness and shear stiffness of the cross-section are mainly provided by the plates of the pontoon. Contribution of the T stiffeners on the plates to the torsional stiffness and shear stiffness is negligible. Therefore, to calculate the $S_{z_{inp}}$, $S_{y_{inp}}$, A_0, $I_{z_{inp}}$ and $I_{y_{inp}}$ in Eq.(8), the thickness of the thin-wall of the box-shape cross-section is specified as 0.016 m which is equal to the thickness of the plates of the pontoon. Consequently, t_c, in Eq.(8), is 0.016 m.

For each design condition, 10 1-h time-domain simulations are conducted to account for statistical uncertainty. For each 1-h time-domain simulation, simulation length is 4,600 seconds. The first 1,000 seconds is considered as transient process and is excluded in post-analysis. We find that averaged ranges of the normal stress (σ_x) and shear stress (τ) of the eight points on the cross-section in the 21 design conditions are -83 MPa to 38 MPa and -21 MPa to 28 MPa respectively.

Buckling utilization factors for the stiffened plate in all the combinations of the design loads, i.e. σ_{hp}, σ_1, σ_2 and τ_{12}, are calculated by using the S3 element code of PULS [19]. PULS is a computerized buckling code for thin-walled plate construction and accepted by DNV-RP-C201 [20] for checking buckling strength of plated structures. The code implements the Marguerre's non-linear plate theory in combination with stress control criteria. The boundary conditions for the edges of the stiffened plate are described in [19].To be conservative, we specify the hydro-pressure on the stiffened plate (σ_{hp}) as 0.5 MPa although the operating draft is 30 m. The ranges of the nominal uniform stress in stiffener direction (σ_1) and shear stress (τ_{12}) are obtained by applying a 1.3 load factor on the averaged ranges of the normal stress (σ_x) and shear stress (τ) respectively. Consequently, we specify that the σ_1 varies in the range of -110 MPa to 50 MPa with 10-MPa intervals, while τ_{12} varies in the range of -30 MPa to 40 MPa with 10-MPa intervals. The combinations of the σ_1 and τ_{12} are on the safe side since the critical value of σ_1 and critical value of τ_{12} may not necessary appear at the same time and/or at the same position on the cross-section. We assume that the nominal uniform stress in perpendicular to stiffener direction (σ_2) is induced by hydrostatic pressure forces on the side surfaces of the pontoon. We specify σ_2 as -60 MPa.

The maximum buckling utilization factor is 0.62 and indicates that the stiffened plate has sufficient buckling strength. The buckling utilization factors are very sensitive to the length of the stiffened plate (l_1). The maximum buckling utilization factor will be increased from 0.62 to 1.14 if the l_1 is increased from 3 m to 4 m.

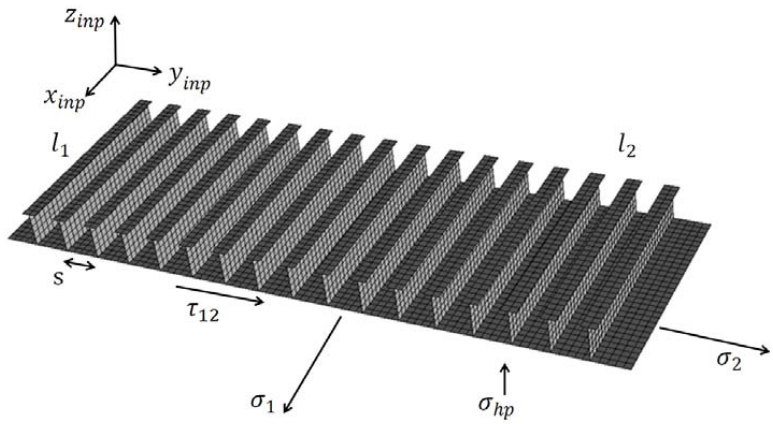

Figure 7 stiffened plate of the bottom of the Pontoon 1 of the 5-MW-CSC

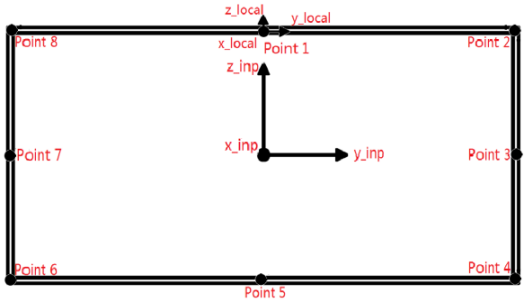

Figure 8 A simplified thin-wall box-shape cross-section (for global analysis)

5 CONCLUSIONS

Design of a braceless steel semi-submersible wind turbine has been introduced in present paper. The hull of the design is composed of a central column, three side columns and three pontoons and designed to support a 5-MW NREL reference wind turbine in offshore sites with harsh environmental conditions, e.g. the northern North Sea. Dimensions of the columns and pontoons, distributions of ballast water and steel and design parameters of the mooring system have been tabulated.

The design has very good intact stability. The intact stability of the design has been checked based on the righting and overturning moment curves. In the most critical situation, the ratio of the area under the corresponding righting moment curve from 0 degrees to the second intersection to the corresponding area under the design overturning moment curve is 1.63, which satisfies the intact stability criterion.

Natural periods and modes of the design have been well designed to avoid resonant rigid-body motions and structural vibrations excited by the 1P effect and first order wave loads. Due to the shape of the natural modes of the pontoons and columns, the 3P effect excited vibrations of the pontoons and columns are negligible.

The design exhibits relatively small motions under different combined wind and wave conditions. In extreme wind and wave conditions, 1-h surge, heave, pitch and yaw motions are in range of -7 m to 11 m, -5 m to 5.5 m, -3 degrees to 10 degrees and -2.25 degrees to 2.5 degrees respectively. No instable motions, which are induced by the misalignment of the winds and waves, are observed.

PULS has been used to check ultimate strength of a stiffened plate at the bottom of the Pontoon 1. We assume that the stiffened plate is nearby a specified cross-section of the Pontoon 1. Specifications for the sizes and thickness of the plate and spans and dimensions of the T stiffeners have been given. The steel weight of the stiffened plate is close to the corresponding estimated steel weight.

PULS accounts for local and global load effects on the ultimate strength of the stiffened plate. Buckling utilization factors for the stiffened plate in all the combinations of the design loads, i.e. σ_{hp}, σ_1, σ_2 and τ_{12}, have been calculated by using the S3 element code of PULS.

The nominal uniform stress in stiffener direction (σ_1) and shear stress (τ_{12}) have been derived from the global forces and moments in the specified cross-section of the Pontoon 1. Global time-domain analysis has been carried out to calculate the global forces and moments in 21 selected combined wind and wave design conditions.

The maximum buckling utilization factor is 0.62 and indicates that the stiffened plate has sufficient buckling strength. The buckling utilization factors are very sensitive to the distance of the girders of the pontoon.

ACKNOWLEDGMENTS

The authors acknowledge the financial support provided by the Research Council of Norway granted through the Centre for Ships and Ocean Structures; the Norwegian Research Centre for Offshore Wind Technology (NOWITECH), NTNU; and the Centre for Autonomous Marine Operations and Systems (AMOS), NTNU. Partial financial support from the EU FP-7 project MARINA Platform project (Grant Agreement 241402) is also acknowledged.

REFERENCES

[1] Twidell, J. and Gaudiosi, G., (2009), "*Offshore Wind Power*", Multi-Science Publishing Co.Ltd.

[2] Roddier, D., Cermelli, C., Aubault, A., and Weinstein, A., (2010), "WindFloat: A floating foundation for offshore wind turbines", Journal of Renewable and Sustainable Energy 2, 033104, doi:10.1063/1.3435339.

[3] Roddier, D., Peiffer, A., Aubault, A., and Weinstein, J., (2011), "A generic 5 MW WindFloat for numerical tool validation & comparison against a generic spar", In 30th International Conference on Ocean, Offshore and Arctic Engineering, no, OMAE2011-50278, Rotterdam, the Netherlands.

[4] Robertson, A., Jonkman, J., Masciola, M., Song, H., Goupee, A., Coulling, A., and Luan C., (2012), "Definition of the Semisubmersible Floating System for Phase II of OC4", Offshore Code Comparison Collaboration Continuation (OC4) for IEA Task 30.

[5] Huijs, F., Mikx, J., Savenije, F., and Ridder, E., (2013), "Integrated design of floater, mooring and control system for a semisubmersible floating wind turbine", European Wind Energy Association (EWEA) Offshore, Frankfurt.

[6] Viselli, A. M., Goupee, A. J., and Dagher, H., (2014), "Model Test of a 1:8 Scale Floating Wind Turbine Offshore in the Gulf of Maine", In 33th International Conference on Ocean, Offshore and Arctic Engineering, no, OMAE2014-23639, San Francisco, CA, USA.

[7] Dr.techn.Olav Olsen AS, (2015), http://www.olavolsen.no/en/node/17, accessed 8.April.2015.

[8] Jonkman J., Butterfield, S., Musial, W. and Scott, G., (2009), "Definition of a 5-MW Reference Wind Turbine for Offshore System Development", NREL/TP-500-38060, National Renewable Energy Laboratory, Golden, CO, U.S.A.

[9] Li, L., Gao, Z., Moan, T., (2015), "Joint Distribution of Environmental Condition at Five European Offshore Sites for Design of Combined Wind and Wave Energy Devices", Journal of Offshore Mechanics and Arctic Engineering. 137(3), 031901 (16 pages). doi: 10.1115/1.4029842.

[10] Jonkman J., (2010), "Definition of the Floating System for Phase IV of OC3", NREL/TP-500-47535, National Renewable Energy Laboratory, Golden, CO, USA

[11] IEC, (2005), "Wind turbines – Part 1: Design requirements", IEC-61400-1, International Electrotechnical Commission.

[12] MARINTEK, (2013). RIFLEX User's Manual.

[13] DNV, (2010), "Recommended Practice - Enivronmental Conditions and Environmental Loads", DNV-RP-C205, Det Norske Veritas.

[14] Moriarty, P. J., and Hansen, A. C., (2005), AeroDyn theory manual, Tech. Rep, NREL/TP-500-36881.

[15] DNV, (2013), "Offshore standard – Design of Floating Wind turbine Structures", DNV-OS-J103, Det Norske Veritas.

[16] Luan, C., Gao, Z. and Moan, T., (2016), "A novel time-domain method for determining global forces and moments in structural members of floating wind turbines", Plan to be submitted to Marine structures.

[17] DNV, (2013), SESAM User Manual HydroD.

[18] Gao, Z., Luan, C., Moan, T., Skaare, B., Solberg, T. and Lygren, J.E., (2011), "Comparative Study of Wind- and Wave-Induced Dynamic Responses of Three Floating Wind Turbines Supported by Spar, Semi-Submersible and Tension-Leg Floaters". Proceedings of the 2011 International Conference on Wind Energy and Ocean Energy (ICOWEOE'11). 31 October- 2 November 2011 - Beijing, China.

[19] DNV, (2009), "Nauticus Hull User Manual PULS", Det Norske Veritas.

[20] DNV, (2010), "Recommended Practice – Buckling strength of plated structures", DNV-RP-C201, Det Norske Veritas

APPENDIX A

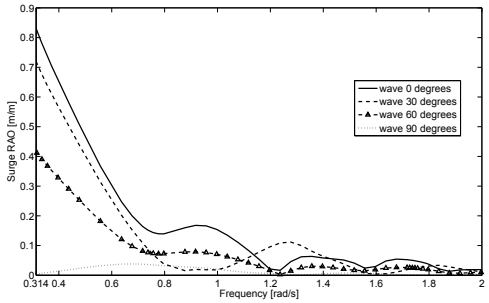

Figure 1. Surge RAO of the 5-MW-CSC

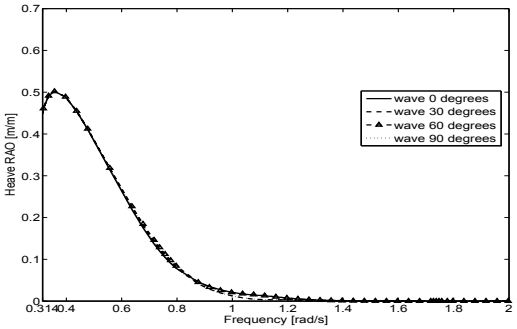

Figure 2. Heave RAO of the 5-MW-CSC

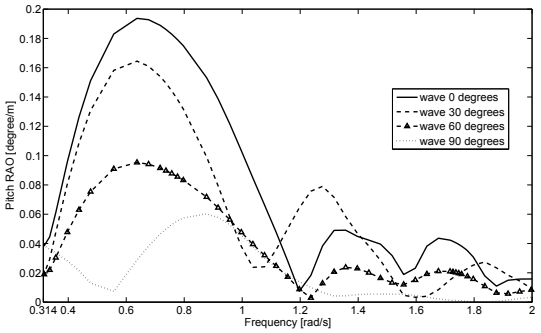

Figure 3. Pitch RAO of the 5-MW-CSC

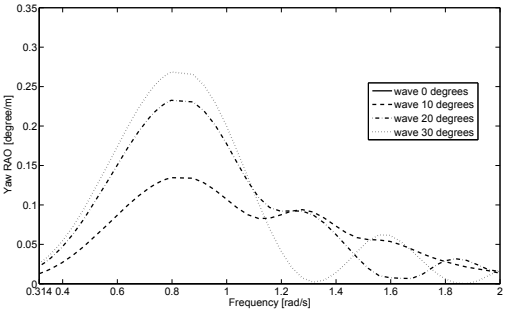

Figure 4. Yaw RAO of the 5-MW-CSC

APPENDIX B

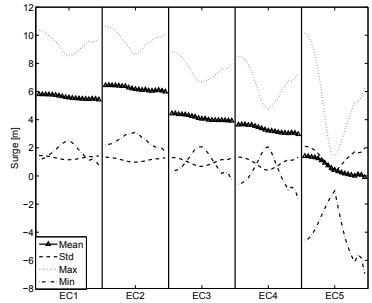

Figure 1. Statistical properties for surge motion of the 5-MW-CSC in extreme combined winds and waves, for each condition, wave direction varies from 0 to 180 degrees with 10 degrees interval

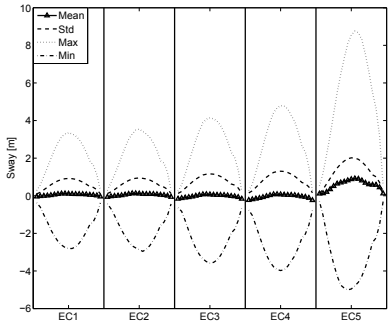

Figure 2. Statistical properties for sway motion of the 5-MW-CSC in extreme combined winds and waves, for each condition, wave direction varies from 0 to 180 degrees with 10 degrees interval

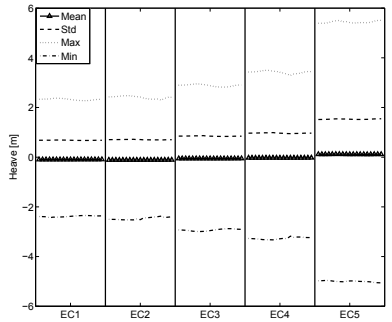

Figure 3. Statistical properties for heave motion of the 5-MW-CSC in extreme combined winds and waves, for each condition, wave direction varies from 0 to 180 degrees with 10 degrees interval

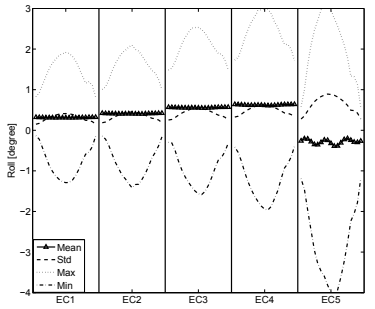

Figure 4. Statistical properties for roll motion of the 5-MW-CSC in extreme combined winds and waves, for each condition, wave direction varies from 0 to 180 degrees with 10 degrees interval

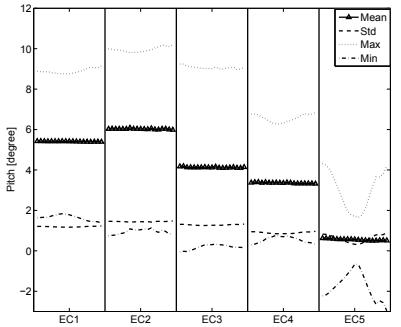

Figure 5. Statistical properties for pitch motion of the 5-MW-CSC in extreme combined winds and waves, for each condition, wave direction varies from 0 to 180 degrees with 10 degrees interval

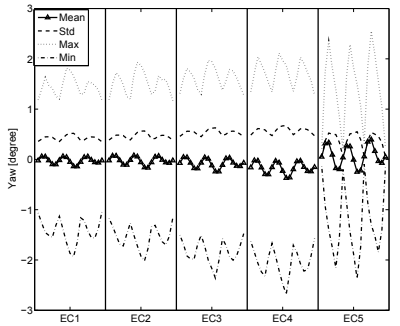

Figure 6. Statistical properties for yaw motion of the 5-MW-CSC in extreme combined winds and waves, for each condition, wave direction varies from 0 to 180 degrees with 10 degrees interval

Appendix B

Appended paper

B.1 Paper B1

Paper B1:
Simplified method for conceptual design
Chenyu Luan, Zhen Gao and Torgeir Moan

Criteria, procedure and simplification for conceptual design of MW level horizontal axis semi-submersible wind turbine hulls with respect to safety

Chenyu Luan*
Email: chenyu.luan@ntnu.no
PhD Candidate
Norwegian Research Centre for Offshore Wind Technology (NOWITECH)
Centre for Ships and Ocean Structures (CeSOS), NTNU
Centre for Autonomous Marine Operations and Systems (AMOS), NTNU
NO-7491 Trondheim, Norway

Zhen Gao
Email: zhen.gao@ntnu.no
PhD, Professor
CeSOS and AMOS, NTNU
Department of Marine Technology, NTNU
NO-7491 Trondheim, Norway

Torgeir Moan
Email: torgeir.moan@ntnu.no
PhD, Professor
CeSOS and AMOS, NTNU
NOWITECH
Department of Marine Technology, NTNU
NO-7491 Trondheim, Norway

Abstract:

This paper deals with the design criteria, procedure and simplifications for developing conceptual design of semi-submersible wind turbine hulls based on the authors' experience with respect to design and analysis of semi-submersible wind turbines in the past six years. The wind turbine systems must be designed for serviceability and safety. This paper focuses on limit state design with respect to the safety. The safety factors used in the partial safety factor format should be calibrated by reliability methods. While, there is a trade-off between the minimum required safety level and construction, installation and maintenance costs. Cost efficient design with acceptable reliability is preferred. It is suggested that floating wind turbines be considered strongly coupled systems. The importance of the interactions of the subsystems of floating wind turbines, i.e., the rotor-nacelle-assembly, control system, tower, hull and mooring system, is discussed. Criteria with respect to stability, natural periods and modes and structural strength are highlighted. The design space for the overall dimensions of the semi-submersible hull can be developed based on simplified stability criterion, natural period requirements and simplified steel mass estimation methods. Simplifications for ULS and FLS design checks are discussed based on a review of relevant publications.

1 Introduction

Offshore wind energy has become a significant area of development. Offshore wind power has several advantages over onshore wind power [1]. First, offshore wind sites generally produce stronger winds with less turbulence on average because the sea surface is considerably smoother than the land surface. Second, the effects of noise and visual pollution from these sites on humans are negligible because of their distance from populated areas. Third, in most countries, the sea is owned by the government rather than private landlords, which allows for the development of large offshore wind farms. Finally, good sea transport capabilities allow for the construction of large wind turbines with high rated power (e.g., 5-10 MW).

In relatively deep water, e.g. deeper than 80 meters, floating platforms might be more economically competitive than bottom fixed structures. Compared with spar-type and TLP wind turbines, the advantages of semi-submersible wind turbines include, but are not limited to, 1) greater flexibility in terms of varying sea bed conditions and drafts and 2) significantly reduced installation costs due to their simpler installation, with full assembly at dock[2]. Most of the proposed semi-submersible wind turbine concepts feature either three columns with a wind turbine on one side column or four columns with a wind turbine on the central column. The columns are connected by braces (as in WindFloat [2,3] and OC4-Semi[4]) or pontoons (as in the 5-MW GustoMSC Tri-Floater [5], VolturnUS [6], Dr.techn.Olav Olsen's concept[7] and 5-MW-CSC concept [42]).

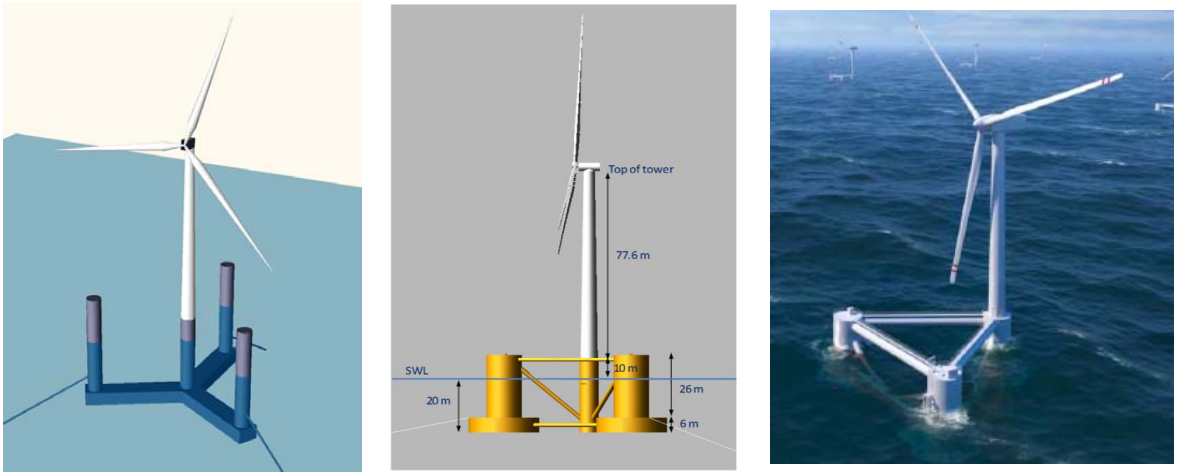

Figure 1 Configuration of 5-MW-CSC (left), OC4-Semi (middle) and WindFloat (right)

Successful experience accumulated by the offshore oil and gas industry and wind power industry over the past decades are combined and used for design of floating wind turbines. However, to develop a cost efficient design with an acceptable reliability to ensure attractive profit for developing offshore energy in deep water, in depth understanding with respect to special features of floating wind turbines needs to be accumulated by systematically carrying out numerical and experimental analyses with respect to load effect on reference floating wind turbines. Consequently, developments of designs of reference floating wind turbines, and numerical and experimental approaches for modelling and simulation are needed before pilot and/or commercial floating wind turbines are constructed and operated in real.

Innovative floating wind turbine concepts are promoted as breakthrough comes from innovation. However, to be practical, the concepts must be designed for serviceability and safety, while, reasonable and practical simplifications and assumptions are needed to control work load for design. Design is an iterative process.

This paper deals with the design criteria, procedure and simplifications for developing conceptual design of semi-submersible wind turbine hulls based on the authors' experience with respect to design and analysis of semi-submersible wind turbines in the past six years and focuses on limit state design with respect to the safety.

2 Conceptual design criteria for the hull of semi-submersible wind turbines

2.1 General

Floating wind turbine systems consist of a rotor-nacelle-assembly (RNA), control system, tower, hull and mooring system. The basis of the design of such systems is the experience accumulated by the O&G and offshore wind industries. The IEC 61400-1 design standard [9] specifies the design requirement for land-based wind turbines. The IEC 61400-3 design standard [10] supplements the IEC 61400-1 design standard with design requirements for bottom-fixed offshore wind turbines. The guidelines and standards from GL and DNV are also extensively used [11,12]. For the design of floating wind turbine structures, DNV-OS-J103 [13] is one of the very few references to date. Wind turbine systems are generally designed for serviceability and safety. The main serviceability criterion relates to stable power production, while the safety criteria relate to a leveled failed probability for all hazards throughout the planned lifetime. Due to a lack of commercial offshore wind farms using floating wind turbines, reliability methods based on results of numerical simulations and analysis could be employed to estimate the safety levels for floating wind turbines. Alternatively, to achieve a specified safety level that is quantitatively represented by the probability of failure (P_f), characteristic load effect (S_c) and characteristic resistance (R_c) in limited states are required to be calculated and satisfy partial safety factor format as shown in general by Eq. (1). γ_R and γ_S are partial safety factors for the characteristic resistance and load effect, respectively, corresponding to the limited states. P_f is related to γ_R, γ_S and the methods used to calculate R_c and S_c.

$$R_c/\gamma_R > S_c \times \gamma_S \qquad (1)$$

The safety criteria require that floating wind turbines should have sufficient stability, well designed natural periods and modes (for rigid-body motions and structural vibrations) and reasonable structural design, while, floating wind turbines should be considered strongly coupled systems. In addition, trade-off between the safety levels and cost of developing floating wind turbines should be considered and addressed.

In general, the cost of floating wind turbines increases significantly when higher safety levels are incorporated. Reducing the costs of the produced power to a competitive level is an important challenge for the offshore wind energy development. Unlike offshore O&G platforms, floating wind turbines are unmanned during operation, limiting the consequences of failures to economic losses rather than loss of human life and/or environmental damage. The safety criteria should therefore be based on balanced total costs. For example, a redundant mooring system, which limits failure, is used in offshore O&G platforms but not necessarily in wind turbines. Another example is related to the damaged stability design criterion, which is applied for manned units. The damage stability criterion implies that the hull should be compartmented to prevent capsizing induced by such damage as ship collisions. Consequently, the cost of the hull will be increased significantly. To date, there is no consensus regarding the trade-off between safety and costs for floating wind turbines.

To reduce complexity and cost, some requirements and considerations with respect to fabrication and offshore transportation, installation, maintenance and decommission are discussed in [2] and are considered to be applicable to a generic semi-submersible wind turbine. The safety level could be significantly increased if leak, cracks and other critical hazards could be detected and fixed by humans or robots in their early phase. Therefore, appropriate inspection and monitoring methods and access should be thoroughly considered. In general, joints, e.g. in between of a column and a pontoon or a brace, are critical components. Variable ballast and draft may be essential for inspecting and maintaining the joint in a dry environment. Alternatively, semi-submersible wind turbines could be towed back to dry dock. However, the dry dock solution may neither be economic nor efficient for large commercial offshore wind farms, where hundreds of semi-submersible wind turbines may need to be maintained and inspected annually.

2.2 Discussions on coupled system behaviours of floating wind turbines

Hull design for floating wind turbines should not be performed in isolation; rather, the interactions of the subsystems, i.e., the RNA, control system, tower, hull and mooring system, should be appropriately considered. The consistency of standards for the different subsystems needs to be harmonized, e.g., the treatment of fault conditions is currently not well-defined and the

drivetrain standards are also problematic.

Bachynski et al [14] conducted a dynamic analysis of floating wind turbines during pitch actuator fault, grid loss and shutdown. The impulse load induced by shutdown could be critical to the design of the rotor and nacelle but has a very limited or negligible effect on the tower and hull. The pitch decay induced by the shutdown could result in an extreme load effect and considerable fatigue damage for floating wind turbines with relatively low roll/pitch restoring stiffness. In addition, the shutdown results in rotor torque variations, while the pitch actuator fault results in imbalanced aerodynamic loads on the RNA. As a result, large yaw motion could be excited for floating wind turbines with relatively small yaw moments of inertia, e.g., spar-type wind turbines. Pitch actuator fault, grid loss and shutdown effects on a spar-type wind turbine are discussed further in [15-18].

Butterfield et al [19] note that coupling of the turbine and platform is an engineering challenge for floating wind turbines. Xing et al [20,21] investigated the effect of the nacelle motions of a spar-type floating wind turbine on drivetrain dynamics by comparing the main shaft loading and internal drivetrain responses between the floating wind turbine and its equivalent land-based wind turbine. For spar-type floating wind turbines, the main shaft loading and internal drivetrain responses increased. Nejad et al [22] studied the performance of a 5 MW drivetrain mounted on a spar-type platform, a TLP, two semi-submersible platforms and a land-based wind turbine. Due to the large wave-induced axial force on the main shaft of the drivetrain, the fatigue damage of the main bearing of spar-type wind turbines could exceed that of land-based wind turbines under high wind speeds. Meanwhile, the gearbox damage is nearly equal for TLP and land-based wind turbines. Whether criteria related to nacelle accelerations should be applied in the design of floating wind turbines is still under discussion.

For horizontal-axis wind turbines with pitch actuators, appropriately designed controllers [23-28] could be used to diminish the negative aerodynamic damping effect [23]. Sandner et al [29] recently presented a design procedure that integrates the optimization of the PI-controller parameters into the design space of the overall hull dimensions for a spar-type floating wind turbine. Linearized numerical models that can appropriately account for the strong non-linear effect induced by the aero-hydro-servo-elastic feature of floating wind turbines are required by the proposed procedure. The work of Gao et al [30] indicates that semi-submersible wind turbines could be less sensitive to the negative aerodynamic damping effect.

2.3 Criteria for intact stability

The intact and damaged stability could be checked based on the curves of the righting and design overturning moments.

Overturning moments come from aerodynamic loads on the RNA, tower and hull and make the semi-submersible wind turbine rotate with respect to a heeling axis in the water plane area. Righting moment is generated by hydrostatic pressure forces on wetted body surface of the hull and gravity of the semi-submersible wind turbine. To find the most critical situation, overturning moments and righting moments corresponding to several different heeling axes need to be calculated and checked. The righting moment curves corresponding to different rotational axes (represented by ϕ) and design overturning moment curve of the 5-MW-CSC are given in Figure 2 as an example [42]. Standards, such as the DNV-OS-J103, require that the ratio of the area under the righting moment curve from 0 degrees heeling angle to the second intersection to the corresponding area under the design overturning moment curve should be more than a specified value, e.g. 1.3.

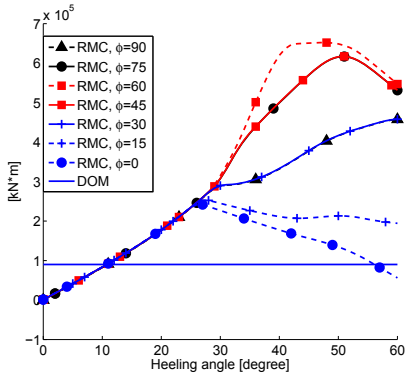

Figure 2 Righting moment curve (RMC) v.s. design overturning moment curve (DOM), intact stability analysis, ϕ represents different heeling axis.

2.4 Criteria for natural periods and modes

Resonant responses excited by dynamic excitation can result in large sectional forces and moments, and expensive structures (in order to have sufficient structural strength). Therefore, natural periods and modes should be well designed to, at least, avoid resonant responses induced by excitations with considerable energy, e.g., first-order wave load (3-25 seconds) and 1P and 3P effects [1].

In general, a given 1-hour turbulent wind may include a wide range of frequency component. Resonance excited by wind loads cannot be avoid by tuning the natural periods, however, the resonance can be limited by aerodynamic and hydrodynamic damping which may be quite considerable [50, 51]. In addition, vibration modes and frequencies should also be considered. Vibration (flexible) modes may be excited due to: 1) the motivation of cost reduction may result in a flexible hull; 2) high-frequency rotor loads, e.g., the 3P effect; and 3) the modes and frequencies are affected by the strong coupling effect between the hull and other components of floating wind turbines. If structural vibrations are excited by first-order wave loads, the effect of hydroelasticity on the hull must be considered.

2.5 Structural design checks

Limit state design should be employed to check the structural strength subjected to global and local load effects. It is suggested that characteristic load effect (S_c) be calculated by time-domain models to appropriately address the aero-hydro-servo-elastic feature [49]. The partial safety factors (i.e., γ_R and γ_S) and characteristic resistance (R_c) could be selected based on the methods and formulas described in relevant standards, e.g., IEC61400-3 and DNV-OS-J103. For conceptual design, simplified methods for the estimation of S_c and R_c could be employed to reduce the workload. γ_R and γ_S must be calibrated by appropriate methods, such as reliability analysis, to ensure that the required safety level can be achieved when using the simplified methods.

3 Conceptual design procedure for the hull of semi-submersible wind turbines

Simplified methods that could be used for the conceptual design of semi-submersible wind turbine hulls are discussed in this section. We assume that the design configuration of the RNA, tower and controller has been selected. The overall dimensions and mass distribution of the semi-submersible hull should be specified. Note that design is an iterative process.

Semi-submersible wind turbine hulls may include several columns, pontoons and braces. The wind turbine could be located at center of water plane area of the hull supporting by a central column as shown in, e.g., OC4 semi, or supporting by braces as shown in, e.g., HiPRwind [31]. Alternatively, the wind turbine could be located on a side column as shown in, e.g., WindFloat. The columns could be connected by braces and/or pontoons as shown in, e.g. OC4 semi and 5-MW-CSC. Heave plates could be mounted at bottom of the columns to introduce added mass and viscous damping, as shown in, e.g. WindFloat.

3.1 Simplified design approaches for developing initial designs of semi-submersible hulls

In the initial design stage, the dimensions of the columns, pontoons and braces could be selected based on the simplified stability criterion and a criterion with respect to natural periods of rigid-body motions, see Eq. (2, 3).

$$\frac{M}{K} \leq \theta_a \qquad (2)$$

$$T_i \geq 25\ s \quad (i = 1,2,3,4,5,6) \qquad (3)$$

Eq. (2) works as a simplified indicator for intact stability, and is developed on the base of the area-ratio-based intact stability design check criterion with the most critical righting moment curve and design overturning moment curve. As water plane area of semi-submersible wind turbines are formed by columns, for which diameter of each column along axial direction of the column is a constant value, the most critical righting moment curve can be approximately represented by a line until θ_1, e.g. see Figures 2 and 3. At θ_1, at least one column is fully merged in water. K denotes value of the slope of the line in between the origin and θ_1 and is known as the linearized heeling restoring stiffness about the most critical rotational axis with respect to zero degrees heeling angle. K is calculated by using Eq. (4).

$$K = \rho g I + \rho g V Z_B - m_{hull} g Z_{G,hull} - m_{RNA+tower} g Z_{G,RNA+tower} \qquad (4)$$

where ρ is density of sea water; g is gravity acceleration; I is second moment of water plane area; V is displaced volume of the hull; Z_B is vertical position of the center of buoyancy; m_{hull} is mass of the hull (including steel mass and ballast mass); $Z_{G,hull}$ is vertical position of the center of gravity of the hull (including steel mass and ballast mass); $m_{RNA+tower}$ is mass of the RNA and tower; $Z_{G,RNA+tower}$ is vertical position of the center of gravity of the RNA and tower. Note that Z_B, $Z_{G,hull}$ and $Z_{G,RNA+tower}$ are described in an earth-fixed coordinate system for which the origin of the coordinate system is located at geometrical center of the water plane area of the hull when the semi-submersible wind turbine is in calm water.

Overturning moments on the semi-submersible wind turbines decrease with the increase of heeling angle. Therefore, a simplification which make the values on the overturning moment curve be constantly equal to the value of the most critical overturning moment multiplying by a corresponding safety factor will lead to a conservative design. We denote the design overturning moment as M. Consequently, the static heeling angle (θ_0) under the design overturning moment (M) can be calculated by using Eq. (5) as long as $\theta_0 \leq \theta_1$

$$\theta_0 = \frac{M}{K} \qquad (5)$$

When the heeling angle exceeds θ_1, we assume that the righting moment will linear decrease with the increase of the heeling angle until θ_2. The assumption is supported by the shape of the most critical righting moment curve shown in Figure 2.

In practice, we suggest that θ_a which represents the upper limit of θ_0 can be specified as a criterion to control the intact stability, see Eq. (2). It could be very expensive to achieve a design of semi-submersible wind turbine with a very small value of θ_a while a large value of θ_a means large variations in configuration, and forces and moments in structural components of the design. Meanwhile, attention should also be paid on dynamic responses of the design. For the 5-MW-CSC, as an example, θ_a is specified as 8 degrees.

Note that effect of mooring system on intact stability is excluded as required by DNV-OS-J103. However, at least, the designs of the 5-MW-CSC and 5-MW GustoMSC Tri-Floater have shown that effect of catenary mooring system on roll/pitch restoring stiffness is considerable [42, 52].

θ_1 increases with increase of freeboard of the columns. Freeboard of a selected design, which satisfies the criterion with respect to the θ_a, can be adjusted to make the design to satisfy the intact stability criteria specified in section 2.3.

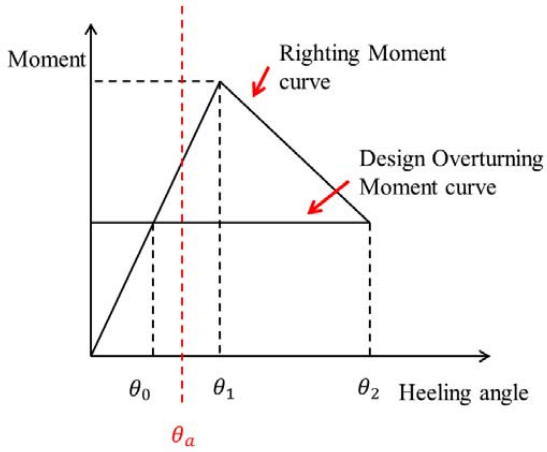

Figure 3 Righting moment curve and design overturning moment curve. At θ_1, at least one column is fully merged in water.

In Eq. (3), T_i $(i = 1,2,3,4,5,6)$ represent the natural periods of the rigid-body motions, i.e. surge, sway, heave, roll, pitch and yaw. As discussed in section 2.4, designers are suggested to develop designs with natural periods that are away from the frequency ranges, which include considerable energy, e.g., first-order wave load (3-25 seconds) and 1P and 3P effects.

For a semi-submersible concept with a catenary mooring system, the horizontal restoring stiffness is expected to be soft. Therefore, the surge, sway and yaw natural periods are far from the wave frequency range. In general, based on linear theory, the uncoupled and undamped heave natural period (T_3) is a good approximation for the actual heave natural period, as the heave motion is uncoupled from the other rigid-body motions, see Eq. (6).

$$T_3 = 2\pi\left(\frac{M_{33} + A_{33}}{C_{33}}\right)^{\frac{1}{2}} \qquad (6)$$

where, M_{33} is mass of displaced water; A_{33} is added mass in heave induced by heave motion of the hull at resonant frequency in calm water; C_{33} is linearized restoring stiffness corresponding to heave motion induced restoring force in heave direction. See Eq. (7).

$$C_{33} = \rho * g * A_w \qquad (7)$$

where, A_w is mean water plane area when the hull is in calm water.

In the initial design, the natural periods of roll (T_4) and pitch (T_5) could be estimated by the uncoupled and undamped expressions, which are similar to Eq. (6) but with updated mass, added mass and linear restoring stiffness terms. Due to the coupling effect between the rigid-body motions, T_4 and T_5 must be further checked by solving the eigenvalue problem of the equations of rigid-body motions in the frequency-domain. In addition, slenderness of the columns, pontoons and braces are related to vibration (flexible) modes and frequencies. The vibration modes and frequencies should be checked by applying analysis approaches such as Lanczos' method. More details are discussed in later part of this paper.

Estimations of the mass and its distribution are essential for estimating the intact stability, natural periods and modes and structural strength. For a steel semi-submersible wind turbine, the mass of the hull includes the steel mass and ballast mass. Based on experience accumulated by the O&G industry, the steel mass of a semi-submersible platform can be estimated empirically by Eq. (8).

$$M_{steel\_i} = C_{steel\_i} * \rho * V_i \qquad (8)$$

where, M_{steel_i} and V_{c_i} represent estimated steel mass and volume of the structural component i respectively. $C_{steel\_}i$ is an empirical coefficient.

Experiences of offshore oil semi-submersible platforms show that C_{steel}_i should be approximately equal to or greater than 0.2-0.25 which is dominated by design for resistance against fatigue damage and hydro pressure induced local load effects and compartmentalization against accidental flooding events. Possible benefit for implementing compartmentalization needs to be analyzed in future in view of risk assessment of the whole floating wind farm. More analyses with respect to design for resistance against global load effects are needed [40]. In addition, it should also be noted that, for some structural components of some semi-submersible wind turbines, there is a possibility that the local load effect can be moderated. For instance, the design of the 5-MW-CSC uses three pontoons to connect four columns as an integrated structure. The pontoons are designed to be full filled by water as ballast. The pressure of the water inside the pontoons could be increased to against the pressure of the sea water outside the pontoons to moderate the local load effect on stiffened plates of the pontoons.

Alternatively, equivalent plate thickness could be specified directly based on experience. The experience accumulated by the O&G industry show that the unit weights for semi-submersible components range from approximately 150 kg/m^2 (20 mm equivalent plate thickness) for the upper columns to 250 kg/m^2 or more for the pontoons and lower columns (depending on draft). Note that the suggested unit weights are functions of the geometry and local loading only. An increase, e.g., by 15–20%, could be essential to account for the global load effect as suggested by [53].

The distribution of the steel mass could initially be represented by an equivalent thickness of the hull, which equals the total estimated steel mass divided by the surface of the semi-submersible hull. In reality, the steel mass may vary in vertical levels due to the variation of hydrostatic pressure. Especially, thickness of plates and steel mass for girders of the pontoons and columns that are located in relatively deep water can be dominated by local hydrostatic pressure. For pontoons that are subjected to large global loads, more steel mass for longitudinal stiffeners are needed. At the joints between the columns and pontoons, more steel mass may be needed to introduce sufficient stiffness, transfer the internal loads smoothly and reduce hotspot stresses.

Ballast mass is used to achieve the design draft. The lower locations of the ballast mass are helpful for increasing the intact stability. Access for inspection, especially at the joints of the pontoons and columns, should be considered. Water and/or concrete could be used as the ballast mass.

Experience with semi-submersible wind turbines remains limited. An overly conservative design would introduce unnecessary cost. However, a reasonable structural design is needed to withstand global and local load effects. Consequently, structural assessment must be appropriately carried out. Structural vibration modes and frequencies may need to be checked. Global finite element models may need to be developed to analyze global responses, e.g. motions and sectional forces and moments, of the initial designs in design conditions. Local finite element models, which include structural details, may need to be developed to analyze the global and local load effects induced structural responses. To limit the computational costs and to save the computational time, necessary simplifications for 1) the design conditions used in, for example, ULS and FLS design checks, 2) the approaches for developing the relevant finite element models and 3) the methods for assessing structural resistance are needed.

3.2 Analysis and discussions on design space of semi-submersible wind turbine hulls

Discussions with respect to determination of the dimensions of the columns, pontoons and braces of the semi-submersible hulls based on the simplified design criteria as shown in Eq. (2, 3) are given in this section.

To satisfy Eq. (2), K must be a positive value and larger than $\frac{M}{\theta_a}$. We assume that the design configuration of the RNA, tower and controller has been selected. Consequently, the design overturning moment (M), $m_{RNA+tower}$ and $Z_{G,RNA+tower}$ are known while $-m_{RNA+tower}gZ_{G,RNA+tower}$ is a large negative value. Note that the vertical position of center of gravity discussed in this paper is described in an earth fixed coordinate system with origin located at geometrical center of water plane area.

We denote ρgI as K_1 and $\rho gVz_B - m_{hull}gz_{G,hull}$ as K_2. K_1 will always be a positive value, while K_2 could be a positive value or a negative value. As the origin of the earth-fixed coordinate system is on still water plane, z_B will always be a

negative value, while $z_{G,hull}$ could be a positive or a negative value. When $z_{G,hull}$ is a positive value, K_2 will be a negative value. This means that the second moment of water plane area must be large enough to ensure K_1 will be a sufficiently large positive value against K_2 and $-m_{RNA+tower}gZ_{G,RNA+tower}$. When $z_{G,hull}$ is a negative value, K_2 could be a positive value. Note that ρVg, $m_{hull}g$ and resultant of vertical components of pretensions at fairleads of the attached mooring lines are in equilibrium. This means that m_{hull} is less than ρV. Consequently, in order to achieve a positive value of K_2, $z_{G,hull}$ must be lower than z_B. Regarding to the design for which $z_{G,hull}$ is lower than z_B, we have that z_B is equal to $z_{G,hull}$ plus d_z. d_z, which takes a positive value, represents the distance from $z_{G,hull}$ to z_B. Consequently, K_2 increases with increase of d_z.

For semi-submersible concepts, d_z is expected to be small, e.g., d_z is 0.31 m for the OC4 semi-submersible wind turbine and is 1.93 m for the 5-MW-CSC. The reasons are: 1) seawater is used as the ballast mass (d_z could be increased by using blast mass with a higher value of density, e.g. concrete), and 2) the relatively small draft (e.g. no more than 30 meters) limits the value of d_z.

When d_z is relatively small, the roll/pitch restoring stiffness mainly originates from K_1. However, the appropriate design of z_B, d_z and V can further improve the stability and reduce the cost. We use $m_{v,mooring}g$ to represent the value of the resultant of vertical components of pretensions at fairleads of the attached mooring lines. Consequently, K_2 can be write as $K_2 = m_{hull}gd_z + (m_{RNA+tower} + m_{v,mooring})gz_B$. We can see that K_2 linearly increases with z_B with a slope of $m_{RNA+tower} + m_{v,mooring}$. To exclude effect of the mooring lines on intact stability analysis of semi-submersible wind turbines, as required by [13], the slope could be reduce to $m_{RNA+tower}$. This fact means that moving z_B toward the still water line is a potential mean of increasing the roll/pitch restoring stiffness for designs with relatively small d_z, while moving z_B toward the still water line may increase the hydrodynamic loads on the hull. If d_z is relatively large, it is more attractive to increase K_2 by increasing V, as. The OC3-Hywind spar [32] is an example of using large draft, d_z and V to achieve the roll/pitch restoring stiffness required by the stability criterion.

In general, for semi-submersible wind turbines, the restoring stiffness mainly comes from K_1 which is determined by diameter and arrangement of the side columns. Rotational axis of the overturning moment varies with variations of incident wind, wave and currents. Therefore, symmetrical arrangement with respect to the vertical axis through the geometrical center of water plane area, as shown in Figure 4 for example, is preferred to make the righting moment curves be approximately homogeneous with respect to the rotational axes unit the critical heel angle θ_1, see Figures 2 and 3.

A central column may be used to support the tower and RNA at the geometrical center. The side columns and central column are connected by pontoons and or braces as an integrated structure.

As shown in EE2, We denote diameter of the central column and side column as d_c and d_s, respectively, while the distance between the vertical axis through the geometrical center and central line of a side column is denoted as d_{cs}. We could expect that contribution of the central column on second moment of water plane area is negligible when compared to the contribution by the side columns while the second moment of water plane area increases with increase of number of the side columns. The 4-side-column semi-submersible wind turbine has larger second moment of water plane area than the 3-side-column semi-submersible wind turbine. However, the area of water plane area increases with increase of the number of the side columns. If the area of water plane area is increased, to satisfy the design criterion given in Eq. (3), the corresponding mass and added mass terms must be increased correspondingly. This means displaced volume of the columns, pontoons and braces need to be increased and/or heave plates are needed to result in increase of added mass terms of the hull. Consequently, cost of construction of the hull increases. We could approximately calculate second moment of water plane area of a semi-submersible which includes n ($n \geq 3$) side columns with respect to a given rotational axis in the water plane (denoted as I_n) by using Eq. (9). We denote the area of water plane area of the hull as A_n. Numerical results show that $\frac{I_n}{A_n}$, for n in range from 3 to 100, constantly equal $0.5d_{cs}^2$. Note that with increase of number of side columns, more steel is needed to integrate the side columns as an integrated structure. These facts suggests that a semi-submersible wind turbine which includes 3 side columns could be more cost efficient when compared to its counterpart for which more than 3 side columns are included.

Consequently, in this paper, we focus on the 3-side-column semi-submersible wind turbines, with and without a central column.

$$I_n = \sum_{i=1}^{n} \frac{\pi}{4} d_s^2 (d_{cs} \sin(\frac{2\pi}{n} i))^2, n \geq 3 \qquad (9)$$

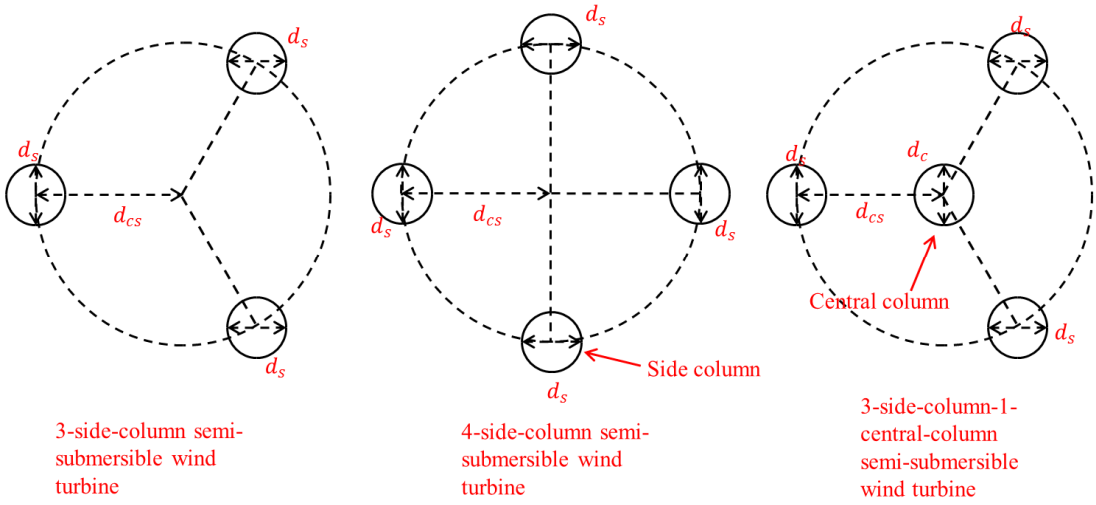

Figure 4 Water plane area of 3-side-clolumn semi-submersible wind turbines with and without a central column and a 4-side-column semi-submersible wind turbine

K_1 is approximately proportional to the square of d_s and the square of d_{cs}. The upper limits for d_s and d_{cs} should be noted. Increasing d_{cs} increases the displaced water and global load effect on the semi-submersible hull. As a result, the dimensions and thickness of the braces and pontoons used to connect the columns must be increased, which may increase the cost significantly. Increasing d_s increases the hydrodynamic load on the side columns and water plane area, and requires more mass and added mass in heave to maintain the same value of T_3. A_{33} is related to configuration of wetted body surface of the hull. For large-volume semi-submersible wind turbines without heave plates, we could initially assume that A_{33} is equal to M_{33}. Therefore, a significant increase in M_{33} is needed for semi-submersible wind turbines with relatively large d_s to increase its heave natural period. High values of M_{33} correspond to large hydrodynamic loads, large steel mass and high cost. Compared to d_s, d_c has a negligible contribution on roll/pitch restoring stiffness, but it could introduce a considerable area of the water plane area. Consequently, removing the central column is helpful for achieving a small value of the ratio of the displaced water to the rated power (R_{dp}), as in, e.g., WinFloat and HiPRWind. Large heave plates can introduce a large added mass and reduce the required M_{33}. However, the application of heave plates will significantly increase the system complexity and construction and maintenance costs. The experience of design of the 5-MW-CSC and OC4 semi indicate that, for semi-submersible wind turbines without heave plates, a relatively high roll/pitch restoring stiffness and the restriction of the heave natural period to beyond the wave range result in a large displaced volume and steel mass of the semi-submersible hull.

3.3 Discussions on natural periods and modes (rigid-body motions and structural vibrations)

The dimensions and mass of the semi-submersible hull for several initial designs could be selected based on the design space and criterion as mentioned in sections 3.1 and 3.2. Simplified expressions for the natural periods of 6 degrees of freedom rigid-body motions are used in sections 3.1 and 3.2. However, in principle, the natural periods and modes should be calculated by solving the eigenvalue problem. Lanczos' method [33] is widely used in commercial codes to solve the eigenvalue problem, which is related to the generalized mass and stiffness. The stiffness of the pontoons, columns, and braces could be represented by beam elements with simplified cross-sections. For example, Figure 5 shows a realistic cross-section of a pontoon with

structural details. The realistic cross-section is represented by a simplified box-shape cross-section. The mass could be represented by mass points attached to the beam elements. Similarly, the mass and stiffness of the RNA and tower could be represented by mass points and beam elements. Note that the natural frequencies for the natural modes of the generator and drivetrain are expected to be very high. Therefore, the nacelle could be simply modeled by a mass point attached to a beam element, which represents the global structural stiffness of the nacelle.

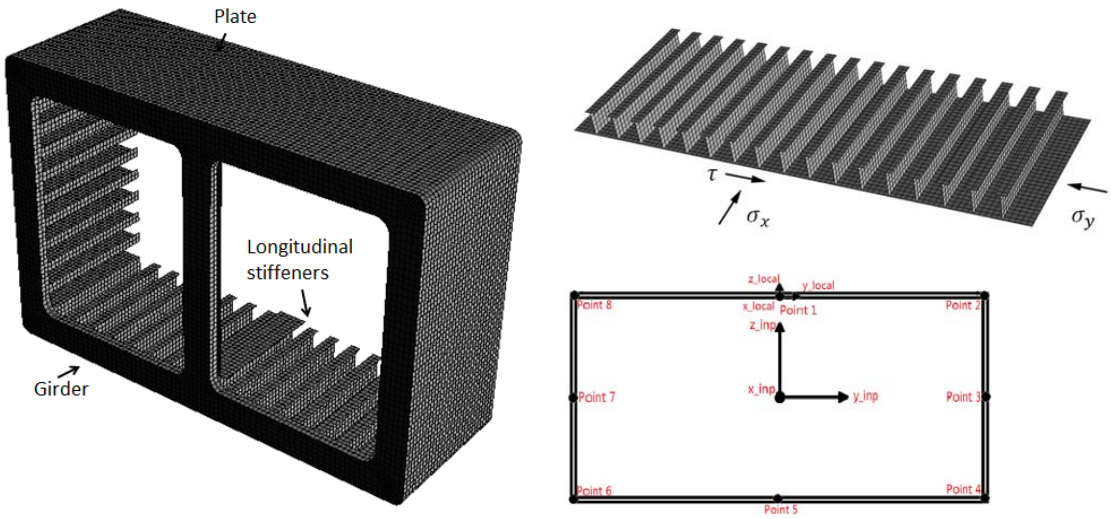

Figure 5 A realistic cross-section (left), stiffened plates (right top), and simplified box shape cross-section with equivalent thickness (right bottom)

In analysis for natural periods and modes, it is important to appropriately account for effect of flexibility of the hull, tower, RNA, mooring system, added mass and fluctuations of hydrostatic pressure and gravity on the natural modes and frequencies. For instance, as shown in Figure 6, numerical analysis shows that natural frequency of the side-to-side tower central column bending mode is increased from 0.325 Hz to 0.463 Hz if real flexibility of the hull is replaced by an assumption that the hull is considered as a rigid body. Rigid-body assumption for the hull is used in some conventional time-domain computer codes for analyzing global responses, e.g. bending moment in tower base, rigid-body motions of the hull and mooring line tensions [40]. The rigid-body assumption may result in artificial resonant structural vibrations exited by, for example, the 1P and 3P effects.

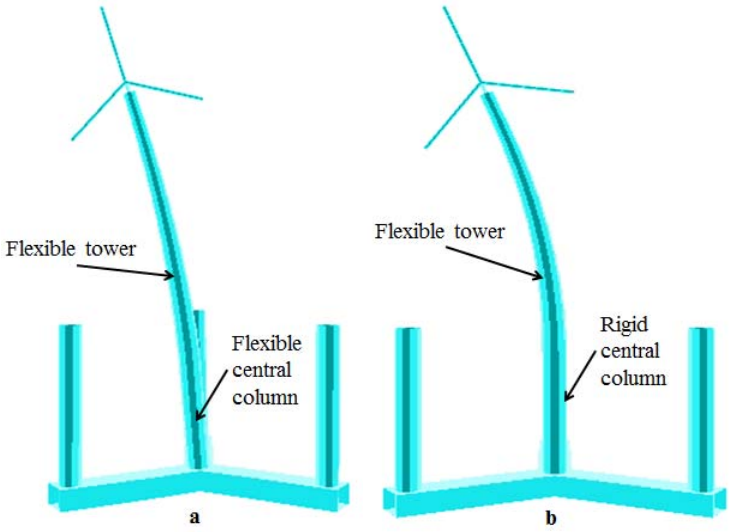

Figure 6 Side–to-side tower central column bending mode

3.4 Simplifications for the design conditions used in ULS and FLS design checks

Simplifications are proposed with respect to the variables of the time-domain simulations for each short-term analysis and the number of short-term environmental conditions.

In each short-term analysis, the combined wind and wave environmental condition is considered as a stationary process represented by such parameters as 1) the duration of the stationary process, e.g., 10 min, 1 h, 3 h; 2) the mean wind speed at a specified reference height in the space ($U_{w,m}$); 3) the turbulence intensity factor; 4) the significant wave height (H_s); 5) the peak period of wave spectrum (T_p); 6) the type of wind spectrum, e.g., Kaimal; 7) the type of wave spectrum; and 8) the wind direction (d_{wind}) and wave direction (d_{wave}).

It is a common practice to assume 10 min stationary wind for numerical simulations for on-shore and offshore fixed wind turbines, whereas 1-6 h simulations are required for wave loads on floating wind turbines [13] to account for the slow varying second-order wave load effect. Van der Hoven [34] showed that the power spectrum for wind measured over longer periods has small variations. Therefore, the assumption of a 1-3 h stationary wind field could be reasonable. The work of Burton et al [35] proved that the 1 h stationary wind field assumption can give satisfactory models in the wind industry. Therefore, each of the combined wind and wave environmental conditions could be considered stationary over 1 hour.

For each short-term analysis, the uncertainty of the fatigue damage is related to the simulation length and could be reduced by using the expected value. Kvittem & Moan [36] studied the effect of simulation length on fatigue for tower base a semi-submersible wind turbine. The expected fatigue damage induced by 155 environmental conditions in 20 years is estimated by 3 h time-domain simulation for each short-term analysis (D_{3h}), 1 h time-domain simulation for each short-term analysis (D_{1h}) and 10 min time-domain simulation for each short-term analysis (D_{10mins}). The difference between D_{3h} and D_{1h} is no more than 4%, while that between D_{3h} and D_{10mins} is less than 10%. Therefore, 1 h fatigue damage based on 3 samples could be used to reasonably account for stochastic uncertainties in short-term fatigue damage estimation with respect to tower base. Similar researches with respect to fatigue damage of structural components of the hull are needed in future as structural responses of the structural components could be dominated by different load components when compared to structural responses of tower base [51].

The number of the environmental conditions for fatigue assessment is related to the bin sizes for $U_{w,m}$, H_s, T_p, d_{wind} and d_{wave}. A bin size of 2 m/s for $U_{w,m}$, 0.5 m for H_s and 0.5 s for T_p is recommended by IEC6140-3. Kvittem & Moan [36] show that fatigue damage could be considerably underestimated if the bin sizes for $U_{w,m}$, H_s and T_p failed to include critical

environmental conditions that result in large fatigue damage. However, small bin sizes correspond to a large number of environmental conditions and require expensive computations.

The computational effort could be significantly reduced by conducting the FLS and ULS design checks based on a few representative design conditions selected from all of the environmental conditions possible in the design life. The challenge is how to select such representative environmental conditions. For the ULS design check, a possible solution is to employ the contour line/surface method. The contour line/surface method is a mature method for predicting extreme load effects for offshore structures under wave loads. For offshore wind turbines, the contour line/surface method must be calibrated by the full long-term analysis because 1) the critical extreme load effect induced by aerodynamic loads is likely to occur at operational wind conditions, rather than extreme wind conditions under which the wind turbine rotor is parked to reduce the wind load; 2) the load effect on the hull could be more sensitive to the value of T_p than the value of H_s; and 3) floating wind turbines should be considered strongly coupled system. Modified environmental contour method to determine the long-term extreme responses of offshore fixed and floating wind turbines are discussed in [54-57].

3.5 Simplification of the methods for estimating the load effect on the hull

Load effects on the hull need to be calculated by using finite element method with emphasis on the aero-hydro-servo-elastic feature and reasonable computational expenses. For example, Luan et al proposed a novel time-domain finite element method [40] for calculating sectional loads in the pontoons in a straight-forward manner by modeling the semi-submersible hull as a multi-body system.

As pointed in [40], finite element analysis in frequency-domain is very cost-effective. However, the major limitations are that 1) it is a big challenge to appropriately account for the strong non-linear dynamic characteristics, which is known as the aero-hydro-servo-elastic feature, of floating wind turbines; and 2) transient loading events, such as wind turbine faults, cannot be modeled in frequency domain. However, the work of Luan el al [51] shows that sectional forces and moments of some structural components, e.g. the side columns of the 5-MW-CSC, in wind and waves could be dominated by first order wave excitation loads, and inertial and radiation loads which are related to wave induced motions. Consequently, these structural components could be designed based on wave induced responses calculated by using the conventional frequency-domain approach described as follows:

- The semi-submersible wind turbine, which composes these structural components, could be assumed as a rigid-body oscillating around its mean position in wind and waves with 6 d.o.f.s, while the rigid-body motions are obtained by generating and solving corresponding motion equations in frequency-domain, and are used to derive the inertial loads on the hull of the semi-submersible wind turbine [46].
- Wave to hydrodynamic pressure force transfer function, for a given point on mean wetted body surface of the hull, could be calculated by generating and solving the corresponding boundary value problem as described in potential flow theory [46].
- Incident wave spectrum, and corresponding motion responses and wave to hydrodynamic pressure force transfer function could be used to derive the wave excitation and radiation loads on the hull.
- The derived inertial, wave excitation and radiation loads can be mapped in a beam element finite element model for the hull to analyze wave induced sectional forces and moments and/or a shell element finite element model (including structural details) for the hull to analyze wave induced stresses.
- If the hull is a static determinate structure, e.g. the 5-MW-CSC, a specified cross-section on a structural component, such as a column or a pontoon, of the hull could divide the hull into two parts, see [40]. Forces and moments in the specified cross-section could be obtained by integrating the derived inertial, wave excitation and radiation loads on mean wetted body surface of one of the two parts.
- Mean position of the semi-submersible wind turbine depends on environmental condition subjected to the model. As analyzed in [51] the mean wetted body-surface used in the boundary value problem and for integrating the derived loads should correspond to the mean position of the semi-submersible wind turbine. Otherwise, the simulated

responses may have a considerable deviation when compared to responses in real.

Regarding the load effect on the global level, we suggest the simplification of pontoons, columns and braces as beam elements with simplified cross-sections. Stresses induced by the global load effect could be derived based on the sectional forces and moments in the beam elements. Figure 5 shows a simplified cross-section of a box-shape pontoon. The sectional forces and moments are represented by F_x, F_y, F_z, M_x, M_y, and M_z at the geometrical center of the cross-section (the origin of the x_inp-y_inp-z_inp coordinate system). For an arbitrary point (y_{inp}, z_{inp}) on the cross-section, the nominal normal stress (σ_x) and nominal shear stress (τ) induced by the sectional forces and moments could be calculated by Eq. (10, 11) based on the Euler-Bernoulli beam theory and assumption that stress distribution induced by each load can be linearly combined.

$$\sigma_x(y_{inp}, z_{inp}) = \frac{F_x}{A} + \frac{M_y}{w_{y\_inp}} + \frac{M_z}{w_{z\_inp}} \quad (10)$$

$$\tau(y_{inp}, z_{inp}) = \frac{M_x}{2A_0 t_c} + \frac{F_y S_{z\_inp}}{I_{z\_inp} t_c} + \frac{F_z S_{y\_inp}}{I_{y\_inp} t_c} \quad (11)$$

where, A is area of the cross-section. w_{y_inp} and w_{z_inp} are the corresponding section moduli. A_0 is the circumscribed area of the cross-section. t_c is the equivalent thickness of the cross-section. S_{y_inp} and S_{z_inp} are static moments corresponding to the y_inp and z_inp axes and the position of the point on the cross-section. I_{y_inp} and I_{z_inp} are the second moments of area of the cross-section.

Compared with a realistic cross-section, which includes structural details, such as stiffeners, the thin wall box-shape approximation with t_c will underestimate the maximum shear stresses because the stiffeners carry the shear force inefficiently. Therefore, a reduction factor could be applied to t_c to compensate the underestimations for the shear stresses.

Wave to sectional forces transfer functions and wave to stresses transfer functions could be sensitive to the wave directions, wave frequencies and position of the hull.

3.6 Methods for estimating structural resistance

The buckling strength of the pontoons and columns could be considered as stiffened plate subjected to local and global load effects. Relevant standards and practices such as DNV-RP-C201[38] could be applied. A preliminary detailed structural design is required. An application example is available in [42].

Fatigue analysis for the components of the hull is normally conducted by the S-N Palmgren-Miner rule approach. The stress ranges used in the S-N fatigue approach could be calculated by applying the rainflow counting method to the time series of the hot-spot stress. Appropriate SN curves should be selected based on relevant standards, e.g., DNV-RP-C203 [39].

The hot-spot stresses are induced by stress concentration effect in particular at the structural intersections or joints. The fatigue life is very sensitive to the hot-spot stresses (in the order of 3-5 due to the slope of the S-N curves), which may appear at the joints between the columns, pontoons or braces. Therefore, the structural details need to be well designed to reduce the hot-spot stresses. For a complex joint, it is recommended that the hot-spot stress be calculated by finite element analysis [39].

For the compartments of the pontoons and columns that are in between of the joints, in general, the stress concentration effect is not critical. Therefore, we propose that the fatigue life for such compartments could be estimated by the normal stresses of several representative points in the corresponding cross-section of the compartment multiplied by a specified stress concentration factor (SCF). A sensitivity study for the fatigue damage with respect to SCF is needed.

4 Conclusions

This paper deals with the design criteria, procedure and simplifications for developing conceptual design of MW level horizontal axis semi-submersible wind turbine hulls. Analysis and discussions presented in this paper are based on the authors' experience with respect to design and analysis of semi-submersible wind turbines in the past six years.

The wind turbine systems must be designed for serviceability and safety. The safety of the design could be checked by the limit state design, whereas the safety factors used in the partial safety factor format should be calibrated by reliability methods. While, there is a trade-off between the minimum required safety level and construction, installation and maintenance costs. Cost

efficient design with acceptable reliability is preferred.

Hull design for floating wind turbines should not be performed in isolation; rather, the interactions of the subsystems, i.e., the RNA, control system, tower, hull and mooring system, should be appropriately considered as floating wind turbines are considered strongly coupled systems requiring sufficient stability, appropriately designed natural periods and modes and reasonable structural design.

Design is an iterative process. We assume that the design configuration of the RNA, tower and controller has been selected. Consequently, the allowable heeling angle, which is the upper limit of the critical heeling angle induced by the design overturning moment about the critical axis, could be used as a simplified stability criterion, in together with a criterion with respect to natural periods of rigid-body motions of semi-submersible wind turbines and two practical approaches for estimating value and distribution of steel and ballast mass of the hull, for developing initial designs of semi-submersible hulls.

Design space of semi-submersible wind turbine hulls which is developed by using these criteria and simplified approaches are thoroughly analyzed and discussed. The restoring stiffness mainly comes from second moment of water plane area which is determined by diameter and arrangement of the side columns. Symmetrical arrangement with respect to the vertical axis through the geometrical center of the water plane area, in together with three side columns with or without a central column, is preferred. To satisfy the criterion with respect to natural periods of rigid-body motions, sufficient added mass and mass of displaced water are required. Heave plates could be used to efficiently increase added mass of the hull but will significantly increase the system complexity and construction and maintenance costs. For semi-submersible wind turbines without heave plates, a relatively high roll/pitch restoring stiffness and the restriction of the heave natural period to beyond the wave range result in a large displaced volume and steel mass of the semi-submersible hull.

Natural periods and modes should eventually be checked by solving the eigenvalue problem which is related to the generalized mass and stiffness. It is important to appropriately account for effect of flexibility of the hull, tower, RNA, mooring system, added mass and fluctuations of hydrostatic pressure and gravity on the natural modes and frequencies.

Simplifications for the design conditions used in ULS and FLS design checks are discussed based on a review of relevant publications. Each of the combined wind and wave environmental conditions could be considered stationary over 1 hour, while 1 h fatigue damage based on 3 samples could be used to reasonably account for stochastic uncertainties in short-term fatigue damage estimation with respect to tower base. Similar researches with respect to fatigue damage of structural components of the hull are needed in future. The modified environmental contour method could be used to determine the long-term extreme responses of offshore fixed and floating wind turbines. More efforts are needed to shed lights on approaches for identifying critical environmental conditions for fatigue damage.

Simplification of the methods for estimating the load effect on the hull is discussed. To appropriately account for the aero-hydro-servo-elastic feature of semi-submersible wind turbines, time-domain finite element analysis should be used. However, for some design, structural responses of some structural components in wind and waves could be dominated by first order wave excitation loads, and inertial and radiation loads which are related to wave induced motions. Consequently, these structural components could be designed based on wave induced responses calculated by using the frequency-domain approach described in this paper.

Methods for estimating structural resistance are referred to relevant standards and practices.

A detailed analysis with respect to design of the semi-submersible hull against accidental events, such as ship collision, loss of a mooring line and flooding in a column, is scheduled in future.

ACKNOWLEDGMENTS

The authors acknowledge the financial support provided by the Research Council of Norway granted through the Centre for Ships and Ocean Structures; the Norwegian Research Centre for Offshore Wind Technology (NOWITECH), NTNU; and the Centre for Autonomous Marine Operations and Systems (AMOS), NTNU. Partial financial support from the EU FP-7 project MARINA Platform project (Grant Agreement 241402) is also acknowledged.

REFERENCES

[1] Twidell, J. and Gaudiosi, G., (2009), "*Offshore Wind Power*", Multi-Science Publishing Co.Ltd.

[2] Roddier, D., Cermelli, C., Aubault, A., and Weinstein, A., (2010), "WindFloat: A floating foundation for offshore wind turbines", Journal of Renewable and Sustainable Energy 2, 033104, doi:10.1063/1.3435339.

[3] Roddier, D., Peiffer, A., Aubault, A., and Weinstein, J., (2011), "A generic 5 MW WindFloat for numerical tool validation & comparison against a generic spar", In 30th International Conference on Ocean, Offshore and Arctic Engineering, no, OMAE2011-50278, Rotterdam, the Netherlands.

[4] Robertson, A., Jonkman, J., Masciola, M., Song, H., Goupee, A., Coulling, A., and Luan C., (2012), "Definition of the Semisubmersible Floating System for Phase II of OC4", Offshore Code Comparison Collaboration Continuation (OC4) for IEA Task 30.

[5] Huijs, F., Mikx, J., Savenije, F., and Ridder, E., (2013), "Integrated design of floater, mooring and control system for a semisubmersible floating wind turbine", European Wind Energy Association (EWEA) Offshore, Frankfurt.

[6] Viselli, A. M., Goupee, A. J., and Dagher, H., (2014), "Model Test of a 1:8 Scale Floating Wind Turbine Offshore in the Gulf of Maine", In 33th International Conference on Ocean, Offshore and Arctic Engineering, no, OMAE2014-23639, San Francisco, CA, USA.

[7] Dr.techn.Olav Olsen AS, (2015), http://www.olavolsen.no/en/node/17, accessed 2nd.January.2018.

[8] Jonkman J., Butterfield, S., Musial, W. and Scott, G., (2009), "Definition of a 5-MW Reference Wind Turbine for Offshore System Development", NREL/TP-500-38060, National Renewable Energy Laboratory, Golden, CO, U.S.A.

[9] IEC, (2005), "Wind turbines – Part 1: Design requirements", IEC-61400-1, International Electrotechnical Commission.

[10] IEC, (2009), "Wind turbines: Part 3: Design requirements for offshore wind turbines", IEC-61400-3, International Electrotechnical Commission.

[11] DNV, (2013), "Offshore standard – Design of Offshore Wind Turbine Structures", DNV-OS-J101, Det Norske Veritas.

[12] DNVGL, (2016), "Support structures for wind turbines". DNVGL-ST-126, DNV GL Group AS

[13] DNV, (2013), "Offshore standard – Design of Floating Wind turbine Structures", DNV-OS-J103, Det Norske Veritas.

[14] Bachynski, E.E., Etemaddar, M., Kvittem, M.I., Luan, C., Moan, T., (2013) "Dynamic analysis of floating wind turbines during pitch actuator fault, grid loss, and shutdown", Energy Procedia vol. 35, 210-222. doi:10.1016/j.egypro.2013.07.174

[15] Jiang, Z., Karimirad, M. and Moan, T., (2012), "Steady State Response of a Parked Spar-Type Wind Turbine Considering Blade Pitch Mechanism Fault", Proceedings of the 22nd International Offshore and Polar Engineering Conference, Rhodes, Greece.

[16] Jiang, Z., Moan, T., Gao, Z. and Karimirad, M., (2013), "Effect of Shut-Down Strategies on the Dynamic Responses of a Spar-Type Floating Wind Turbine", Proceedings of the 32nd International Conference on Ocean, Offshore and Arctic Engineering, Nantes, France.

[17] Jiang, Z., Karimirad, M. and Moan, T., (2013), "Response Analysis of a Parked Spar-Type Wind Turbine Considering Blade Pitch Mechanism Fault", International Journal of Offshore and Polar Engineering, 2013; 23 (2): 120–128.

[18] Jiang, Z., Karimirad, M. and Moan, T., (2013), "Dynamic Response Analysis of Wind Turbines Under Blade Pitch System Fault, Grid Loss and Shutdown Events". Wind Energy, doi:10.1002/we.1639

[19] Butterfield, S., Musial, W., Jonkman, J. and Sclavounos, P., (2007), "Engineering challenges for floating offshore wind turbines", Technical report NREL/CP-500-38776, National Renewable Energy Laboratory.

[20] Xing, Y., Karimirad. M. and Moan, T., (2014), "Modelling and Analysis of Floating Spar-Type Wind Turbine Drivetrain", Wind Energy. (online first) doi:10.1002/we.1590

[21] Xing, Y., Karimirad, M. and Moan, T., (2012), "Effect of Spar-Type Floating Wind Turbine Nacelle Motion on Drivetrain Dynamics", Proceedings of EWEA 2012 Annual Event, Copenhagen, Denmark.

[22] Nejad, A.R.; Bachynski, E.E.; Kvittem, M.I., Luan, C.; Gao, Z. and Moan, T., (2015), "Stochastic Dynamic Load Effect

and Fatigue Damage Analysis of Drivetrains in Land-based and TLP, Spar and Semi-Submersible Floating Wind Turbines", Accepted by Marine structures.

[23] Larsen, T. J., and Hanson, T. D., (2007). "A method to avoid negative damped low frequent tower vibrations for a floating pitch controlled wind turbine". Journal of Physics: Conference Series, 75.

[24] Jonkman, J., (2008). "Influence of Control on the Pitch Damping of a Floating Wind Turbine". In Proceedings of the ASME Wind Energy Symposium.

[25] Lackner, M. a., and Rotea, M. a.,(2011). "Structural control of floating wind turbines". Mechatronics, 21(4), June, pp. 704–719.

[26] Fischer, B., (2012). "Reducing rotor speed variations of floating wind turbines by compensation of non-minimum phase zeros". In Proceedings of the EWEA, pp. 144–147.

[27] Veen, G. V. D., Couchman, Y., and Bowyer, R., (2012), "Control of floating wind turbines". In Proceedings of the American Control Conference ACC, pp. 3148–3153.

[28] Skaare, B., Hanson, T. D., Nielsen, F. G., Yttervik, R., Hansen, A. M., Thomsen, K. and Larsen, T. J. (2007). "Integrated dynamic analysis of floating offsore wind turbines". European Wind Energy Conference and Exhibition.

[29] Sandner, F., Schlipf, D., Matha, D. and Cheng, P. W., (2014), "Integrated optimization of floating wind turbine systems", Proceedings of the 33nd International Conference on Ocean, Offshore and Arctic Engineering, San Francisco, CA, USA.

[30] Gao, Z., Luan, C., Moan, T., Skaare, B., Solberg, T. and Lygren, J.E., (2011), "Comparative Study of Wind- and Wave-Induced Dynamic Responses of Three Floating Wind Turbines Supported by Spar, Semi-Submersible and Tension-Leg Floaters". Proceedings of the 2011 International Conference on Wind Energy and Ocean Energy (ICOWEOE'11). 31 October- 2 November 2011 - Beijing, China.

[31] The HiPRWind project, (2015), http://hiprwind.eu/, accessed 2nd.January.2018.

[32] Jonkman J., (2010), "Definition of the Floating System for Phase IV of OC3", NREL/TP-500-47535, National Renewable Energy Laboratory, Golden, CO, USA

[33] Nour-Omid, B., Parlett, B.N.,Taylor, R.L.,(1983), "Lanczos versus Subspace Iteration for Solution of Eigenvalue Problems", International Journal for Numerical Methods in Engineering, Vol. 19, pp. 859-871.

[34]Van der Hoven, I., (1957), "Power spectrum of horizontal wind speed in the frequency range from 0.0007 to 900 cycles per hour", Journal of Meteorology, 14(2):160–164.

[35]Burton, T., Jenkins, N., Sharpe, D. and Bossanyi, E., (2011), "*Wind energy handbook*", John Wiley & Sons.

[36]Kvittem, M. I., Moan, T., (2015), "Time domain analysis procedures for fatigue assessment of a semi-submersible wind turbine", Marine Structures. vol. 40.

[37] Li, L., Gao, Z., Moan, T., (2015), "Joint Distribution of Environmental Condition at Five European Offshore Sites for Design of Combined Wind and Wave Energy Devices", Journal of Offshore Mechanics and Arctic Engineering. 137(3), 031901 (16 pages). doi: 10.1115/1.4029842.

[38] DNV, (2010), "Recommended Practice – Buckling strength of plated structures", DNV-RP-C201, Det Norske Veritas

[39] DNV, (2010), "Recommended Practice – Fatigue Design of Offshore Steel Structures", DNV-RP-C203, Det Norske Veritas.

[40] Luan, C., Gao, Z. and Moan, T., (2017), "Development and verification of a time-domain approach for determining forces and moments in structural components of floaters with an application to floating wind turbines". Marine Structures. vol. 5 pp 87-109.

[41] Marin, T.I., (2014), "Fatigue Analysis of the Column-Pontoon Connection in a Semi-Submersible Floating Wind Turbine", Master thesis, Norwegian University of Science and Technology, Trondheim, Norway.

[42] Luan, C., Gao, Z., and Moan, T., (2016). "Design and analysis of a braceless steel 5-mw semi-submersible wind turbine". Proceedings of the 35th International Conference on Ocean, Offshore and Arctic Engineering, OMAE2016-54848, Busan, Korea, June 19–24.

[43] DNV, (2004), "Offshore standard – Position Mooring", DNV-OS-E301, Det Norske Veritas.

[44] Moriarty, P. J., and Hansen, A. C., (2005), AeroDyn theory manual, Tech. Rep, NREL/TP-500-36881.
[45] MARINTEK, (2013). RIFLEX User's Manual.
[46] DNV, (2013), SESAM User Manual HydroD.
[47] Bachynski, E.E., Chabaud, V. and Sauder, T., (2015), "Real-time hybrid model testing of floating wind turbines: sensitivity to limited actuation", Energy Procedia, Vol. 80, pp. 2-12.
[48] PULS user manual
[49] Cordle, A., and Jonkman, J., (2011), "State of the art in floating wind turbine design tools", Proceedings of the 21st International Offshore and Polar Engineering Conference, Maui, Hawaii, USA. Vol. 1, pp. 367–374.
[50] Luan, C., Chabaud, V., Bachynski, E., Gao, Z., and Moan, T., (2017), "Experimental validation of a time-domain approach for determining sectional loads in a floating wind turbine hull subjected to moderate waves", Energy Procedia, Vol. 137, pp. 366-381.
[51] Luan, C., Gao, Z., and Moan, T., (2018). "Comparisons and analysis of numerical simulated and experimental measured motions and sectional loads in a floating wind turbine hull subjected to combined wind and waves", under review at Engineering Structures
[52] Huijs, F (2015), "The influence of the mooring system of the motions and stability of a semi-submersible floating wind turbine", Proceedings of the 34th International Conference on Ocean, Offshore and Arctic Engineering, OMAE2015-41947, St. john's, Canada, May 31-June 5.
[53] Moan, T., Gao, Z., and Muliawan, M., (2013), "Modelling methodology for concept assessment", Deliverable D.41, MARINA-Platform.
[54] Li, Q., Gao, Z., and Moan T., (2017), "Modified environmental contour method to determine the long-term extreme responses of a semi-submersible wind turbine", Ocean Engineering, Volume 142, pp 563-576.
[55] Li, Q., Gao, Z., and Moan T., (2016), "Modified environmental contour method for predicting long-term extreme responses of bottom-fixed offshore wind turbines", Marine Structures, Volume 48, pp 15-32.
[56] Li, Q., Gao, Z., and Moan T., (2014), "Long-term extreme response analysis for a fixed offshore wind turbine considering blade-pitch-actuator fault and normal transient events", In 33th International Conference on Ocean, Offshore and Arctic Engineering, no, OMAE2014-23621, San Francisco, CA, USA.
[57] Li, Q., Gao, Z., and Moan T., (2013), "Extreme response analysis for a jacket-type offshore wind turbine using environmental contour method", Proceedings of the 11th International Conference on Structural Safety and Reliability, ICOSSAR 2013, pp. 5597-5604.

Appendix C

List of previous Ph.D theses at Dept. of Marine Tech.

Previous PhD theses published at the Departement of Marine Technology
(earlier: Faculty of Marine Technology)
NORWEGIAN UNIVERSITY OF SCIENCE AND TECHNOLOGY

Report No.	Author	Title
	Kavlie, Dag	Optimization of Plane Elastic Grillages, 1967
	Hansen, Hans R.	Man-Machine Communication and Data-Storage Methods in Ship Structural Design, 1971
	Gisvold, Kaare M.	A Method for non-linear mixed -integer programming and its Application to Design Problems, 1971
	Lund, Sverre	Tanker Frame Optimalization by means of SUMT-Transformation and Behaviour Models, 1971
	Vinje, Tor	On Vibration of Spherical Shells Interacting with Fluid, 1972
	Lorentz, Jan D.	Tank Arrangement for Crude Oil Carriers in Accordance with the new Anti-Pollution Regulations, 1975
	Carlsen, Carl A.	Computer-Aided Design of Tanker Structures, 1975
	Larsen, Carl M.	Static and Dynamic Analysis of Offshore Pipelines during Installation, 1976
UR-79-01	Brigt Hatlestad, MK	The finite element method used in a fatigue evaluation of fixed offshore platforms. (Dr.Ing. Thesis)
UR-79-02	Erik Pettersen, MK	Analysis and design of cellular structures. (Dr.Ing. Thesis)
UR-79-03	Sverre Valsgård, MK	Finite difference and finite element methods applied to nonlinear analysis of plated structures. (Dr.Ing. Thesis)
UR-79-04	Nils T. Nordsve, MK	Finite element collapse analysis of structural members considering imperfections and stresses due to fabrication. (Dr.Ing. Thesis)
UR-79-05	Ivar J. Fylling, MK	Analysis of towline forces in ocean towing systems. (Dr.Ing. Thesis)
UR-80-06	Nils Sandsmark, MM	Analysis of Stationary and Transient Heat Conduction by the Use of the Finite Element Method. (Dr.Ing. Thesis)
UR-80-09	Sverre Haver, MK	Analysis of uncertainties related to the stochastic modeling of ocean waves. (Dr.Ing. Thesis)
UR-81-15	Odland, Jonas	On the Strength of welded Ring stiffened cylindrical Shells primarily subjected to axial Compression
UR-82-17	Engesvik, Knut	Analysis of Uncertainties in the fatigue Capacity of

		Welded Joints
UR-82-18	Rye, Henrik	Ocean wave groups
UR-83-30	Eide, Oddvar Inge	On Cumulative Fatigue Damage in Steel Welded Joints
UR-83-33	Mo, Olav	Stochastic Time Domain Analysis of Slender Offshore Structures
UR-83-34	Amdahl, Jørgen	Energy absorption in Ship-platform impacts
UR-84-37	Mørch, Morten	Motions and mooring forces of semi submersibles as determined by full-scale measurements and theoretical analysis
UR-84-38	Soares, C. Guedes	Probabilistic models for load effects in ship structures
UR-84-39	Aarsnes, Jan V.	Current forces on ships
UR-84-40	Czujko, Jerzy	Collapse Analysis of Plates subjected to Biaxial Compression and Lateral Load
UR-85-46	Alf G. Engseth, MK	Finite element collapse analysis of tubular steel offshore structures. (Dr.Ing. Thesis)
UR-86-47	Dengody Sheshappa, MP	A Computer Design Model for Optimizing Fishing Vessel Designs Based on Techno-Economic Analysis. (Dr.Ing. Thesis)
UR-86-48	Vidar Aanesland, MH	A Theoretical and Numerical Study of Ship Wave Resistance. (Dr.Ing. Thesis)
UR-86-49	Heinz-Joachim Wessel, MK	Fracture Mechanics Analysis of Crack Growth in Plate Girders. (Dr.Ing. Thesis)
UR-86-50	Jon Taby, MK	Ultimate and Post-ultimate Strength of Dented Tubular Members. (Dr.Ing. Thesis)
UR-86-51	Walter Lian, MH	A Numerical Study of Two-Dimensional Separated Flow Past Bluff Bodies at Moderate KC-Numbers. (Dr.Ing. Thesis)
UR-86-52	Bjørn Sortland, MH	Force Measurements in Oscillating Flow on Ship Sections and Circular Cylinders in a U-Tube Water Tank. (Dr.Ing. Thesis)
UR-86-53	Kurt Strand, MM	A System Dynamic Approach to One-dimensional Fluid Flow. (Dr.Ing. Thesis)
UR-86-54	Arne Edvin Løken, MH	Three Dimensional Second Order Hydrodynamic Effects on Ocean Structures in Waves. (Dr.Ing. Thesis)
UR-86-55	Sigurd Falch, MH	A Numerical Study of Slamming of Two-Dimensional Bodies. (Dr.Ing. Thesis)
UR-87-56	Arne Braathen, MH	Application of a Vortex Tracking Method to the Prediction of Roll Damping of a Two-Dimension Floating Body. (Dr.Ing. Thesis)

UR-87-57	Bernt Leira, MK	Gaussian Vector Processes for Reliability Analysis involving Wave-Induced Load Effects. (Dr.Ing. Thesis)
UR-87-58	Magnus Småvik, MM	Thermal Load and Process Characteristics in a Two-Stroke Diesel Engine with Thermal Barriers (in Norwegian). (Dr.Ing. Thesis)
MTA-88-59	Bernt Arild Bremdal, MP	An Investigation of Marine Installation Processes – A Knowledge - Based Planning Approach. (Dr.Ing. Thesis)
MTA-88-60	Xu Jun, MK	Non-linear Dynamic Analysis of Space-framed Offshore Structures. (Dr.Ing. Thesis)
MTA-89-61	Gang Miao, MH	Hydrodynamic Forces and Dynamic Responses of Circular Cylinders in Wave Zones. (Dr.Ing. Thesis)
MTA-89-62	Martin Greenhow, MH	Linear and Non-Linear Studies of Waves and Floating Bodies. Part I and Part II. (Dr.Techn. Thesis)
MTA-89-63	Chang Li, MH	Force Coefficients of Spheres and Cubes in Oscillatory Flow with and without Current. (Dr.Ing. Thesis
MTA-89-64	Hu Ying, MP	A Study of Marketing and Design in Development of Marine Transport Systems. (Dr.Ing. Thesis)
MTA-89-65	Arild Jæger, MH	Seakeeping, Dynamic Stability and Performance of a Wedge Shaped Planing Hull. (Dr.Ing. Thesis)
MTA-89-66	Chan Siu Hung, MM	The dynamic characteristics of tilting-pad bearings
MTA-89-67	Kim Wikstrøm, MP	Analysis av projekteringen for ett offshore projekt. (Licenciat-avhandling)
MTA-89-68	Jiao Guoyang, MK	Reliability Analysis of Crack Growth under Random Loading, considering Model Updating. (Dr.Ing. Thesis)
MTA-89-69	Arnt Olufsen, MK	Uncertainty and Reliability Analysis of Fixed Offshore Structures. (Dr.Ing. Thesis)
MTA-89-70	Wu Yu-Lin, MR	System Reliability Analyses of Offshore Structures using improved Truss and Beam Models. (Dr.Ing. Thesis)
MTA-90-71	Jan Roger Hoff, MH	Three-dimensional Green function of a vessel with forward speed in waves. (Dr.Ing. Thesis)
MTA-90-72	Rong Zhao, MH	Slow-Drift Motions of a Moored Two-Dimensional Body in Irregular Waves. (Dr.Ing. Thesis)
MTA-90-73	Atle Minsaas, MP	Economical Risk Analysis. (Dr.Ing. Thesis)
MTA-90-74	Knut-Aril Farnes, MK	Long-term Statistics of Response in Non-linear Marine Structures. (Dr.Ing. Thesis)
MTA-90-75	Torbjørn Sotberg, MK	Application of Reliability Methods for Safety Assessment of Submarine Pipelines. (Dr.Ing.

		Thesis)
MTA-90-76	Zeuthen, Steffen, MP	SEAMAID. A computational model of the design process in a constraint-based logic programming environment. An example from the offshore domain. (Dr.Ing. Thesis)
MTA-91-77	Haagensen, Sven, MM	Fuel Dependant Cyclic Variability in a Spark Ignition Engine - An Optical Approach. (Dr.Ing. Thesis)
MTA-91-78	Løland, Geir, MH	Current forces on and flow through fish farms. (Dr.Ing. Thesis)
MTA-91-79	Hoen, Christopher, MK	System Identification of Structures Excited by Stochastic Load Processes. (Dr.Ing. Thesis)
MTA-91-80	Haugen, Stein, MK	Probabilistic Evaluation of Frequency of Collision between Ships and Offshore Platforms. (Dr.Ing. Thesis)
MTA-91-81	Sødahl, Nils, MK	Methods for Design and Analysis of Flexible Risers. (Dr.Ing. Thesis)
MTA-91-82	Ormberg, Harald, MK	Non-linear Response Analysis of Floating Fish Farm Systems. (Dr.Ing. Thesis)
MTA-91-83	Marley, Mark J., MK	Time Variant Reliability under Fatigue Degradation. (Dr.Ing. Thesis)
MTA-91-84	Krokstad, Jørgen R., MH	Second-order Loads in Multidirectional Seas. (Dr.Ing. Thesis)
MTA-91-85	Molteberg, Gunnar A., MM	The Application of System Identification Techniques to Performance Monitoring of Four Stroke Turbocharged Diesel Engines. (Dr.Ing. Thesis)
MTA-92-86	Mørch, Hans Jørgen Bjelke, MH	Aspects of Hydrofoil Design: with Emphasis on Hydrofoil Interaction in Calm Water. (Dr.Ing. Thesis)
MTA-92-87	Chan Siu Hung, MM	Nonlinear Analysis of Rotordynamic Instabilities in Highspeed Turbomachinery. (Dr.Ing. Thesis)
MTA-92-88	Bessason, Bjarni, MK	Assessment of Earthquake Loading and Response of Seismically Isolated Bridges. (Dr.Ing. Thesis)
MTA-92-89	Langli, Geir, MP	Improving Operational Safety through exploitation of Design Knowledge - an investigation of offshore platform safety. (Dr.Ing. Thesis)
MTA-92-90	Sævik, Svein, MK	On Stresses and Fatigue in Flexible Pipes. (Dr.Ing. Thesis)
MTA-92-91	Ask, Tor Ø., MM	Ignition and Flame Growth in Lean Gas-Air Mixtures. An Experimental Study with a Schlieren System. (Dr.Ing. Thesis)
MTA-86-92	Hessen, Gunnar, MK	Fracture Mechanics Analysis of Stiffened Tubular Members. (Dr.Ing. Thesis)

MTA-93-93	Steinebach, Christian, MM	Knowledge Based Systems for Diagnosis of Rotating Machinery. (Dr.Ing. Thesis)
MTA-93-94	Dalane, Jan Inge, MK	System Reliability in Design and Maintenance of Fixed Offshore Structures. (Dr.Ing. Thesis)
MTA-93-95	Steen, Sverre, MH	Cobblestone Effect on SES. (Dr.Ing. Thesis)
MTA-93-96	Karunakaran, Daniel, MK	Nonlinear Dynamic Response and Reliability Analysis of Drag-dominated Offshore Platforms. (Dr.Ing. Thesis)
MTA-93-97	Hagen, Arnulf, MP	The Framework of a Design Process Language. (Dr.Ing. Thesis)
MTA-93-98	Nordrik, Rune, MM	Investigation of Spark Ignition and Autoignition in Methane and Air Using Computational Fluid Dynamics and Chemical Reaction Kinetics. A Numerical Study of Ignition Processes in Internal Combustion Engines. (Dr.Ing. Thesis)
MTA-94-99	Passano, Elizabeth, MK	Efficient Analysis of Nonlinear Slender Marine Structures. (Dr.Ing. Thesis)
MTA-94-100	Kvålsvold, Jan, MH	Hydroelastic Modelling of Wetdeck Slamming on Multihull Vessels. (Dr.Ing. Thesis)
MTA-94-102	Bech, Sidsel M., MK	Experimental and Numerical Determination of Stiffness and Strength of GRP/PVC Sandwich Structures. (Dr.Ing. Thesis)
MTA-95-103	Paulsen, Hallvard, MM	A Study of Transient Jet and Spray using a Schlieren Method and Digital Image Processing. (Dr.Ing. Thesis)
MTA-95-104	Hovde, Geir Olav, MK	Fatigue and Overload Reliability of Offshore Structural Systems, Considering the Effect of Inspection and Repair. (Dr.Ing. Thesis)
MTA-95-105	Wang, Xiaozhi, MK	Reliability Analysis of Production Ships with Emphasis on Load Combination and Ultimate Strength. (Dr.Ing. Thesis)
MTA-95-106	Ulstein, Tore, MH	Nonlinear Effects of a Flexible Stern Seal Bag on Cobblestone Oscillations of an SES. (Dr.Ing. Thesis)
MTA-95-107	Solaas, Frøydis, MH	Analytical and Numerical Studies of Sloshing in Tanks. (Dr.Ing. Thesis)
MTA-95-108	Hellan, Øyvind, MK	Nonlinear Pushover and Cyclic Analyses in Ultimate Limit State Design and Reassessment of Tubular Steel Offshore Structures. (Dr.Ing. Thesis)
MTA-95-109	Hermundstad, Ole A., MK	Theoretical and Experimental Hydroelastic Analysis of High Speed Vessels. (Dr.Ing. Thesis)
MTA-96-110	Bratland, Anne K., MH	Wave-Current Interaction Effects on Large-Volume Bodies in Water of Finite Depth. (Dr.Ing. Thesis)
MTA-96-111	Herfjord, Kjell, MH	A Study of Two-dimensional Separated Flow by a Combination of the Finite Element Method and

		Navier-Stokes Equations. (Dr.Ing. Thesis)
MTA-96-112	Æsøy, Vilmar, MM	Hot Surface Assisted Compression Ignition in a Direct Injection Natural Gas Engine. (Dr.Ing. Thesis)
MTA-96-113	Eknes, Monika L., MK	Escalation Scenarios Initiated by Gas Explosions on Offshore Installations. (Dr.Ing. Thesis)
MTA-96-114	Erikstad, Stein O., MP	A Decision Support Model for Preliminary Ship Design. (Dr.Ing. Thesis)
MTA-96-115	Pedersen, Egil, MH	A Nautical Study of Towed Marine Seismic Streamer Cable Configurations. (Dr.Ing. Thesis)
MTA-97-116	Moksnes, Paul O., MM	Modelling Two-Phase Thermo-Fluid Systems Using Bond Graphs. (Dr.Ing. Thesis)
MTA-97-117	Halse, Karl H., MK	On Vortex Shedding and Prediction of Vortex-Induced Vibrations of Circular Cylinders. (Dr.Ing. Thesis)
MTA-97-118	Igland, Ragnar T., MK	Reliability Analysis of Pipelines during Laying, considering Ultimate Strength under Combined Loads. (Dr.Ing. Thesis)
MTA-97-119	Pedersen, Hans-P., MP	Levendefiskteknologi for fiskefartøy. (Dr.Ing. Thesis)
MTA-98-120	Vikestad, Kyrre, MK	Multi-Frequency Response of a Cylinder Subjected to Vortex Shedding and Support Motions. (Dr.Ing. Thesis)
MTA-98-121	Azadi, Mohammad R. E., MK	Analysis of Static and Dynamic Pile-Soil-Jacket Behaviour. (Dr.Ing. Thesis)
MTA-98-122	Ulltang, Terje, MP	A Communication Model for Product Information. (Dr.Ing. Thesis)
MTA-98-123	Torbergsen, Erik, MM	Impeller/Diffuser Interaction Forces in Centrifugal Pumps. (Dr.Ing. Thesis)
MTA-98-124	Hansen, Edmond, MH	A Discrete Element Model to Study Marginal Ice Zone Dynamics and the Behaviour of Vessels Moored in Broken Ice. (Dr.Ing. Thesis)
MTA-98-125	Videiro, Paulo M., MK	Reliability Based Design of Marine Structures. (Dr.Ing. Thesis)
MTA-99-126	Mainçon, Philippe, MK	Fatigue Reliability of Long Welds Application to Titanium Risers. (Dr.Ing. Thesis)
MTA-99-127	Haugen, Elin M., MH	Hydroelastic Analysis of Slamming on Stiffened Plates with Application to Catamaran Wetdecks. (Dr.Ing. Thesis)
MTA-99-128	Langhelle, Nina K., MK	Experimental Validation and Calibration of Nonlinear Finite Element Models for Use in Design of Aluminium Structures Exposed to Fire. (Dr.Ing. Thesis)
MTA-99-	Berstad, Are J., MK	Calculation of Fatigue Damage in Ship Structures.

129		(Dr.Ing. Thesis)
MTA-99-130	Andersen, Trond M., MM	Short Term Maintenance Planning. (Dr.Ing. Thesis)
MTA-99-131	Tveiten, Bård Wathne, MK	Fatigue Assessment of Welded Aluminium Ship Details. (Dr.Ing. Thesis)
MTA-99-132	Søreide, Fredrik, MP	Applications of underwater technology in deep water archaeology. Principles and practice. (Dr.Ing. Thesis)
MTA-99-133	Tønnessen, Rune, MH	A Finite Element Method Applied to Unsteady Viscous Flow Around 2D Blunt Bodies With Sharp Corners. (Dr.Ing. Thesis)
MTA-99-134	Elvekrok, Dag R., MP	Engineering Integration in Field Development Projects in the Norwegian Oil and Gas Industry. The Supplier Management of Norne. (Dr.Ing. Thesis)
MTA-99-135	Fagerholt, Kjetil, MP	Optimeringsbaserte Metoder for Ruteplanlegging innen skipsfart. (Dr.Ing. Thesis)
MTA-99-136	Bysveen, Marie, MM	Visualization in Two Directions on a Dynamic Combustion Rig for Studies of Fuel Quality. (Dr.Ing. Thesis)
MTA-2000-137	Storteig, Eskild, MM	Dynamic characteristics and leakage performance of liquid annular seals in centrifugal pumps. (Dr.Ing. Thesis)
MTA-2000-138	Sagli, Gro, MK	Model uncertainty and simplified estimates of long term extremes of hull girder loads in ships. (Dr.Ing. Thesis)
MTA-2000-139	Tronstad, Harald, MK	Nonlinear analysis and design of cable net structures like fishing gear based on the finite element method. (Dr.Ing. Thesis)
MTA-2000-140	Kroneberg, André, MP	Innovation in shipping by using scenarios. (Dr.Ing. Thesis)
MTA-2000-141	Haslum, Herbjørn Alf, MH	Simplified methods applied to nonlinear motion of spar platforms. (Dr.Ing. Thesis)
MTA-2001-142	Samdal, Ole Johan, MM	Modelling of Degradation Mechanisms and Stressor Interaction on Static Mechanical Equipment Residual Lifetime. (Dr.Ing. Thesis)
MTA-2001-143	Baarholm, Rolf Jarle, MH	Theoretical and experimental studies of wave impact underneath decks of offshore platforms. (Dr.Ing. Thesis)
MTA-2001-144	Wang, Lihua, MK	Probabilistic Analysis of Nonlinear Wave-induced Loads on Ships. (Dr.Ing. Thesis)
MTA-2001-145	Kristensen, Odd H. Holt, MK	Ultimate Capacity of Aluminium Plates under Multiple Loads, Considering HAZ Properties. (Dr.Ing. Thesis)
MTA-2001-146	Greco, Marilena, MH	A Two-Dimensional Study of Green-Water

		Loading. (Dr.Ing. Thesis)
MTA-2001-147	Heggelund, Svein E., MK	Calculation of Global Design Loads and Load Effects in Large High Speed Catamarans. (Dr.Ing. Thesis)
MTA-2001-148	Babalola, Olusegun T., MK	Fatigue Strength of Titanium Risers – Defect Sensitivity. (Dr.Ing. Thesis)
MTA-2001-149	Mohammed, Abuu K., MK	Nonlinear Shell Finite Elements for Ultimate Strength and Collapse Analysis of Ship Structures. (Dr.Ing. Thesis)
MTA-2002-150	Holmedal, Lars E., MH	Wave-current interactions in the vicinity of the sea bed. (Dr.Ing. Thesis)
MTA-2002-151	Rognebakke, Olav F., MH	Sloshing in rectangular tanks and interaction with ship motions. (Dr.Ing. Thesis)
MTA-2002-152	Lader, Pål Furset, MH	Geometry and Kinematics of Breaking Waves. (Dr.Ing. Thesis)
MTA-2002-153	Yang, Qinzheng, MH	Wash and wave resistance of ships in finite water depth. (Dr.Ing. Thesis)
MTA-2002-154	Melhus, Øyvin, MM	Utilization of VOC in Diesel Engines. Ignition and combustion of VOC released by crude oil tankers. (Dr.Ing. Thesis)
MTA-2002-155	Ronæss, Marit, MH	Wave Induced Motions of Two Ships Advancing on Parallel Course. (Dr.Ing. Thesis)
MTA-2002-156	Økland, Ole D., MK	Numerical and experimental investigation of whipping in twin hull vessels exposed to severe wet deck slamming. (Dr.Ing. Thesis)
MTA-2002-157	Ge, Chunhua, MK	Global Hydroelastic Response of Catamarans due to Wet Deck Slamming. (Dr.Ing. Thesis)
MTA-2002-158	Byklum, Eirik, MK	Nonlinear Shell Finite Elements for Ultimate Strength and Collapse Analysis of Ship Structures. (Dr.Ing. Thesis)
IMT-2003-1	Chen, Haibo, MK	Probabilistic Evaluation of FPSO-Tanker Collision in Tandem Offloading Operation. (Dr.Ing. Thesis)
IMT-2003-2	Skaugset, Kjetil Bjørn, MK	On the Suppression of Vortex Induced Vibrations of Circular Cylinders by Radial Water Jets. (Dr.Ing. Thesis)
IMT-2003-3	Chezhian, Muthu	Three-Dimensional Analysis of Slamming. (Dr.Ing. Thesis)
IMT-2003-4	Buhaug, Øyvind	Deposit Formation on Cylinder Liner Surfaces in Medium Speed Engines. (Dr.Ing. Thesis)
IMT-2003-5	Tregde, Vidar	Aspects of Ship Design: Optimization of Aft Hull with Inverse Geometry Design. (Dr.Ing. Thesis)
IMT-	Wist, Hanne Therese	Statistical Properties of Successive Ocean Wave

2003-6		Parameters. (Dr.Ing. Thesis)
IMT-2004-7	Ransau, Samuel	Numerical Methods for Flows with Evolving Interfaces. (Dr.Ing. Thesis)
IMT-2004-8	Soma, Torkel	Blue-Chip or Sub-Standard. A data interrogation approach of identity safety characteristics of shipping organization. (Dr.Ing. Thesis)
IMT-2004-9	Ersdal, Svein	An experimental study of hydrodynamic forces on cylinders and cables in near axial flow. (Dr.Ing. Thesis)
IMT-2005-10	Brodtkorb, Per Andreas	The Probability of Occurrence of Dangerous Wave Situations at Sea. (Dr.Ing. Thesis)
IMT-2005-11	Yttervik, Rune	Ocean current variability in relation to offshore engineering. (Dr.Ing. Thesis)
IMT-2005-12	Fredheim, Arne	Current Forces on Net-Structures. (Dr.Ing. Thesis)
IMT-2005-13	Heggernes, Kjetil	Flow around marine structures. (Dr.Ing. Thesis
IMT-2005-14	Fouques, Sebastien	Lagrangian Modelling of Ocean Surface Waves and Synthetic Aperture Radar Wave Measurements. (Dr.Ing. Thesis)
IMT-2006-15	Holm, Håvard	Numerical calculation of viscous free surface flow around marine structures. (Dr.Ing. Thesis)
IMT-2006-16	Bjørheim, Lars G.	Failure Assessment of Long Through Thickness Fatigue Cracks in Ship Hulls. (Dr.Ing. Thesis)
IMT-2006-17	Hansson, Lisbeth	Safety Management for Prevention of Occupational Accidents. (Dr.Ing. Thesis)
IMT-2006-18	Zhu, Xinying	Application of the CIP Method to Strongly Nonlinear Wave-Body Interaction Problems. (Dr.Ing. Thesis)
IMT-2006-19	Reite, Karl Johan	Modelling and Control of Trawl Systems. (Dr.Ing. Thesis)
IMT-2006-20	Smogeli, Øyvind Notland	Control of Marine Propellers. From Normal to Extreme Conditions. (Dr.Ing. Thesis)
IMT-2007-21	Storhaug, Gaute	Experimental Investigation of Wave Induced Vibrations and Their Effect on the Fatigue Loading of Ships. (Dr.Ing. Thesis)
IMT-2007-22	Sun, Hui	A Boundary Element Method Applied to Strongly Nonlinear Wave-Body Interaction Problems. (PhD Thesis, CeSOS)
IMT-2007-23	Rustad, Anne Marthine	Modelling and Control of Top Tensioned Risers. (PhD Thesis, CeSOS)
IMT-2007-24	Johansen, Vegar	Modelling flexible slender system for real-time simulations and control applications
IMT-2007-25	Wroldsen, Anders Sunde	Modelling and control of tensegrity structures.

		(PhD Thesis, CeSOS)
IMT-2007-26	Aronsen, Kristoffer Høye	An experimental investigation of in-line and combined inline and cross flow vortex induced vibrations. (Dr. avhandling, IMT)
IMT-2007-27	Gao, Zhen	Stochastic Response Analysis of Mooring Systems with Emphasis on Frequency-domain Analysis of Fatigue due to Wide-band Response Processes (PhD Thesis, CeSOS)
IMT-2007-28	Thorstensen, Tom Anders	Lifetime Profit Modelling of Ageing Systems Utilizing Information about Technical Condition. (Dr.ing. thesis, IMT)
IMT-2008-29	Refsnes, Jon Erling Gorset	Nonlinear Model-Based Control of Slender Body AUVs (PhD Thesis, IMT)
IMT-2008-30	Berntsen, Per Ivar B.	Structural Reliability Based Position Mooring. (PhD-Thesis, IMT)
IMT-2008-31	Ye, Naiquan	Fatigue Assessment of Aluminium Welded Box-stiffener Joints in Ships (Dr.ing. thesis, IMT)
IMT-2008-32	Radan, Damir	Integrated Control of Marine Electrical Power Systems. (PhD-Thesis, IMT)
IMT-2008-33	Thomassen, Paul	Methods for Dynamic Response Analysis and Fatigue Life Estimation of Floating Fish Cages. (Dr.ing. thesis, IMT)
IMT-2008-34	Pákozdi, Csaba	A Smoothed Particle Hydrodynamics Study of Two-dimensional Nonlinear Sloshing in Rectangular Tanks. (Dr.ing.thesis, IMT/ CeSOS)
IMT-2007-35	Grytøyr, Guttorm	A Higher-Order Boundary Element Method and Applications to Marine Hydrodynamics. (Dr.ing.thesis, IMT)
IMT-2008-36	Drummen, Ingo	Experimental and Numerical Investigation of Nonlinear Wave-Induced Load Effects in Containerships considering Hydroelasticity. (PhD thesis, CeSOS)
IMT-2008-37	Skejic, Renato	Maneuvering and Seakeeping of a Singel Ship and of Two Ships in Interaction. (PhD-Thesis, CeSOS)
IMT-2008-38	Harlem, Alf	An Age-Based Replacement Model for Repairable Systems with Attention to High-Speed Marine Diesel Engines. (PhD-Thesis, IMT)
IMT-2008-39	Alsos, Hagbart S.	Ship Grounding. Analysis of Ductile Fracture, Bottom Damage and Hull Girder Response. (PhD-thesis, IMT)
IMT-2008-40	Graczyk, Mateusz	Experimental Investigation of Sloshing Loading and Load Effects in Membrane LNG Tanks Subjected to Random Excitation. (PhD-thesis, CeSOS)
IMT-2008-41	Taghipour, Reza	Efficient Prediction of Dynamic Response for Flexible amd Multi-body Marine Structures. (PhD-

		thesis, CeSOS)
IMT-2008-42	Ruth, Eivind	Propulsion control and thrust allocation on marine vessels. (PhD thesis, CeSOS)
IMT-2008-43	Nystad, Bent Helge	Technical Condition Indexes and Remaining Useful Life of Aggregated Systems. PhD thesis, IMT
IMT-2008-44	Soni, Prashant Kumar	Hydrodynamic Coefficients for Vortex Induced Vibrations of Flexible Beams, PhD thesis, CeSOS
IMT-2009-45	Amlashi, Hadi K.K.	Ultimate Strength and Reliability-based Design of Ship Hulls with Emphasis on Combined Global and Local Loads. PhD Thesis, IMT
IMT-2009-46	Pedersen, Tom Arne	Bond Graph Modelling of Marine Power Systems. PhD Thesis, IMT
IMT-2009-47	Kristiansen, Trygve	Two-Dimensional Numerical and Experimental Studies of Piston-Mode Resonance. PhD-Thesis, CeSOS
IMT-2009-48	Ong, Muk Chen	Applications of a Standard High Reynolds Number Model and a Stochastic Scour Prediction Model for Marine Structures. PhD-thesis, IMT
IMT-2009-49	Hong, Lin	Simplified Analysis and Design of Ships subjected to Collision and Grounding. PhD-thesis, IMT
IMT-2009-50	Koushan, Kamran	Vortex Induced Vibrations of Free Span Pipelines, PhD thesis, IMT
IMT-2009-51	Korsvik, Jarl Eirik	Heuristic Methods for Ship Routing and Scheduling. PhD-thesis, IMT
IMT-2009-52	Lee, Jihoon	Experimental Investigation and Numerical in Analyzing the Ocean Current Displacement of Longlines. Ph.d.-Thesis, IMT.
IMT-2009-53	Vestbøstad, Tone Gran	A Numerical Study of Wave-in-Deck Impact usin a Two-Dimensional Constrained Interpolation Profile Method, Ph.d.thesis, CeSOS.
IMT-2009-54	Bruun, Kristine	Bond Graph Modelling of Fuel Cells for Marine Power Plants. Ph.d.-thesis, IMT
IMT 2009-55	Holstad, Anders	Numerical Investigation of Turbulence in a Sekwed Three-Dimensional Channel Flow, Ph.d.-thesis, IMT.
IMT 2009-56	Ayala-Uraga, Efren	Reliability-Based Assessment of Deteriorating Ship-shaped Offshore Structures, Ph.d.-thesis, IMT
IMT 2009-57	Kong, Xiangjun	A Numerical Study of a Damaged Ship in Beam Sea Waves. Ph.d.-thesis, IMT/CeSOS.
IMT 2010-58	Kristiansen, David	Wave Induced Effects on Floaters of Aquaculture Plants, Ph.d.-thesis, CeSOS.

IMT 2010-59	Ludvigsen, Martin	An ROV-Toolbox for Optical and Acoustic Scientific Seabed Investigation. Ph.d.-thesis IMT.
IMT 2010-60	Hals, Jørgen	Modelling and Phase Control of Wave-Energy Converters. Ph.d.thesis, CeSOS.
IMT 2010- 61	Shu, Zhi	Uncertainty Assessment of Wave Loads and Ultimate Strength of Tankers and Bulk Carriers in a Reliability Framework. Ph.d. Thesis, IMT/ CeSOS
IMT 2010-62	Shao, Yanlin	Numerical Potential-Flow Studies on Weakly-Nonlinear Wave-Body Interactions with/without Small Forward Speed, Ph.d.thesis,CeSOS.
IMT 2010-63	Califano, Andrea	Dynamic Loads on Marine Propellers due to Intermittent Ventilation. Ph.d.thesis, IMT.
IMT 2010-64	El Khoury, George	Numerical Simulations of Massively Separated Turbulent Flows, Ph.d.-thesis, IMT
IMT 2010-65	Seim, Knut Sponheim	Mixing Process in Dense Overflows with Emphasis on the Faroe Bank Channel Overflow. Ph.d.thesis, IMT
IMT 2010-66	Jia, Huirong	Structural Analysis of Intect and Damaged Ships in a Collission Risk Analysis Perspective. Ph.d.thesis CeSoS.
IMT 2010-67	Jiao, Linlin	Wave-Induced Effects on a Pontoon-type Very Large Floating Structures (VLFS). Ph.D.-thesis, CeSOS.
IMT 2010-68	Abrahamsen, Bjørn Christian	Sloshing Induced Tank Roof with Entrapped Air Pocket. Ph.d.thesis, CeSOS.
IMT 2011-69	Karimirad, Madjid	Stochastic Dynamic Response Analysis of Spar-Type Wind Turbines with Catenary or Taut Mooring Systems. Ph.d.-thesis, CeSOS.
IMT - 2011-70	Erlend Meland	Condition Monitoring of Safety Critical Valves. Ph.d.-thesis, IMT.
IMT – 2011-71	Yang, Limin	Stochastic Dynamic System Analysis of Wave Energy Converter with Hydraulic Power Take-Off, with Particular Reference to Wear Damage Analysis, Ph.d. Thesis, CeSOS.
IMT – 2011-72	Visscher, Jan	Application of Particla Image Velocimetry on Turbulent Marine Flows, Ph.d.Thesis, IMT.
IMT – 2011-73	Su, Biao	Numerical Predictions of Global and Local Ice Loads on Ships. Ph.d.Thesis, CeSOS.
IMT – 2011-74	Liu, Zhenhui	Analytical and Numerical Analysis of Iceberg Collision with Ship Structures. Ph.d.Thesis, IMT.
IMT – 2011-75	Aarsæther, Karl Gunnar	Modeling and Analysis of Ship Traffic by Observation and Numerical Simulation. Ph.d.Thesis, IMT.

Imt – 2011-76	Wu, Jie	Hydrodynamic Force Identification from Stochastic Vortex Induced Vibration Experiments with Slender Beams. Ph.d.Thesis, IMT.
Imt – 2011-77	Amini, Hamid	Azimuth Propulsors in Off-design Conditions. Ph.d.Thesis, IMT.
IMT – 2011-78	Nguyen, Tan-Hoi	Toward a System of Real-Time Prediction and Monitoring of Bottom Damage Conditions During Ship Grounding. Ph.d.thesis, IMT.
IMT- 2011-79	Tavakoli, Mohammad T.	Assessment of Oil Spill in Ship Collision and Grounding, Ph.d.thesis, IMT.
IMT- 2011-80	Guo, Bingjie	Numerical and Experimental Investigation of Added Resistance in Waves. Ph.d.Thesis, IMT.
IMT- 2011-81	Chen, Qiaofeng	Ultimate Strength of Aluminium Panels, considering HAZ Effects, IMT
IMT- 2012-82	Kota, Ravikiran S.	Wave Loads on Decks of Offshore Structures in Random Seas, CeSOS.
IMT- 2012-83	Sten, Ronny	Dynamic Simulation of Deep Water Drilling Risers with Heave Compensating System, IMT.
IMT- 2012-84	Berle, Øyvind	Risk and resilience in global maritime supply chains, IMT.
IMT- 2012-85	Fang, Shaoji	Fault Tolerant Position Mooring Control Based on Structural Reliability, CeSOS.
IMT- 2012-86	You, Jikun	Numerical studies on wave forces and moored ship motions in intermediate and shallow water, CeSOS.
IMT- 2012-87	Xiang ,Xu	Maneuvering of two interacting ships in waves, CeSOS
IMT- 2012-88	Dong, Wenbin	Time-domain fatigue response and reliability analysis of offshore wind turbines with emphasis on welded tubular joints and gear components, CeSOS
IMT- 2012-89	Zhu, Suji	Investigation of Wave-Induced Nonlinear Load Effects in Open Ships considering Hull Girder Vibrations in Bending and Torsion, CeSOS
IMT- 2012-90	Zhou, Li	Numerical and Experimental Investigation of Station-keeping in Level Ice, CeSOS
IMT- 2012-91	Ushakov, Sergey	Particulate matter emission characteristics from diesel enignes operating on conventional and alternative marine fuels, IMT
IMT- 2013-1	Yin, Decao	Experimental and Numerical Analysis of Combined In-line and Cross-flow Vortex Induced Vibrations, CeSOS

IMT-2013-2	Kurniawan, Adi	Modelling and geometry optimisation of wave energy converters, CeSOS
IMT-2013-3	Al Ryati, Nabil	Technical condition indexes doe auxiliary marine diesel engines, IMT
IMT-2013-4	Firoozkoohi, Reza	Experimental, numerical and analytical investigation of the effect of screens on sloshing, CeSOS
IMT-2013-5	Ommani, Babak	Potential-Flow Predictions of a Semi-Displacement Vessel Including Applications to Calm Water Broaching, CeSOS
IMT-2013-6	Xing, Yihan	Modelling and analysis of the gearbox in a floating spar-type wind turbine, CeSOS
IMT-7-2013	Balland, Océane	Optimization models for reducing air emissions from ships, IMT
IMT-8-2013	Yang, Dan	Transitional wake flow behind an inclined flat plate-----Computation and analysis, IMT
IMT-9-2013	Abdillah, Suyuthi	Prediction of Extreme Loads and Fatigue Damage for a Ship Hull due to Ice Action, IMT
IMT-10-2013	Ramìrez, Pedro Agustìn Pèrez	Ageing management and life extension of technical systems- Concepts and methods applied to oil and gas facilities, IMT
IMT-11-2013	Chuang, Zhenju	Experimental and Numerical Investigation of Speed Loss due to Seakeeping and Maneuvering. IMT
IMT-12-2013	Etemaddar, Mahmoud	Load and Response Analysis of Wind Turbines under Atmospheric Icing and Controller System Faults with Emphasis on Spar Type Floating Wind Turbines, IMT
IMT-13-2013	Lindstad, Haakon	Strategies and measures for reducing maritime CO2 emissons, IMT
IMT-14-2013	Haris, Sabril	Damage interaction analysis of ship collisions, IMT
IMT-15-2013	Shainee, Mohamed	Conceptual Design, Numerical and Experimental Investigation of a SPM Cage Concept for Offshore Mariculture, IMT
IMT-16-2013	Gansel, Lars	Flow past porous cylinders and effects of biofouling and fish behavior on the flow in and around Atlantic salmon net cages, IMT
IMT-17-2013	Gaspar, Henrique	Handling Aspects of Complexity in Conceptual Ship Design, IMT
IMT-18-2013	Thys, Maxime	Theoretical and Experimental Investigation of a Free Running Fishing Vessel at Small Frequency of Encounter, CeSOS
IMT-19-2013	Aglen, Ida	VIV in Free Spanning Pipelines, CeSOS

IMT-1-2014	Song, An	Theoretical and experimental studies of wave diffraction and radiation loads on a horizontally submerged perforated plate, CeSOS
IMT-2-2014	Rogne, Øyvind Ygre	Numerical and Experimental Investigation of a Hinged 5-body Wave Energy Converter, CeSOS
IMT-3-2014	Dai, Lijuan	Safe and efficient operation and maintenance of offshore wind farms ,IMT
IMT-4-2014	Bachynski, Erin Elizabeth	Design and Dynamic Analysis of Tension Leg Platform Wind Turbines, CeSOS
IMT-5-2014	Wang, Jingbo	Water Entry of Freefall Wedged – Wedge motions and Cavity Dynamics, CeSOS
IMT-6-2014	Kim, Ekaterina	Experimental and numerical studies related to the coupled behavior of ice mass and steel structures during accidental collisions, IMT
IMT-7-2014	Tan, Xiang	Numerical investigation of ship's continuous- mode icebreaking in leverl ice, CeSOS
IMT-8-2014	Muliawan, Made Jaya	Design and Analysis of Combined Floating Wave and Wind Power Facilities, with Emphasis on Extreme Load Effects of the Mooring System, CeSOS
IMT-9-2014	Jiang, Zhiyu	Long-term response analysis of wind turbines with an emphasis on fault and shutdown conditions, IMT
IMT-10-2014	Dukan, Fredrik	ROV Motion Control Systems, IMT
IMT-11-2014	Grimsmo, Nils I.	Dynamic simulations of hydraulic cylinder for heave compensation of deep water drilling risers, IMT
IMT-12-2014	Kvittem, Marit I.	Modelling and response analysis for fatigue design of a semisubmersible wind turbine, CeSOS
IMT-13-2014	Akhtar, Juned	The Effects of Human Fatigue on Risk at Sea, IMT
IMT-14-2014	Syahroni, Nur	Fatigue Assessment of Welded Joints Taking into Account Effects of Residual Stress, IMT
IMT-1-2015	Bøckmann, Eirik	Wave Propulsion of ships, IMT
IMT-2-2015	Wang, Kai	Modelling and dynamic analysis of a semi-submersible floating vertical axis wind turbine, CeSOS
IMT-3-2015	Fredriksen, Arnt Gunvald	A numerical and experimental study of a two-dimensional body with moonpool in waves and current, CeSOS
IMT-4-2015	Jose Patricio Gallardo Canabes	Numerical studies of viscous flow around bluff bodies, IMT

IMT-5-2015	Vegard Longva	Formulation and application of finite element techniques for slender marine structures subjected to contact interactions, IMT
IMT-6-2015	Jacobus De Vaal	Aerodynamic modelling of floating wind turbines, CeSOS
IMT-7-2015	Fachri Nasution	Fatigue Performance of Copper Power Conductors, IMT
IMT-8-2015	Oleh I Karpa	Development of bivariate extreme value distributions for applications in marine technology,CeSOS
IMT-9-2015	Daniel de Almeida Fernandes	An output feedback motion control system for ROVs, AMOS
IMT-10-2015	Bo Zhao	Particle Filter for Fault Diagnosis: Application to Dynamic Positioning Vessel and Underwater Robotics, CeSOS
IMT-11-2015	Wenting Zhu	Impact of emission allocation in maritime transportation, IMT
IMT-12-2015	Amir Rasekhi Nejad	Dynamic Analysis and Design of Gearboxes in Offshore Wind Turbines in a Structural Reliability Perspective, CeSOS
IMT-13-2015	Arturo Jesùs Ortega Malca	Dynamic Response of Flexibles Risers due to Unsteady Slug Flow, CeSOS
IMT-14-2015	Dagfinn Husjord	Guidance and decision-support system for safe navigation of ships operating in close proximity, IMT
IMT-15-2015	Anirban Bhattacharyya	Ducted Propellers: Behaviour in Waves and Scale Effects, IMT
IMT-16-2015	Qin Zhang	Image Processing for Ice Parameter Identification in Ice Management, IMT
IMT-1-2016	Vincentius Rumawas	Human Factors in Ship Design and Operation: An Experiential Learning, IMT
IMT-2-2016	Martin Storheim	Structural response in ship-platform and ship-ice collisions, IMT
IMT-3-2016	Mia Abrahamsen Prsic	Numerical Simulations of the Flow around single and Tandem Circular Cylinders Close to a Plane Wall, IMT
IMT-4-2016	Tufan Arslan	Large-eddy simulations of cross-flow around ship sections, IMT

IMT-5-2016	Pierre Yves-Henry	Parametrisation of aquatic vegetation in hydraulic and coastal research,IMT
IMT-6-2016	Lin Li	Dynamic Analysis of the Instalation of Monopiles for Offshore Wind Turbines, CeSOS
IMT-7-2016	Øivind Kåre Kjerstad	Dynamic Positioning of Marine Vessels in Ice, IMT
IMT-8-2016	Xiaopeng Wu	Numerical Analysis of Anchor Handling and Fish Trawling Operations in a Safety Perspective, CeSOS
IMT-9-2016	Zhengshun Cheng	Integrated Dynamic Analysis of Floating Vertical Axis Wind Turbines, CeSOS
IMT-10-2016	Ling Wan	Experimental and Numerical Study of a Combined Offshore Wind and Wave Energy Converter Concept
IMT-11-2016	Wei Chai	Stochastic dynamic analysis and reliability evaluation of the roll motion for ships in random seas, CeSOS
IMT-12-2016	Øyvind Selnes Patricksson	Decision support for conceptual ship design with focus on a changing life cycle and future uncertainty, IMT
IMT-13-2016	Mats Jørgen Thorsen	Time domain analysis of vortex-induced vibrations, IMT
IMT-14-2016	Edgar McGuinness	Safety in the Norwegian Fishing Fleet – Analysis and measures for improvement, IMT
IMT-15-2016	Sepideh Jafarzadeh	Energy effiency and emission abatement in the fishing fleet, IMT
IMT-16-2016	Wilson Ivan Guachamin Acero	Assessment of marine operations for offshore wind turbine installation with emphasis on response-based operational limits, IMT
IMT-17-2016	Mauro Candeloro	Tools and Methods for Autonomous Operations on Seabed and Water Coumn using Underwater Vehicles, IMT
IMT-18-2016	Valentin Chabaud	Real-Time Hybrid Model Testing of Floating Wind Tubines, IMT
IMT-1-2017	Mohammad Saud Afzal	Three-dimensional streaming in a sea bed boundary layer
IMT-2-2017	Peng Li	A Theoretical and Experimental Study of Wave-induced Hydroelastic Response of a Circular Floating Collar
IMT-3-2017	Martin Bergström	A simulation-based design method for arctic maritime transport systems

IMT-4-2017	Bhushan Taskar	The effect of waves on marine propellers and propulsion
IMT-5-2017	Mohsen Bardestani	A two-dimensional numerical and experimental study of a floater with net and sinker tube in waves and current
IMT-6-2017	Fatemeh Hoseini Dadmarzi	Direct Numerical Simualtion of turbulent wakes behind different plate configurations
IMT-7-2017	Michel R. Miyazaki	Modeling and control of hybrid marine power plants
IMT-8-2017	Giri Rajasekhar Gunnu	Safety and effiency enhancement of anchor handling operations with particular emphasis on the stability of anchor handling vessels
IMT-9-2017	Kevin Koosup Yum	Transient Performance and Emissions of a Turbocharged Diesel Engine for Marine Power Plants
IMT-10-2017	Zhaolong Yu	Hydrodynamic and structural aspects of ship collisions
IMT-11-2017	Martin Hassel	Risk Analysis and Modelling of Allisions between Passing Vessels and Offshore Installations
IMT-12-2017	Astrid H. Brodtkorb	Hybrid Control of Marine Vessels – Dynamic Positioning in Varying Conditions
IMT-13-2017	Kjersti Bruserud	Simultaneous stochastic model of waves and current for prediction of structural design loads
IMT-14-2017	Finn-Idar Grøtta Giske	Long-Term Extreme Response Analysis of Marine Structures Using Inverse Reliability Methods
IMT-15-2017	Stian Skjong	Modeling and Simulation of Maritime Systems and Operations for Virtual Prototyping using co-Simulations
IMT-1-2018	Yingguang Chu	Virtual Prototyping for Marine Crane Design and Operations
IMT-2-2018	Sergey Gavrilin	Validation of ship manoeuvring simulation models
IMT-3-2018	Jeevith Hegde	Tools and methods to manage risk in autonomous subsea inspection,maintenance and repair operations
IMT-4-2018	Ida M. Strand	Sea Loads on Closed Flexible Fish Cages
IMT-5-2018	Erlend Kvinge Jørgensen	Navigation and Control of Underwater Robotic Vehicles

IMT-6-2018	Bård Stovner	Aided Intertial Navigation of Underwater Vehicles
IMT-7-2018	Erlend Liavåg Grotle	Thermodynamic Response Enhanced by Sloshing in Marine LNG Fuel Tanks
IMT-8-2018	Børge Rokseth	Safety and Verification of Advanced Maritime Vessels
IMT-9-2018	Jan Vidar Ulveseter	Advances in Semi-Empirical Time Domain Modelling of Vortex-Induced Vibrations
IMT-10-2018	Chenyu Luan	Design and analysis for a steel braceless semi-submersible hull for supporting a 5-MW horizontal axis wind turbine